



All Theses and Dissertations

2008-03-20

Liquefaction Mitigation Using Vertical Composite Drains and Liquefaction Induced Downdrag on Piles: Implications for Deep Foundation Design

Spencer R. Strand
Brigham Young University - Provo

Follow this and additional works at: <https://scholarsarchive.byu.edu/etd>

 Part of the [Civil and Environmental Engineering Commons](#)

BYU ScholarsArchive Citation

Strand, Spencer R., "Liquefaction Mitigation Using Vertical Composite Drains and Liquefaction Induced Downdrag on Piles: Implications for Deep Foundation Design" (2008). *All Theses and Dissertations*. 1648.
<https://scholarsarchive.byu.edu/etd/1648>

This Dissertation is brought to you for free and open access by BYU ScholarsArchive. It has been accepted for inclusion in All Theses and Dissertations by an authorized administrator of BYU ScholarsArchive. For more information, please contact scholarsarchive@byu.edu, ellen_amatangelo@byu.edu.

LIQUEFACTION MITIGATION USING VERTICAL COMPOSITE
DRAINS AND LIQUEFACTION-INDUCED DOWNDRAW
ON PILES: IMPLICATIONS FOR DEEP
FOUNDATION DESIGN

by

Spencer R. Strand

A dissertation submitted to the faculty of

Brigham Young University

in partial fulfillment of the requirement for the degree of

Doctor of Philosophy

Department of Civil and Environmental Engineering

Brigham Young University

April 2008

BRIGHAM YOUNG UNIVERSITY

GRADUATE COMMITTEE APPROVAL

of a dissertation submitted by

Spencer R. Strand

This dissertation has been read by each member of the following graduate committee and by a majority vote has been found satisfactory.

_____	_____
Date	Kyle M. Rollins, Chair
_____	_____
Date	Steven F. Bartlett
_____	_____
Date	Travis M. Gerber
_____	_____
Date	E. James Nelson
_____	_____
Date	T. Leslie Youd

BRIGHAM YOUNG UNIVERSITY

As chair of the candidate's graduate committee, I have read the dissertation of Spencer R. Strand in its final form and have found that (1) its format, citations and bibliographical styles are consistent and acceptable and fulfill university and department style requirements; (2) its illustrative materials including figures, tables, and charts are in place; and (3) the final manuscript is satisfactory to the graduate committee and is ready for submission to the university library.

Date

Kyle M. Rollins
Chair, Graduate Committee

Accepted for the Department

E. James Nelson
Graduate Coordinator

Accepted for the College

Alan R. Parkinson
Dean, Ira A. Fulton College of Engineering
and Technology

ABSTRACT

LIQUEFACTION MITIGATION USING VERTICAL COMPOSITE DRAINS AND LIQUEFACTION-INDUCED DOWNDRAG ON PILES: IMPLICATIONS FOR DEEP FOUNDATION DESIGN

Spencer R. Strand

Department of Civil and Environmental Engineering

Doctor of Philosophy

Deep foundations constructed in liquefiable soils require specialized design. The design engineer of such foundations must consider the effects of liquefaction on the foundation and overlying structure, such as excessive settlement, loss of skin friction at the soil-pile interface, and the development of downdrag on the pile.

Controlled blasting was employed to liquefy a loose, saturated sand in order to test the liquefaction prevention capabilities of full-scale, vertical composite earthquake (EQ) drains and to investigate the development of downdrag on full-scale test piles. Blasting produced liquefaction at a test site without EQ drains which eventually resulted in 270 mm of settlement. Liquefaction caused the skin friction on the test pile to decrease to zero immediately following blasting. As pore pressures dissipated and the

sand settled, negative skin friction developed, with a maximum magnitude of about one-half of the positive skin friction.

Blasting also produced liquefaction at a site with drains but the settlement was reduced to 225 mm, a decrease of 17% relative to the untreated site. Nevertheless, the dissipation rate dramatically increased. Skin friction did not decrease to zero in the liquefied sand and negative skin friction increased to a value equal to the positive skin friction in the liquefied layer.

The computer software, FEQDrain, was utilized to develop a calibrated model of the soil profile using pore pressure and settlement data measured during blast testing. This model was then used to simulate drainage systems with smaller drain spacing and larger drain diameter. Results indicated that pore pressures and settlement could be limited to levels acceptable for many applications. However, development of downdrag on deep foundations would not likely be prevented.

EQ drains provide an attractive method of liquefaction mitigation. Furthermore, liquefaction can cause significant amount of downdrag on pile foundations which should be accounted for in deep foundation design.

ACKNOWLEDGMENTS

I would like to express my appreciation to Dr. Kyle M. Rollins and his invitation to assist him in his research into liquefaction and deep foundations. I thank him also for his continued support and guidance. The burden of many long hours was often lightened by his humor. I would also like to thank all the members of my graduate committee for their invaluable input.

I also express my gratitude to the many generous benefactors who supported me financially. Most particularly I would like to thank the Ralph Rollins family; the scholarships they funded made my education possible.

Research funding was provided by a grant from the National Cooperative Highway Research Program-Ideas Deserving Exploratory Analysis (NCHRP-IDEA) program as project 103. This support is gratefully acknowledged.

I also wish to express appreciation to the British Columbia Ministry of Transportation for granting the use of the Vancouver test site. Nilex, Inc. donated all equipment, personnel and materials necessary to install the drains at the test site which made this project possible. Advanced Drainage Systems, Inc. donated the EQ-Drain pipes installed at the test areas. ConeTec, Inc. provided equipment and personnel necessary to perform CPT soundings at no cost to the project. These donations and contributions made this project feasible.

Finally, I would like give a special thanks to my wife, Shelly, who was a source of constant support and encouragement. Without her support, I never would have even begun the journey that is a doctoral degree.

TABLE OF CONTENTS

1	Introduction	1
1.1	Liquefaction Mitigation	4
1.1.1	Liquefaction mitigation through pore pressure dissipation	4
1.1.2	Liquefaction mitigation through foundation design	7
1.2	Investigative Approach	8
1.2.1	Earthquake drain testing	9
1.2.2	Pile testing	10
1.2.3	Concurrent studies	10
2	Literature Review	13
2.1	Performance of EQ Drains	13
2.1.1	Behavior of vertical gravel drains	14
2.1.1.1	Brennan and Madabhushi, 2002	14
2.1.1.2	Brennan and Madabhushi, 2006	16
2.1.2	Behavior of EQ drains	17
2.1.2.1	Rathje et al., 2004	17
2.1.2.2	Rollins et al., 2004	19
2.1.2.3	Rollins and Anderson, 2004	21
2.2	Development of Downdrag on Piles During Liquefaction	22

	2.2.1 Bozozuk, 1981	23
	2.2.2 Boulanger and Brandenberg, 2004	27
2.3	Summary	29
	2.3.1 Performance of EQ drains	29
	2.3.2 Development of downdrag on a pile	30
3	Site Characterization	31
	3.1 CPT Data	35
	3.2 Shear Wave Velocity	42
	3.3 Permeability Testing	42
	3.4 Grain-Size Distribution Tests	46
	3.5 In-situ Density and Moisture Content	48
	3.6 SPT Blow Count Correlations	49
4	Pilot Liquefaction Testing at Site 1	53
	4.1 Test Blasting Design	53
	4.2 Blast Hole Installation	56
	4.2.1 Blast hole installation induced settlement	60
	4.3 Pore Pressure Monitoring	60
	4.3.1 Determination of the degree of liquefaction	62
	4.4 Settlement	63
	4.4.1 Total ground surface settlement	63
	4.4.2 Real-time settlement	64
	4.4.3 Depth-related settlement	65

4.5	Results of Preliminary Blast Testing at Site 1	66
4.5.1	Blast induced excess pore pressure	66
4.5.2	Blast induced settlement	70
4.5.2.1	Real-time ground surface settlement	70
4.5.2.2	Total ground surface settlement	72
4.5.2.3	Depth-related ground settlement	77
5	Pile Foundation Design, Instrumentation, and Installation	81
5.1	Pile Foundation Design and Installation	83
5.1.1	Pile design	86
5.1.1.1	LCPC method	86
5.1.1.2	Eslami and Fellenius method	87
5.1.1.3	Determination of pile length	88
5.1.2	Instrumented test pile construction	93
5.1.3	Pile driving	94
5.1.4	Reaction frame construction	96
6	Site 2–Untreated Area Pile Testing	99
6.1	Test Layout and Instrumentation	99
6.1.1	Monitoring of real-time ground surface settlement	103
6.2	Blast Hole Installation and Influence on Surrounding Soil	104
6.3	Pile Installation and Influence on Surrounding Soil	105
6.4	Pile Load Testing Prior to Blasting	109
6.4.1	First static load test	109

	6.4.2	Second static load test	111
	6.4.3	Effect of setup on pile capacity	112
	6.4.4	Comparison of measured response with predictive response	121
	6.4.4.1	Comparison of unit side resistance	121
	6.4.4.2	Comparison of end-bearing	130
	6.4.4.3	Comparisons with predictive methods summarized . . .	131
6.5		Blast Test 1	132
	6.5.1	Excess pore pressure generation and dissipation	133
	6.5.2	Blast induced settlement	135
	6.5.3	Pile load transfer variations due to liquefaction	137
6.6		Blast Test 2	141
	6.6.1	Pre-blast skin friction mobilization	142
	6.6.2	Excess pore pressure generation and dissipation	145
	6.6.3	Blast-induced settlement	147
	6.6.4	Pile load transfer variations due to liquefaction	151
	6.6.5	Absence of Downdrag in Upper “Crust”	155
6.7		Post-Blast Site Characterization	158
7		Earthquake Drains	161
	7.1	Drain Properties	161
	7.2	Drain Installation	162
	7.3	Drain Installation and Influence on Surrounding Soil	164
8		Site 3—Treated Area Pile Testing	169

8.1	Test Layout and Instrumentation	169
8.2	Pile Installation and Influence on Surrounding Soil	173
8.3	Pile Load Testing Prior to Blasting	175
	8.3.1 Load transfer	177
	8.3.2 Comparison of measured response with predicted response	184
	8.3.2.1 Comparison of unit side resistance	184
	8.3.2.2 Comparison of end-bearing	188
	8.3.2.3 Comparisons with predictive methods summarized ...	189
8.4	Blast Test	190
	8.4.1 Pre-blast skin friction mobilization	190
	8.4.2 Excess pore pressure generation and dissipation	192
	8.4.3 Blast-induced settlement	199
	8.4.4 Pile load transfer variations due to liquefaction	204
9	Computer Analysis of Blast Liquefaction Tests	209
9.1	Mathematical Formulation	210
	9.1.1 Soil compressibility	211
	9.1.2 Pore pressure generation	212
	9.1.3 Boundary conditions	213
9.2	Calibration of Computer Model	216
	9.2.1 Selection of soil input parameters	216
	9.2.1.1 Hydraulic conductivity	216
	9.2.1.2 Modulus of compressibility	218

	9.2.1.3	Relative density	220
	9.2.1.4	Number of cycles to cause liquefaction	221
	9.2.1.5	Summary of calibrated values	221
	9.2.1.6	Drain input properties	221
	9.2.2	Other required input parameters	222
	9.2.3	Measured and computed pore pressure and settlement	223
9.3		EQ Drain Performance with Different Drain Arrangements	226
9.4		EQ Drain Performance Under Different Earthquake Loadings	229
9.5		Considerations in Design of Drain Spacing	232
10		Site 4—Statnamic Testing	235
10.1		Site Description	235
10.2		Test Description	236
	10.2.1	Test apparatus description	239
10.3		Test Instrumentation and Monitoring	239
	10.3.1	Test pile	239
	10.3.2	Blast hole layout	240
	10.3.3	Pore pressure monitoring	242
	10.3.4	Settlement monitoring	242
10.4		Statnamic Load Testing	242
10.5		Blast Testing	245
	10.5.1	Ground surface settlement	245
	10.5.2	Pore pressure generation	247

10.5.3 Load transfer	248
10.6 Implications for Design of Deep Foundations	253
11 Conclusions	257
References	261
Appendix A	265

LIST OF TABLES

Table 3.1. Summary of dry unit weight, in situ moisture content and moist unit weight determined with a nuclear density gauge at several depths in the hand-excavated pit.	50
Table 3.2. Summary of in situ unit weight and moisture content for Unit 2 at Vancouver test site. Samples were recovered using a shelby tube.	50
Table 4.3. Depth to water table immediately before each blast test.	63
Table 5.4. Values of C_s used in the Eslami and Fellenius method to compute unit side friction.	90
Table 5.5. Summary of side resistance and end-bearing resistance predicted by LCPC and Eslami and Fellenius methods for layers in the soil profile at test sites.	90
Table 6.6. Unit side resistance developed by the pile during static load testing at Site 2, transformed onto the generalized soil profile.	126
Table 6.7. Total side resistance developed by the test pile during both static load tests at Site 2.	129
Table 6.8. Comparison of calculated and predicted values of end-bearing at Site 2.	130
Table 6.9. Comparison of unit side resistance (skin friction) developed within the target zone immediately before blasting and at the end of settlement with predicted values of skin friction.	141
Table 6.10. Summary of unit side resistance, τ , as measured immediately before the second blast test at Site 2 compared with maximum unit side resistance values measured during the second static load test.	145
Table 6.11. Comparison of unit side resistance values within the liquefied zone measured immediately before blasting and at the end of settlement with values predicted by the LCPC and Eslami and Fellenius methods.	155

Table 8.12. Comparison of transformed values of unit side resistance for Site 3.	185
Table 8.13. Side resistance developed during static load testing at Site 3.	188
Table 8.14. Comparison of calculated and predicted values of end-bearing.	189
Table 8.15. Summary of unit side resistance, τ , as measured immediately before the second blast test at Site 2 compared with maximum unit side resistance values measured during the second static load test.	191
Table 8.16. Comparison of unit side resistance values within the liquefied zone measured immediately before blasting and at the end of settlement with values predicted by the LCPC and Eslami and Fellenius methods.	205
Table 8.17. Comparison of unit side resistance (skin friction) values developed within the target zone immediately before blasting and at the end of settlement measured during the blast tests at Sites 2 and 3 with values predicted by the LCPC and Eslami and Fellenius methods.	207
Table 9.1. Typical values for horizontal hydraulic conductivity (k_h) from Pestana <i>et al.</i> , 1997 (after Terzaghi and Peck, 1948).	217
Table 9.2. Relationship between k_h and k_y from Pestana <i>et al.</i> (1997).	218
Table 9.3. Summary of input properties for FEQDrain analyses.	222
Table 9.4. Summary of results for various drain size and spacing configuration simulations with FEQDrain.	226
Table 9.5. Equivalent number of cycles due to earthquake load, N_{eq} (from Seed and Idriss, 1982).	230
Table 9.6. Duration of earthquake strong motion (from Seed <i>et al.</i> , 1975).	230
Table 9.7. Summary of input parameters and analysis results for the maximum design earthquake with limiting excess pore pressure ratio located at 5.5 m depth.	232
Table 10.1. Comparison of unit side resistance (skin friction) values developed within the target zone immediately before blasting and at the end of settlement measured during the blast test at Sites 2, 3, and 4 with values predicted by the LCPC and Eslami and Fellenius methods.	252
Table A1. Summary of pile driving data for the pile foundation installed at Site 2.	265

Table A2. Summary of pile driving data for the pile foundation installed at Site 3. . . .	267
Table A3. Summary of unit side resistance, T (kN/m ²), for the six simplified load-depth curves for the first static load test at Site 2.	269
Table A4. Summary of unit side resistance, T (kN/m ²), for the nine simplified load-depth curves for the second static load test at Site 2.	270
Table A5. Summary of calculated deflections, Z (mm), for the six simplified load-depth curves for first static load test at Site 2.	270
Table A6. Summary of calculated pile deflection, Z (mm), for the nine simplified load-depth curves for the second static load test at Site 2.	270
Table A7. Summary of unit side resistance, T (kN/m ²), for the simplified load-depth curves for the first static load test at Site 3.	271
Table A8. Summary of unit side resistance, T (kN/m ²), for the simplified load-depth curves for the second static load test at Site 3.	271
Table A9. Summary of calculated pile deflection, Z (mm), for the simplified load-depth curves for the first static load test at Site 3.	271
Table A10. Summary of calculated pile deflection, Z (mm), for the simplified load-depth curves for the second static load test at Site 3.	272

LIST OF FIGURES

Figure 1.1 1964 Niigata Japan: Showa Bridge collapsed due to pier collapse caused by liquefaction.	2
Figure 1.2 1983 Nihonkai-Chubu: Liquefaction caused unstable soils to fail. Flagpole foundation foreground was placed shallowly. School building to the left was founded on a pile foundation and suffered no damage.	3
Figure 1.3 1964 Niigata Japan: Liquefaction caused major settlement. The building at center rotated 70 degrees from vertical. Surprisingly, little structural damage occurred to the apartment buildings. Some buildings were later righted and re-inhabited.	3
Figure 1.4 Typical soil improvement techniques for densifying loose saturated sands to prevent earthquake-induced liquefaction (after www.haywardbaker.com).	4
Figure 1.5 Vertical drains for mitigating the liquefaction hazard posed by loose saturated sand.	5
Figure 1.6 Normalized coefficient of volume compressibility versus pore pressure ratio for sands at various relative densities. Settlement is negligible when peak pore pressure ratio remains below approximately 0.40 (after Seed <i>et al.</i> , 1975a).	6
Figure 2.1 Excess pore pressure ratio time histories induced by vibrosies oil-prospecting truck for sand volume with and without EQ drain (reproduced from Rathje <i>et al.</i> , 2004).	18
Figure 2.2 Theoretical load distribution in pile pre-stressed by downdrag under applied load (after Bozozuk, 1981).	24
Figure 2.3 Load distribution in test pile at various levels of applied load (from Bozozuk, 1981).	26
Figure 3.1 Location of test site on Deas Island, south of Vancouver, British Columbia, Canada.	32

Figure 3.2 Location of test site relative to previous study sites and the CANLEX Phase II site.	33
Figure 3.3 Detailed schematic drawing of the layout of the test site.	34
Figure 3.4 Results of the preliminary CPT performed at Site 1.	36
Figure 3.5 Results of the preliminary CPT performed at Site 2.	37
Figure 3.6 Results of the preliminary CPT performed at Site 3.	38
Figure 3.7 Generalized soil profile interpreted from CPT results.	39
Figure 3.8 Comparison of cone tip resistance, q_c , and relative density, D_r , for Sites 1, 2, and 3, from the preliminary CPT soundings.	41
Figure 3.9 Shear wave velocity versus depth profiles at Site 1 and nearby test sites.	43
Figure 3.10 Horizontal permeability versus depth curves from several tests near Site 1.	45
Figure 3.11 Range of grain size distributions for Fraser River sand between 5.5m to 11.5m depth (from Gohl, 2002).	46
Figure 3.12 Grain size distribution curves for soil samples of Fraser River sand recovered during the course of sensor installation at site 1.	47
Figure 3.13 Grain size distribution curves for soil samples recovered from a hand-excavated pit and a Shelby tube sampler.	48
Figure 3.14 Void ratio versus depth curves developed as part of the CANLEX study (after Wride <i>et al</i> , 2000).	51
Figure 4.1 Layout of blast holes and instrumentation used during preliminary blast testing at Site 1.	55
Figure 4.2 Drain installation was accomplished with the use of a 70 ton crane and a vibratory hammer and mandrel.	57
Figure 4.3 Mandrels used in EQDrain and blast hole installation. Mandrel on left has three “fins” designed to transfer vibrational energy to surrounding soil. Mandrel on right is smooth.	58

Figure 4.4 Photograph of an EQDrain tied to an anchor. Anchors measured 305 mm x 305 mm x 12.5 mm. Generally, the anchors had the corners bent over; this one did not.	59
Figure 4.5 Schematic drawing of pore pressure transducer and hard nylon protective body (after Rollins and Anderson, 2004).	61
Figure 4.6 Schematic sketch of the layout of the survey measurement points used at Sites 1, 2, and 3 to monitor total ground surface settlement.	64
Figure 4.7 Generation of pore pressure during the first blast test at Site 1.	67
Figure 4.8 Dissipation of pore pressure after the first blast test at Site 1.	68
Figure 4.9 Generation of pore pressure during the third blast test at Site 1.	69
Figure 4.10 Dissipation of pore pressure after the third blast test at Site 1.	69
Figure 4.11 Real-time ground surface settlement measured by the string potentiometers during the first blast test at Site 1.	71
Figure 4.12 Real-time ground surface settlement measured by the string potentiometers during the third blast test at Site 1.	72
Figure 4.13 Contour plot of ground surface settlement resulting from the first blast test at Site 1.	73
Figure 4.14 Contour plot of ground surface settlement resulting from the third blast test at Site 1.	74
Figure 4.15 Average settlement with increasing distance from the center of Site 1 caused by the first test blast.	75
Figure 4.16 Variation of average ground surface settlement with increasing distance from center of Site 1 caused by the third test blast.	75
Figure 4.17 Comparison of maximum ground surface settlement measured by the string potentiometers and the level survey for the first blast test at Site 1.	76
Figure 4.18 Comparison of maximum ground surface settlement measured by the string potentiometers and the level survey for the third blast test at Site 1.	77
Figure 4.19 Comparison of settlement as a function of depth as measured with the Sondex tube for the first and third blast tests at Site 1.	78

Figure 5.1 Diagram of the development of skin friction.	82
Figure 5.2 Plan view of pile foundations installed at both Sites 2 and 3.	84
Figure 5.3 Profile view of pile foundations installed at both Sites 2 and 3.	85
Figure 5.4 Relationship between unit side friction and cone tip resistance for driven steel pipe pile in sand and clay based on the LCPC method.	87
Figure 5.5 Soil profiling chart developed by Eslami and Fellenius (1997) used in their method to determine soil type.	89
Figure 5.6 Total and side resistance for the test piles at Sites 2 and 3 predicted by the LCPC method.	91
Figure 5.7 Side and total resistance for the test piles at Sites 2 and 3 predicted by the Eslami and Fellenius method.	92
Figure 5.8 Welding the instrumented segments of the test piles before driving.	95
Figure 5.9 Photograph of test pile being driven with 2500 kg drop hammer.	96
Figure 5.10 Photograph of the completed test frame. The wooden frame in the foreground was part of the test apparatus involved with the vane shear test.	97
Figure 6.11 Plan view of pile foundation and instrument layout at Site 2.	101
Figure 6.12 Profile view of pile foundation and instrumentation layout at Site 2.	102
Figure 6.13 Comparison of CPT results from Site 2.	107
Figure 6.14 Comparison of CPT soundings performed at Site 2.	108
Figure 6.15 Comparison of the pile-head-load versus pile-head-deflection curves resulting from the two static load tests performed at Site 2.	110
Figure 6.16 Load-depth curves from the static load test performed one day after pile driving at Site 2.	113
Figure 6.17 Load-depth curves from the static load test performed one month after pile driving at Site 2.	114

Figure 6.18 Simplified load-depth curves used to develop T-Z curves for the first static load test performed at Site 2.	115
Figure 6.19 Simplified load-depth curves used to develop T-Z curves for the second static load test at Site 2.	116
Figure 6.20 T-Z curves for the first static load test performed at Site 2.	117
Figure 6.21 T-Z curves for the second static load test performed at Site 2.	117
Figure 6.22 T-Z curves for the second static load test performed at Site 2, excluding the top and bottom depth intervals.	119
Figure 6.23 Comparison of T-Z curves for the first and second static load tests at Site 2.	120
Figure 6.24 Comparison of measured values of unit side resistance for the first static load test with estimated values for Site 2.	122
Figure 6.25 Comparison of measured values of unit side resistance for the second static load test with estimated values for Site 2.	123
Figure 6.26 Comparison of measured and estimated values of unit side resistance values for the first static load test at Site 2. All values have been transformed such that layer boundaries correspond to the generalized soil profile.	125
Figure 6.27 Comparison of measured values of unit side resistance for the second static load test with estimated values. All values have been transformed such that layer boundaries correspond to the generalized soil profile.	125
Figure 6.28 Load-depth curves corresponding to the largest sustained loads during each of the two static load tests performed at Site 2.	128
Figure 6.29 Plot of generation of pore pressure during the first blast test at Site 2.	134
Figure 6.30 Dissipation of pore pressures during the first blast test at Site 2.	134
Figure 6.31 Contour plot of ground surface settlement caused by the first blast test at Site 2.	135
Figure 6.32 Variation of average settlement versus radial distance from the center of the test area caused by the first blast test at Site 2.	136

Figure 6.33 Settlement as a function of depth measured by the Sondex tube for the first test blast at Site 2.	137
Figure 6.34 Load applied to test pile at Site 2 during the first blast test.	138
Figure 6.35 Variation of load transfer during the first blast test at Site 2.	139
Figure 6.36 Measured and simplified load-depth curves for the test pile immediately before the second blast test at Site 2.	143
Figure 6.37 Comparison of unit side resistance values measured immediately before the second test blast and maximum measured values of unit side resistance at Site 2 with estimated unit side resistance values.	144
Figure 6.38 Generation of pore pressure during the second blast test at Site 2.	146
Figure 6.39 Dissipation of pore pressure after the second blast test at Site 2.	147
Figure 6.40 Contour plot of settlement caused by the second test blast at Site 2.	148
Figure 6.41 Comparison of average ground surface settlement caused by both blast tests at Site 2.	149
Figure 6.42 Comparison of settlement measured by the Sondex tube at Site 2 for both test blasts.	149
Figure 6.43 Real-time ground surface settlement measured by the string potentiometers during the second blast test at Site 2.	151
Figure 6.44 Load applied to test pile at Site 2 during the second blast test.	152
Figure 6.45 Variation of load transfer during the second blast test at Site 2.	153
Figure 6.46 Comparison of CPT data for all soundings performed at Site 2.	159
Figure 7.1 Section of EQ Drain; light suspended on the inside illuminates the slots (after Rollins and Anderson, 2002).	162
Figure 7.2 Layout of EQ drains at Site 3.	163
Figure 7.3 Contour plot of ground surface settlement caused by installation of earthquake drains at Site 3.	165

Figure 7.4 Average settlement versus distance curve caused by installation of EQ drains and blast holes at Site 3.	166
Figure 7.5 Comparison of CPT soundings taken performed at Site 3.	167
Figure 7.6 View of localized settlement surrounding an EQ Drain. Localized settlement immediately surrounding the drains commonly exceeded 300 mm.	168
Figure 8.1 Plan view of pile foundation and instrumentation at at Site 3.	170
Figure 8.2 Profile view of pile foundation and instrumentation layout at Site 3.	171
Figure 8.3 Comparison of CPT results from Site 3.	174
Figure 8.4 Pile-head-load versus pile-head-deflection curves from the two static axial load tests performed on the test pile at Site 3.	176
Figure 8.5 Comparison of pile-head-load versus pile-head-deflection curves for all static load tests performed at Sites 2 and 3.	177
Figure 8.6 Load versus depth curves for the first static load test performed at Site 3.	178
Figure 8.7 Load versus depth curves for the second static load test performed at Site 3.	178
Figure 8.8 Simplified load-depth curves for the first static load test performed at Site 3.	179
Figure 8.9 Simplified load-depth curves for the second static load test performed at Site 3.	179
Figure 8.10 T-Z curves developed for the first static load test at Site 3.	180
Figure 8.11 T-Z curves developed for the second static load test at Site 3.	181
Figure 8.12 T-Z curves developed for the first static load test at Site 3 excluding data from the top depth interval.	182
Figure 8.13 T-Z curves developed for the second static load test at Site 3 excluding data from the top depth interval.	182
Figure 8.14 Comparison of measured unit side resistance values with those values predicted by the LCPC and Eslami and Fellenius methods.	184

Figure 8.15 Comparison of transformed measured and predicted values of unit side resistance for Site 3.	185
Figure 8.16 Load-depth curves corresponding to the largest sustained loads applied during each of the two static load tests at Site 3.	187
Figure 8.17 Comparison of unit side resistance mobilized immediately prior to blast testing with maximum values at Site 3.	191
Figure 8.18 Comparison of pore pressure generation at Sites 2 and 3 recorded at 6.7 m and 6.4 m depth. The piezometer at Site 2 was located at 6.6 m and the piezometer at Site 3 was located at 6.4 m depth.	193
Figure 8.19 Comparison of pore pressure generation at Sites 2 and 3 recorded at 8.5 m depth.	193
Figure 8.20 Comparison of pore pressure generation at Sites 2 and 3 recorded at 10.7 m depth.	194
Figure 8.21 Comparison of pore pressure generation at Sites 2 and 3 recorded at 12.8 m and 12.5 m depth. The piezometer at Site 2 was located at 12.8 m depth and the piezometer at Site 3 was located at 12.5 m depth.	194
Figure 8.22 Comparison of pore pressure generation at Sites 2 and 3 recorded at 16.8 m depth.	195
Figure 8.23 Comparison of pore pressure dissipation at Sites 2 and 3 recorded at 6.7 m and 6.4 m depth. The piezometer at Site 2 was located at 6.7 m and the piezometer at Site 3 was located at 6.4 m depth.	196
Figure 8.24 Comparison of pore pressure dissipation at Sites 2 and 3 recorded at 8.5 m depth. Piezometers at both sites were located at 8.5 m depth.	197
Figure 8.25 Comparison of pore pressure dissipation at Sites 2 and 3 at 10.7 m depth. Piezometers at both sites were located at 10.7 m depth.	197
Figure 8.26 Comparison of pore pressure dissipation at Sites 2 and 3. The piezometer at Site 2 was located at 12.8 m depth and the piezometer at Site 3 was located at 12.5 m depth.	198
Figure 8.27 Comparison of pore pressure dissipation at Sites 2 and 3 measured by piezometers located at 16.8 m depth.	198

Figure 8.28 Contours of ground surface settlement caused by blasting at Site 3.	199
Figure 8.29 Comparison of average ground surface settlement caused by blast testing at Sites 2 and 3.	200
Figure 8.30 Settlement profile measured with the Sondex tube at Site 3.	201
Figure 8.31 Real-time settlement measured during blast testing at Site 3.	203
Figure 8.32 Comparison of normalized settlement at Sites 2 and 3.	203
Figure 8.33 Load applied to the test pile during blast testing at Site 3.	204
Figure 8.34 Plot of load in test pile at Site 3 immediately before the blast, immediately after the blast, and the end of settlement.	205
Figure 8.35 Comparison of load versus depth curves for the test piles at Sites 2 and 3.	208
Figure 9.1 Boundary conditions for analysis of EQ drains (after Pestana <i>et al.</i> , 1997).	214
Figure 9.2 Comparison of calibrated values of horizontal hydraulic conductivity (k_h) versus depth with values measured in situ by Rollins and Anderson (2004).	219
Figure 9.3 Variation in normalized coefficient of compressibility (M_v/M_{vi}) versus peak pore pressure ratio (R_u) for sands of various relative densities (D_r) from (a) laboratory tests (after Lee and Albaisa, 1974), and (b) as modeled in FEQDrain (after Seed <i>et al.</i> , 1975a).	220
Figure 9.4 Comparison of measured and computed excess pore pressure ratios for the blast test at Site 3 at a depth of 6.7 m.	224
Figure 9.5 Comparison of measured and calculated excess pore pressure ratios for the blast test at Site 3 at a depth of 8.5 m.	224
Figure 9.6 Comparison of measured and calculated excess pore pressure ratios for the blast test at Site 3 at a depth of 10.8 m.	225
Figure 9.7 Comparison of measured and calculated excess pore pressure ratios for the blast test at Site 3 at a depth of 12.8 m.	225
Figure 9.8 Comparison of R_u values measured during blast testing and calculated values for Simulations 1 through 3 at 6.7 m depth.	227

Figure 9.9 Comparison of excess pore pressure ratios measured during blast testing and values calculated by FEQDrain for Simulations 1 through 3 for a depth of 8.5 m.	228
Figure 9.10 Comparison of excess pore pressure values measured during blast testing and values calculated by FEQDrain for Simulations 1 through 3 at a depth of 10.8 m.	228
Figure 9.11 Comparison of excess pore pressure values measured during blast testing and values calculated by FEQDrain for Simulations 1 through 3 at a depth of 12.8 m.	229
Figure 10.1 Results of the CPT sounding performed at Site 4.	237
Figure 10.2 Comparison of cone tip resistance, Q_c , and relative density, D_r , for all four test sites from the first CPT soundings performed at each test site.	238
Figure 10.3 Photograph of the statnamic testing apparatus installed at Site 4.	240
Figure 10.4 Schematic diagram of the statnamic testing apparatus. Drawing not to scale.	241
Figure 10.5 Pile-head-load versus pile-head-deflection curves from the two statnamic load tests performed at Site 4.	243
Figure 10.6 Comparison of pile-head-load versus pile-head-deflection curves for Sites 2, 3, and 4.	244
Figure 10.7 Average ground surface settlement versus distance caused by blasting at Site 4.	246
Figure 10.8 Generation of pore pressure during the blast test at Site 4.	247
Figure 10.9 Comparison of load-depth curves from Sites 2, 3, and 4.	249

1 Introduction

Each year earthquakes cause enormous amounts of damage worldwide. Much of the damage can be directly attributed to liquefaction. For instance, liquefaction caused nearly \$1 billion worth of damage in the 1964 Niigata, Japan earthquake (NRC, 1985). Liquefaction was also responsible for about \$100 million in damage in the 1989 Loma Prieta earthquake (Holzer, 1998) and over \$11.8 billion in damage just to port and wharf facilities during the 1995 Kobe, Japan earthquake (EQE, 1995).

Liquefaction occurs naturally during earthquakes in loose, saturated, cohesionless soils. Strong ground shaking causes the loose soil to compact. However, the water in the interparticle voids cannot escape immediately. As the soil attempts to compress, the pore pressure increases, temporarily decreasing the effective stress felt by the soil particles. If the pore pressure increases enough, the water will carry most, if not all the weight of the overlying soil and structures above. At this point the particle-to-particle forces in the soil are reduced to essentially zero and the soil begins to behave as a viscous liquid and is said to be “liquefied”.

Pore pressures need not increase to the point that the effective stress is reduced to zero in order to cause the soil to fail. For instance, flow deformation can occur when

increased pore pressures reduce the strength of the soil sufficiently that the driving forces overcome the resisting forces in the soil.

Liquefied soils loose shear strength and are susceptible to large lateral displacements—very gentle slopes have exhibited the propensity for lateral movement. Liquefied soil is also incapable of supporting concentrated vertical loads, allowing excessive settlement to occur. Common signs of liquefaction include sand boils, ground distortion, and ground fissures (see Figure 1.1 through Figure 1.3).

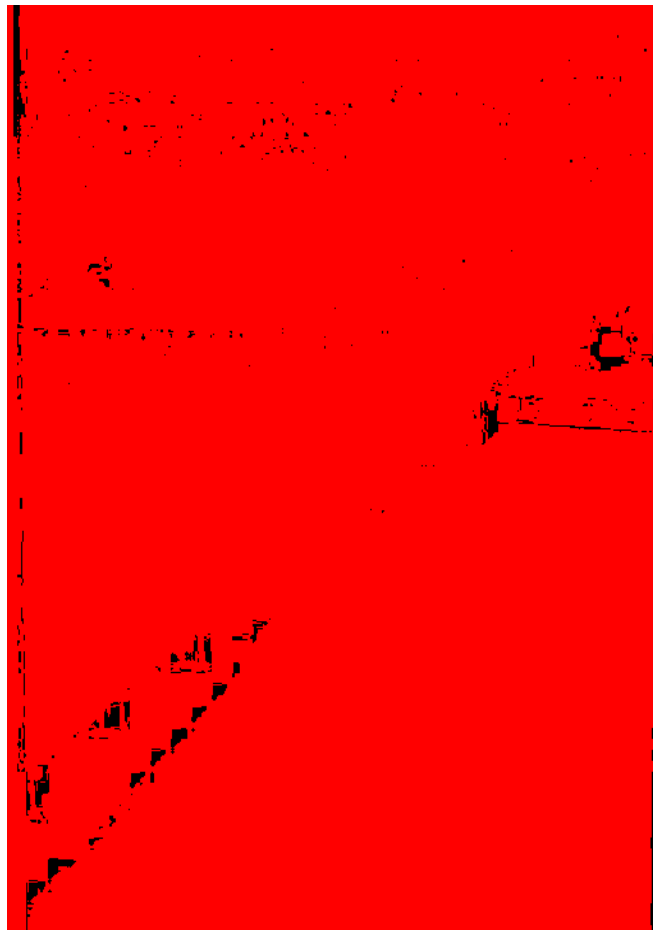


Figure 1.1 1964 Niigata Japan: Showa Bridge collapsed due to pier collapse caused by liquefaction.



Figure 1.2 1983 Nihonkai-Chubu: Liquefaction caused unstable soils to fail. Flagpole foundation foreground was placed shallowly. School building to the left was founded on a pile foundation and suffered no damage.



Figure 1.3 1964 Niigata Japan: Liquefaction caused major settlement. The building at center rotated 70 degrees from vertical. Surprisingly, little structural damage occurred to the apartment buildings. Some buildings were later righted and re-inhabited.

1.1 Liquefaction Mitigation

Liquefaction hazards have typically been mitigated using two types of techniques: usage of specialized foundation types and *in situ* soil improvement (Lew and Hudson, 2004). Soil improvement techniques typically involve some type of soil densification process, such as vibro-compaction, deep soil mixing, dynamic compaction, or compaction grouting, as illustrated in Figure 1.4. These techniques tend to compact the soil, reducing the tendency for contraction during an earthquake, and thus reduce the effects of liquefaction. Although these techniques are generally effective, they are also relatively expensive and time-consuming.

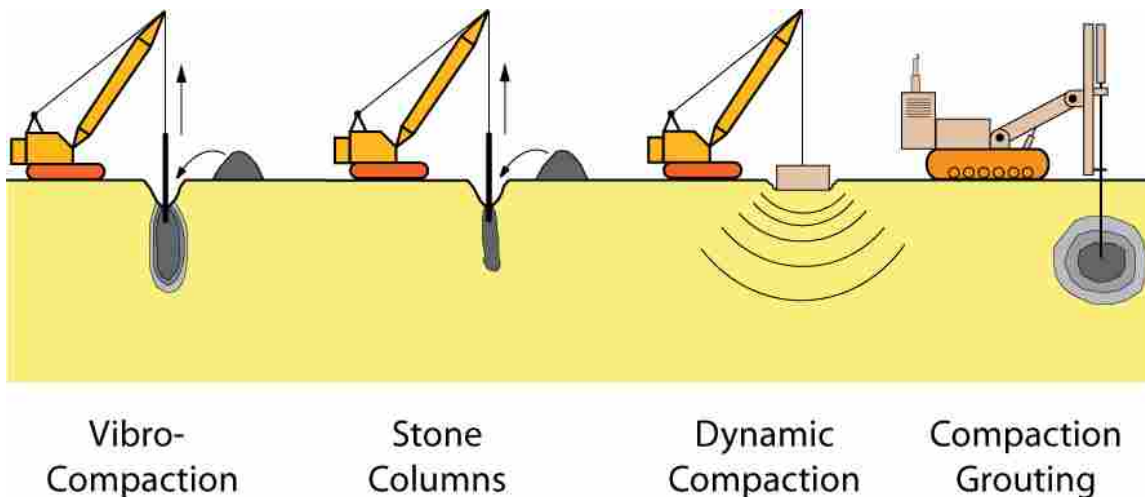


Figure 1.4 Typical soil improvement techniques for densifying loose saturated sands to prevent earthquake-induced liquefaction (after www.haywardbaker.com).

1.1.1 Liquefaction mitigation through pore pressure dissipation

An alternative to soil densification is to provide for rapid pore pressure dissipation to prevent liquefaction. Seed and Booker (1977) pioneered the development of vertical gravel drains for that purpose. Vertical drains allow for pore pressure

dissipation through horizontal flow, as shown in Figure 1.5, which significantly decreases the drainage path length. When drainage is impeded by a horizontal silt or clay layer, vertical drains can be particularly effective. The effectiveness of the drains increases as drain diameter increases and/or drain spacing decreases.

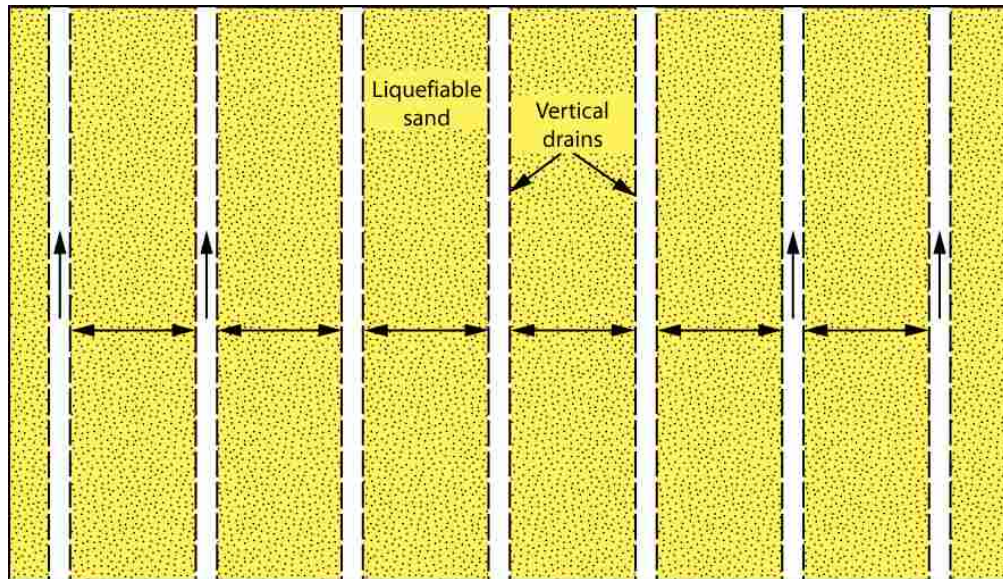


Figure 1.5 Vertical drains for mitigating the liquefaction hazard posed by loose saturated sand.

Although gravel drains have been utilized at many sites for liquefaction mitigation, most designers have relied on the densification caused by drain installation rather than the drainage which they provide (Rollins and Anderson, 2004). Some designers have worried that the use of drainage alone would still allow unacceptable settlement to develop. Inasmuch as soil compressibility of a soil of given relative density increases as excess pore pressure increases (shown in Figure 1.6), the key to limiting settlement appears to be in keeping excess pore pressures below a given threshold. As shown in Figure 1.6, this threshold is located at an excess pore pressure

ratio, R_u , equal to 0.40. Below this threshold, the compressibility of the soil is negligible, above this threshold, soil compressibility increases markedly and excessive settlement could result.

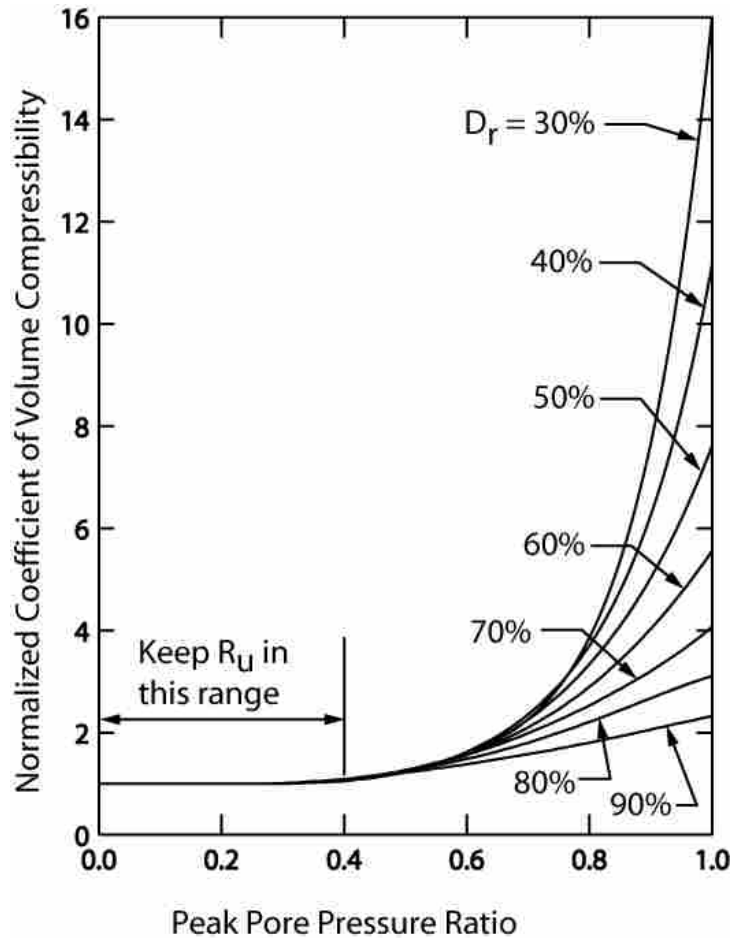


Figure 1.6 Normalized coefficient of volume compressibility versus pore pressure ratio for sands at various relative densities. Settlement is negligible when peak pore pressure ratio remains below approximately 0.40 (after Seed *et al.*, 1975a).

Composite vertical earthquake drains (EQ drains) have the potential to provide the rapid pore pressure dissipation associated with gravel drains while at the same time reducing the time and cost of installation. EQ drains consist of perforated plastic drain pipes 75 to 150 mm in diameter sheathed in a “sock” of geosynthetic filter fabric. The

drains are installed vertically with a vibrating mandrel in much the same way that pre-fabricated vertical drains (PVD's) are installed for consolidation of clays.

EQ drains are typically installed in a triangular pattern with center-to-center spacings of about 1 to 2 m, depending upon the permeability of the soil to be treated. In contrast to PVD's, which have a limited flow rate ($2.8 \times 10^{-5} \text{ m}^3/\text{s}$ at a hydraulic gradient of 0.25), a 100-mm-dia. EQ drain can carry a very large flow volume ($0.093 \text{ m}^3/\text{s}$ at the same gradient) which is sufficient to relieve pore pressure in sands. This flow volume is more than 10 times that provided by a 1- m diameter gravel column ($6.5 \times 10^{-3} \text{ m}^3/\text{s}$).

Filter fabric sleeves are placed around the drains to prevent infiltration of soil.

EQ drains can be installed in a fraction of the time and cost of some commonly used mitigation techniques. For example, for treatment of a 12 m thick layer, stone columns would typically cost $\$107/\text{m}^2$ of surface area and vibro-compaction would cost $\$75/\text{m}^2$, while EQ drains would cost only $\$48$ per square meter. Also, the EQ drains can be installed in about one-third to one-half the time necessary for conventional techniques.

While EQ drains have been installed at several locations, none have experienced an earthquake, leaving EQ drains untested in real-world field conditions. Neither have any full-scale experiments proven the effectiveness of EQ drains to mitigate liquefaction. This lack of full-scale performance data constitutes the largest obstacle to the widespread use of EQ drains.

1.1.2 Liquefaction mitigation through foundation design

Due to the geologic setting in which earthquakes commonly occur, areas prone to earthquakes commonly have an overabundance of surficial deposits of soft soils (silts,

clays, etc.) underlain by or interbedded with liquefiable sand layers. Hence, special foundations must be designed to accommodate the soft and liquefiable soils. Commonly, mat foundations are used to “raft” the structure above the unstable soils, distributing the load across a large area and decreasing the stress applied to the soil. These foundations must be capable of withstanding both the total and differential settlements caused by liquefaction (Lew and Hudson, 2004).

Another common method is to use pile foundations to transfer loads through weak, near-surface deposits to deeper, stiffer soils. Because liquefied soils are prone to lateral spreading, the piles must be designed to withstand lateral forces. In addition, they must be designed to accommodate any downdrag forces that may develop due to the subsequent settlement of liquefied soils. However, methods for calculating the downdrag caused by liquefaction are not well developed nor have they been verified with field tests. This study will begin building a database of field data that can be used to further develop the methods discussed above.

1.2 Investigative Approach

The testing undertaken as part of this dissertation had three main objectives: (1) assess the capability of EQ drains to prevent liquefaction and associated vertical settlement, (2) quantify the amount of downdrag developed during a liquefaction event, and (3) investigate the relationship between the use of EQ drains and the development of downdrag on pile foundations. Field work was organized into four major phases utilizing four test sites. Phase I consisted of preliminary blast testing and installation of EQ drains. The preliminary blast testing was performed to determine the size of explosive

charge to be used in later tests and took place at Site 1. EQ drains were also installed at Site 3 during this phase. During Phase II, steel piles were installed at Sites 2, 3, and 4. Final blast testing was performed during Phase III at both Sites 2 and 3. Finally, Phase IV was carried out at Site 4 which consisted of blast testing in conjunction with static testing.

1.2.1 Earthquake drain testing

Sites 2, 3, and 4 were the locations of actual test blasting, all exhibiting essentially the same soil profile and characteristics. Site 2 was maintained as the control area, without ground treatment, where explosive charges were detonated to liquefy the soil. Pore pressure was monitored before, during, and after blasting to determine the rate of pore pressure dissipation without the benefit of EQ drains (see Chapter 6). After blasting was completed at Site 2, the same size explosive charges were used at Site 3 to test the capability of the drains to dissipate pore pressures rapidly enough to prevent liquefaction (see Chapter 8). Again, pore pressures were monitored before, during, and after blasting. The pore pressures developed in Site 3 were then compared to those of Site 2 to determine the effectiveness of the drains. Furthermore, the pore pressures recorded at Site 3 were used to calibrate a numerical model of the test site (using FEQDrain) to investigate the effects that different drain sizes and spacings have on pore pressure (see Chapter 9).

1.2.2 Pile testing

Pile foundations necessary for load testing were installed at the centers of both Sites 2 and 3. One test pile, instrumented with vertical strain gauges was installed at the center of each site and was surrounded by four reaction piles. A reaction frame was connected to the reaction piles so that hydraulic jacks could apply axial loads to the test pile. A complete description of the construction of the test foundations is provided in Chapter 5. During blasting, a constant vertical load on the pile was maintained by the jack. Data collected from the strain gauges was then analyzed to examine the soil/pile interaction before, during, and after liquefaction. Site 4 consisted of a single instrumented pile over which the static testing apparatus was erected. Blast testing was performed with the same size explosive charges used at Sites 2 and 3 in conjunction with static testing in order to more fully investigate the development of downdrag on a pile (see Chapter 10).

1.2.3 Concurrent studies

Several other studies were performed concurrently with this one. These studies include: a comparison of results from static and static pile load tests in collaboration with Prof. Gray Mullins from the University of South Florida; field evaluation of the undrained shear strength of liquefied soil based on *in situ* vane shear tests in collaboration with Prof. Travis Gerber from Brigham Young University; field evaluation of colloidal silica grouting techniques for preventing liquefaction with Prof. Patricia Gallagher from Drexel University; and doctoral research involving the development of a numerical model to simulate blast-induced liquefaction by Wayne Lee, of Brigham

Young University (Lee, 2006). Since these studies reach beyond the scope of this paper, they will not be discussed here; however, each of these studies yielded significant new findings which will appear in the technical literature in the future.

2 Literature Review

While EQ drains have been utilized at several sites around the United States, no site has experienced an earthquake. As a result, the efficacy of EQ drains in preventing liquefaction remains untested under earthquake conditions. Nor is it clear the extent to which EQ drains may reduce or prevent the loss of skin friction of a pile foundation or improve bearing capacity under a mat foundation during liquefaction. Furthermore, while much research has studied lateral spreading as it relates to pile foundations, very little has focused on the development of negative skin friction (downdrag) and other vertical aspects of the soil/pile interaction related to liquefaction. This lack of field performance and research data has been a major impediment to further the use of EQ drains for liquefaction mitigation.

2.1 Performance of EQ Drains

In the absence of earthquake performance data, both laboratory and field tests have been performed in attempts to verify the performance of EQ drains. While some research has employed composite drains of various designs, the majority of research has focused on the use of granular materials as a drainage medium. Furthermore, several

installations of this type of drain have been subjected to real earthquakes, providing a database of performance data under real-world conditions.

2.1.1 Behavior of vertical gravel drains

Seed and Booker (1977) pioneered the utilization of rapid pore pressure dissipation as a method of liquefaction mitigation. In so doing, they focused on the use of coarse granular materials (gravel and crushed stone) to form highly permeable columns (commonly called gravel drains) through which high, earthquake-induced pore pressures could drain from the surrounding liquefiable soil. Continued research has refined and further developed the use of gravel drains as a method of liquefaction mitigation.

While the subject of this dissertation is the performance of composite drains, it is thought instructive to review the behavior of gravel drains, inasmuch as their behavior should be analogous to the behavior of composite drains and, thus, can provide a valuable reference upon which to base analysis of composite drain behavior.

2.1.1.1 Brennan and Madabhushi, 2002

Brennan and Madabhushi utilized centrifuge tests to investigate the development of pore pressures and behavior of gravel drains during liquefaction. In these tests, a liquefiable soil was modeled using loose, Leighton Buzzard grade E sand with a relative density, D_r , equal to 45.4 percent. A single drain made of grade B sand was installed at the center of the soil and penetrated the full depth of the model. The permeability of the drain was approximately 10 times greater than that of the surrounding soil. Viscous

silicone oil was used in place of water in order to account for the high accelerations (up to 50 g) of the centrifuge model. Instruments were arranged in such a manner as to record vertical and horizontal pore pressure distributions and the movement of flow fronts. Earthquake shaking was simulated by vibrating the model at 1 Hertz for 25 seconds, with input accelerations of 0.142, 0.182, and 0.242 g.

The results of the tests confirmed several of the assumptions upon which design of vertical drains has been based. The excess pore pressures generated by shaking create a vertical hydraulic gradient acting such that pore fluid tends to move upwards towards the surface. As the drain has a higher permeability than the surrounding soil, both the dissipation of pore pressures and the movement of fluid occur more rapidly in the drain than in the surrounding soil. This in turn causes the development of horizontal hydraulic gradients in the soil as pore water flows radially towards the drain from zones of higher pore pressure.

At any given time, the horizontal plan can be separated into two zones: one in which horizontal hydraulic gradients exist (termed the near field) and the second where those gradients do not exist (the far field). The boundary separating the two zones is called the flow front. The tests showed that the flow front first formed near the drain and gradually expanded radially outwards as shaking continued. Outside the flow front, no pore water moves towards the drain, thus only the near field realizes the presence of the drain. For a liquefiable soil to be treated by a group of vertical drains, the intention is to install the drains such that the flow fronts of each individual drain overlap, thus leaving no portion of the treated soil outside the influence of the drains.

Finally, this set of tests showed that drainage began with the lowest layers first; upper layers began draining only once pore pressures in the drain dissipate sufficiently to equilibrate with those in the upper layers.

2.1.1.2 Brennan and Madabhushi, 2006

Brennan and Madabhushi continued the research discussed above and focused on the effect of drains of varying depths on the rate of pore pressure dissipation. Brennan and Madabhushi (2002) showed that dissipation begins with the lower layers of soil first and that upper layers begin to drain only once the lower layers have completed drainage. It was hypothesized that the use of a combination of fully-penetrating and partially penetrating drains would increase the rate of pore pressure dissipation. Since the partial drains do not penetrate the full depth of the liquefied layer, it may be possible that those drains may begin draining shallower soils even before the deeper soils have dissipated their excess pore pressures.

Again, centrifuge modeling was employed, using a model very similar to the one used previously. In these tests, the control model utilized only fully penetrating drains while the test model contained both full and partial drains. Results showed clearly that the use of partially penetrating drains did not increase the rate of pore pressure dissipation. Rather, it was seen that drainage from shallow soil began only once drainage had occurred in the lower layers, as seen in the tests mentioned above. Therefore, drainage can be accelerated only by increasing the rate of dissipation of the deepest layers through the use of full-depth drains.

While the underlying causes of this behavior are not yet fully explained, the practical result is that pore pressure dissipation is optimized by the use of drains that penetrate the full depth of the liquefied zone.

2.1.2 Behavior of EQ drains

Though the development of gravel drains continues, composite drains have more recently been the focus of research regarding the use of rapid pore pressure dissipation to mitigate liquefaction hazards.

2.1.2.1 Rathje *et al.*, 2004

Rathje *et al.* (2004) performed field tests on a volume of reconstituted, saturated sand measuring 1.2 m x 1.2 m x 1.2 m, surrounded by an impervious membrane. Tests were conducted with and without an EQ drain in the center of the test volume. The relative density of the sand for both tests was approximately 35 percent. Stress cycles were applied using a large Vibroseis oil-prospecting truck, with pore pressure and acceleration measured at several points within the test volume.

Plots of the measured excess pore pressure ratio with and without a drain from this test are presented in Figure 2.1. Without a drain, liquefaction was produced during the application of 60 stress cycles (3 second total duration), while the excess pore pressure ratio did not exceed 25% for the test volume with a drain subjected to the same vibrations. Volumetric strain decreased from 2.1% without a drain to less than 0.5% with a drain in place.

While EQ drains successfully prevented liquefaction at this reduced scale, it remains to be seen whether equal performance can be obtained at full scale. Of particular concern is the observation made by Brennan and Madabhushi (2002, 2006) that shallower soils drain after deeper soils. In a liquefiable soil only 1.2 m thick, this phenomenon may not fully develop or indeed may not occur at all.

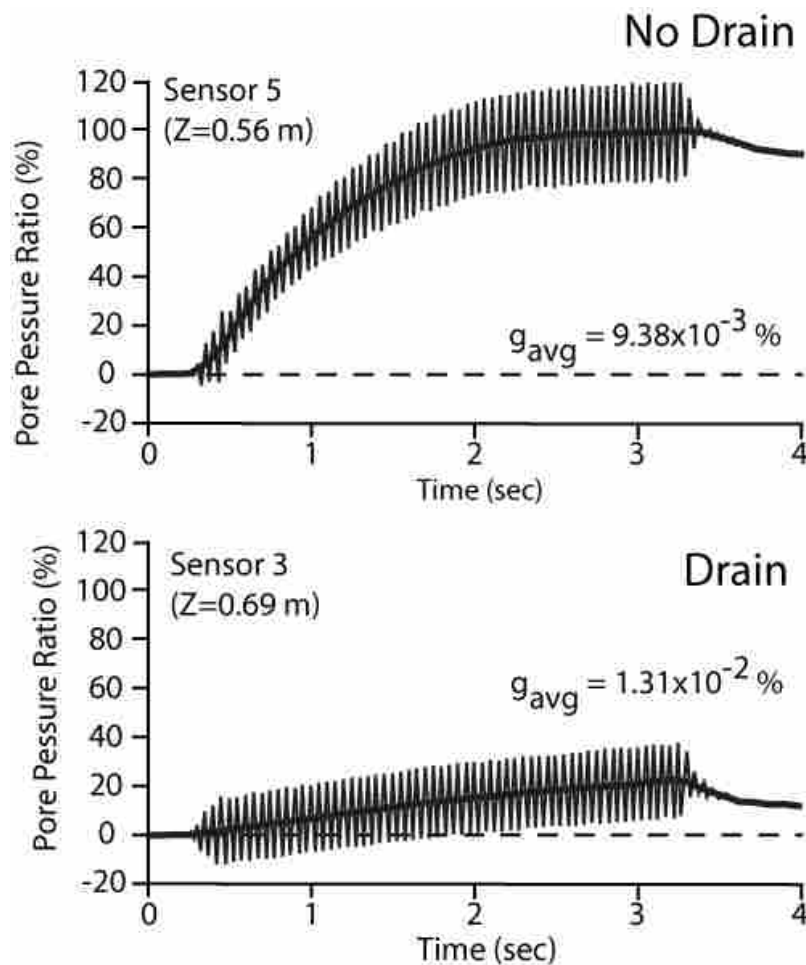


Figure 2.1 Excess pore pressure ratio time histories induced by vibrosies oil-prospecting truck for sand volume with and without EQ drain (reproduced from Rathje *et al.*, 2004).

2.1.2.2 Rollins *et al.*, 2004

Rollins *et al.* (2004) employed controlled blasting techniques to generate excess pore pressures to test full-scale EQ drains at test sites on Treasure Island in San Francisco Bay and in Vancouver, British Columbia. These tests investigated the pore pressure dissipation properties of EQ drains and the densification produced during drain installation.

At Treasure Island, the test site consisted of two sets of blast holes with several test regions surrounding the blast holes. Each test region contained a cluster of seven EQ drains installed in a triangular grid pattern, incorporating various combinations of drain spacings, use of a filter sock, and amount of vibration used during installation. One region was retained as a control and had no drains installed.

A single CPT sounding was performed within one drain cluster approximately one week after installation of EQ drains. The cone tip resistance typically increased by 20 to 35% and the estimated relative density increased by 5 to 10 percentage points. This increase in soil density provided increased liquefaction resistance as an additional benefit to the pore pressure dissipation provided by the drains.

Due to the rapid loading rate from the explosive charges, the EQ drains were unable to prevent liquefaction. However, dissipation rates were substantially increased. Furthermore, post-liquefaction settlements were reduced from about 100 mm in the control region to less than 25 mm in several of the regions treated with drains. Computer analyses were performed using FEQDrain (Pestana *et al.*, 1997) in an effort to estimate the performance of EQ drains under the slower loading conditions of earthquake shaking.

After calibrating the computer model using the measured pore pressure and settlement data, a M7.75 event was simulated. The maximum computed excess pore pressure ratio was 0.35 and the maximum settlement was 18 mm.

One finding of particular interest was the importance of using a filter sock with suitable filtering properties. Post blast test observations indicated that significant amounts of sand had infiltrated the EQ drains, reducing their discharge capacity. Subsequent laboratory tests confirmed that the filter fabric used in testing did not adequately filter the sand.

At Vancouver, EQ drain performance was evaluated by installing a cluster of 35 EQ drains at one test site and comparing the pore pressure and settlement behavior with an adjacent, untreated control site. The EQ drains used in this series of tests were exactly the same as the EQ drains used at Treasure Island, with the exception of an improved filter sock.

At the test site, the EQ drains were installed using a vibratory mandrel in a triangular grid pattern with a spacing of 1.22 m center-to-center. Drain installation caused the soil within the boundaries of the cluster to settle, with a maximum settlement of over 350 mm occurring near the center and decreasing to approximately 50 mm near the edges of the cluster.

Sixteen explosive charges were used to induce liquefaction. Even though a 500 millisecond delay was used between blasts, the drains were again unable to prevent liquefaction. Nevertheless, pore pressure dissipation rates were much higher with the drain than without. The drains were also able to reduce the total amount of settlement by

30 to 65% when compared to the untreated site. In addition, the relative density of the treated soil was increased from approximately 40% to 60% after drain installation and blast testing. Of the 20 percentage point increase, an estimated 10 percentage points were due to drain installation itself.

Computer simulations using FEQDrain were again used to analyze the response of the EQ drains and predict their behavior under earthquake conditions. Once the model was calibrated with measured data, various earthquake scenarios were simulated, the results of which indicated that EQ drain could be effective at preventing liquefaction and excessive surface settlement. For instance, simulated earthquakes ranging from M6.0 to M7.5 were predicted to cause 31 to 45 mm of settlement, as compared to the 310 mm of settlement caused by blast testing. Furthermore, maximum excess pore pressure ratio ranged from 0.40 for the M6.0 event to 0.65 for the M7.5 event.

2.1.2.3 Rollins and Anderson, 2004

Rollins and Anderson (2004) furthered the work of Rollins *et al.* (2004), in part by evaluating the extent to which various levels of vibration during installation of EQ drains effected the drains' performance.

At the Vancouver, B.C., test site discussed in Rollins *et al.* (2004), two sets of EQ drains were installed using two levels of vibration—high and low. Installation was accomplished using a pipe mandrel attached to an ICE Model 44 vibratory hammer suspended from a crane (see Section 7.2 for a more complete description of EQ drain installation using this method). In the low-vibration configuration, the hammer was operated at the low vibration setting and a smooth mandrel was used. The high-vibration

configuration utilized the maximum vibration setting on the hammer and a “finned” mandrel designed to transmit vibrational energy into the surrounding soil (see Section 7.2 and Figure 4.3 for further information regarding the use of the smooth and finned mandrel).

This study showed that the use of EQ drains, besides providing rapid pore pressure dissipation, also caused significant amounts of settlement during installation. This leads to increased density and decreased compressibility, reducing the amount of settlement produced during liquefaction. The use of high vibration during drain installation increased the relative density of the soil by 10 percentage points and produced volumetric strains of 2.5%. The use of EQ drains decreased the settlement in treated sites to only 60% of that measured at the untreated sites.

2.2 Development of Downdrag on Piles During Liquefaction

Downdrag loads can be an important factor in the design of pile foundations. While the development of downdrag due to the consolidation of clays has long been observed (Fellenius, 1972), little information is available regarding the development of downdrag due to liquefaction. Bozozuk (1981) studied the variation of skin friction in a pile pre-loaded by downdrag due to consolidating clay. While the mechanisms involved with consolidating clay differ from those involved with soil reconstitution following liquefaction, certain phenomena associated with the variation of skin friction distribution are similar. In the absence of experimental data, Boulanger and Brandenberg (2004) developed a method for determining the location of the neutral plane based on modifications made to a neutral plane solution applicable to consolidating clays.

2.2.1 Bozozuk, 1981

Bozozuk (1981) investigated the variation of load distributions in a pile preloaded by downdrag before being subjected to static load tests. Bozozuk first considered a hypothetical pile driven into a soil profile consisting mainly of clayey soils. After some time, negative skin friction will develop as the clayey soils consolidate, causing downdrag on the pile and the load distribution will appear as shown in Figure 2.2. The negative skin friction developed between O and N_p in Figure 2.2 is balanced by positive skin friction and end-bearing below point N_p . The reversal in skin friction at point N_p is called the neutral plane. The maximum axial load in the pile caused by downdrag, P_N , is also located at the neutral plane.

Bozozuk (1981) hypothesized that any vertical load less than or equal to P_N , applied to the pile for a short time would be carried by the prestress in the upper portions of the pile caused by negative skin friction. The axial compression in the pile caused by the additional load would relieve the vertical strains in the soil that generated the downdrag. If the load were applied for too long, the continued consolidation of the clayey soils would restore the negative skin friction previously present which would then be added to the applied load.

To verify this hypothesis, a test pile was driven through a highway embankment into clayey soils and the load distribution observed for 10 years, at which point load testing was carried out. At the end of ten years, the embankment had settled over 2.5 m causing the test pile to settle 694 mm; the load distribution at the time of the load testing is shown in Figure 2.3. In brief, the load testing consisted of loading the test pile

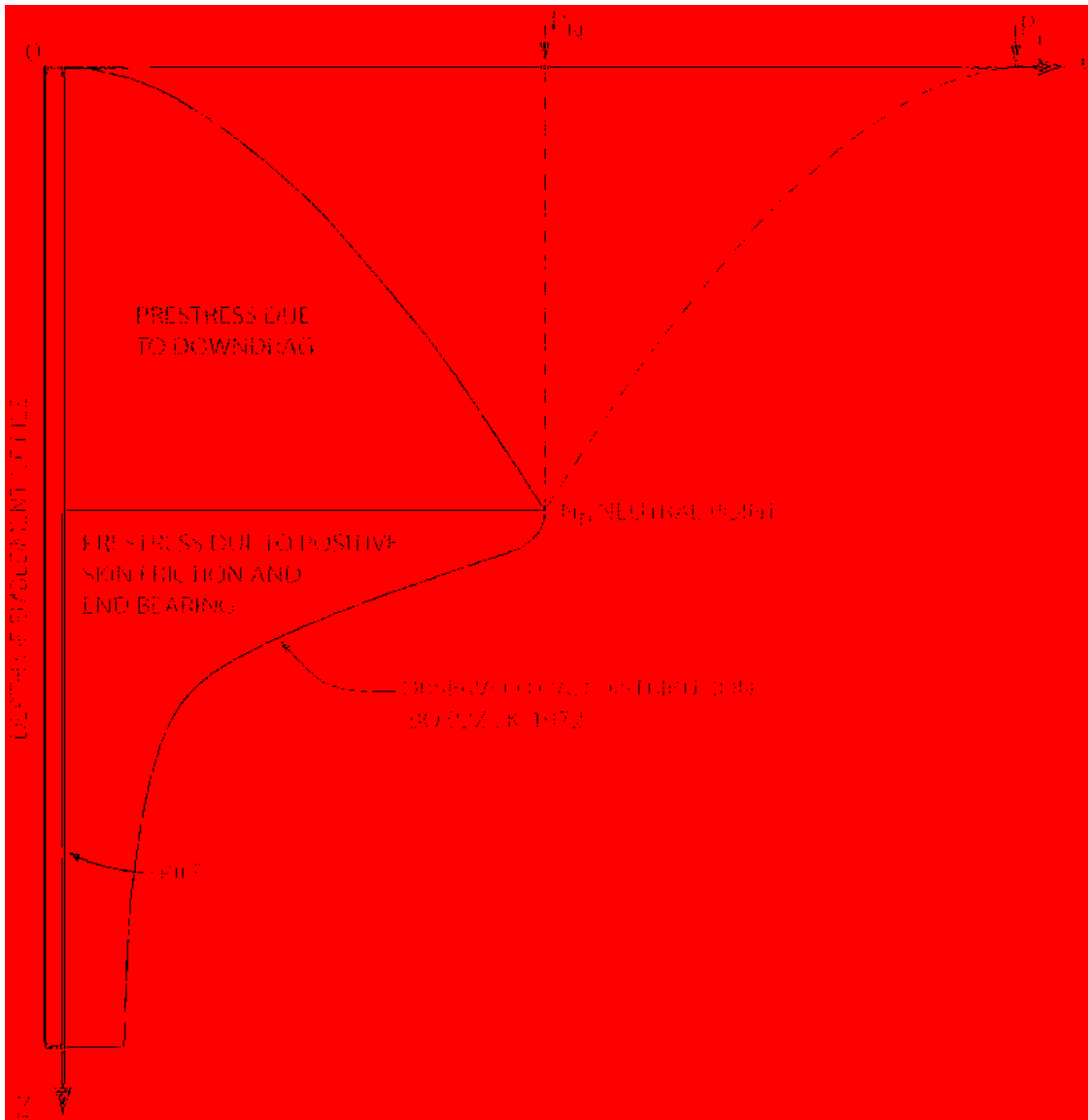


Figure 2.2 Theoretical load distribution in pile pre-stressed by downdrag under applied load (after Bozouk, 1981).

incrementally to loads of $1/3 \times P_N$, $2/3 \times P_N$, $1 \times P_N$, and $4/3 \times P_N$, which were maintained for a relatively short period of time (generally approximately 18 hours).

Referring to Figure 2.3, it can be seen that positive skin friction was increasingly mobilized as the applied load increased. At $1/3 \times P_N$ (0.51 MN), the settlement of the pile relative to the soil was small, serving only to lessen the amount of negative skin friction. At $2/3 \times P_N$ (1.02 MN), the relative movement of the test pile was enough to counteract the negative skin friction in the upper three meters. In other words, this load caused the pile to settle relative to the soil so that the negative skin friction decreased to the point that essentially no skin friction, positive or negative, developed. It should be noted that the relative pile-soil movement necessary to fully mobilize skin friction is typically on the order to 2 to 5 mm.

When a load equal to P_N was applied (1.52 MN), the relative settlement increased to the point that the negative skin friction in the upper five to six meters completely reversed and positive skin friction developed. Notice that even though positive skin friction developed in the upper five to six meters, negative skin friction still existed below that point. The depth at which skin friction reversal occurred became progressively deeper as the applied load increased. This indicates that the vertical strains in the soil causing the negative skin friction are relieved from the top down. At $2 \times P_N$ (3.04 MN), essentially all of the negative skin friction was completely overcome by the applied load and the pile began to plunge.

While the results of this testing are not immediately applicable to the conditions of the current set of tests, they will help to explain the pattern of load distribution observed and will be discussed later.

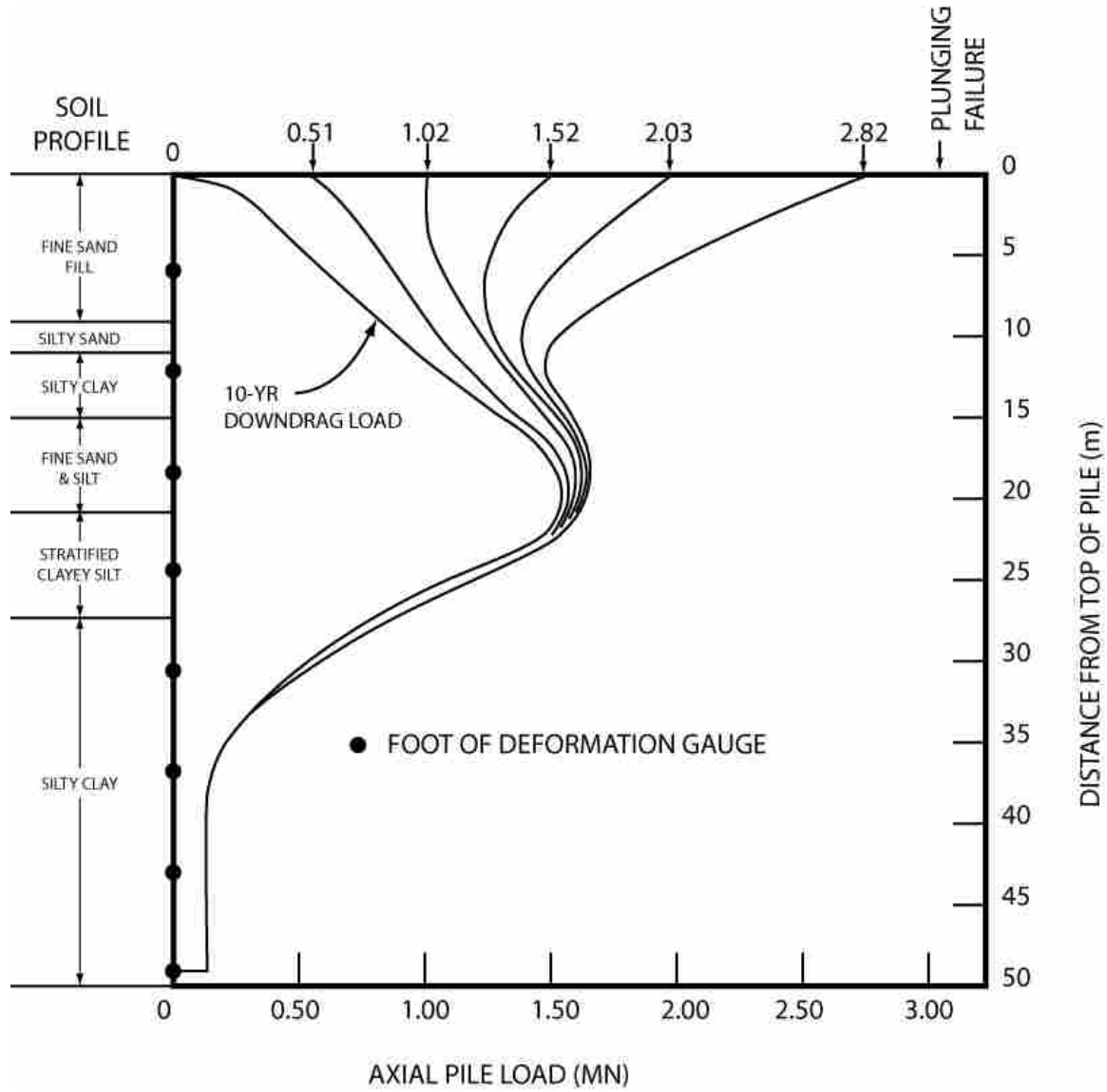


Figure 2.3 Load distribution in test pile at various levels of applied load (from Bozozuk, 1981).

2.2.2 Boulanger and Brandenburg, 2004

The common consensus regarding liquefaction-induced downdrag is that liquefied soil does not contribute to skin resistance while the soil remains liquefied. Further, as the liquefied soil reconsolidates, any non-liquefied soil overlying the liquefied soil will add a drag load to the pile. It is also conceivable that the liquefied soil itself will contribute an additional drag load during reconsolidation. However, there is no experimental data to quantify the amount of downdrag caused by liquefaction. In the absence of suitable data, pile foundations are generally designed and analyzed using methods developed for other conditions, leaving the accuracy of such designs and analyses suspect.

As a first estimate of the soil-pile interaction during liquefaction, Boulanger and Brandenburg developed a neutral-plane solution for liquefaction-caused downdrag by modifying the Fellenius solution (Fellenius, 1972).

The modifications essentially account for the changing soil properties during liquefaction. For instance, the shaft friction (f_s) within the liquefied sand was modeled to be proportional to the effective stress in the sand by the following equation

$$f_s = \sigma'_{v0} K_0 \tan(\delta)(1 - R_u) \quad (1)$$

where σ'_{v0} = vertical effective consolidation stress
 K_0 = coefficient of lateral earth pressure at rest
 δ = the interface friction angle
and R_u = the excess pore pressure ratio.

Because pore pressures vary with time during liquefaction, σ'_v also varies with time. Though the values of K_0 and δ change during liquefaction, in the absence of relationships describing their change, K_0 and δ were held constant.

As in the Fellenius (1972) solution, forces acting on the pile are summed in two direction: downwards from the pile head (Q_{down}) and upwards from the pile tip (Q_{up}). The neutral plane is then located where Q_{down} equals Q_{up} . However, since f_s varies with pore pressure, Q_{down} and Q_{up} must be calculated at different time steps incorporating isochrones describing the variation of pore pressure with depth through the soil profile.

The amount of settlement in the pile is equal to the amount of soil settlement at the location of the neutral plan. Again, since f_s changes during liquefaction, the depth of the neutral plane also changes. Therefore, pile settlement is calculated by determining the position of the neutral plane and its associated soil settlement at the same time steps as above; these are then integrated over the entire time period to produce the total pile settlement.

To test their new method, Boulanger and Brandenburg performed a parametric study for the case of a lower permeability layer settling over a liquefied sand layer, allowing them to make several conclusions regarding the implications of this new method on pile design. According to their analysis, the downdrag forces caused by liquefaction arise primarily from the overlying, non-liquefied soil (or “crust”)—relatively small drag loads occur within the liquefied layer itself. Thus, for design purposes, downdrag from within the liquefied soil can safely be neglected. Furthermore, as with conventional downdrag problems, pile settlements will be small provided that the sum of the expected

service load and peak downdrag loads from the settling crust remain equal to or less than the resisting forces below the liquefied layer.

2.3 Summary

The following summarizes the current state of knowledge concerning the performance of EQ drains and the development of liquefaction-induced downdrag on piles.

2.3.1 Performance of EQ drains

Many of the arguments supporting the usage of EQ drains to mitigate liquefaction hazards are based on the observed behavior of vertical gravel drains, under both full-scale field conditions and small-scale laboratory conditions; it appears reasonable that the behavior of EQ drains should be similar to that of gravel drains. Because dissipation of pore pressures begins at the bottom of the liquefied zone and proceeds upwards, all drains should be installed to the full depth of the liquefiable zone. No advantage is gained by installing partially penetrating drains as those drains do not contribute to pore pressure dissipation until pore pressures in lower layers have dissipated.

Experiments performed by Rathje *et al.* (2004), showed that small-scale EQ drains were successful in preventing liquefaction when liquefaction was induced using a vibroseis truck. Rollins *et al.* (2004) and Rollins and Anderson (2004) demonstrated that full-scale EQ drains dramatically increased the rate of pore pressure dissipation when liquefaction was induced using explosive charges. In both studies, loading rates from the explosives exceeded the ability of the EQ drains to prevent liquefaction.

In order to evaluate the performance of EQ drains, this study incorporated the use of a blasting sequence designed to more closely approximate the loading rate that would be expected during an earthquake.

2.3.2 Development of downdrag on a pile

Currently, the professional literature is devoid of any reports of any experimental studies involving the development of downdrag on a pile due to liquefaction. The theory behind the development of liquefaction-induced downdrag remains underdeveloped, with the modified neutral plane solution by Boulanger and Brandenberg (2004) representing the sole attempt to develop the theory.

This study seeks to make a significant contribution to the field by reporting the results of the first full-scale experiments regarding the development of downdrag on a pile.

3 Site Characterization

The test sites are located on Deas Island next to the south portal of the George Massey tunnel on Route 99 near Vancouver, British Columbia as shown in Figure 3.1. Situated in the delta region of the Fraser River, Deas Island is formed of naturally emplaced channel and alluvial sands. The soil deposits are only about 200 years old according to studies by Monahan *et al.* (1995). Previous site characterization consisting of cone penetration tests, standard penetration tests, shear wave logging, and undisturbed sampling was performed during studies associated with the CANLEX project (Robertson *et al.*, 2000; Monahan *et al.*, 1995) along with previous research performed for the British Columbia Ministry of Transportation (Gohl, 2002) as well as by Rollins and Anderson (2004). Similar site characterization efforts were incorporated into this project to provide site-specific data at each test location.

The area is relatively flat lying and grass covered. The centers of the three test sites lie along a line 18.3 m east of the access road. The test sites are located approximately 150 meters south of a CANLEX Phase II test site (the Massey site) and approximately 30 meters north of the previous EQ drain test sites (see Figure 3.2). Figure 3.3 shows a detailed view of the test site layout.

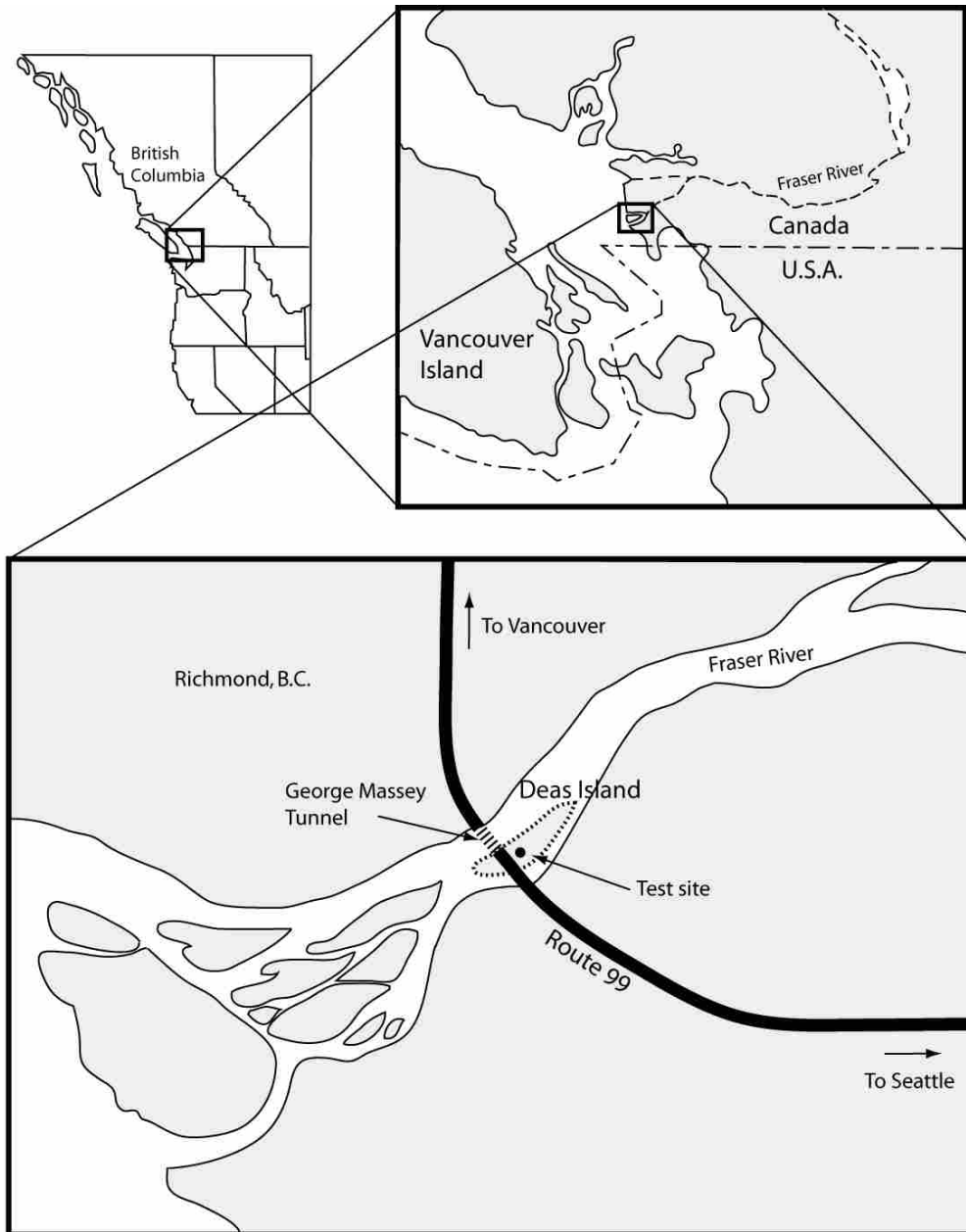


Figure 3.1 Location of test site on Deas Island, south of Vancouver, British Columbia, Canada.

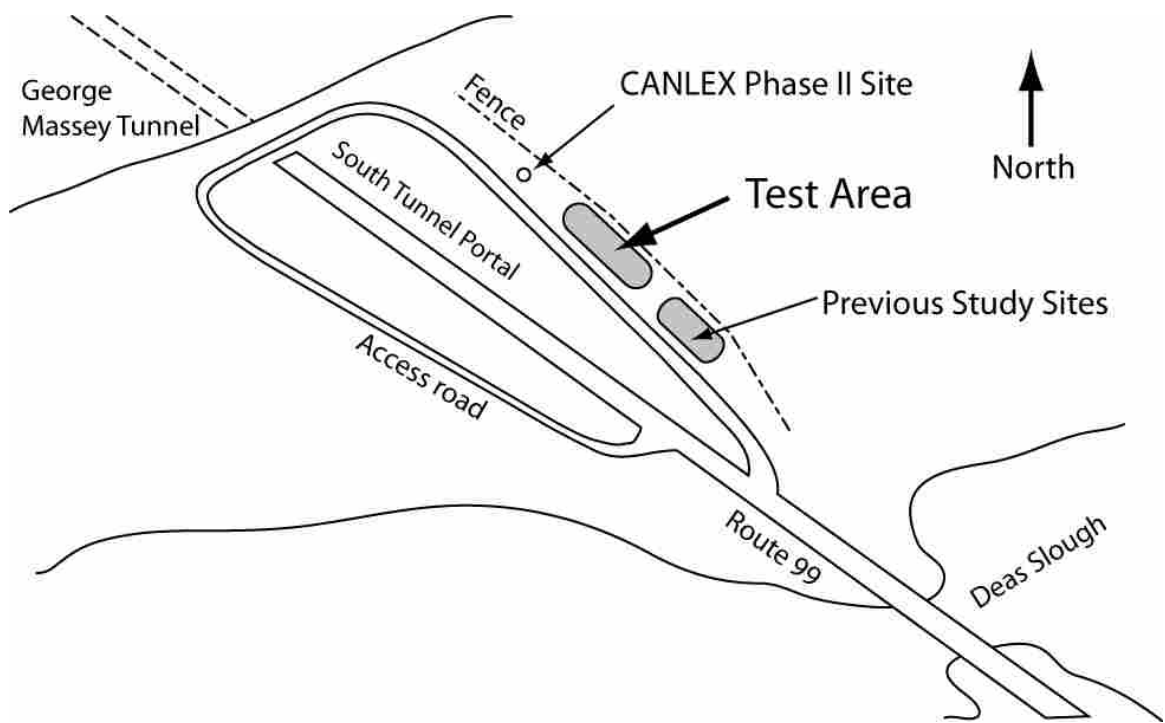


Figure 3.2 Location of test site relative to previous study sites and the CANLEX Phase II site.

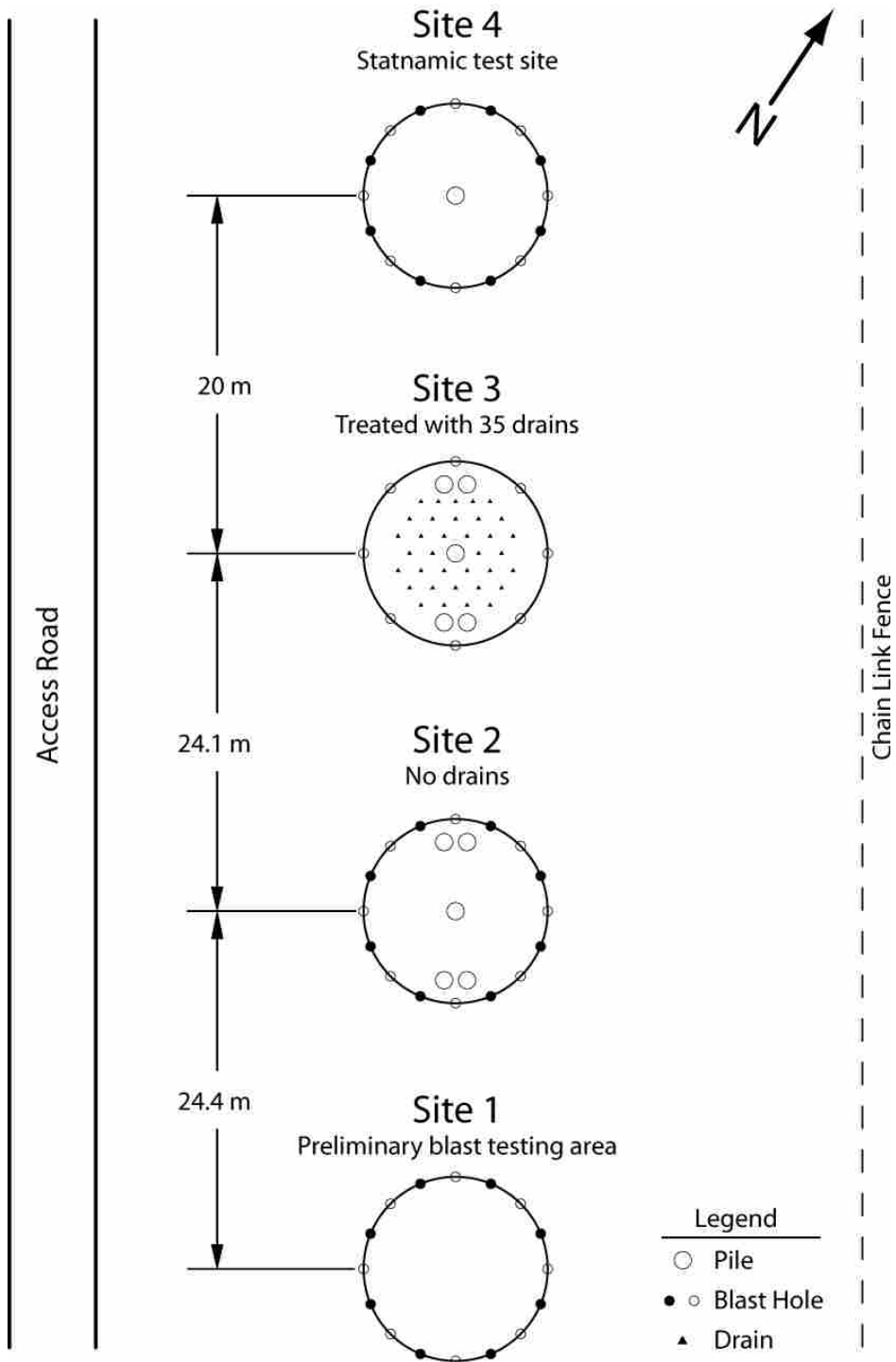


Figure 3.3 Detailed schematic drawing of the layout of the test site.

3.1 CPT Data

Prior to installation of any sensors, drains, or piles, cone penetration tests (CPT's) were performed by ConeTec Investigations Ltd., at the center of each of the three sites to confirm the assumed soil properties and profile. All tests used an integrated electronic piezocone and were carried out in general accordance with ASTM D-5778-95. Each test recorded tip resistance, sleeve friction, and dynamic penetration pore pressure at 0.025-m depth intervals. Relative density was estimated from CPT cone tip resistance measurements using an equation developed by Kulhawy and Mayne (1990),

$$D_r = \left[\frac{q_c C_n}{\frac{P_a}{305}} \right]^{0.5} \quad (2)$$

where: D_r = relative density,
 q_c = cone tip resistance, in tons per square foot
 $C_n = (P_a / \sigma'_o)^{0.5}$
 P_a = atmospheric pressure
 σ'_o = initial effective stress
and P_a and σ'_o are in the same units

Figure 3.4, Figure 3.5, and Figure 3.6 show the results of the preliminary CPT's from Site 1, Site 2 and Site 3, respectively. The soil profile at each site was interpreted according to Robertson *et al.* (1986). The generalized soil profile shown in Figure 3.7 was developed from the preliminary CPT's just mentioned.

Test Site 1

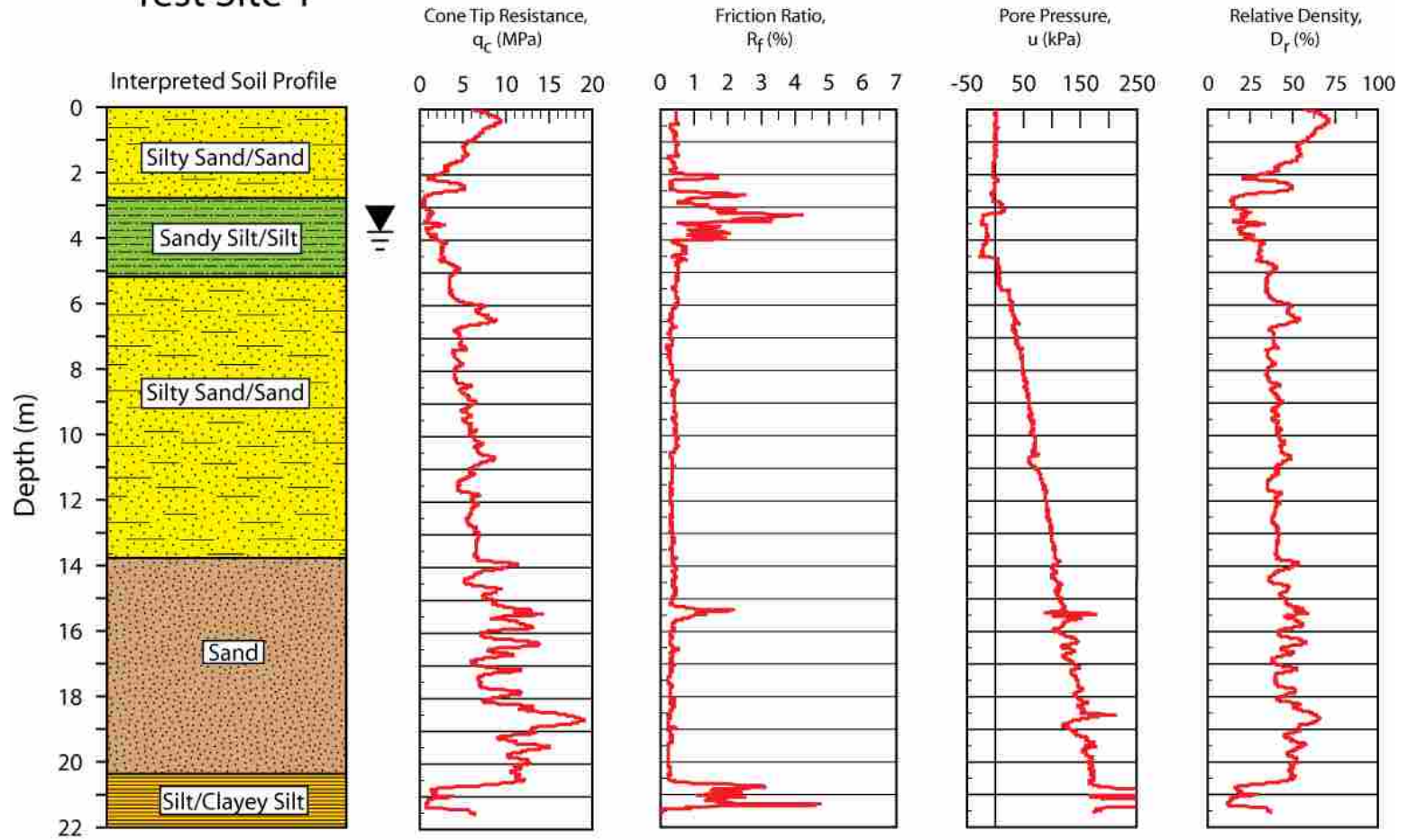


Figure 3.4 Results of the preliminary CPT performed at Site 1.

Test Site 2

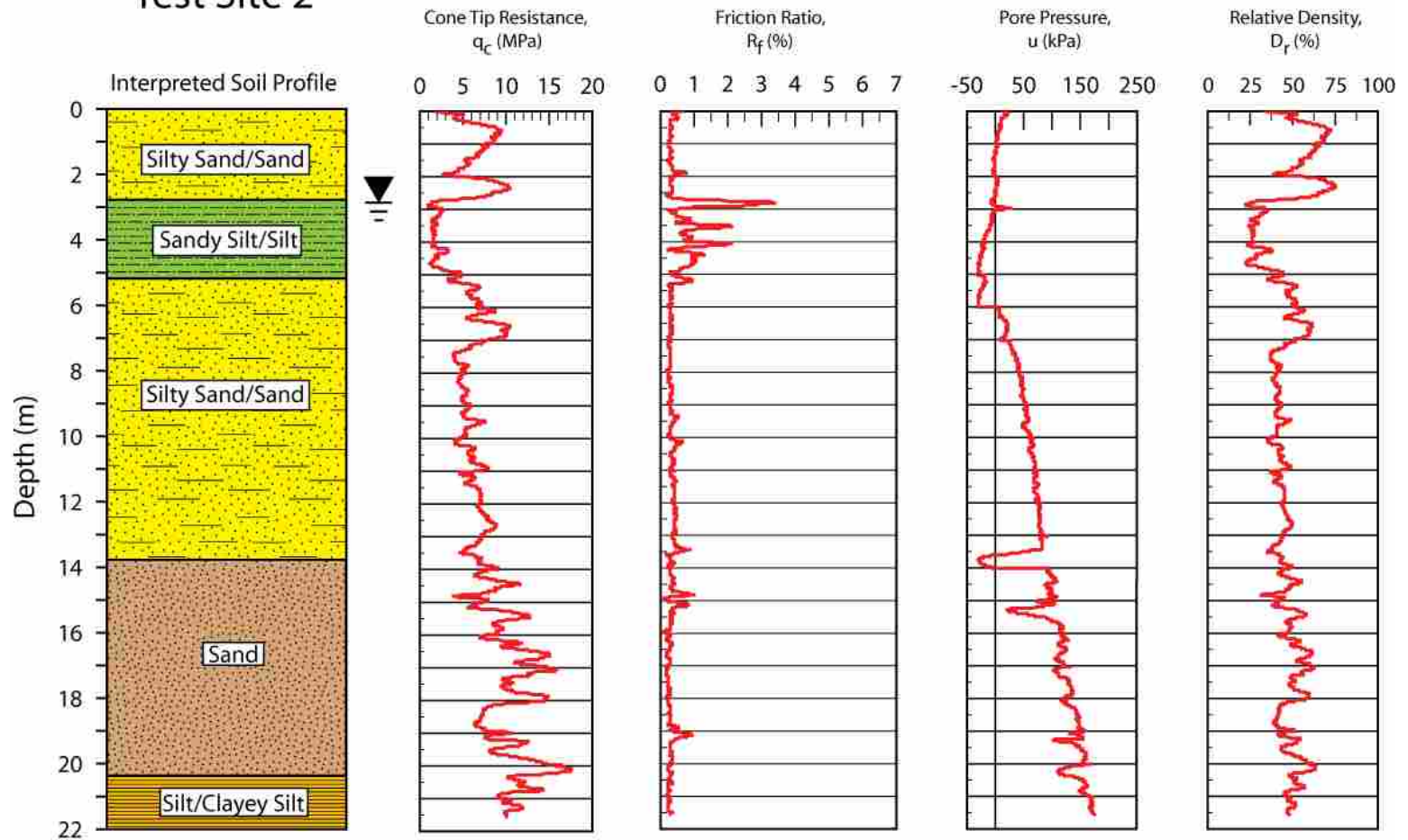


Figure 3.5 Results of the preliminary CPT performed at Site 2.

Test Site 3

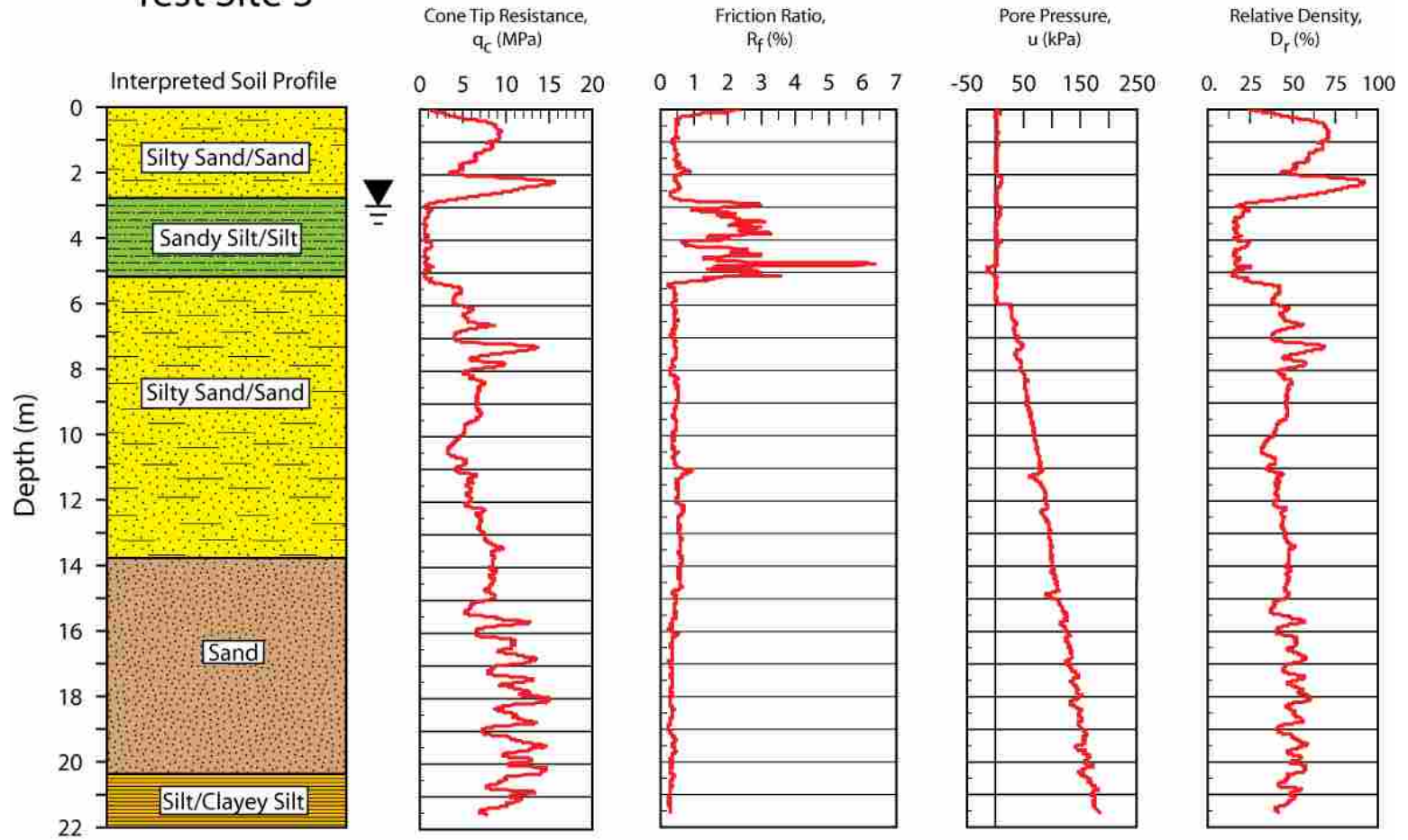


Figure 3.6 Results of the preliminary CPT performed at Site 3.

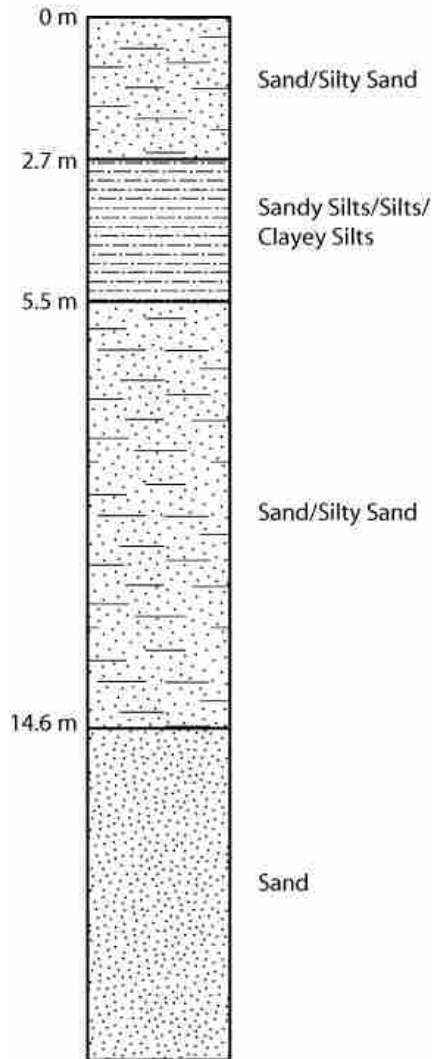


Figure 3.7 Generalized soil profile interpreted from CPT results.

In general the soil profile consists of four major units (see Figure 3.7). The top unit, approximately 2.7 m thick, consists of interlayered sand and silty sand. The second unit, approximately 2.8 m thick (from 2.7 to 5.5 m depth), consists of sandy silts, silts, and clayey silts. The third unit, approximately 9.1 m thick (5.5 to 14.6 m depth) consists of silty sands and sand. The target zone in which liquefaction will be produced in this study extends from 6 m to 13 m depth and is contained within this unit. The fourth unit, comprising everything below 14.6 m depth, consists mostly of clean sands with some thin beds of silty sand.

At Site 1 a fifth unit, consisting of silts and clayey silts was penetrated at 20.7 m depth. Subsequent CPT's failed to reveal this unit and therefore it is unclear whether the unit extends beyond a very localized zone. This unit is irrelevant as no drains, sensors, or piles were installed at this depth and thus this layer does not affect the study.

The third unit, which contains the target layer, is relatively uniform throughout the test area on Deas Island and should be susceptible to liquefaction. Figure 3.8 contains a comparison of cone tip resistance and relative density for all three sites. From the figure it can be seen that all three test sites are comparable and should behave similarly. Between a depth of two and three meters, all three CPT soundings penetrated a relatively dense sand with each CPT returning dramatically different relative densities. However, apart from this layer, the average relative density is approximately 40% with a standard deviation of about 7% . In contrast, the relative density of unit 1 is typically 50 to 70%.

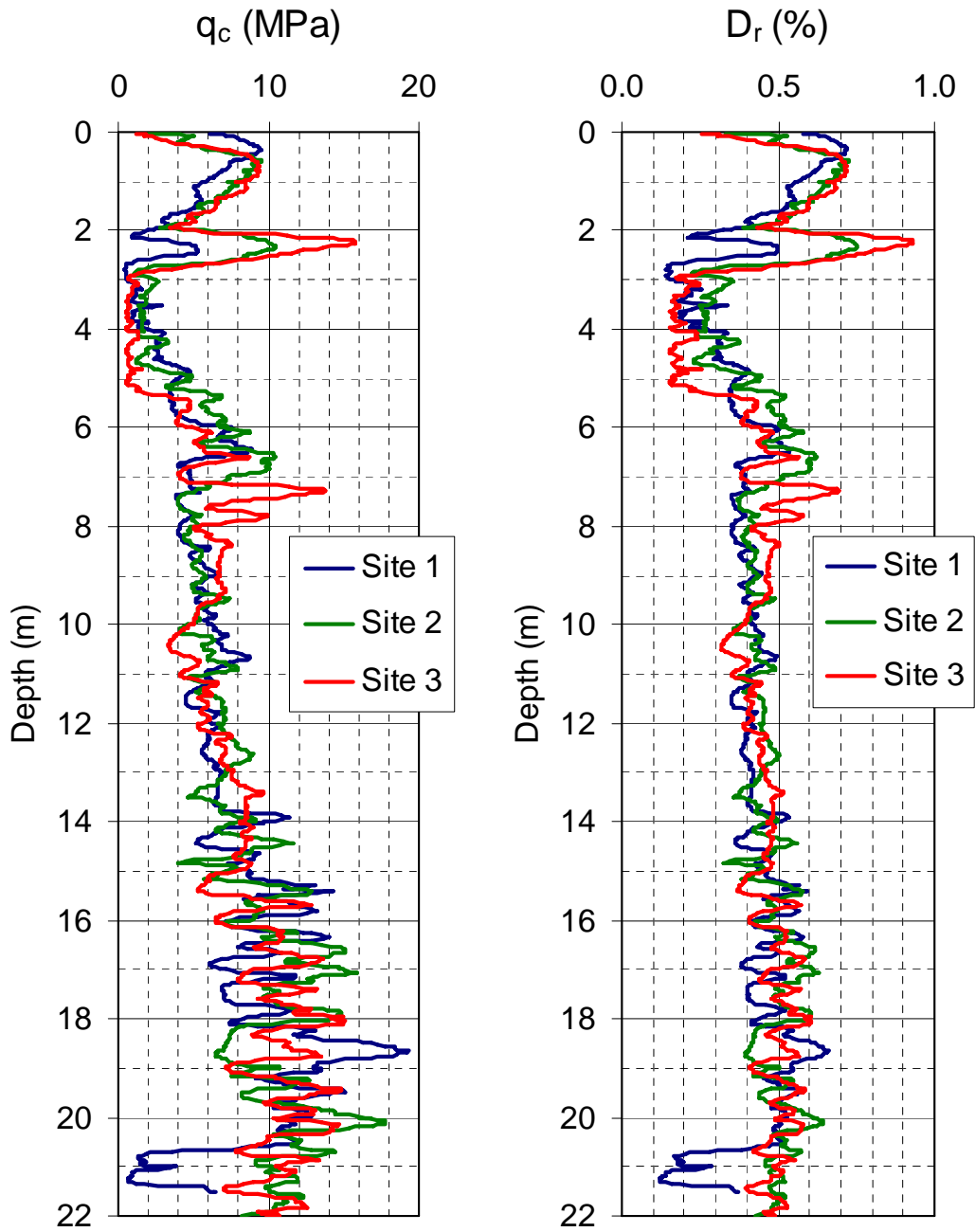


Figure 3.8 Comparison of cone tip resistance, q_c , and relative density, D_r , for Sites 1, 2, and 3, from the preliminary CPT soundings.

3.2 Shear Wave Velocity

Shear wave velocity measurements were taken at 1-m intervals during cone penetration testing at Site 1. Shear waves were created by striking a steel I-beam coupled to the ground by the weight of the test rig with an instrumented hammer. Shear wave velocity (V_s) measurements were made in general accordance with procedures described by Robertson *et al.* (1986). Figure 3.9 shows the results of the test at Site 1 along with V_s measurements made previously at the CANLEX project test site (Wride *et al.*, 2000) and at a nearby test site by Rollins and Anderson (2004). The shear wave velocity profile at Site 1 for this study was quite similar to that for the CANLEX project but was somewhat higher than that measured at adjacent sites. According to Andrus and Stokoe (2000), sands with V_s values less than about 190 m/s are susceptible to liquefaction. The shear wave velocity data in Figure 3.9 indicates that the target zone of Site 1 is clearly susceptible to liquefaction based on the Andrus and Stokoe criterion.

3.3 Permeability Testing

Rollins and Anderson (2004) conducted permeability tests at an adjacent site about 30 m south of Site 1. Considering the relative similarity in soil profile, geology, and cone penetration resistance, permeability characteristics at this new test site are likely to be similar. The horizontal Darcy permeability coefficient or hydraulic conductivity (k_h) profile in these tests was measured *in situ* using double packer borehole permeability tests along with well drawdown tests. These tests were performed and interpreted in

general accordance with designation E-18 in the US Bureau of Reclamation Earth Manual (1972) using equations originally developed by Hvorslev.

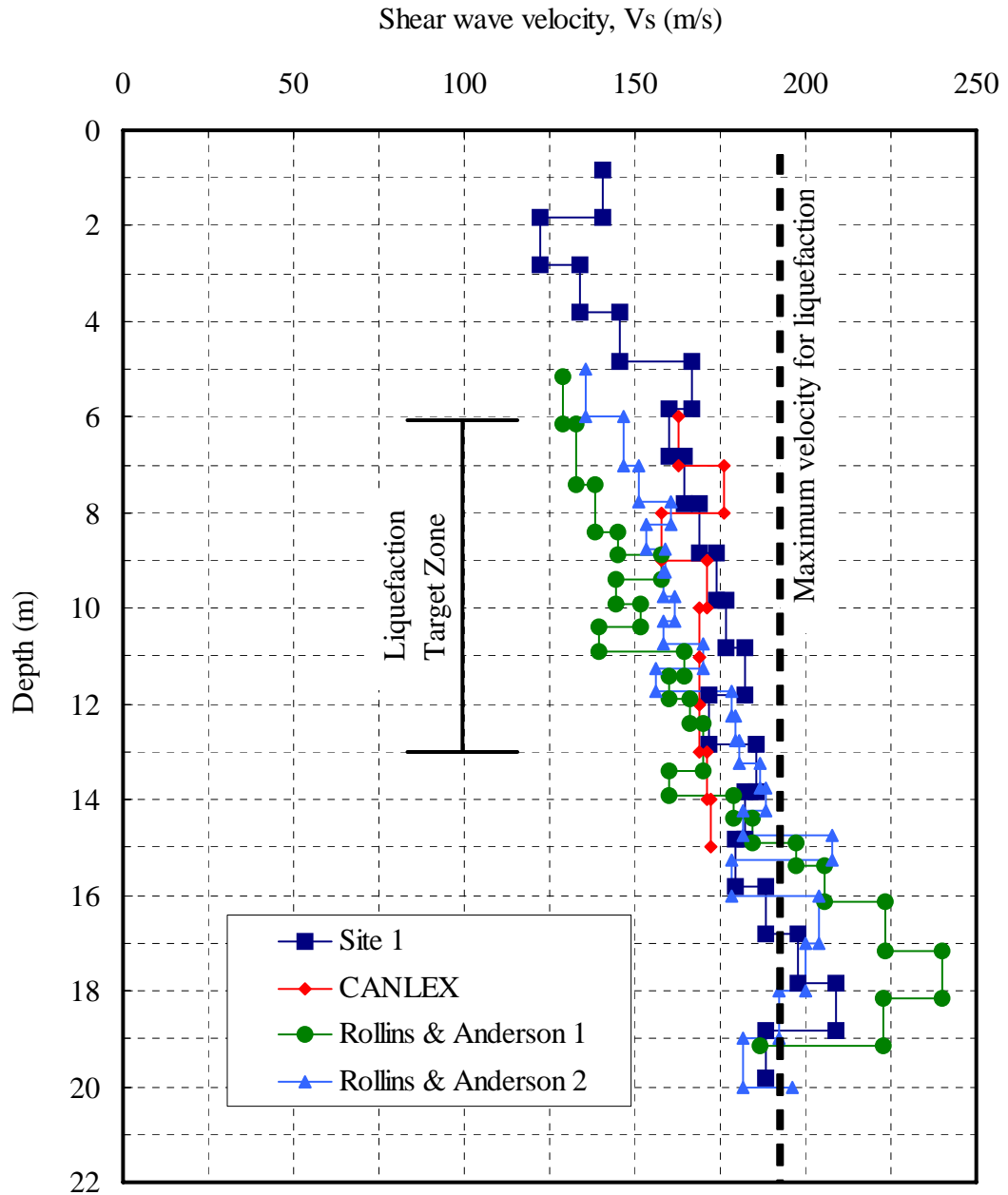


Figure 3.9 Shear wave velocity versus depth profiles at Site 1 and nearby test sites.

The tests were actually performed inside EQ-Drain pipe and a double packer system was used to isolate the flow within either a 0.61 or a 1.82-m-long segment along the length of the pipe. These tests provide an indication of potential variations in permeability within the profile. Drawdown tests were also performed by pumping at one drain location and measuring the drawdown at two adjacent drains. This test provides an overall average k_h within the pervious segment of the drain below the water table.

The k_h values computed from the packer tests and the drawdown test are plotted as a function of depth in Figure 3.10. The results from the packer tests suggest that k_h increases gradually with depth from a low of about 8×10^{-3} cm/s at a depth of 4 m to a high of about 5×10^{-2} cm/s at a depth of 11.5 m. The k_h computed from the drawdown tests (8×10^{-3} cm/s) is somewhat lower than that from the packer test but certainly within the typical range of variation expected for hydraulic conductivity measurements considering natural soil variation and measurement uncertainties.

The hydraulic conductivity interpreted from a CPT sounding performed at the CANLEX site by Conetec, Inc., (Weller, 2003, personal communication), is also depicted in Figure 3.10 for comparison purposes. The agreement between the k_h values obtained by the two methods is relatively good. The largest discrepancy occurs within the sandy silt layer, which appears to be a little thicker and to have a somewhat lower k_h based on the CPT sounding, than measured at the drain test site. The profile interpreted from the CPT sounding also indicates the presence of a few silt or sandy lenses within the clean sand layer with permeability coefficients which are two orders of magnitude lower than that in the clean sand. These thin, low permeability layers do not significantly affect the

equivalent horizontal permeability of the layer; therefore, they do not significantly affect the test results from the borehole packer tests. Overall, the results from the packer tests, drawdown test and CPT sounding are relatively consistent and provide relatively tight constraints on the values which are used in the subsequent computer analyses of the pore pressure generation and dissipation during the blast liquefaction testing.

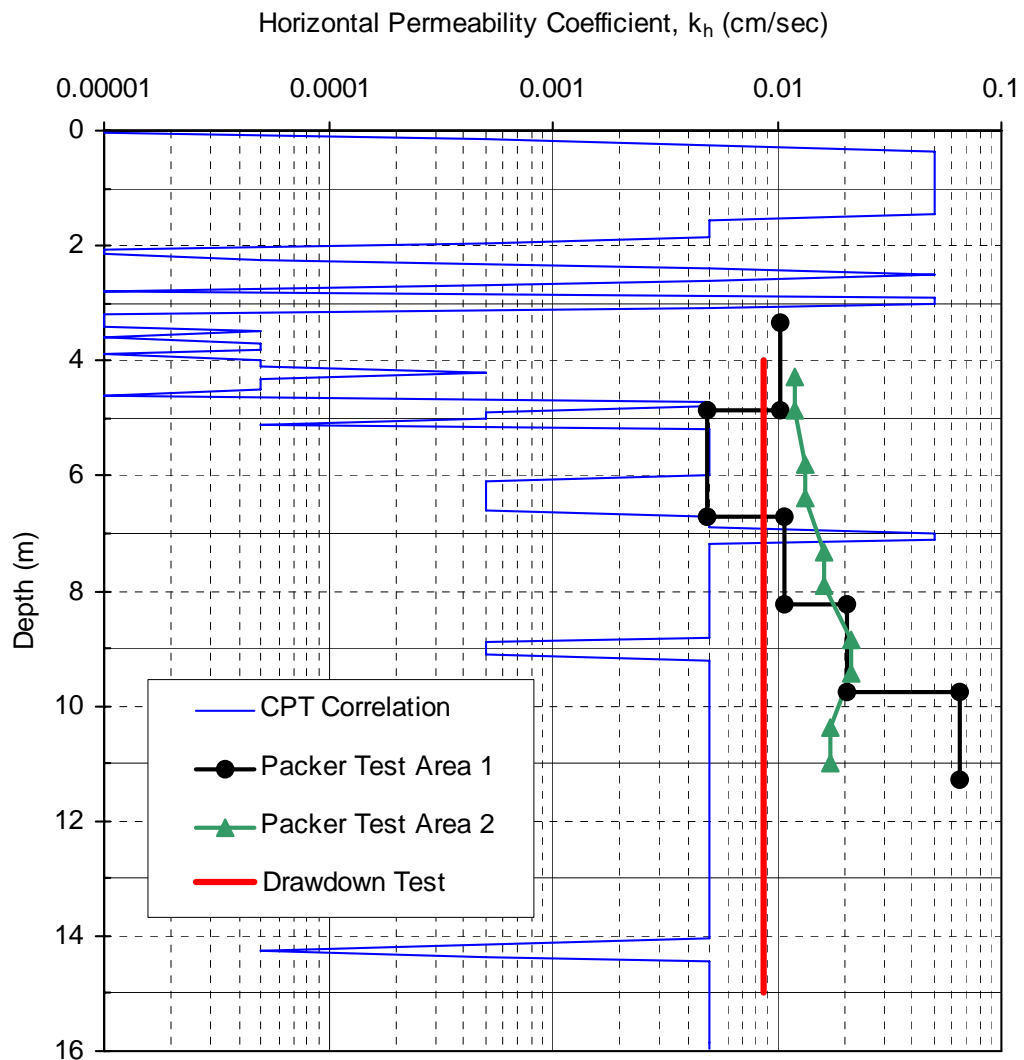


Figure 3.10 Horizontal permeability versus depth curves from several tests near Site 1.

3.4 Grain-Size Distribution Tests

Figure 3.11 shows upper and lower boundaries of grain size distribution developed by Gohl (2002) for the soil in the target zone (6 to 13 m). Based on these curves the sands are poorly graded clean to silty fine sands and classify as SP to SP-SM according to the Unified Soil Classification System.

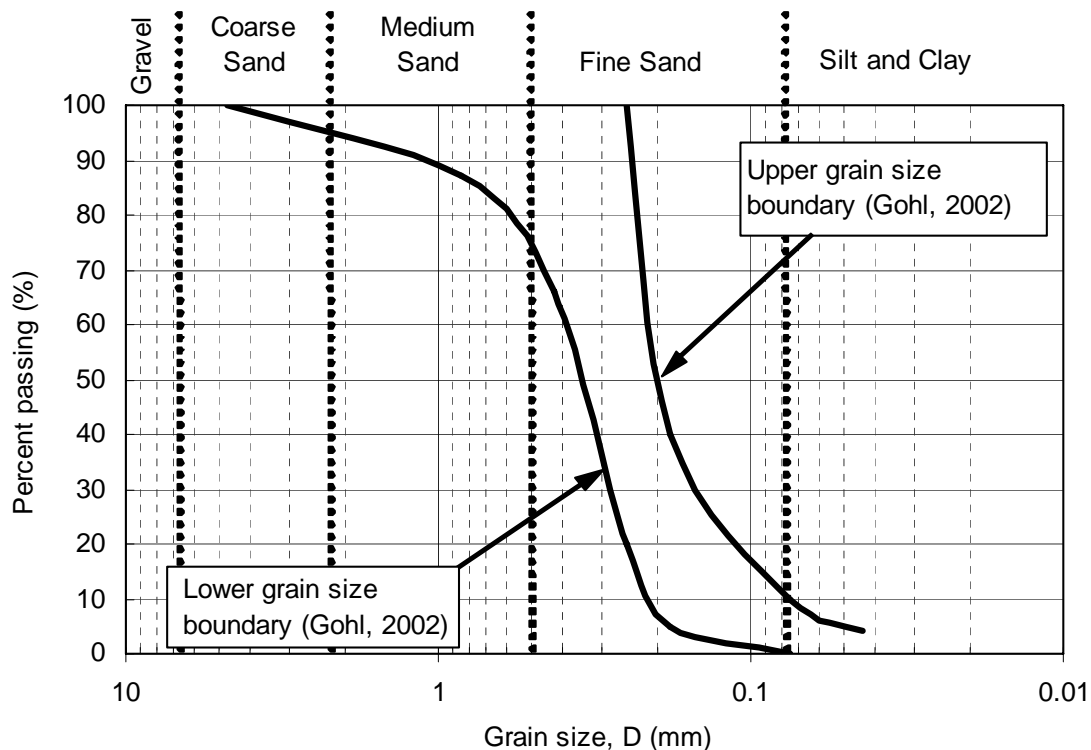


Figure 3.11 Range of grain size distributions for Fraser River sand between 5.5m to 11.5m depth (from Gohl, 2002).

During the course of sensor installation at Site 1 in preparation for preliminary blast testing, a standard penetration test was performed and a soil sample retrieved from a depth interval of 7.93 meters to 8.38 meters. Another sample was retrieved during the course of blast-hole installation from a depth estimated to be between 7.5 meters to 10

meters. Sieve analyses were performed on these two samples and the grain size distribution curves are plotted in Figure 3.12. The boundaries plotted in Figure 3.11 are re-plotted in Figure 3.12 for reference. Both samples were quite similar, consisting almost entirely of fine-grained sand with a fines content of 10% or less. Both of these samples classify as SP-SM and plot near the upper boundary as reported by Gohl (2002).

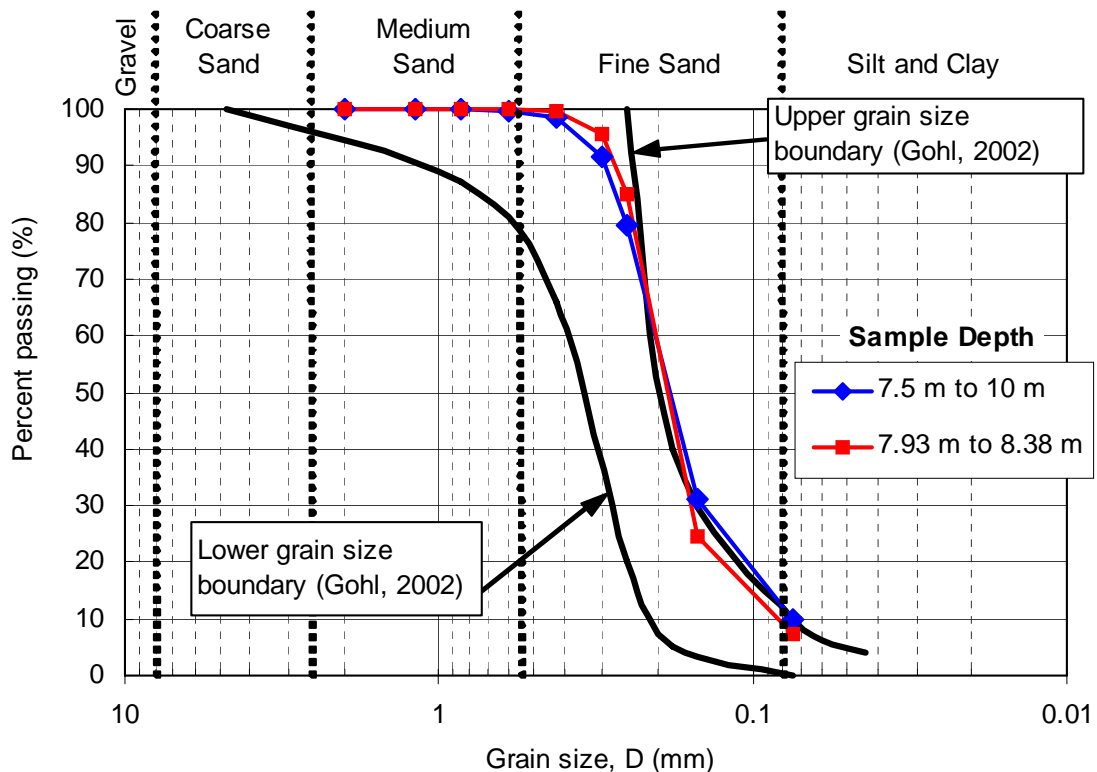


Figure 3.12 Grain size distribution curves for soil samples of Fraser River sand recovered during the course of sensor installation at site 1.

Samples of the sand from the upper 0 to 1.33 m of the profile were obtained from a hand-excavated test pit adjacent to Site 2. Grain size distribution curves for these samples obtained from laboratory testing are plotted in Figure 3.13 . Grain size boundary curves are re-plotted again for reference. These samples classified as SP type soils and

were very similar to the sands from 5.5 to 11.5 m. A sample of the silty- and clayey-sands found in Unit 2 was recovered in a Shelby tube. Grain size distribution analyses were performed on the sample and the results are also plotted in Figure 3.13.

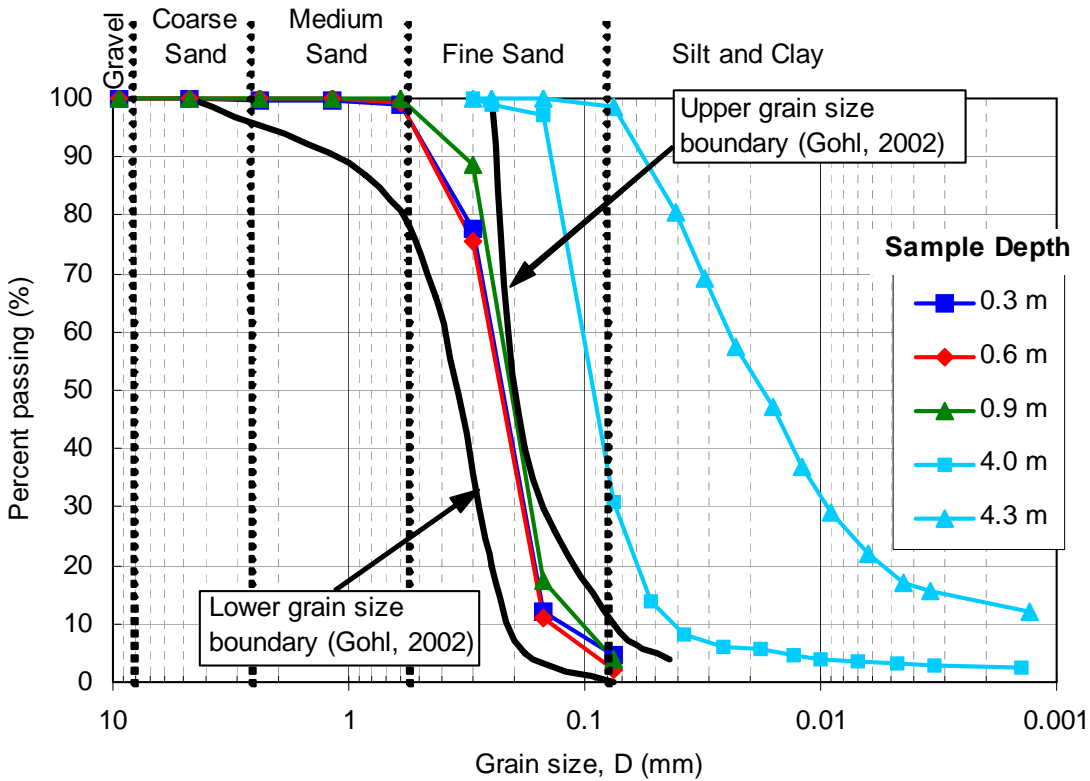


Figure 3.13 Grain size distribution curves for soil samples recovered from a hand-excavated pit and a Shelby tube sampler.

3.5 In-situ Density and Moisture Content

A variety of tests were performed to better define the unit weights of the soil layers in the profile. The dry unit weight and natural moisture content of the sands in the upper 1.4 m of the profile were determined by nuclear density gauge tests performed by Trow Inc., in the same hand-excavated trench from which the samples discussed above were taken. A summary of the test results is presented in Table 3.1.

The unit weight and natural moisture content of the more fine-grained materials within Unit 2 were obtained from thin-walled Shelby tube samples obtained from a depth between 4.0 and 4.4 m at the test site. Test results are listed in Table 3.2.

Finally, unit weights for the poorly graded sands (Unit 3) in the target zone from 6 to 13 m were evaluated based on previous CANLEX testing. In this unit, the *in situ* void ratio was computed from two geophysical soundings along with a number of undisturbed frozen samples. A plot of the void ratio versus depth in this layer is provided in Figure 3.14. The void ratio in the depth range from 6 to 13 m typically ranges from about 0.9 to 1.1 with an average value of approximately 0.95. With a measured specific gravity of 2.68, this average void ratio translates into a dry unit weight of 13.5 kN/m³, a moisture content of 35.4%, and a saturated unit weight of 18.5 kN/m³.

3.6 SPT Blow Count Correlations

As part of the CANLEX project, a site specific correlation between CPT q_c values and the $(N_1)_{60}$ values was developed. For the Massey site (the CANLEX site approximately 300 m north of the test site), the average value of $q_c/(N_1)_{60}$ was 0.58 with a standard deviation of 0.17 (Wride *et al*, 2000). At Site 1, an average value of q_c equal to 5.6 MPa in the target layer results in an estimated $(N_1)_{60}$ value of approximately 10. For Sites 2 and 3, average q_c values in the target zone were 5.5 MPa and 6 MPa respectively and also have estimated $(N_1)_{60}$ values of 10. According to Youd *et al* (2001), soils with $(N_1)_{60}$ values less than about 25 to 30 are susceptible to liquefaction. Accordingly, all three test sites should be easily liquefied.

Table 3.1. Summary of dry unit weight, in situ moisture content and moist unit weight determined with a nuclear density gauge at several depths in the hand-excavated pit.

Depth (m)	Dry Unit Weight γ_d (kN/m ³)	Moisture Content w (%)	Moist Unit Weight γ (kN/m ³)
0.1	12.24	12.7	13.79
0.2	12.69	11.4	11.14
0.4	13.56	7.3	14.55
0.5	14.63	6.1	15.52
0.7	14.00	8.1	15.13
0.8	13.78	7.7	14.84
1.0	14.15	10.9	15.69
1.1	14.07	10.5	15.55
1.3	11.95	20.7	14.43
1.4	12.92	16.3	15.07
Average	13.4	11.17	14.57

Table 3.2. Summary of in situ unit weight and moisture content for Unit 2 at Vancouver test site. Samples were recovered using a shelly tube.

Depth (m)	Dry Unit Weight γ_d (kN/m ³)	Moisture Content w (%)	Moist Unit Weight γ (kN/m ³)	USCS Symbol
4.0 - 4.2	13.78	33.1	18.34	SM
4.2 - 4.4	13.09	41.3	17.98	ML
Average	13.44	37.2	18.16	

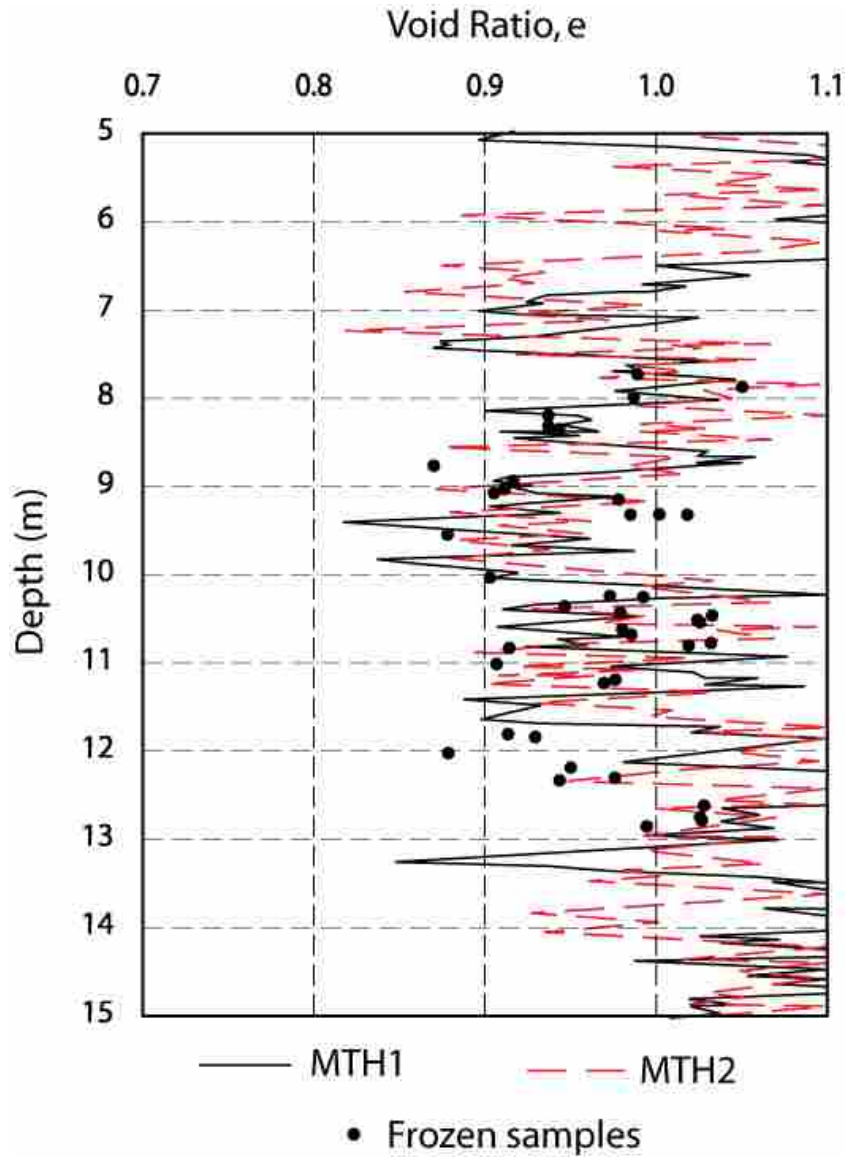


Figure 3.14 Void ratio versus depth curves developed as part of the CANLEX study (after Wride *et al*, 2000).

4 Pilot Liquefaction Testing at Site 1

As noted in Section 2.1.2, previous testing involving controlled blasting used sequences that caused a very rapid rise in pore pressures, overwhelming the ability of the EQ drains to prevent liquefaction. Rather than inducing liquefaction in a couple of seconds with one or two large charge detonations, a better simulation of an earthquake event would be produced with sequential detonation of smaller charges with a duration of 10 to 16 seconds. Ideally, the explosive charges would be sized such that they would induce liquefaction in the untreated area without overpowering the drains in the treated area. Accordingly, Site 1 was chosen as the location to carry out preliminary blast testing in order to determine the appropriate size of charges. These tests were monitored for changes in pore pressure, ground movement, and settlement.

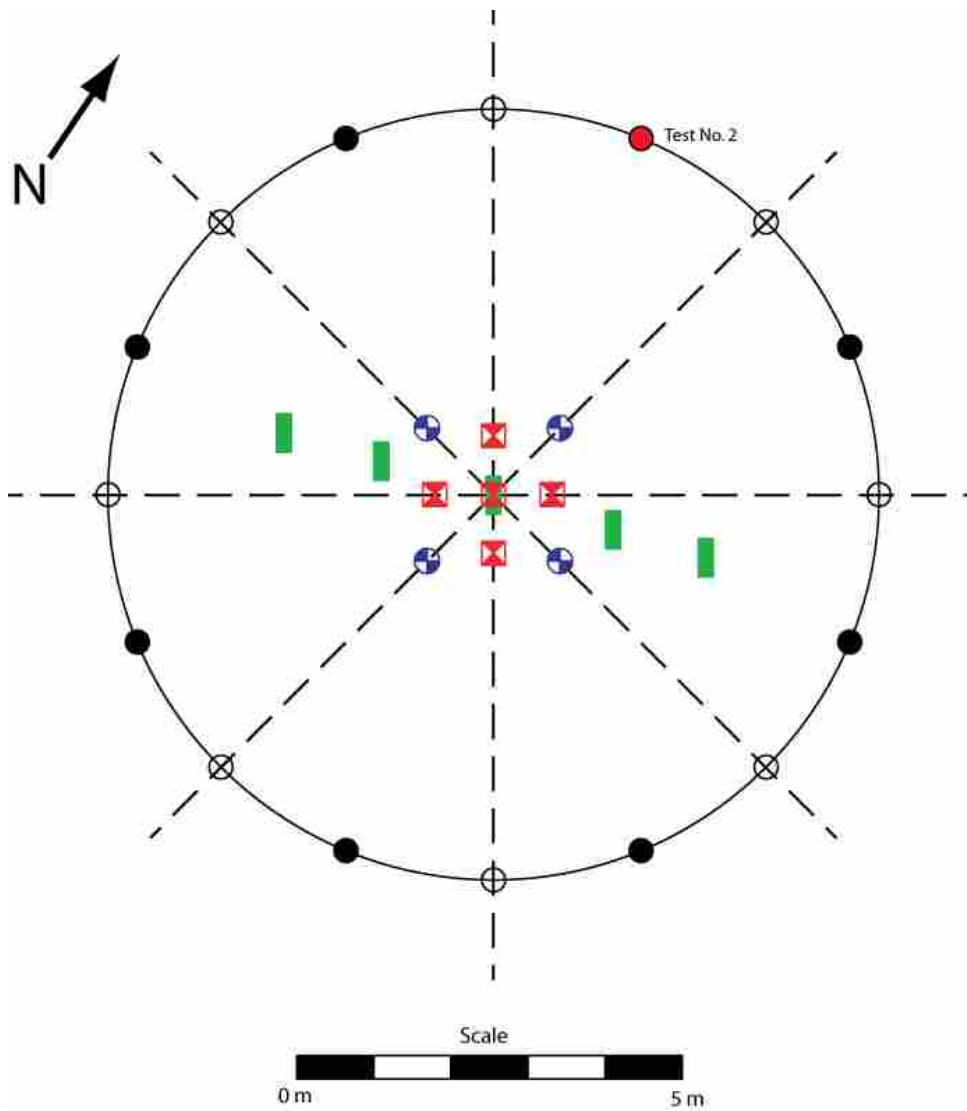
4.1 Test Blasting Design

Three separate blast tests were used in the pilot blast testing. In the first test, a total of 24, 0.227 kg (½ lb) explosive charges were placed in eight blast holes, three charges in each hole. The eight blast holes were equally spaced around a circle 10 m in diameter (see Figure 4.1). The explosive charges in each hole were placed into three levels or “decks.” The lowest deck was placed at 10.1 m depth; the middle deck at 8.5 m

depth; and the top deck of charges at 6.4 m depth. Each charge consisted of Pentex explosive, which is a commercial form of Pentolite 50/50. Pentolite 50/50 is an organic explosive compound consisting of 50% pentaerythritol tetra nitrate (PETN) and 50% trinitrotoluene (TNT), with excellent water resistance characteristics. In addition, Pentex is resistant to sympathetic detonation from other charges. Gravel stemming was packed in between the charges to prevent premature detonation and to direct the energy of each charge radially, rather than just vertically. All handling, installation, wiring, and detonation of the explosives were performed by professional, licensed blasters. The explosives were detonated sequentially, with a one-second delay between charges using two electrical blasting boards. Blasting began in the bottom deck and proceeded upwards, with all charges in a deck being detonated before continuing to the deck above.

The first blast series generated pore pressure much lower than expected. This appears to be a result of the blast hole installation as discussed subsequently. When the first blast test generated less-than-expected pore pressures, a second blast test was performed to determine the increase in pore pressure produced by an individual charge. Thus, the second blast test consisted of a single, 1.135 kg (2.5 lb) explosive charge placed at 8.5 m depth in the blast hole indicated in Figure 4.1.

With the results of the first two blast tests, the third blast test was performed using 1.36 kg (3 lb) charges. A total of 21 charges were placed in three decks in the seven blast holes as indicated in Figure 4.1. Detonation of the charges followed the same procedure used in the first test. The third blast test indicated that the 1.36 kg charges would provide the desired results.



Legend







	Accelerometer		Test No. 1
	Pore Pressure Transducer		Test No. 3
	String Potentiometer		Survey Ray

Figure 4.1 Layout of blast holes and instrumentation used during preliminary blast testing at Site 1.

4.2 Blast Hole Installation

Blast holes were consisted of a 120-mm-dia. flexible plastic drain pipe wrapped in a geosynthetic filter fabric with a steel anchor. The drain pipe, geosynthetic fabric and anchors used for the blast holes were identical to those used for the drains (see Section 7.1).

The blast holes were installed using a 13.4-m-long pipe mandrel clamped to an ICE Model 44 vibratory hammer (500 N-m energy) suspended from a 70-ton mobile crane (see Figure 4.2). The mandrel consisted of a 165-mm-dia. steel pipe with 9.5-mm-thick walls (see Figure 4.3). In Figure 4.3, the mandrel in the foreground has three cleated “fins” equally spaced about the circumference of the mandrel. This mandrel was used in the installation of the EQ drains, discussed subsequently in Section 7.2.

The drain pipe/filter fabric/anchor assemblies were “bottom loaded” into the mandrel using a rope attached to the top of the drains. The rope traveled up through the mandrel and out the side of the mandrel over a pulley positioned within the wall of the mandrel. With the bottom of the mandrel suspended approximately 1.5 m above the ground, a workman on the ground would lift the drain up into the mandrel as another workman guided the drain. The drains were pulled up tight into the mandrel to ensure that the anchor plate fit flush with the bottom of the mandrel.

Once the drain was pulled into the mandrel, the hammer was turned on and the mandrel vibrated slowly into the ground. After the drains reached the design depth of 12.8 m, the hammer was turned off for about a minute to allow the soil to reconsolidate around the anchor. Then, as the mandrel was removed, the hammer was turned back on

for a few moments, the vibrations causing the mandrel to disengage from the surrounding soil so it could be more easily extracted.



Figure 4.2 Drain installation was accomplished with the use of a 70 ton crane and a vibratory hammer and mandrel.

The anchors used during the installation of the blast holes consisted of a 150 mm x 150 mm x 12.5 mm steel plate with a loop formed from approximately 8-mm-dia. steel rod to which the filter sock was tied. This type of anchor proved difficult to use as they often did not anchor properly in the soil. It was discovered that the mandrel had to be lowered twice in the same hole to install the drains. The first time the mandrel was lowered with only an anchor plate to prevent the mandrel from plugging with soil. The

second time the mandrel was lowered with the drain as described above. This “double penetration” approach required up to eight minutes to install one drain.



Figure 4.3 Mandrels used in EQDrain and blast hole installation. Mandrel on left has three “fins” designed to transfer vibrational energy to surrounding soil. Mandrel on right is smooth.

Because of difficulties encountered in anchoring the earthquake drain pipes used for the blast holes, a larger anchor was used for the earthquake drains. This anchor consisted of a cylindrical section attached to a square plate measuring 305 mm x 305 mm (see Figure 4.4). This anchor was successful in efficiently anchoring the drains into the loose sand so that the installation time for a 12.8-m-long drain was approximately 3 minutes.



Figure 4.4 Photograph of an EQDrain tied to an anchor. Anchors measured 305 mm x 305 mm x 12.5 mm. Generally, the anchors had the corners bent over; this one did not.

Due to the use of “hanging leads” during blast hole installation, it was difficult to maintain verticality. Rotation of the mandrel occurred which fractured the connection between the mandrel and the vibratory hammer. Fortunately another smooth mandrel was on hand and blast hole installation was only temporarily delayed.

The use of the drain pipe kept the blast hole open, allowing the explosive charges and gravel stemming to be positioned as desired. For the first blast test, eight holes were installed in a circular pattern with a 4.9-m radius, 45 degrees between each hole (see Figure 4.1). After the first blast another eight blast holes were installed in a similar manner. This second set of holes was rotated 22.5 degrees from the first set. Unfortunately, rotation of the mandrel during the drain installation procedure also appears to have created small gaps around the periphery of the drain pipe which appear to

have reduced the energy transmitted by the explosive charge to the surrounding sand. In addition, the perforations in the drain pipes may have allowed more gas to be injected into the surrounding sand during the detonation process than with a solid casing.

4.2.1 Blast hole installation induced settlement

A level survey was conducted immediately after installation of the first set of eight blast holes. At two individual points settlement was measured to be 15 mm. In general, however, settlement was less than 9 millimeters. The procedure used to conduct the level survey is discussed further in Section 4.4.1.

4.3 Pore Pressure Monitoring

Figure 4.1 shows the locations of the various types of sensors and instruments used to monitor the preliminary blast testing. Pore pressures were monitored using six piezometers located at depths of 5.5 m, 7.6 m, 11.6 m, and 13.7 m (two piezometers were installed at 7.6 m). One piezometer was located at the center of Site 1; four more were located 0.76 m from the center, spaced 90 degrees apart. The sixth piezometer was located 6.22 m from the center. This sixth piezometer was used mainly in conjunction with the *in situ* vane shear test mentioned in the introduction. For clarity, the location of the vane shear apparatus and the sixth piezometer are not included in Figure 4.1 and the results from this piezometer will not be discussed here.

The piezometers consisted of a pore pressure transducer encapsulated in a hard nylon protective body (see Figure 4.5). The transducers were designed to withstand a transient blast pressure of up to 41.4 MPa and then record the residual pore pressure with

an accuracy of ± 0.7 kPa. The transducer was screwed into a hard nylon cone tip with ports open to the surrounding ground water. These ports were packed with cotton and boiled to removed any free air prior to assembly with the transducer. The transducer/cone tip assembly was then screwed into the hard nylon protective body and the complete assembly installed to the desired depth. A steel cable attached to the protective body provided a means to withdraw the piezometer once the testing was complete (see Rollins *et. al.*, 2005).

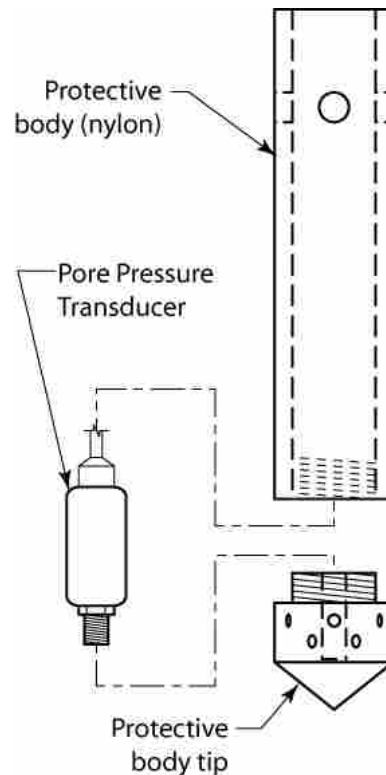


Figure 4.5 Schematic drawing of pore pressure transducer and hard nylon protective body (after Rollins and Anderson, 2004).

The piezometers were installed using a rotary drill rig to first drill to 0.3 m above the desired depth. Drilling mud consisting of bentonite slurry prevented the hole from

collapsing. The sensor was then pushed the remaining 0.3 m to the desired depth using the drill rod. A special adapter was used to connect the piezometer to the drill rod.

4.3.1 Determination of the degree of liquefaction

Typically, the degree of liquefaction is characterized by the excess pore pressure ratio. The excess pore pressure ratio (R_u) is simply the increase in pore pressure above the static pressure caused by blasting as measured by the piezometer divided by the initial effective stress at the level of the piezometer. In mathematical terms,

$$R_u = \Delta u / \sigma'_0 \quad (3)$$

where Δu = increase in pore pressure
 σ'_0 = initial effective vertical stress

An R_u value of 1.0 is generally considered to indicate liquefaction for level ground conditions. Therefore, the definition of liquefaction based upon the excess pore pressure ratio was completely adequate for the purposes of this study. When initial shear stresses are present, due to the presence of a slope, an embankment, or a building foundation, an R_u value of 1.0 may not fully develop. This is also the case for cyclic triaxial shear tests involving anisotropic consolidation. In cases such as these, “liquefaction” may be defined in terms of a strain level (e.g. 5% or 10% strain) which develops as the soil weakens due to the generation of excess pore pressure. This highlights the fact that significant settlement and strength loss can still occur with high R_u values which may not necessarily reach 1.0.

The excess pore pressure ratio produced by blasting was calculated from the pressure data recorded by each piezometer. Accurate evaluation of R_u depends upon an accurate estimate of the effective stress which in turn depends upon accurate measurements of soil unit weights and depth to the water table.

Values of R_u for the preliminary blast testing were calculated using a moist unit weight of 14.72 kN/m³ for Unit 1, and saturated unit weights of 18.16 and 18.2 kN/m³ for Units 2 and 3, respectively, based on field and laboratory testing as described in Section 3.5. The depth to the water table was measured before each blast and the measurements are recorded in Table 4.3.

Table 4.3. Depth to water table immediately before each blast test.

	Site 1		Site 2		Site 3	Site 4
	Blast 1	Blast 3	Blast 1	Blast 2		
Depth to water table (m)	3.05	3.05	2.92	2.91	3.01	2.91

4.4 Settlement

Settlement was monitored using three methods. Total ground surface settlement was measured using a level survey; five string potentiometers measured real-time settlement both during and following blasting; and finally, settlement as a function of depth was measured using a “Sondex tube” as described later in Section 4.4.3.

4.4.1 Total ground surface settlement

Total ground surface settlement was measured using conventional survey equipment to conduct a level survey. Elevation measurements were made before and

after each event that may have produced settlement (such as instrument installation, blast tests, etc.) and the resulting ground surface settlement calculated. Measurements were made at regular intervals along eight rays emanating from the center of the test area and spaced 45 degrees from each other. Survey points were spaced at 0.91 m intervals along each ray for the first 4.57 meters and then at 1.54 m intervals out to 18.3 meters (see Figure 4.6).

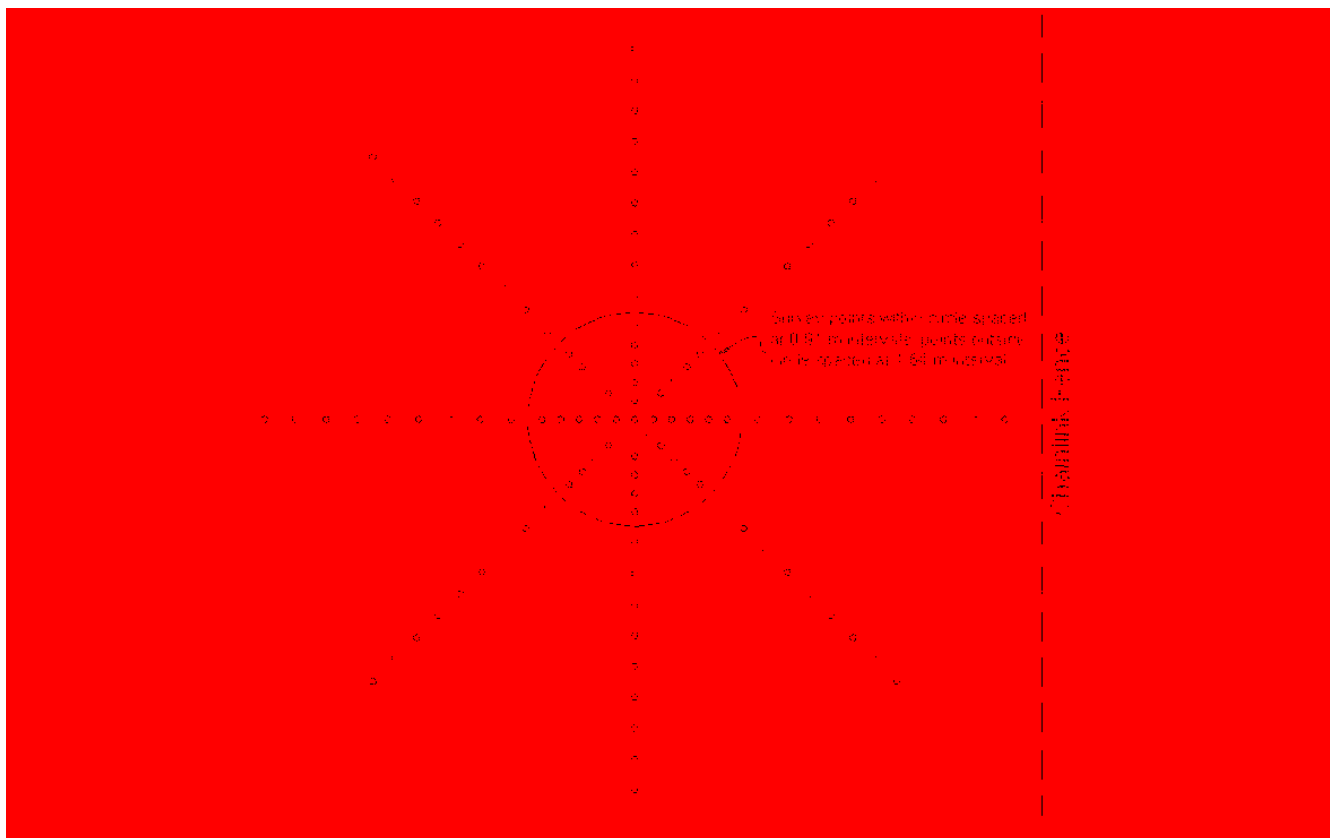


Figure 4.6 Schematic sketch of the layout of the survey measurement points used at Sites 1, 2, and 3 to monitor total ground surface settlement.

4.4.2 Real-time settlement

Ground surface settlement caused by the blast tests was monitored using five string potentiometers attached to a tensioned, steel cable strung above the test site. The

cable was anchored beyond the edges of the test site in an effort to prevent the blast testing from causing the cable to sag. The string potentiometers were spaced 1.2 m apart along a line through the center of the test site (see Figure 4.1). The middle potentiometer was located over the center of the test site. Real-time settlement was measured during the first and third blasting events.

4.4.3 Depth-related settlement

In addition to the surface settlement measurements, settlement as a function of depth was also investigated with a Sondex tube. The Sondex tube is designed to settle with the surrounding ground and the change in elevation at various points along the tube is measured magnetically with a downhole probe. The Sondex tube consisted of a 76-mm-dia., non-perforated flexible corrugated drain pipe inside a sleeve of geosynthetic material and an anchor. The geosynthetic fabric and anchor were of the same type used for the EQ drains. Before covering with the geosynthetic material, thin steel bands that fit in between the corrugations were secured tightly around the outside of the pipe at approximately 0.76 m intervals and wrapped with electrical tape. After tying the anchor on to the bottom of the pipe with the geosynthetic, the assembly was then installed with the vibratory hammer and a smooth mandrel to a depth of 11 meters.

The depth to the steel bands was determined using a Sondex probe which indicated the location of each steel band magnetically. A length of 66-mm-dia., schedule 40 PVC pipe was slipped down the center of the corrugated pipe and seated firmly at the bottom of the hole. The PVC pipe provided a consistent pathway for the Sondex probe and prevented the collapse of the corrugated tubing. The top of the PVC pipe also served

as a reference point for making depth measurements. The flexibility of the plastic drain pipe was such that it could shorten as the surrounding soil settled. The change in depth of the steel bands then revealed how settlement developed with depth. Sondex tubes were also installed at Sites 2 and 3 with this same procedure; however, both tubes collapsed within 6 m of the surface, preventing any measurements. Later, during the installation of the test pile foundations, new Sondex tubes were installed at Sites 2 and 3 using conventional rotary drill equipment.

4.5 Results of Preliminary Blast Testing at Site 1

Preliminary blast testing was performed at Site 1 May 6, 2005.

4.5.1 Blast induced excess pore pressure

Figure 4.7 shows plots of excess pore pressure ratio time histories measured by each of the transducers during the first blast. The plots in Figure 4.7 are limited to the first 30 seconds so that pore pressure generation due to each individual blast can be clearly identified. For each blast a large transient pressure pulse was produced followed by an increased residual excess pore pressure which remained relatively constant until the next charge was detonated. While the sequential blasting did produce a significant progressive increase in the pore pressure ratio, the peak residual values did not exceed about 0.70. Therefore, liquefaction was not achieved in this blast sequence.

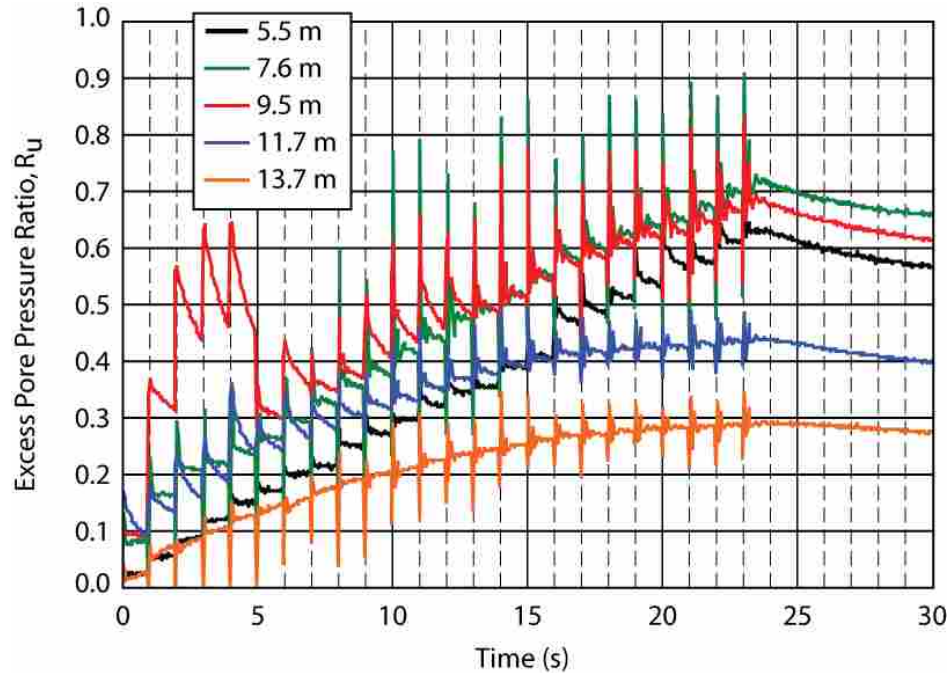


Figure 4.7 Generation of pore pressure during the first blast test at Site 1.

The R_u time histories for most of the piezometers were relatively similar; however, R_u values for the deepest piezometers were somewhat lower because they were further away from the blast charges in general and the sand at this depth was also denser.

Complete time histories showing both the generation and dissipation of R_u are plotted in Figure 4.8. R_u values decreased to about 0.1 within 3 minutes for the lowest piezometer and 10 minutes for the uppermost piezometer. Dissipation progressed more slowly near the top of the soil profile, likely due to the presence of the overlying silty clay layer (Unit 2) which could have provided an impervious boundary or at least impeded drainage.

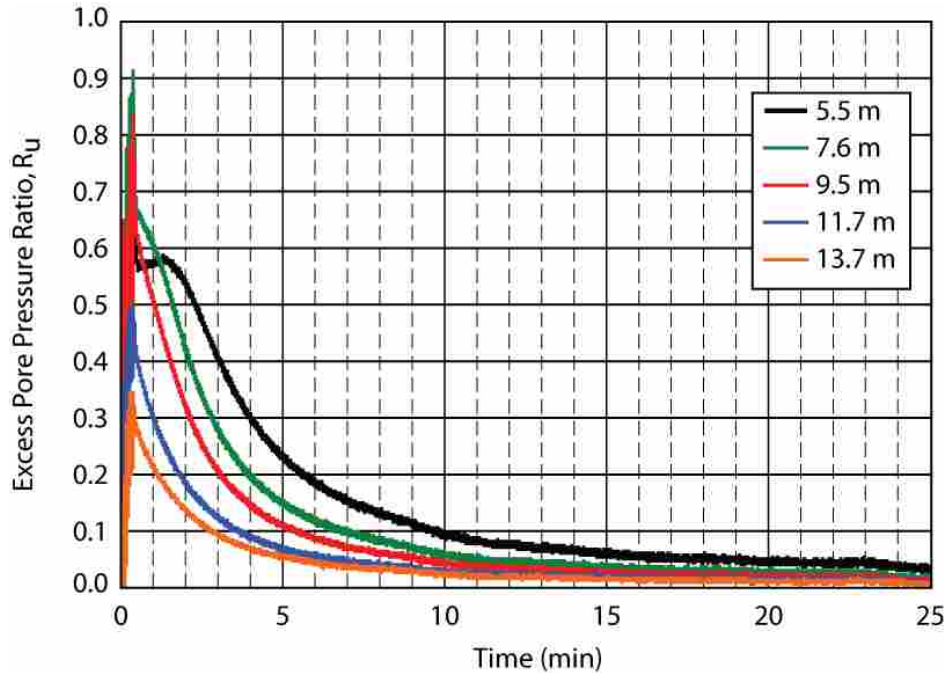


Figure 4.8 Dissipation of pore pressure after the first blast test at Site 1.

Figures 4.9 and 4.10, respectively, depict the generation and dissipation of pore pressure during and after the third blast test at Site 1. As can be seen in these figures, both the generation and dissipation curves have the same general shapes as the corresponding curves for the first blast test. For the third blast test, the maximum excess pore pressure ratios generally exceeded 0.9 indicating that the soil had essentially liquefied. The effectiveness of each charge detonation in generating excess pore pressure appears to decrease with the number of detonations and relatively little extra pore pressure increase was observed after about 12 charges had been detonated.

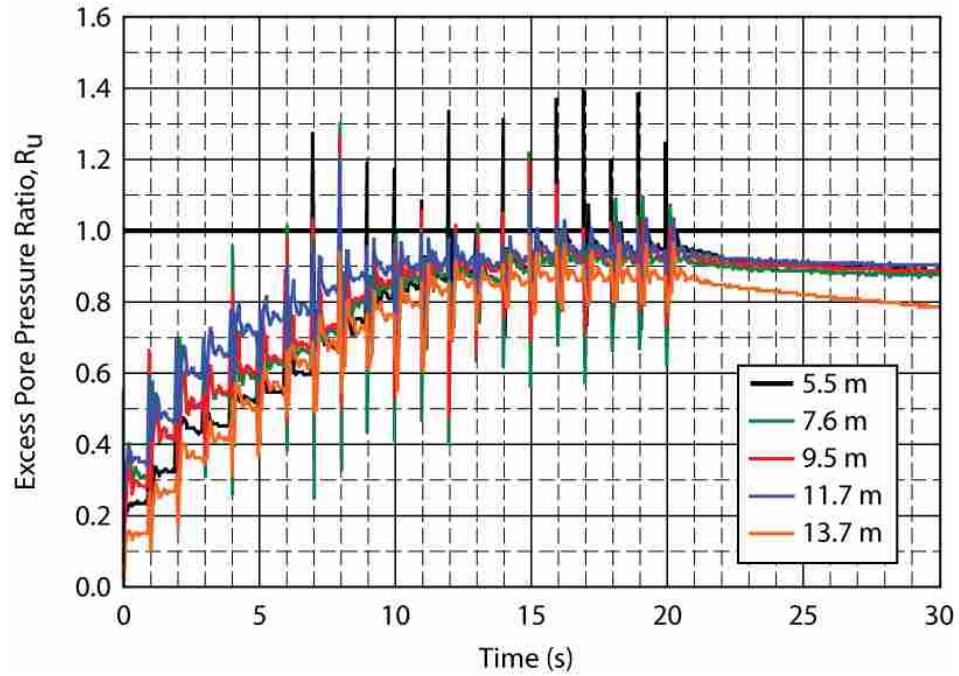


Figure 4.9 Generation of pore pressure during the third blast test at Site 1.

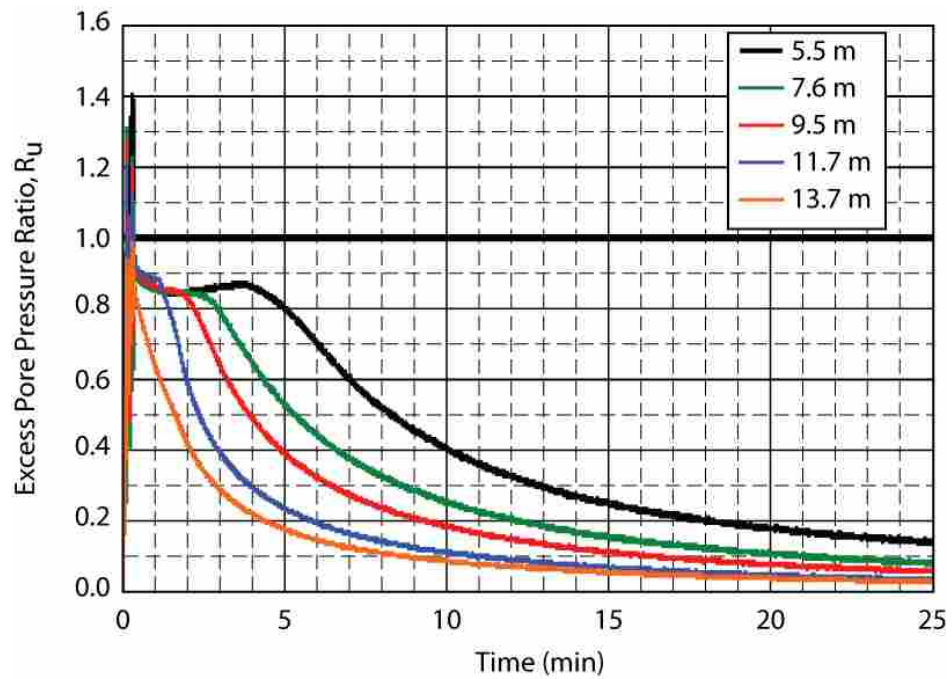


Figure 4.10 Dissipation of pore pressure after the third blast test at Site 1.

R_u values decreased to about 0.1 for the bottom-most piezometer within approximately 10 minutes. Pore pressures were not recorded long enough after the third blast test for the R_u values measured by the top-most piezometer to decrease to the same level. Interpolating beyond the end of the recording, R_u would likely have decreased to 0.1 by about 35 minutes after blasting.

It is obvious that the larger explosive charges generated larger pore pressures which took longer to dissipate than those associated with the first blast test. Again, pore pressures dissipated most rapidly in the lower layers and most slowly near the surface, indicating that the clayey-silt layer (Unit 2) acted to decrease the rate of pore pressure dissipation.

4.5.2 Blast induced settlement

4.5.2.1 Real-time ground surface settlement

Settlement was measured during blasting using five string potentiometers as described above to monitor real-time settlement caused by the blasting. Figure 4.11 shows time histories of the ground surface settlement measured in real-time by the string potentiometers during the first blast test at Site 1. The string potentiometers are identified in Figure 4.11 according to their distance from the center of the test site. Negative distances are to the left of center and positive distances are to the right of center, as shown in Figure 4.1.

All the potentiometers indicate that settlement started very soon after the blasts began and terminated at about 7.5 minutes after blasting, when the excess pore pressure ratio for the bottom four piezometer had decreased below 0.4 and R_u for the top

piezometer was about 0.6. The plots indicate that maximum settlement was approximately 68 mm. Maximum settlement was somewhat greater on the one side than the other but generally decreased with distance from the center. The shapes of the settlement curve are all consistent. Close examination of the curves shows that some of the surface settlement occurred in a step-wise fashion. Two major events are apparent; the first at about 6.5 minutes and the second at about 7.5 minutes. The vertical part of the steps is possibly caused by the collapse of soil bridges which could temporarily arch over the settling sand at depth.

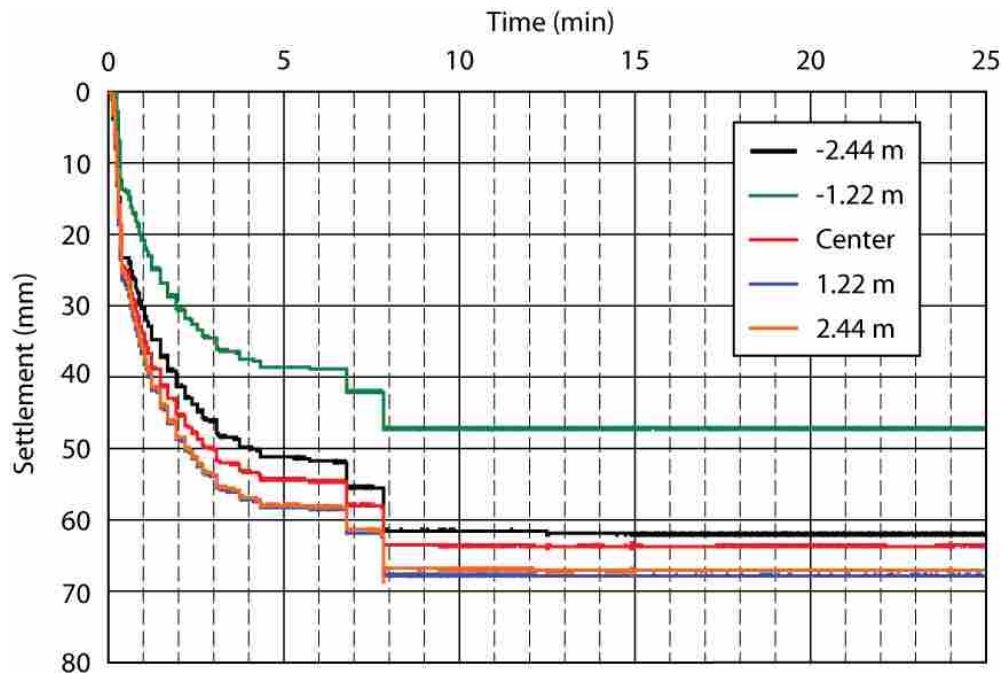


Figure 4.11 Real-time ground surface settlement measured by the string potentiometers during the first blast test at Site 1.

Figure 4.12 shows the real-time settlement due to the third test blast at Site 1.

Again the settlement occurred very soon after blasting and essentially ended within 10 minutes after blasting. Maximum settlement was approximately 250 mm and occurred at

the center potentiometer. Settlement typically decreased with distance from the center point.

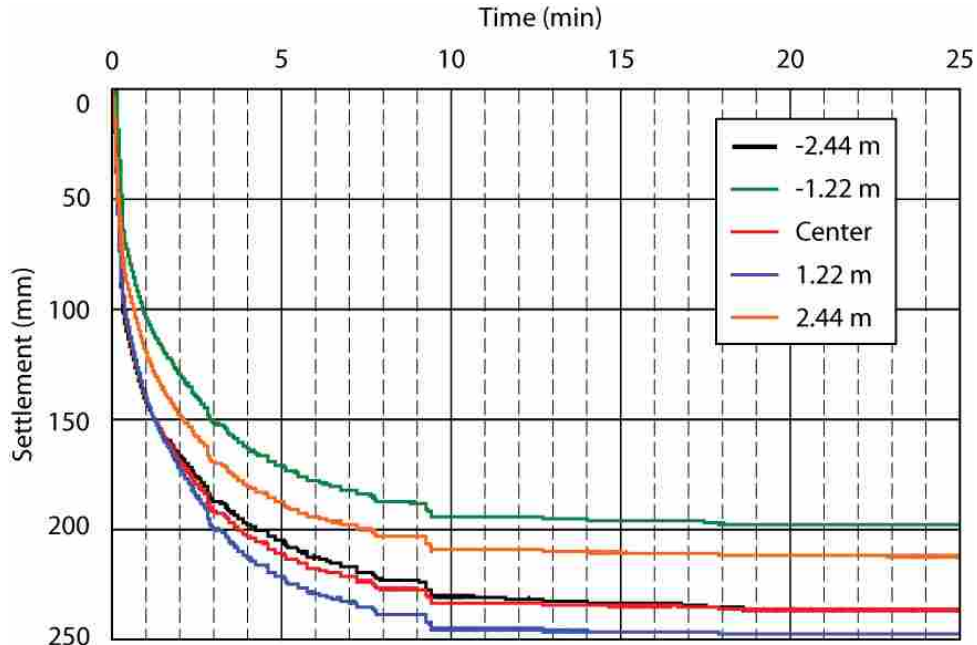


Figure 4.12 Real-time ground surface settlement measured by the string potentiometers during the third blast test at Site 1.

4.5.2.2 Total ground surface settlement

Figure 4.13 is a contour map of the total blast-induced settlement from the first blast test. As expected, the maximum settlement (approximately 110 mm) occurred near the center and the contours are generally concentric about the center. It should be noted that a discrepancy between the settlement measured by the level survey and the string potentiometers was discovered and will be discussed later.

Figure 4.14 is a contour plot of the total ground surface settlement caused by the third blast test at Site 1, similar to that shown in Figure 4.13. Again, the maximum settlement (approximately 425 mm) occurred near the center of the test area and

decreased towards the edges of the site. The contours are fairly concentric about the center, though skewed to the left at lower settlement values.

Obviously, the larger explosive charges used in the third blast test caused much greater settlement as compared to the first blast test. Not only was the maximum settlement greater, but the radius of the “settlement basin” was also much greater.

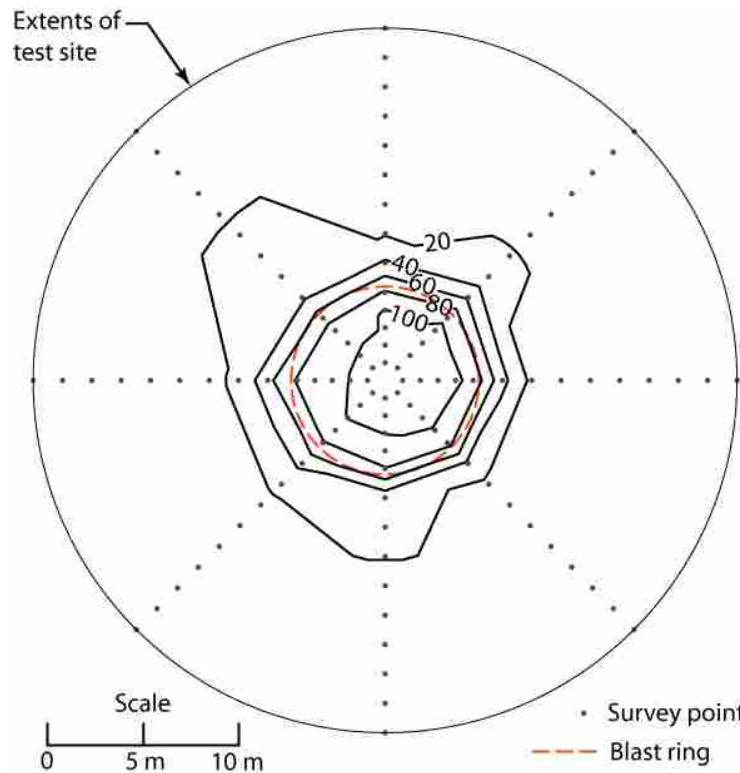


Figure 4.13 Contour plot of ground surface settlement resulting from the first blast test at Site 1.

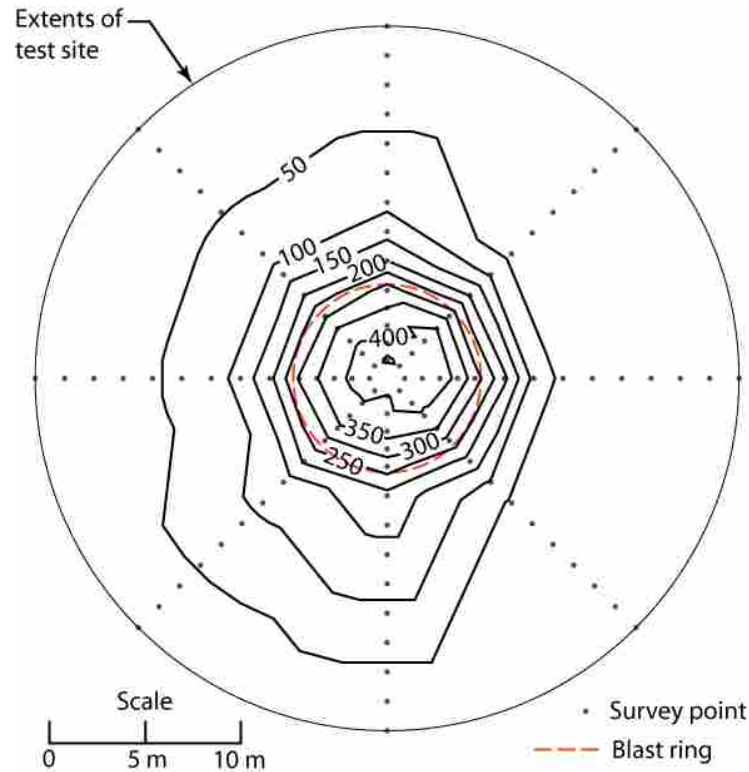


Figure 4.14 Contour plot of ground surface settlement resulting from the third blast test at Site 1.

Plots of average settlement versus radial distance from the center of the site are shown in Figure 4.15 and Figure 4.16 for the first and third blast test, respectively. In both cases, settlement was greatest at the center and decreased with increasing distance from the center of the test site.

The first blast caused little to no settlement beyond a distance of 9 m from the center. Due to time constraints during testing, settlement was not measured beyond a distance of 9 m from the center for the third blast test. However, the trend of the settlement curve in Figure 4.16 indicates that little settlement occurred beyond a distance of approximately 12 m from the center of the test site. The contour maps and settlement

profile figures clearly show that the size of the settlement basin is directly related to the size of the explosive charges used.

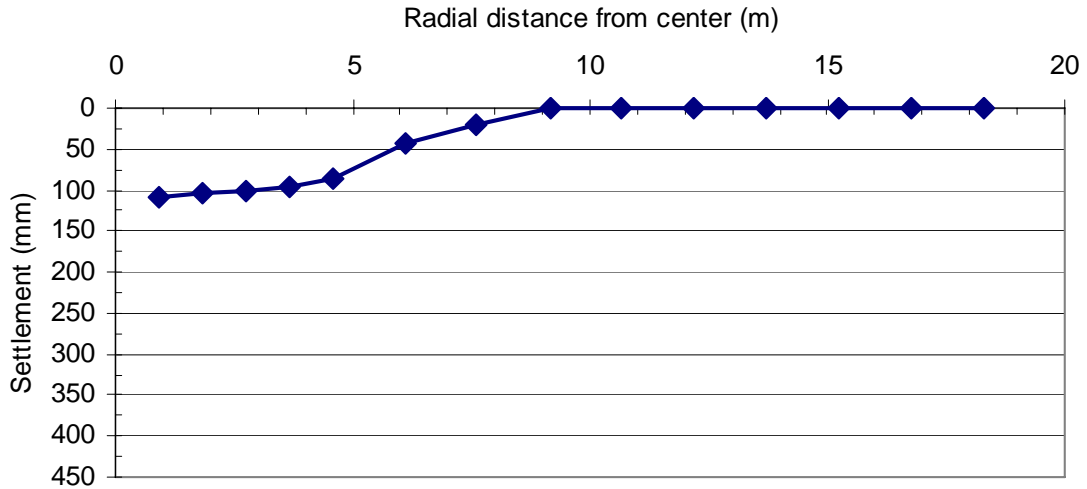


Figure 4.15 Average settlement with increasing distance from the center of Site 1 caused by the first test blast.

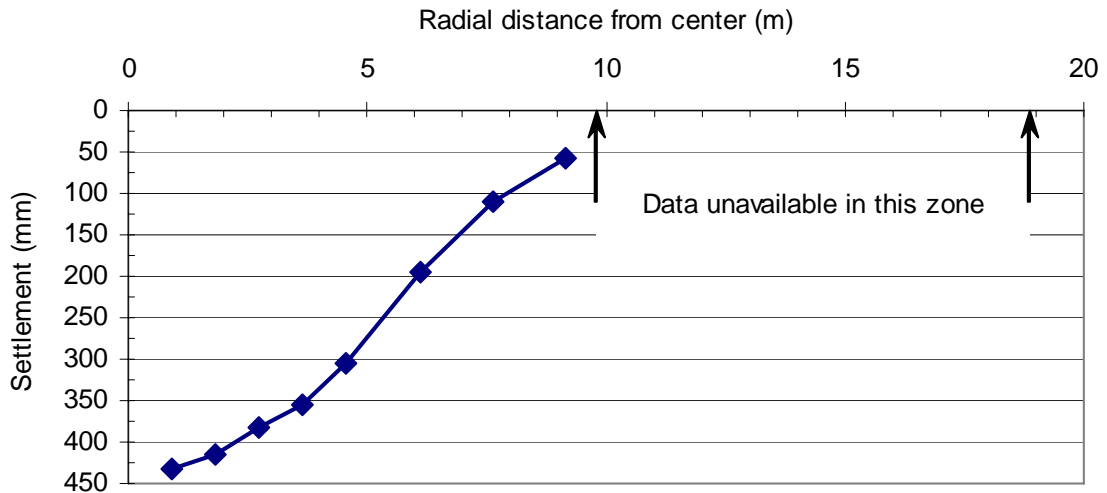


Figure 4.16 Variation of average ground surface settlement with increasing distance from center of Site 1 caused by the third test blast.

A discrepancy was observed between total settlement measurements made by the string potentiometers and the level survey. In general, the string potentiometers measured about 43 mm less settlement than the level survey for the first blast test (see Figure 4.17) and 90 mm less settlement for the third blast test (see Figure 4.18). For Figures 4.17 and 4.18, negative distances along the abscissa indicate distances to the left of center and positive distances are to the right of center as shown in Figure 4.1.

The level survey was made as soon as possible after the blasting to ensure that both measurement methods produced similar measurements. The possibility that the missing settlement occurred between the end of real-time recording and the level survey is refuted by the flat-line trend shown by the string potentiometer data that occurs after about 10 minutes.

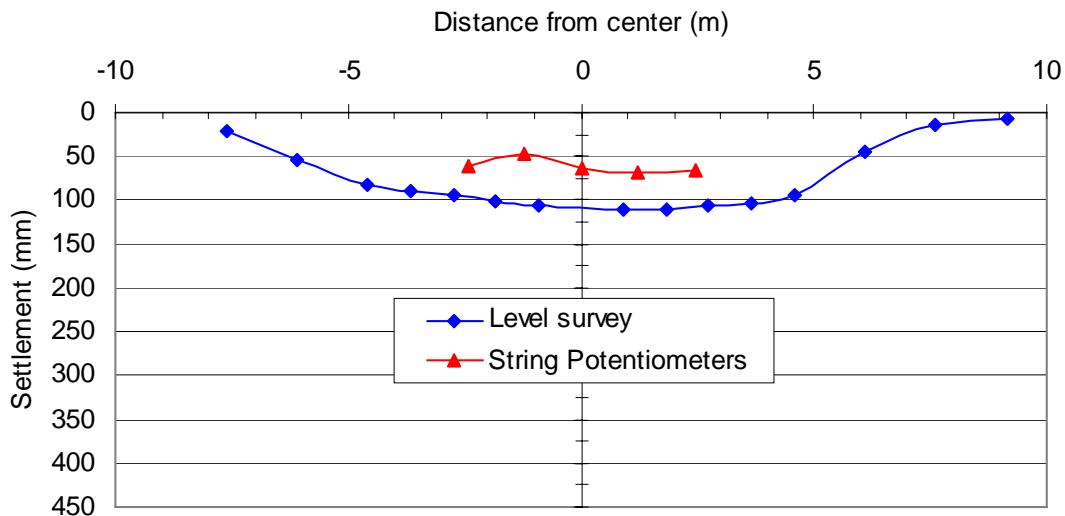


Figure 4.17 Comparison of maximum ground surface settlement measured by the string potentiometers and the level survey for the first blast test at Site 1.

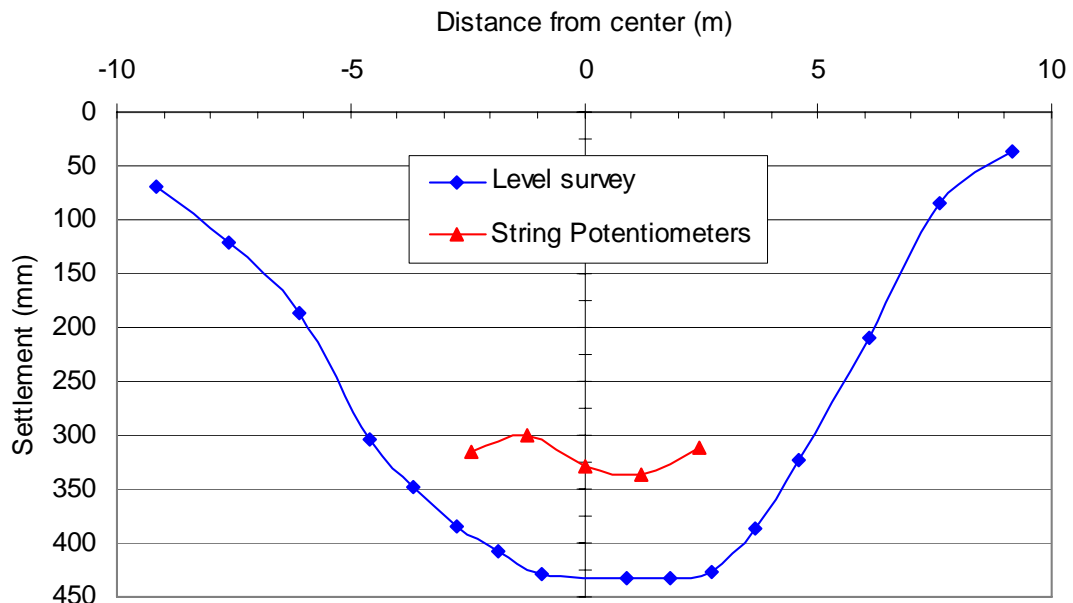


Figure 4.18 Comparison of maximum ground surface settlement measured by the string potentiometers and the level survey for the third blast test at Site 1.

The smaller total settlement measured by the string potentiometers was likely due to a reduction in tension in the cable resulting from minor movement in the support anchors. A relaxation of the cable tension results in greater sag of the cable and less measured settlement. A method to correct settlement measurements for cable sag will be presented in Section 4.4.2 as it relates to the blast tests performed at Sites 2 and 3.

4.5.2.3 *Depth-related ground settlement*

The settlement profiles obtained from the Sondex probe for both the first and third test blasts are plotted in Figure 4.19. The settlement increases relatively linearly within the target zone where excess pore pressures were developed by the blasting, but remains nearly constant in the upper portion of the profile.

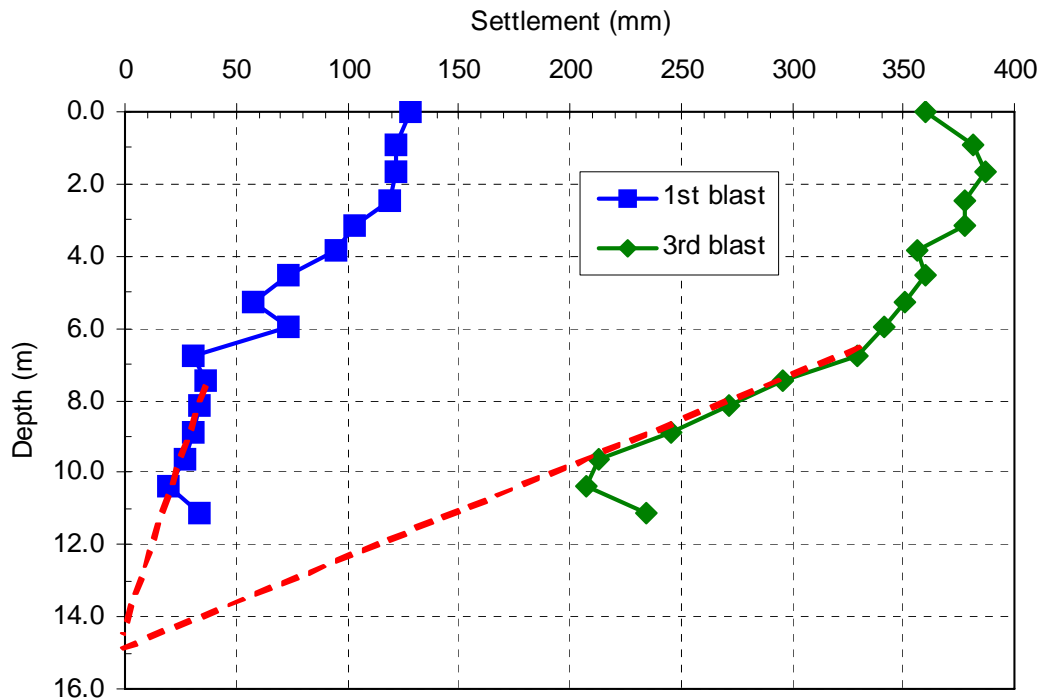


Figure 4.19 Comparison of settlement as a function of depth as measured with the Sondex tube for the first and third blast tests at Site 1.

For the first blast test, the settlement was nearly constant for the upper 2 m; for the third blast test the settlement was nearly constant in the upper 4 meters. This settlement profile indicates that the top layer settled as essentially a single unit due to settlement of the underlying sand layer. The top layer (0 to 5.5 m) consists of an unsaturated sand layer and a clayey silt layer, both of which would be relatively insensitive to blast-induced pore pressure generation. Therefore, the settlement profile seems to match the behavior expected for the soil profile.

The maximum ground surface settlement obtained from the Sondex probe was about 130 mm, for the first blast. Compared to the 110 mm of settlement measured by the level survey, the Sondex measured about 20% more settlement. For the third blast

test, the maximum ground surface settlement measured by the Sondex tube was 360 millimeters. The ground surface settlement at the location of the Sondex tube as measured by the level survey was approximately 375 mm, which is only about 4 percent higher.

Because the Sondex tube extended only to 11 m, it did not fully penetrate the target zone and the bottom of the tube experienced significant settlement. The depth at which settlement would be expected to end was approximated by extending the lower portion of the settlement profiles linearly to zero settlement (refer to the dashed lines in Figure 4.19). As can be seen in Figure 4.19, the extensions of both profiles indicate that settlement should end at approximately 14 m depth.

Inasmuch as settlement would be expected to end at or near the bottom boundary of the liquefied zone, the interpolated lines in Figure 4.19 indicate that the lower boundary of liquefaction should occur at about 14 m depth for this blast sequence. The Sondex tubes for Sites 2 and 3 were installed to depths of 14.5 m in order to anchor the bottom of the Sondex tubes below the lower boundary of liquefaction and capture the entire settlement profile.

In addition to the settlement data, the pore pressure data also indicates that liquefaction was produced below the target zone (see Figure 4.9). Therefore, the third deck of explosives was eliminated for subsequent tests.

5 Pile Foundation Design, Instrumentation, and Installation

As indicated in Section 1.2, the second principle objective of this study was to quantify the extent to which downdrag develops on a pile due to liquefaction. Of particular interest was the development of downdrag during and immediately following a liquefaction event due to settlement and reconsolidation of the liquefied layer.

In a pile foundation, the external load, i.e., the load from the overlying structure, is supported by the shaft and toe resistance of the pile. Shaft resistance is the shear force developed between the side of the pile and the surrounding soil, commonly called skin friction. Toe resistance is the bearing force developed at the base of the pile. This force is, of course, much larger for closed-toe piles than for open-ended piles.

Under normal conditions, the axial load applied to a pile causes the pile to move downward relative to the surrounding soil. Skin friction that resists downward movement of the pile is termed positive skin friction (“positive” because it acts upward, or in the positive direction; see Figure 5.1). Skin friction becomes fully mobilized after a relative displacement of 2 to 5 mm (Bozozuk, 1981).

If the ground around a pile settles relative to the pile for some reason, negative skin friction can develop. Settlement relative to the pile can occur due to placement of additional fill load, long term consolidation of a clay layer, a drop in groundwater

elevation, or liquefaction-induced settlement. As the soil around the pile settles, it tends to “hang” on the pile, transferring a downwardly oriented load to the pile, termed “downdrag”. Negative skin friction develops in the upper part of the pile and the resulting downdrag plus the applied load is counteracted by pile resistance (positive skin friction and end-bearing) in the lower part of the pile. The location at which negative skin friction turns to positive skin friction is called the neutral plane.

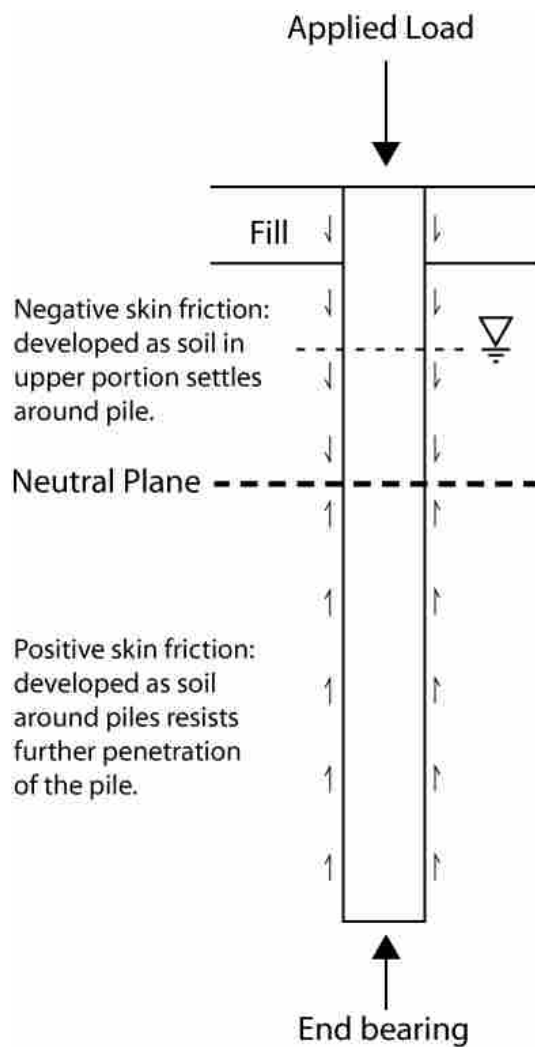


Figure 5.1 Diagram of the development of skin friction.

Because skin friction is proportional to effective stress (Johannessen and Bjerrum, 1965), it can be reasoned that during a liquefaction event, the skin friction in the liquefied layer should drop to zero causing a redistribution of forces in the pile and surrounding soil. As the excess pore pressure dissipates, the liquefied layer reconsolidates and settles around the pile, causing downdrag to develop within the consolidating layer. Furthermore, the soil overlying the liquefied layer would also settle, which should cause a further increase in the downdrag on the pile.

The loss of positive skin friction due to liquefaction and subsequent development of downdrag due to the settling soil will cause the pile to settle. The amount the pile settles is dependent upon the relative displacement needed to mobilize enough pile resistance (positive skin friction and end-bearing) to restore force equilibrium, causing the location of the neutral plane to change. As pore pressures return to static levels, the neutral plane continually readjusts, maintaining force equilibrium.

5.1 Pile Foundation Design and Installation

Figure 5.2 is a plan view of the pile foundations installed at Sites 2 and 3; Figure 5.3 is a profile view. The foundations consisted of an instrumented test pile in the center of the test site flanked by four reaction piles which supported the reaction frame. The pipe piles conformed to ASTM 252 Grade 3 specifications. The outer diameter was 324 mm (12.75 in) and the wall thickness was 9.5 mm (0.375 in.). A 37.5-mm-thick plate was welded to the bottom of the test piles to close the end prior to driving. Using the 0.2% offset method, the yield strength of the piles was specified to exceed 400 MPa (57,000 psi). The reaction piles were spaced at about 3.65 m on either side of the test

pile which is a spacing greater than 11 pile diameters. This spacing exceeds requirements from ASTM and FHWA standards. The two reaction piles were spaced between 1.2 and 1.8 m apart.

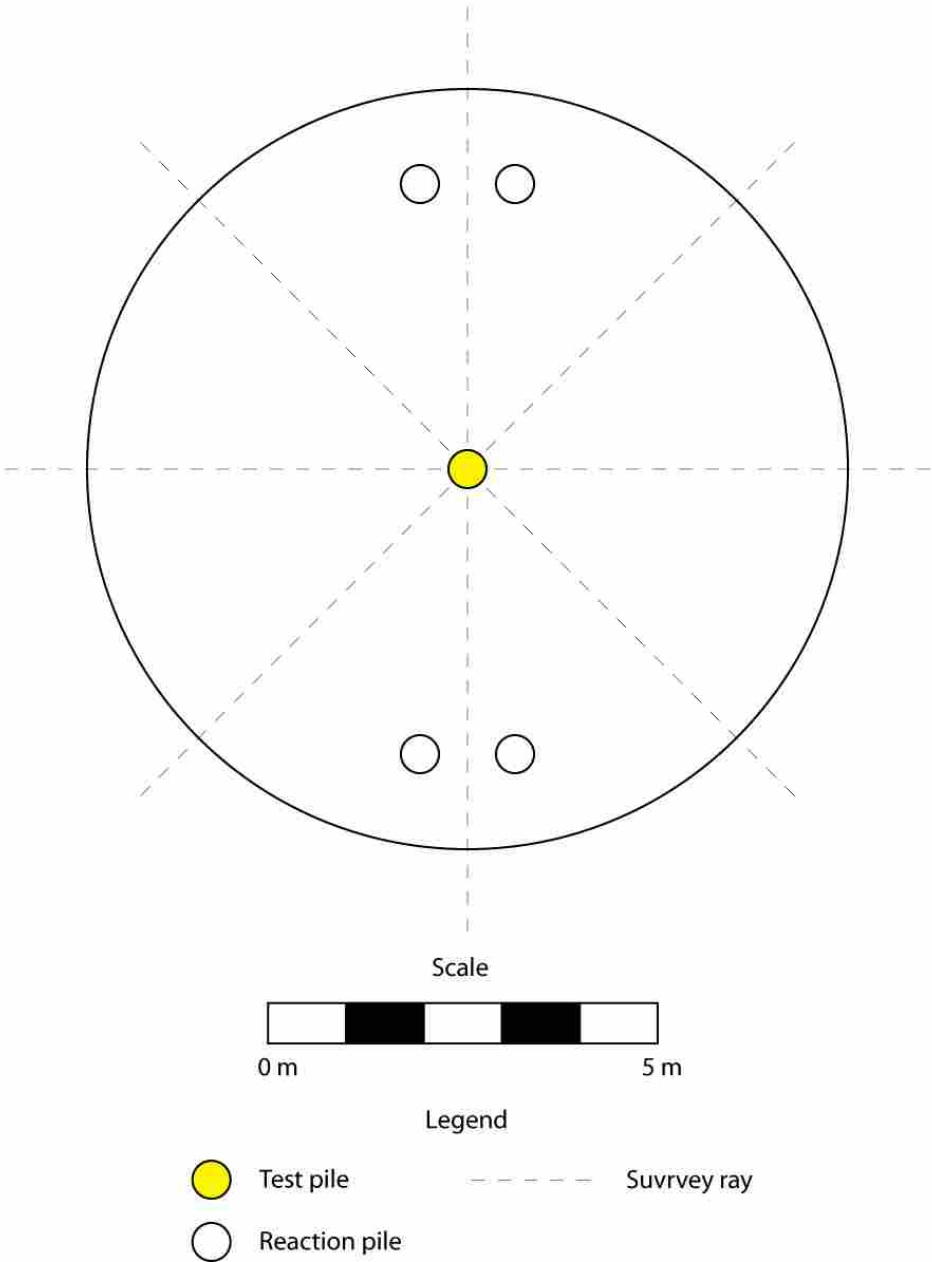


Figure 5.2 Plan view of pile foundations installed at both Sites 2 and 3.

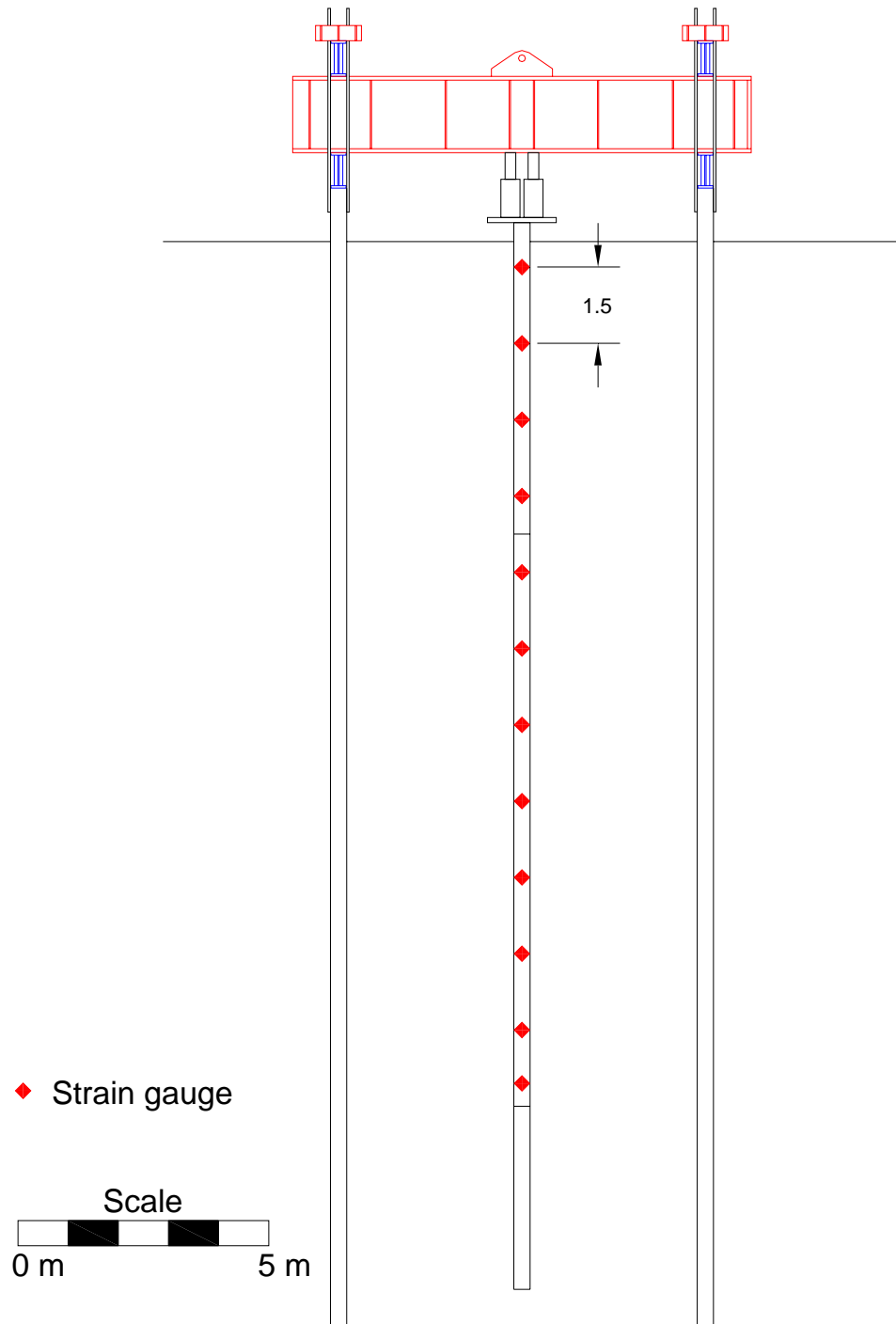


Figure 5.3 Profile view of pile foundations installed at both Sites 2 and 3.

5.1.1 Pile design

The axial pile capacity as a function of depth was computed using two CPT based methods. The first method was developed by the French Central Laboratory for Bridges and Highways (Laboratoire Central des Ponts et Chaussées) and is known as the LCPC method. This approach was first developed by Bustamante and Ganeselli (1982) and was updated by Tucker and Briaud (1986). The second method was developed by Eslami and Fellenius (1997).

5.1.1.1 LCPC method

The LCPC method computes the unit side resistance using equations based on the cone tip resistance, the pile type and the method of installation. For a driven steel pipe pile, the unit side resistance of sand and clay is given as a function of the cone tip resistance using the curves shown in Figure 5.4.

Hyperbolic equations were developed for both of these curves. For sand, the unit side resistance (f_s) in kPa is given as a function of the cone tip resistance values (q_c), in kPa, using the equation,

$$f_s = \frac{q_c}{46.34 + 0.03187q_c} \quad (4)$$

while the unit side resistance in clay is provided by the following equation

$$f_s = \frac{q_c}{10.12 + 0.02466q_c} \quad (5)$$

The unit end-bearing resistance (q_p) is given by the equation

$$q_p = 0.375(q_c)_{avg} \quad (6)$$

where $(q_c)_{avg}$ is the average cone tip resistance within a zone eight pile diameters above the pile tip and four pile diameters below the tip.

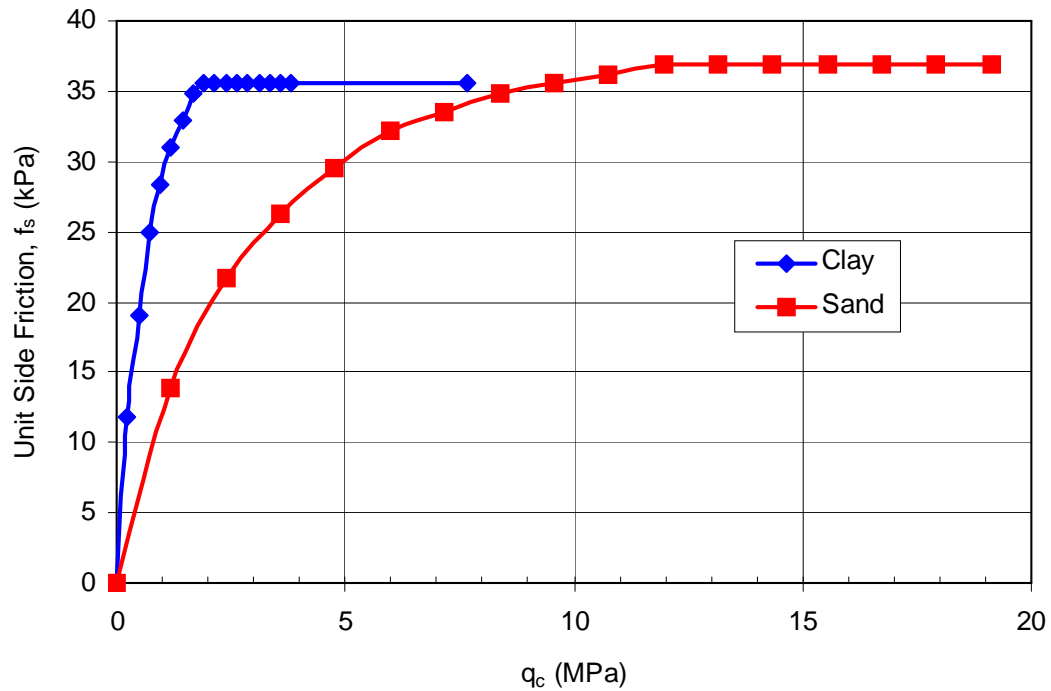


Figure 5.4 Relationship between unit side friction and cone tip resistance for driven steel pipe pile in sand and clay based on the LCPC method.

5.1.1.2 Eslami and Fellenius method

The Eslami and Fellenius method computes the unit side friction using the equation

$$f_s = C_s q_c \quad (7)$$

where C_s is a factor that depends on the soil type and is determined based on the cone tip resistance and sleeve friction using the chart shown in Figure 5.5. The value of C_s is determined based on the soil type as listed in Table 5.4.

The unit end-bearing is given by the equation

$$q_p = (q_{c1}q_{c2}q_{c3}\dots q_{cn})^{1/n} \quad (8)$$

where q_{ci} is the value each cone tip resistance within the zone from eight pile diameters above the pile tip to four pile diameters below the tip and n is the number of cone resistance values in that zone. This geometric mean value helps minimize the influence of large peaks and troughs in the cone resistance near the pile tip.

5.1.1.3 Determination of pile length

Plots of the side resistance and total resistance (side and end-bearing) versus depth for the test piles at Sites 2 and 3 predicted by the LCPC and the Eslami and Fellenius methods are provided in Figure 5.6 and Figure 5.7, respectively. In both figures, the predicted pile resistance is very similar for Sites 2 and 3; however, the resistance predicted by the Eslami and Fellenius method is significantly higher than that predicted by the LCPC method. The average unit skin friction and end-bearing values predicted by these two methods are summarized in Table 5.5. The layers listed in Table 5.5 correspond to the layers shown in the generalized soil profile (see Figure 3.7).

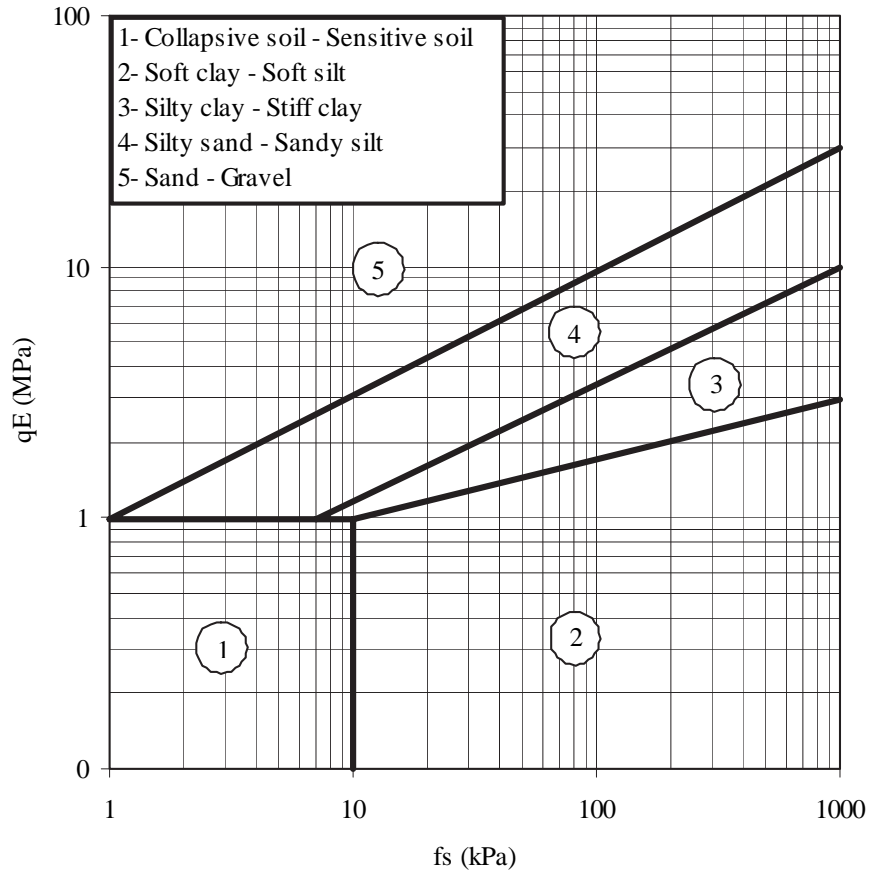


Figure 5.5 Soil profiling chart developed by Eslami and Fellenius (1997) used in their method to determine soil type.

Although the predicted side resistance values are reasonably similar, the end-bearing resistance predicted by the Eslami and Fellenius approach is nearly three times higher than that predicted by the LCPC method. Therefore, the large difference between the predicted ultimate loads is largely due to differences in interpreting end-bearing resistance.

Table 5.4. Values of C_s used in the Eslami and Fellenius method to compute unit side friction.

Soil Type	Soil Description	Range of C_s	Avg. C_s
1	Soft sensitive soils	0.0737-0.0864	0.080
2	Clay	0.0462-0.0556	0.050
3	Stiff clay and mixture of clay and silt	0.0206-0.0280	0.025
4	Mixture of silt and sand	0.0087-0.0134	0.010
5	Sand	0.0034-0.0060	0.004

Table 5.5. Summary of side resistance and end-bearing resistance predicted by LCPC and Eslami and Fellenius methods for layers in the soil profile at test sites.

Soil Layer	Resistance Type	LCPC Unit Resistance (kPa)	Eslami & Fellenius Unit Resistance (kPa)
Fine Sand (0 - 2.7 m)	Side Friction	24.9	42.0
Silty Clay (2.7 - 5.5 m)	Side Friction	30.9	33.5
Sand to Silty Sand (5.5 - 13.6 m)	Side Friction	24.6	31.1
Sand to Silty Sand (13.6 - 22 m)	Side Friction	27.2	44.1
Total Side Friction (kN)		591	844
Sand to Silty Sand (22 m)	End-Bearing (kN)	340	860
Total Resistance (kN)		931	1704

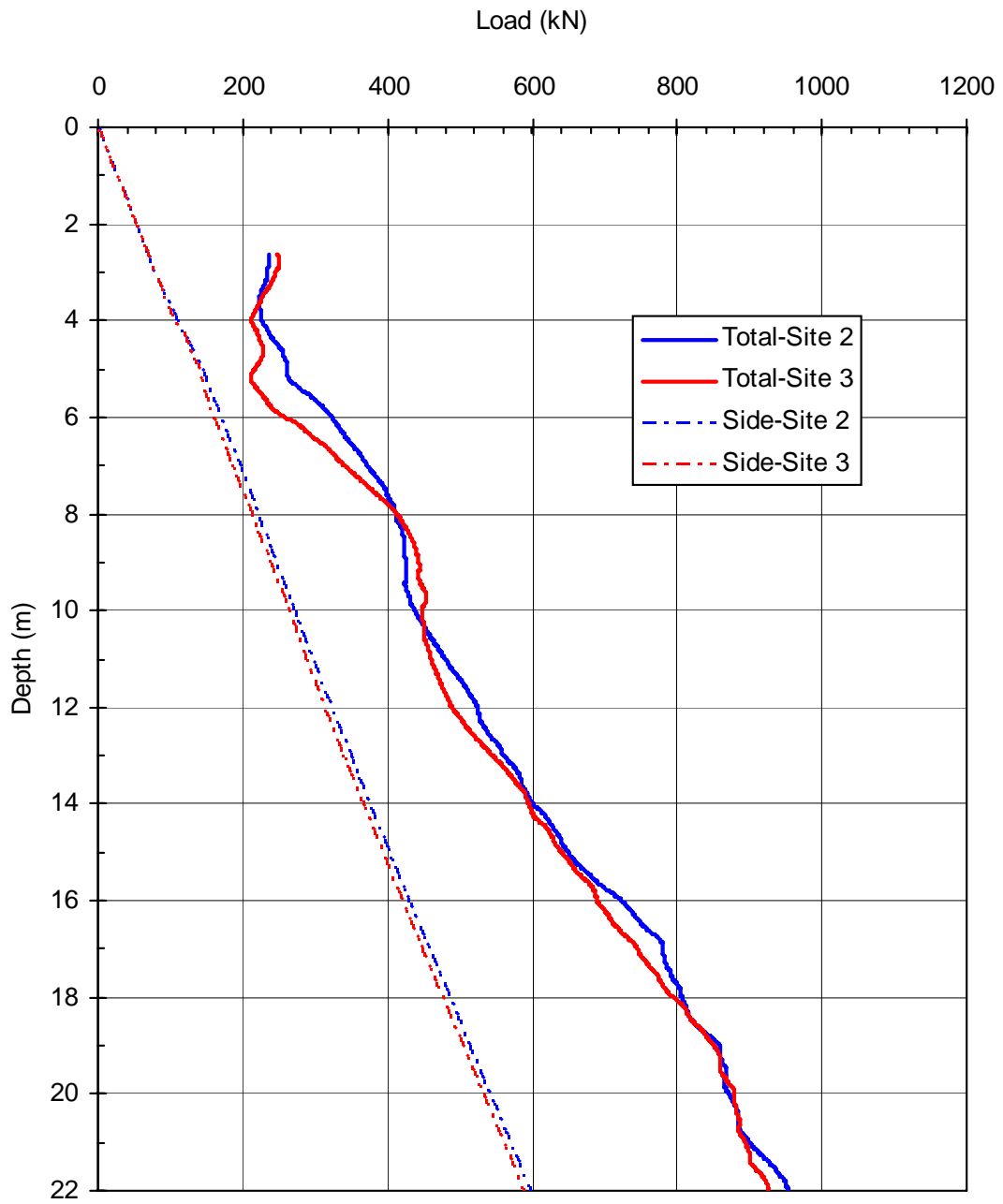


Figure 5.6 Total and side resistance for the test piles at Sites 2 and 3 predicted by the LCPC method.

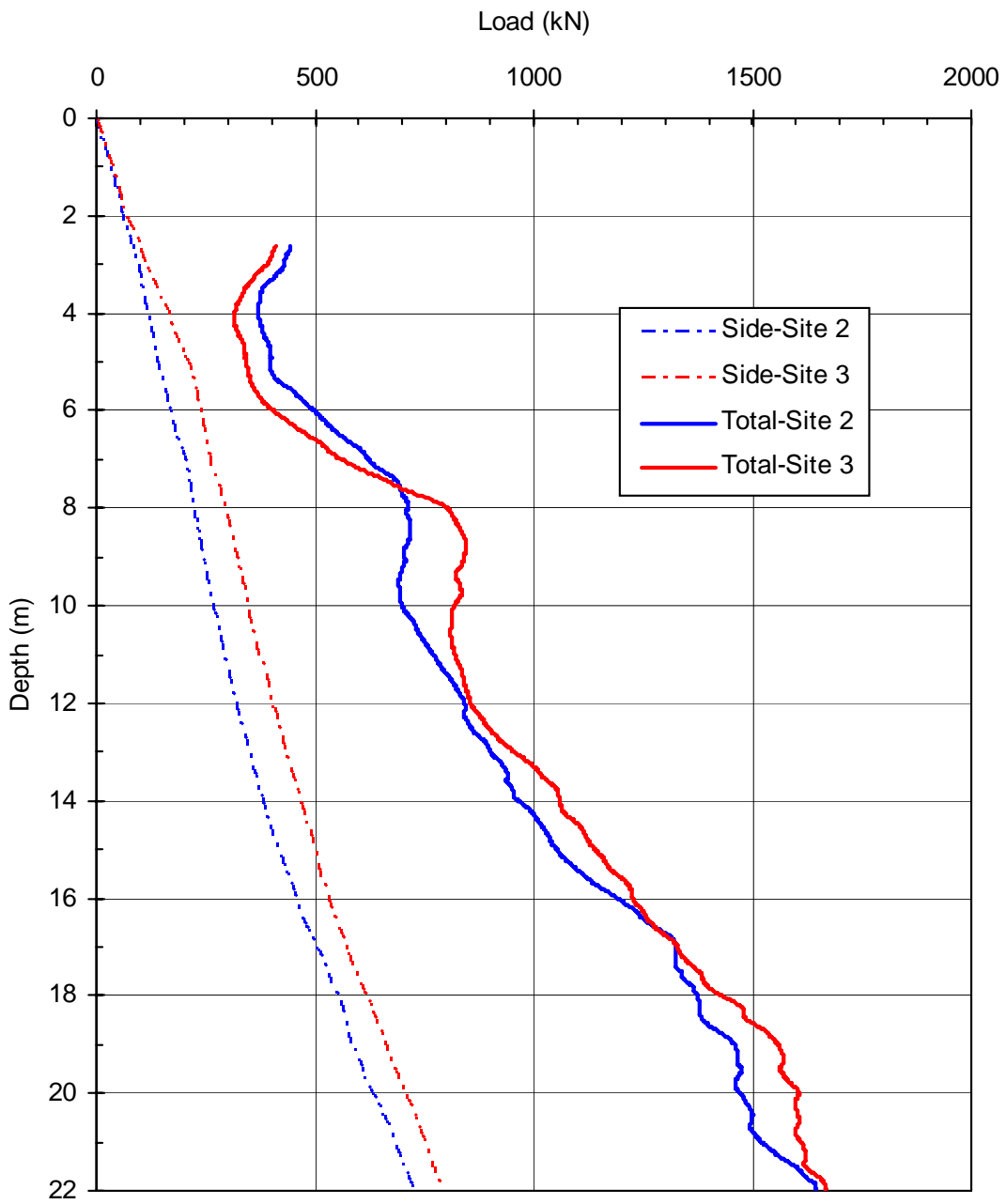


Figure 5.7 Side and total resistance for the test piles at Sites 2 and 3 predicted by the Eslami and Fellenius method.

Preliminary design called for 18.3-m-long closed-end test piles. This length was divided into two instrumented sections with lengths of 6.9 m and 11.4 m to facilitate transport to the site. Subsequent analyses indicated that if the skin friction was as high as predicted by the Eslami and Fellenius method and the end-bearing resistance was as low as predicted by the LCPC method, then the piles could experience a plunging failure if the potential downdrag load was applied to the pile. To reduce the potential for this occurrence, the test piles were lengthened by 3.7 meters. Because the instrumentation of the top two sections had already been completed, it was impossible to instrument the bottom section without much inconvenience and increased cost.

Using the same procedure as was used for the test piles, it was initially determined that the reaction piles needed to be 21.3 meters long. Subsequent estimations determined that the reaction piles should be 22.9 meters long. Fortunately the reaction piles had not yet been cut, allowing the increase in length to be accommodated without much inconvenience. The reaction piles were made from two sections, one 12.8 meters long and the other 10.1 meters long. Since the reaction piles were designed to resist an upwards vertical load and end-bearing was not needed, they were driven open-ended.

5.1.2 Instrumented test pile construction

Prior to pile driving, the test piles were instrumented with strain gauges at approximately 1.5 m intervals along the length of the piles. At each depth interval, four strain gauges were applied to the pile at 90 degree spacings around the circumference of the test pile. The gauges consisted of water-proof electrical resistance type strain gauges manufactured by Texas Measurements, Inc. (model WFLA-6-12). In preparation for

gauge attachment, the surface of the pile was ground, sanded, and polished smooth where each gauge was to be attached. Once the surface preparation was complete, the gauges were attached directly to the pile using an epoxy-based glue. Once all the gauges on a side of the pile were attached, the leads were wrapped together with electrical tape and extended to the top of the pile. A length of angle iron was then placed over the gauges and welded to the pile at regular intervals to protect the gauges during driving. The interior gap between the pile and the angle iron was then filled with expanding polyurethane foam to seal the gauges from soil and water intrusion. The foam also helped shield the gauges from excess vibrations experienced during pile driving.

5.1.3 Pile driving

All piles were driven between June 7 and 10, 2005. After the piles had been delivered to the test site, the two instrumented sections of the test piles were welded together horizontally while still on the ground (see Figure 5.8). This allowed assembly to proceed more easily. Care was taken to ensure that no damage occurred to either the strain gauges or the electrical leads from rough handling, excessive heating from welding, etc.

Due to the limited height capacity of the pile driving rig, the lower 3.7 m section of the test piles could not be attached while all three sections were on the ground. Thus the 3.7 m “starter” section was first driven to within one meter of the ground surface at which point the upper two sections (now welded together) were stood up, positioned over the bottom section, and welded together. Because the starter section was driven to only about 2.7 m, the upper two sections were constantly tethered to the driving

rig during welding and until it had been completely driven. The test piles were driven to a final depth of approximately 20.9 meters.

The piles were driven with a 2500 kg drop hammer which was typically dropped from heights ranging from 1.5 to 2.5 m (see Figure 5.9). The number of hammer drops and the drop heights were recorded at 0.3 m intervals. Summaries of the field data is provided for both test pile foundations in Table A1 and Table A2.

In order to determine the true distribution of strain in a pile, residual strains from driving must be considered (see Fellenius, 2001). Accordingly, the strain in the test piles were measured using the strain gauges. At the end of driving, the residual strains were negligible.



Figure 5.8 Welding the instrumented segments of the test piles before driving.



Figure 5.9 Photograph of test pile being driven with 2500 kg drop hammer.

5.1.4 Reaction frame construction

Once all five piles in a given group were driven, the reaction frame was constructed. The tops of the reaction piles were cut off level with each other, approximately 1 m above the ground surface. The test pile was cut off approximately 0.5 m above the ground surface. The difference in height provided enough clearance to install the hydraulic jacks once the reaction frame had been set up. Figure 5.10 shows a photograph of the completed reaction frame. A short I-beam (the blue beam on the bottom) was placed on top of each pair of reaction piles. The main reaction beam (the red beam in the figure) was then placed on top of these cross-beams. The main beam was carefully positioned to rest on the centers of the bottom beams and pass directly above the center test pile. A second short beam (the top blue beam) was then placed on top of

the main beam at each end, directly above the bottom beam. Dywidag threadbars secured the assembly to the reaction piles. A large plate was placed on top of the test pile to provide a seat for the hydraulic jacks.



Figure 5.10 Photograph of the completed test frame. The wooden frame in the foreground was part of the test apparatus involved with the vane shear test.

6 Site 2–Untreated Area Pile Testing

As indicated in Section 1.2.1, Site 2 was maintained as the control site where no EQ drains were installed. As such, the results of the testing at Site 2 describe the development of downdrag forces without the contributions of the EQ drains.

6.1 Test Layout and Instrumentation

Plan and profile views of the layout of the test pile relative to the blast holes and instrumentation are shown in Figures 6.11 and 6.12, respectively.

The test pile was located at the center of the ring of blast holes having a radius of 4.9 meters. Two sets of eight blast holes were distributed equally around the circumference of the ring so that two independent series of eight blast sequences could be detonated. The second set of blast holes were offset from the first set of eight by 22.5 degrees as shown in Figure 6.11. In each blast hole, blast charges were located at depths of 6.4 and 8.5 m below the ground surface as shown in Figure 6.12. The first series of blast holes used 0.45 kg charges while the second set used 1.35 kg charges. The use of two sets of explosive charges is discussed more fully in Section 6.5.

Load was applied to the pile using two 1,300 kN hydraulic jacks placed between the test pile and the main reaction beam. A 100-mm-thick steel plate attached to the top

of the test pile, upon which the two jacks were placed, distributed the load evenly into the test pile. The load applied by each jack was measured by a load cell placed between the ram and the main beam. The vertical displacement of the pile was measured using two string potentiometers attached to a tensioned cable which was stretched across the site, similar to that described in Section 4.4.2. The cable was anchored at a distance of 19.7 m from the center of test area so that it would not be affected by settlement produced by the blast liquefaction. String potentiometers were also used to measure the deflection of the main reaction beam relative to the tensioned cable and the relative displacement between the main beam and the pile head.

Settlement of the ground surface was monitored using an array of survey points similar to that described in Section 4.4.1. The elevation of these survey markers was determined with a level survey prior to any construction at the site. Subsequent level surveys were used to evaluate settlement due to blast hole installation and pile installation, as well as blast testing. The settlement as a function of depth was monitored using a Sondex settlement tube located at 1.83 m from the center of the test area as shown in Figure 6.11.

The generation and dissipation of excess pore pressure during the blasting process was monitored using five piezometers identical to those used in the preliminary blast testing at Site 1 (see Section 4.3). Piezometers were installed to depths of 6.7, 8.4, 10.7, 12.8 and 16.8 m below the ground surface as shown in Figure 6.12. The piezometers were typically located about 0.75 m from the center of the test pile (see Figure 6.11).

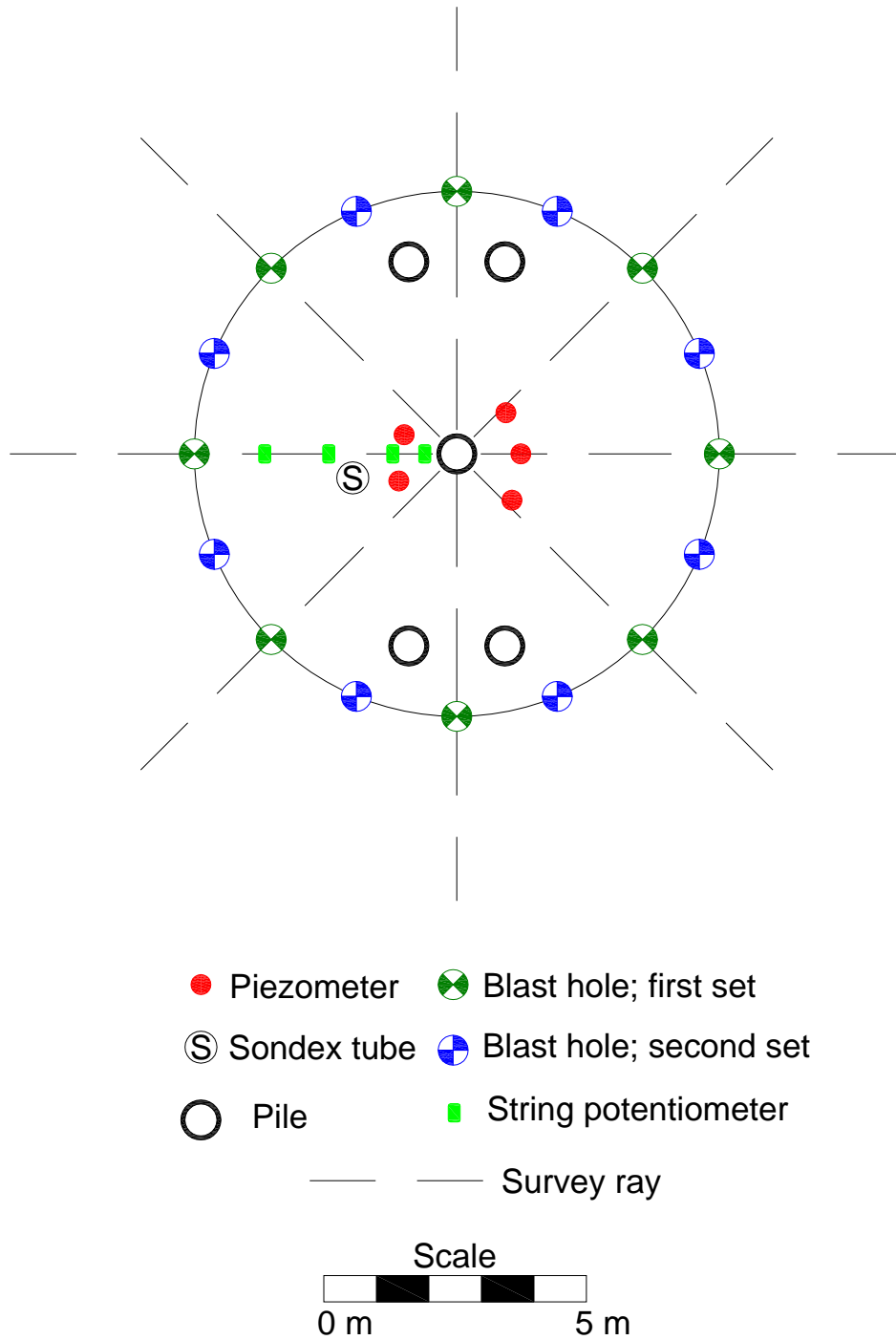


Figure 6.11 Plan view of pile foundation and instrument layout at Site 2.

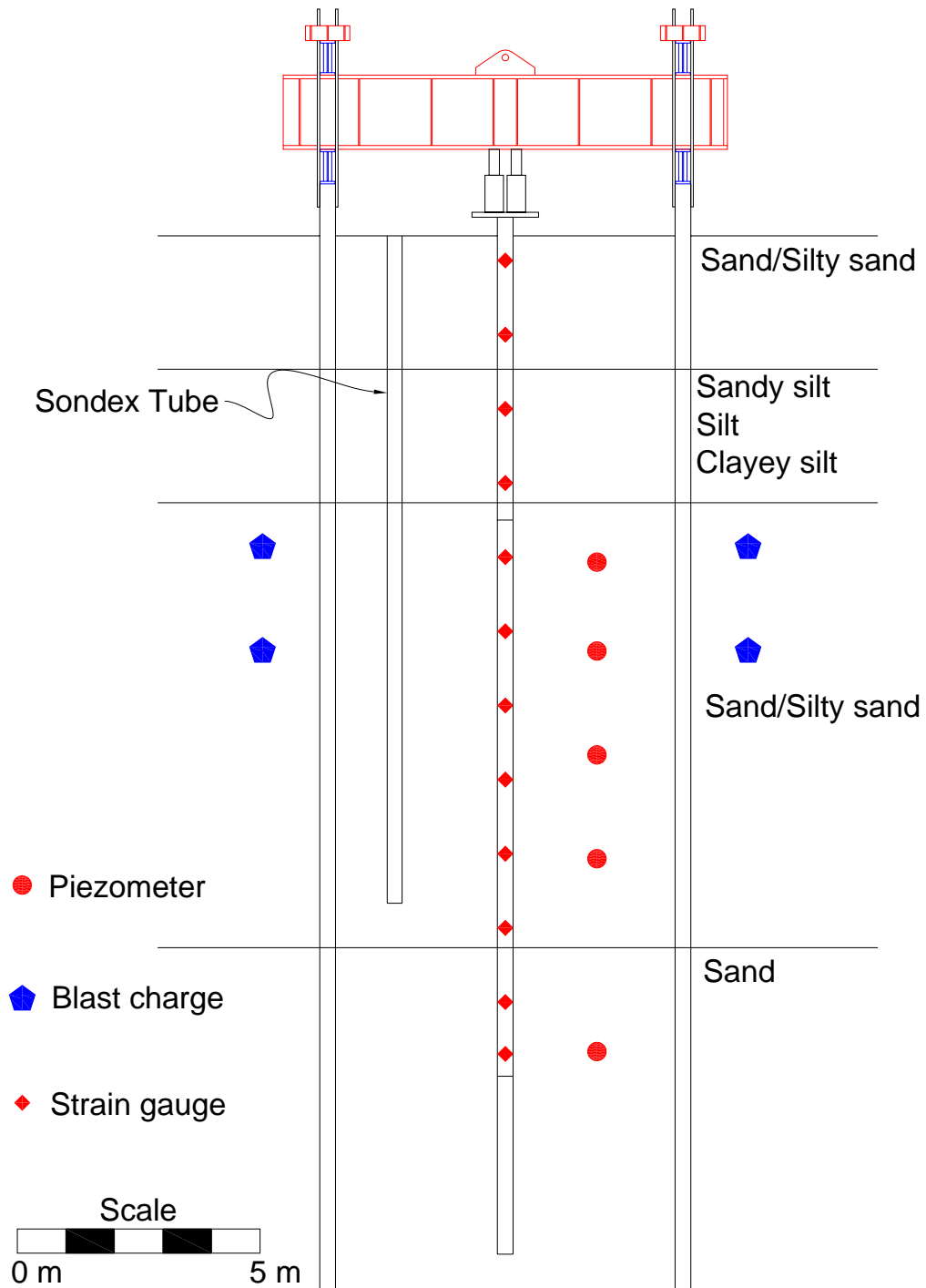


Figure 6.12 Profile view of pile foundation and instrumentation layout at Site 2.

6.1.1 Monitoring of real-time ground surface settlement

In addition to the conventional level surveys, surface settlement was also monitored as a function of time after blasting using an array of vertical string potentiometers attached to the tensioned cable running above the ground surface at the site. The string potentiometers were located at distances of 0.61, 1.2, 2.4 and 3.7 m from the center of the test area (see Figure 6.11). Although the tensioned cable to which these string potentiometers were attached was anchored at a large distance away from the test site in order to prevent the blast testing from causing it to sag, the ground movements caused by blasting introduced a significant amount of sag in the cable. Settlement data from several different sources allowed the amount of sag in the cable to be calculated as a function of time, permitting the settlement of the ground surface to be corrected as described below.

During the pre-blast load testing the deflection of the test pile head was measured using a string potentiometer attached to a stable reference frame independent from the reaction frame. The relative deflection between the test pile head and the reaction frame was measured using another string potentiometer. Subtracting the first measurement from the second produced the deflection of the reaction frame relative to the stable reference frame. When the deflection for the reaction frame was compared to the total load applied by the hydraulic jacks, a relationship was developed to describe the amount of deflection in the reaction frame as a function of total applied load.

Using the relationship developed above, the deflection of the reaction frame could be calculated according to the load applied by the hydraulic jacks. Subtracting this

deflection from the total displacement measured between the reaction frame and the test pile head produced the actual deflection of the test pile head measured relative to a hypothetical stable reference frame. Since the displacement between the tensioned cable and the test pile head was known, the sag of the cable could then be determined. Once the sag of the cable was computed, the settlement of the ground surface measured by the four string potentiometers connected to the tensioned cable could be corrected.

As the cable lost tension, the center portion of the cable would sag more than the outer portions of the cable. Accordingly, each string potentiometer should be corrected individually according to their respective distance from the test pile. However, since the tensioned cable was anchored more than 17 m from the center and all the string potentiometers were within 3.7 m of the center, it was assumed that one correction would be sufficiently accurate for the purposes of this study.

To evaluate the correction procedure explained above, the calculated maximum settlement for the four string potentiometers was compared to the total settlement measured by the level survey. The maximum settlement measured by the four string potentiometers was within 5% of that measured by the level survey.

6.2 Blast Hole Installation and Influence on Surrounding Soil

The 16 blast holes were installed between May 9 and 11, 2005 using the same procedure used to install the blast holes for the pilot liquefaction test. Each blast hole was cased with a 100-mm-dia. EQ drain pipe enclosed in a filter fabric sock to keep the hole open until the time of blasting.

To evaluate potential changes in the sand density due to blast hole installation, the settlement was measured approximately one month after installation and an additional CPT sounding was performed at that same time. The maximum settlement was approximately 18 mm located at the center of the site where the test pile was eventually driven. The average settlement was less than 3 mm, which is within the error of the survey itself. This suggests that very little change in soil density was produced by the installation of the blast holes.

A CPT was performed June 6, 2005, approximately one month after installation of the blast holes, located within one meter of the original CPT sounding. Plots of the measured cone tip resistance, friction ratio, and pore pressure are provided in Figure 6.13 along with curves from the previous CPT sounding at the site along with the interpreted soil profile. A plot of the relative density versus depth was also developed using Equation 2 and is included in Figure 6.13. Although there are some minor variations, there is no indication that there was any consistent increase or decrease in tip resistance, friction ratio or relative density. The observed variations are likely due to natural variations in the soil.

6.3 Pile Installation and Influence on Surrounding Soil

The test pile and four reaction piles were driven at this test site (Site 2) between June 7 and 9, 2005. To evaluate potential changes in the sand density due to pile driving, the settlement was measured approximately one month after installation of the test piles (July 27, 2005) and an additional CPT sounding was performed one day previously (July 26, 2005).

The maximum settlement was approximately 43 mm at a point located between the two northern reaction piles. The majority of the settlement occurred within a circular area 12 m in diameter centered about the test pile at the center of the site. The average settlement within that area was 23 millimeters. Outside the circular area, average settlement was less than 6 millimeters. This change suggests that very little change in soil density was produced by the installation of the piles.

The cone sounding after blast hole installation was performed within a meter of the original CPT sounding. Plots of the measured cone tip resistance, friction ratio, and pore pressure are provided in Figure 6.14 along with average curves from the previous two CPT soundings at the site and the interpreted soil profile. A plot of the relative density versus depth was also developed using Equation 2 and is compared with the plot from the previous two soundings. Although all indications are that the soil settled slightly due to pile driving and excess pore pressures should have been dissipated, the cone tip resistance and relative density for this sounding actually show a minor decrease. It is unclear whether this decrease represents a real change in soil conditions or simply a variation in the CPT data that was used obtained from this series of tests. Nevertheless, the general profile and soil conditions are relatively consistent with previous tests at the site.

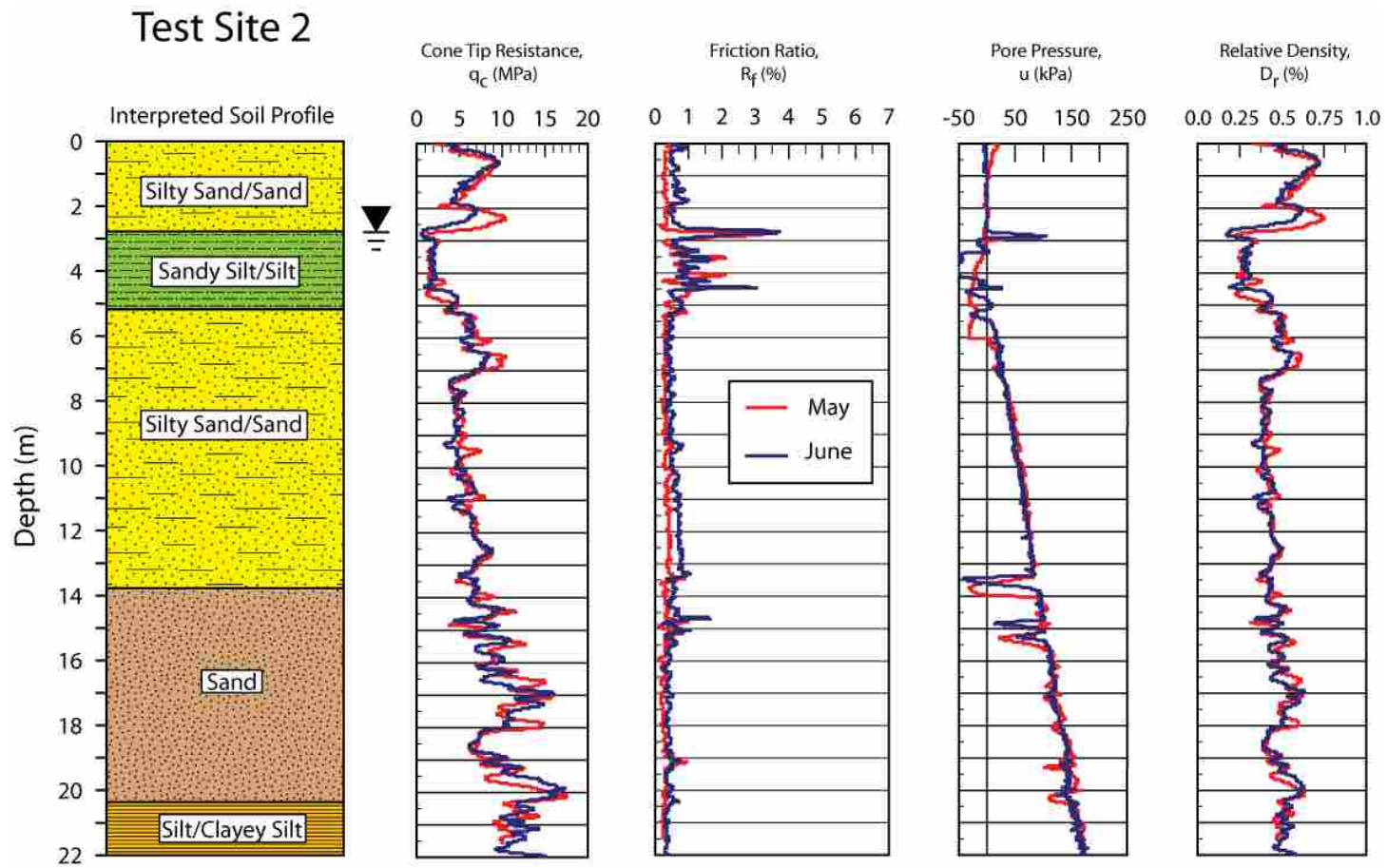


Figure 6.13 Comparison of CPT results from Site 2.

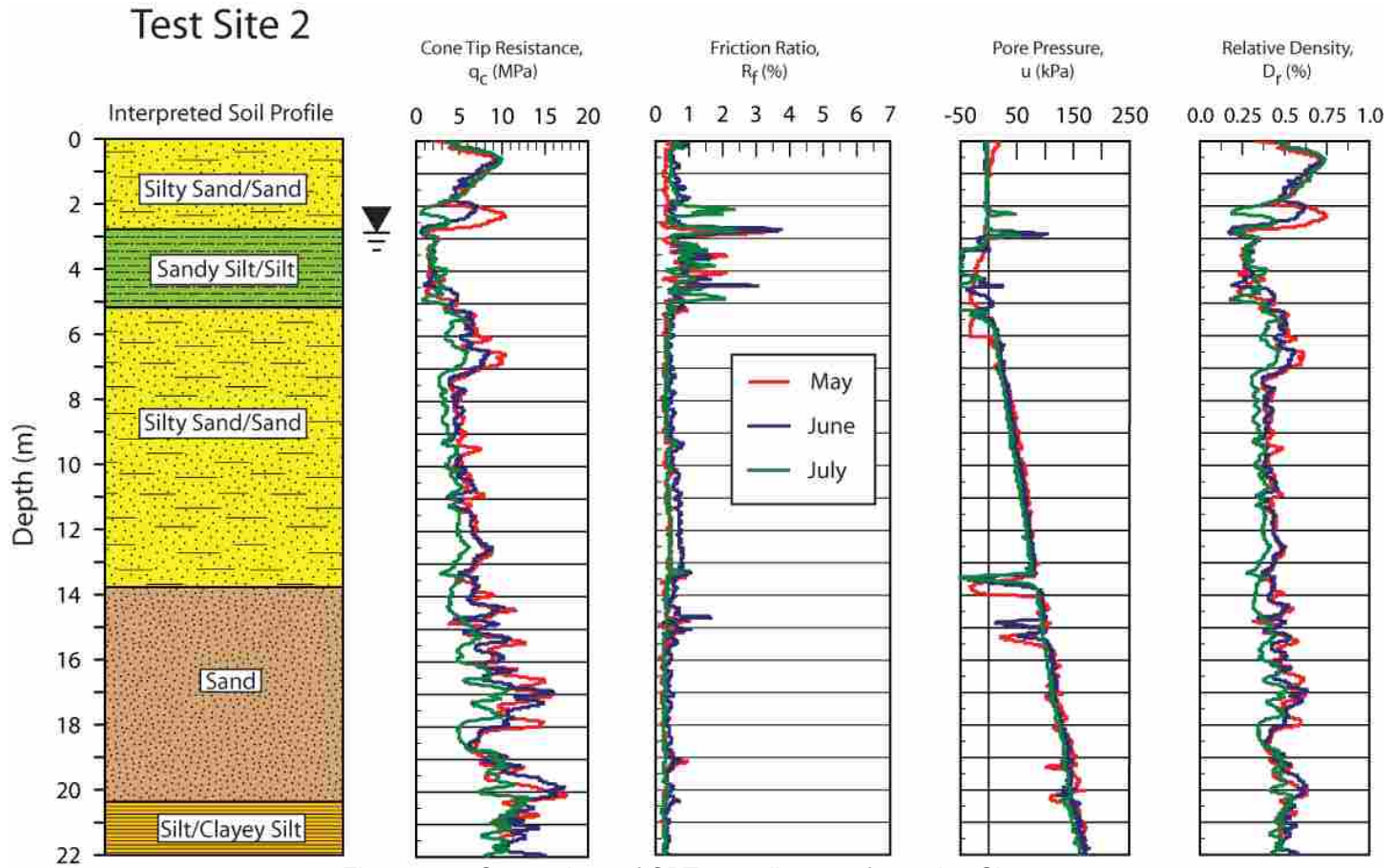


Figure 6.14 Comparison of CPT soundings performed at Site 2.

6.4 Pile Load Testing Prior to Blasting

Before blast testing, two static load tests were performed to characterize the load bearing properties of the test pile.

6.4.1 First static load test

An initial pile load test was carried out on June 10, 2005, about 24 hours after the test pile was driven. This pile test was performed to provide reliable data regarding unit side friction and end-bearing pressures for use in evaluating the thickness of the sand layer to be liquefied. As discussed in Section 5.1.1, the side friction and end-bearing values computed using the LCPC (Bustamante *et al*, 1982) and Eslami and Fellenius (1997) methods were significantly different. Therefore, field measurements were necessary to verify the actual pile resistance.

The test was performed using the quick maintained load procedure. Load was applied incrementally and held for three minutes at each increment. A plot of the measured pile head load versus pile head deflection for the first test is provided in Figure 6.15. The curve is relatively linear up to a load of about 550 kN after which the rate of settlement begins to increase. At a load of approximately 725 kN the pile began to settle very rapidly, or plunge, downward. At the end of the test, the load was released and a residual deflection of 67 mm was not recovered as shown in Figure 6.15.

At the end of the test the residual strains remaining in the pile were inspected and found to be negligible. The small strains remaining in the pile once the load was removed can reasonably be attributed to variations inherent in the strain gauges.

Furthermore, residual strains remaining at the end of all other load tests were analyzed and found to be negligible.

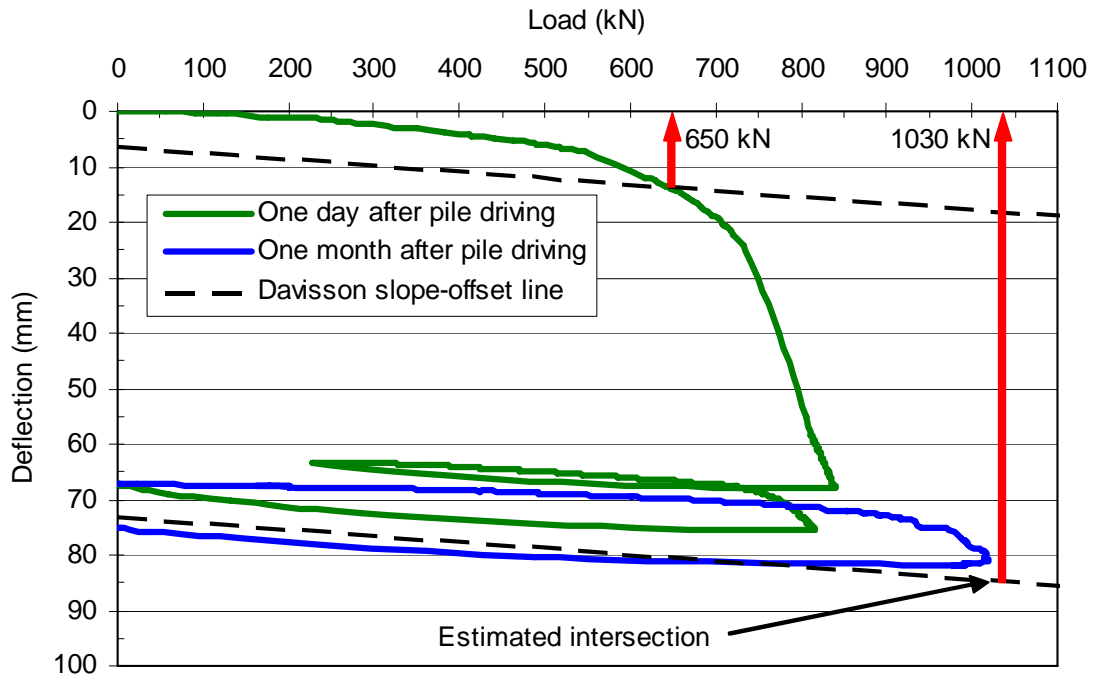


Figure 6.15 Comparison of the pile-head-load versus pile-head-deflection curves resulting from the two static load tests performed at Site 2.

The failure load was interpreted using the Davisson criteria. According to this method the failure load is located where the elastic compression line for the pile intersects the measured load-deflection curve from the load test. The slope of the elastic compression line is equal to AE/L , where A is the cross-sectional area of the pile, E is the modulus of elasticity of the pile and L is the pile length. The starting point for the elastic compression line is offset by a deflection equal to 3.81 mm plus the pile diameter in millimeters divided by 120, which is about 6.5 mm for the 324-mm-dia. test pile.

According to the Davisson criteria, the failure load was 650 kN as shown in Figure 6.15. This is about 60% lower than predicted by the Eslami and Fellenius method and about 32% lower than predicted by the LCPC method.

6.4.2 Second static load test

About one month after the initial pile load test, a second static load test was performed on the test pile prior to the blast liquefaction test. Because the original test was performed so shortly after the pile driving, the second test was performed to determine if setup of the soil might have led to a higher failure load. Again, the quick maintained load procedure was used.

The load versus pile head deflection curve for the second pile load test is plotted in Figure 6.15 along with the curve from the previous load test. Because the load-deflection curve did not intersect the Davisson line, the failure load was estimated to be 1030 kN, which is about 58% higher than the load from the first test. The failure load for the second test is slightly higher than predicted by the LCPC method but still about 30% below the failure load predicted by the Eslami and Fellenius method.

For the second test, the load is significantly greater than that which caused the pile to plunge during the original test. Part of this increased resistance is likely due to the fact that the pile had been previously loaded so that deflections were reduced during re-loading. However, this does not explain the fact that the second load-deflection curve extends beyond the curve from the initial test. This increased resistance may be attributed to setup/re-consolidation effects which developed after the first test. Setup effects are not often reported for piles in sand; however, most load tests are not

performed so soon after driving. Because of the higher permeability in sands, these setup effects likely occur quite rapidly and would not be detected unless the first test was performed very soon after driving as was the case in this study.

6.4.3 Effect of setup on pile capacity

To further investigate the role that setup effects played on the increase in ultimate capacity, plots of unit side resistance versus deflection (T-Z curves) were developed which describe the load transfer properties at the soil-pile interface. In order to do this, load versus depth curves were drawn for each load increment for both static tests.

The load in the pile at the level of each set of strain gauges was computed using the equation

$$P = AE\varepsilon \quad (9)$$

where A = cross sectional area of the test pile
E = modulus of elasticity of steel
 ε is the average measured strain at a given depth in the pile.

Load versus depth curves for the first and second static load tests are plotted in Figures 6.16 and 6.17, respectively. In Figures 6.16 and 6.17, the ground surface is equivalent to a depth of zero meters and the load in the pile at ground surface is equal to the applied load. The decrease in load with depth is a result of load transfer from the pile into the surrounding soil due to side friction, while the load at the base of the pile is provided by end-bearing resistance. In Figures 6.16 and 6.17, no data is shown below a depth of 17 m because strain gauges were not installed on the 3.7-m-long extension that

was added to the test pile after the rest of the test pile had been instrumented. Therefore, the response of the test pile below a depth of 17 m must be extrapolated from the data above.

As the applied load is increased, the side friction is progressively mobilized to greater depths and eventually end-bearing resistance begins to develop. Typically, side friction is fully mobilized at relatively small deflections levels on the order of 2 to 5 mm. In contrast, end-bearing typically requires deflections equal to 4 to 10% of the pile diameter. At the failure load defined by the Davisson criteria, about 55% of the axial resistance is provided by side resistance and 45% is provided by end-bearing.

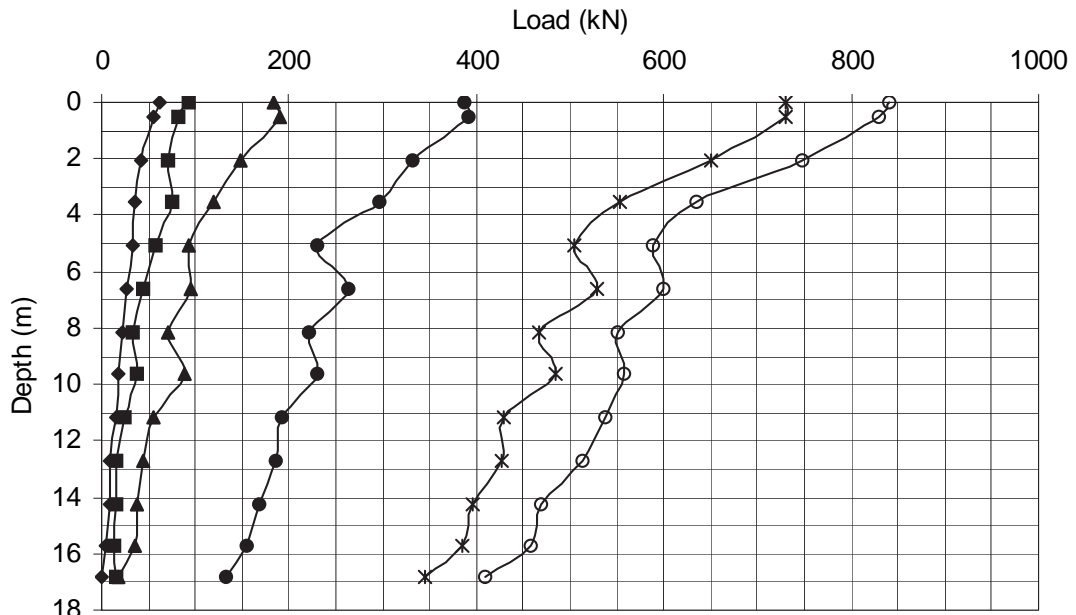


Figure 6.16 Load-depth curves from the static load test performed one day after pile driving at Site 2.

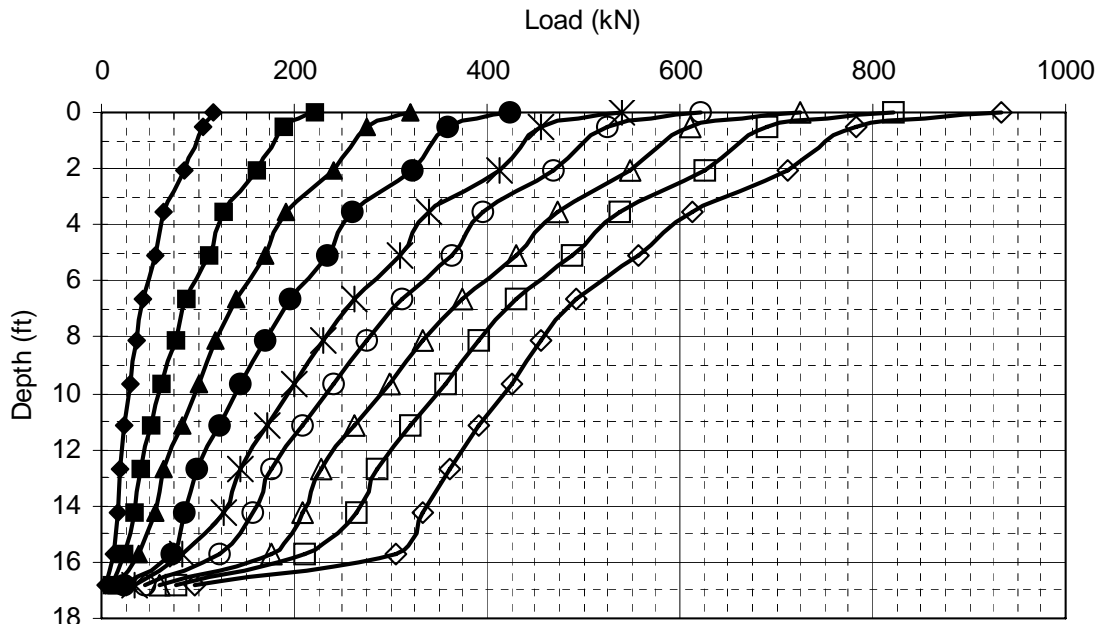


Figure 6.17 Load-depth curves from the static load test performed one month after pile driving at Site 2.

Before the T-Z curves could be drawn, it was necessary to simplify the load versus depth curves. The simplified curves for the first and second static load tests are shown in Figures 6.18 and 6.19, respectively.

The simplified curves were drawn more or less by eye, using piece-wise linear interpolation to capture the “average” response of the pile. The joints in the simplified curves were located at major breaks in slope of the measured load versus depth data.

A comparison of Figures 6.18 and 6.19 shows subtle yet significant differences. While the general shape of the simplified load-depth curves are similar, it will be noticed that the number of breaks-in-slope are different for the two tests. The first test (Figure 6.18) has four distinct sections whereas the second test (Figure 6.19) has five. These different sections delineate different layers defined by the load transfer properties

of the soil-pile interface. The difference in the number of layers, then, indicates that the load transfer properties of the soil profile changed sometime during the one-month interval between tests. The source of this difference will be revealed clearly by a comparison of the T-Z curves, as discussed subsequently.

Once the different layers were located, the unit side resistance was calculated for each layer by dividing the difference in load between the top and bottom of a given layer by the thickness of the layer and the perimeter of the pile. Summaries of the unit side resistance values for the first and second tests are provided in Tables A3 and A4, respectively.

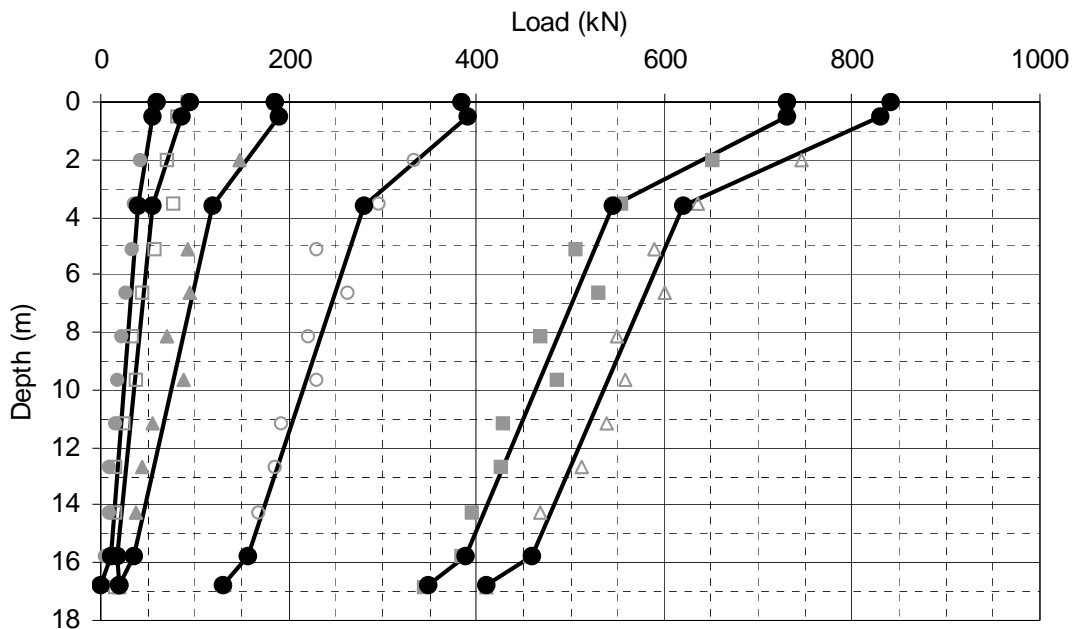


Figure 6.18 Simplified load-depth curves used to develop T-Z curves for the first static load test performed at Site 2.

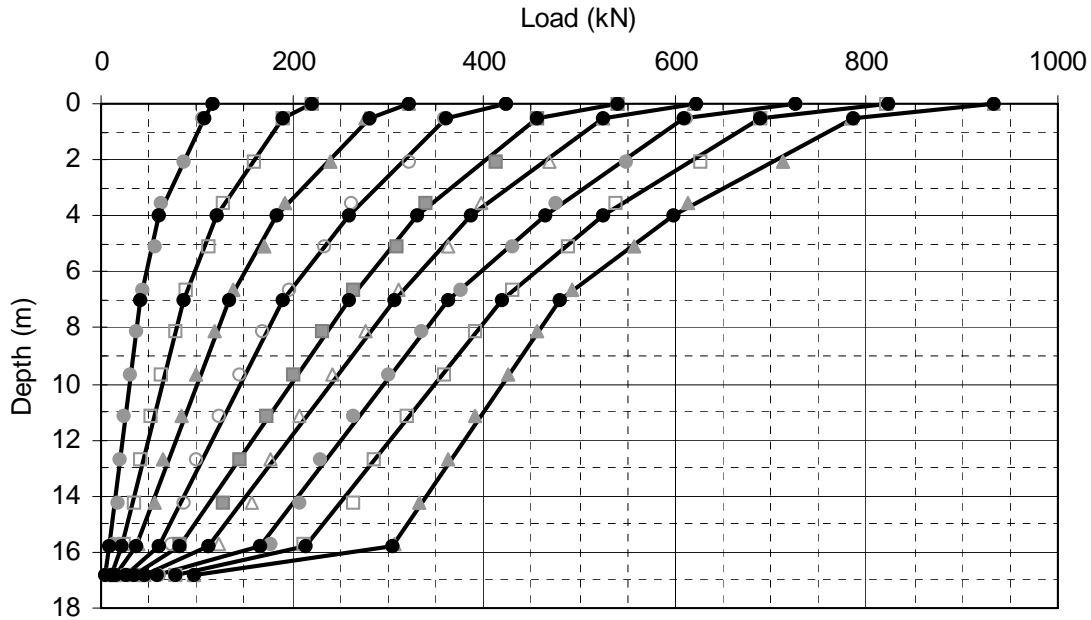


Figure 6.19 Simplified load-depth curves used to develop T-Z curves for the second static load test at Site 2.

In order to plot the T-Z curves it was necessary to determine the deflection in the pile at the top and bottom of each of the four layers. Inasmuch as the simplified load-depth curves utilized interpreted data points, it follows that the accompanying deflections also needed to be interpreted. Therefore the strains in the pile at the boundaries between the four layers were back-calculated from the interpreted loads. The pile deflection at the center of each layer was calculated by subtracting the cumulative strain above the center of the layer in question from the measured deflection of the pile head. Summaries of the calculated deflections for the first and second tests are provided in Tables A5 and A6, respectively. The deflections from the second load test do not include the residual plastic deformation from the first test. The final T-Z curves for the first and second static load tests are plotted in Figures 6.20 and 6.21, respectively.

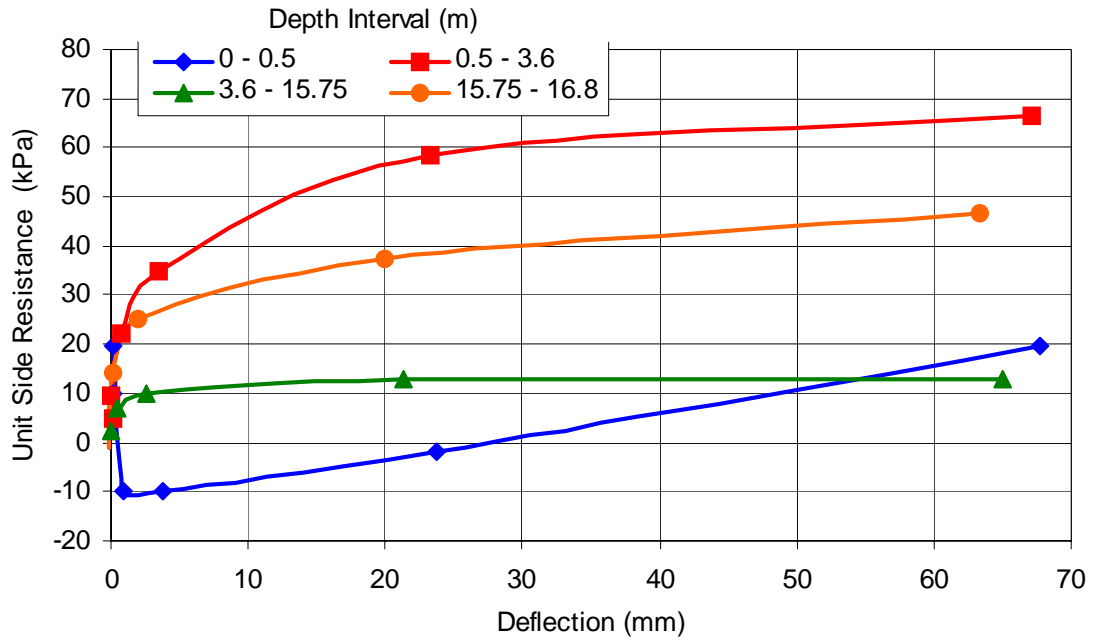


Figure 6.20 T-Z curves for the first static load test performed at Site 2.

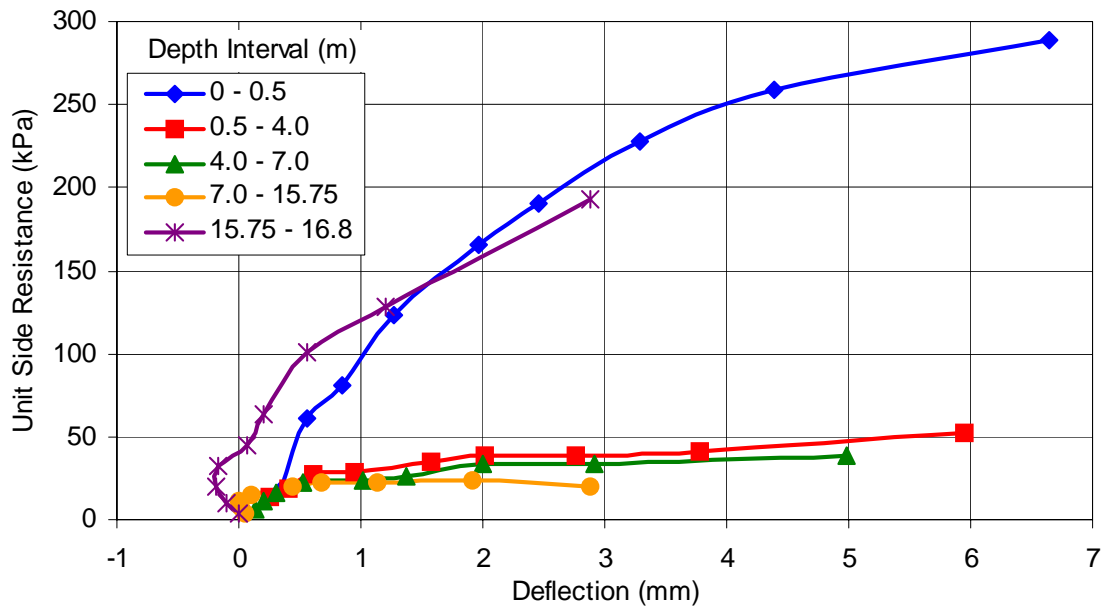


Figure 6.21 T-Z curves for the second static load test performed at Site 2.

In general, each T-Z curve shows that the unit skin friction increases as pile deflection increases. It will be noted that the top and bottom layers in the second test (Figure 6.21) do not match well with the other curves. Specifically, values of skin friction are much larger in the top and bottom depth intervals than for the other intervals.

These anomalies are most likely explained by inaccuracies in the strain gauge data recorded in these layers. For instance, the highest rates of strain gauge attrition were encountered in the top- and bottom-most tiers of gauges. In general, the bottom tier of strain gauges produced data that was obviously incorrect, i.e., gauge values were excessively large or small and could be easily discounted. On the other hand, strain gauge data from the top tier are likely incorrect, but the values are reasonable enough that the data cannot be discounted.

Data from Figure 6.21 is re-plotted in Figure 6.22 without the curves from the top and bottom layers, making the data from the remaining layers much more visible. As can be seen, remarkable similarities exist in the responses of each layer. For instance, all three curves exhibit essentially the same initial rate of increase in skin friction until approximately 0.6 mm, where a small plateau is reached. At that point, the bottom layer (7.0 to 15.75 m) remains flat and begins to decrease at about 2 mm deflection. Skin friction in the upper two layers, however, continues to increase, with both curves essentially parallel.

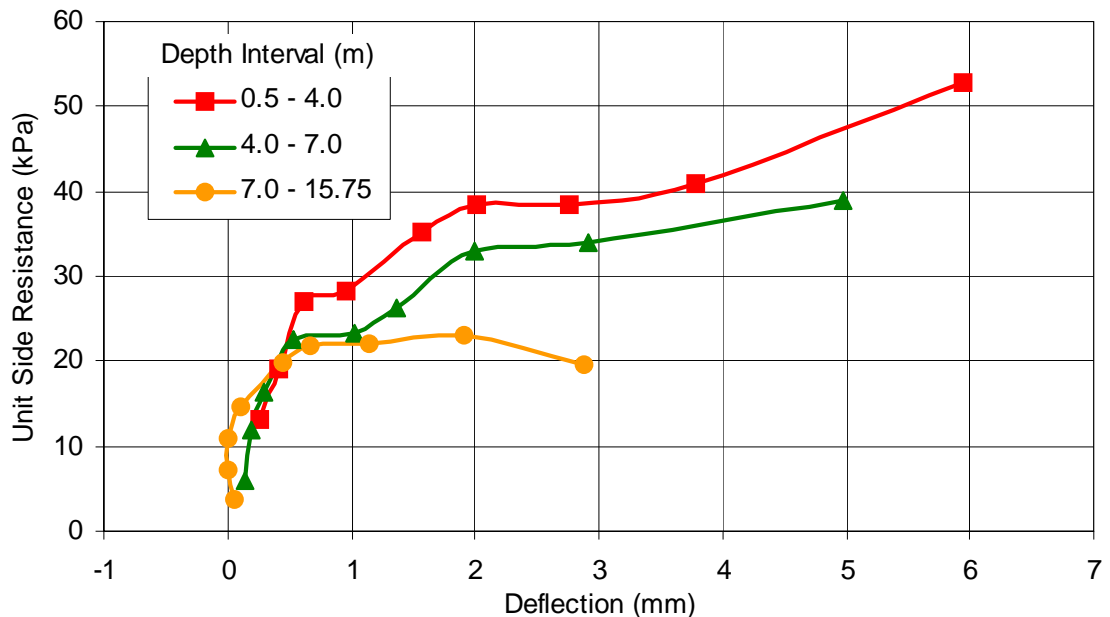


Figure 6.22 T-Z curves for the second static load test performed at Site 2, excluding the top and bottom depth intervals.

In order to more easily determine the cause of the increase in ultimate strength of the test pile, the T-Z curves were plotted together (see Figure 6.23). Data from the top and bottom layers from both tests were not plotted and the scale changed for clarity.

Referring to Figure 6.23, we see that T-Z curves for two layers from the first test and three layers from the second test are plotted. For the first test, the layers are from 0.5-3.6 m and 3.6-15.75 m depth. The three layers from the second test cover this same interval, only in three layers: 0.5-4.0 m; 4.0-7.0 m; and 7.0-15.75 m. A review of Figure 6.23 indicates that the curves for the top layers from both tests match reasonably well, with the second test producing somewhat higher values of unit shear resistance. It can also be seen that the unit side resistance from the two layers (4.0-7.0 m and 7.0-15.75 m) from the second test experiences a dramatic increase relative to the equivalent

layer (3.6-15.75 m) from the first test, where the maximum unit side resistance is about three times higher. The greatest increase is realized in the interval from 4.0-7.0 m depth.

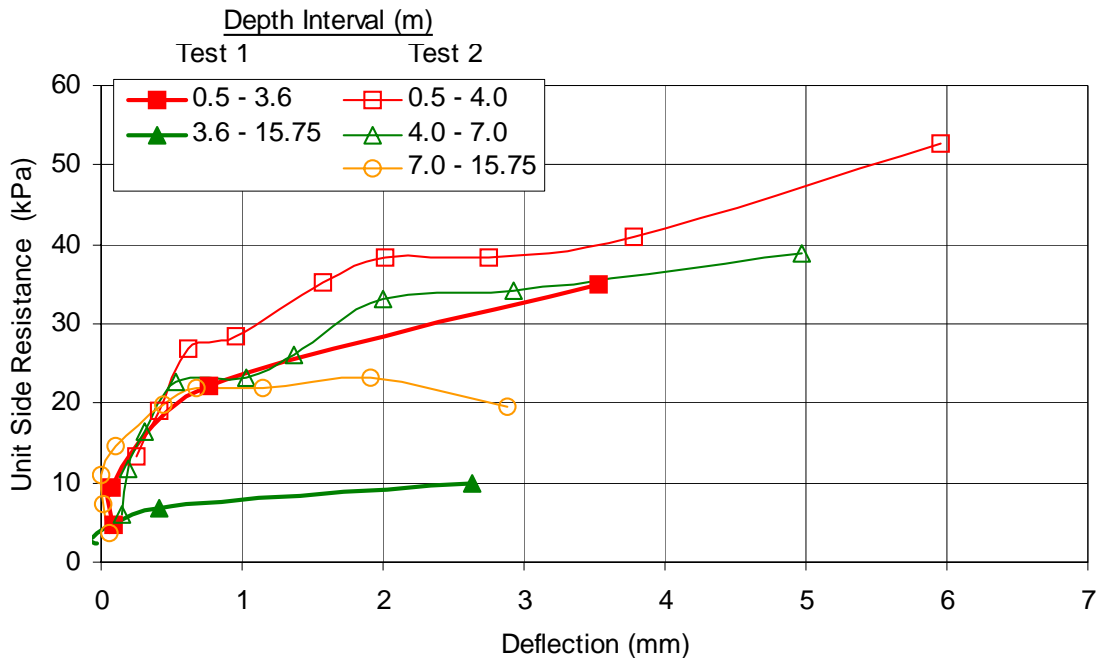


Figure 6.23 Comparison of T-Z curves for the first and second static load tests at Site 2.

Referring back to the generalized soil profile in Figure 3.7, the interval from 4.0-7.0 m spans the lower 1.5 m of the silty/clayey layer and the upper 1.5 m of the silty sand layer. Obviously the transition from the silty/clayey layer to the silty sand layer is not as distinct as that shown in Figure 3.7. Rather, the transition is more gradual, with the upper portion of the silty sand layer having a higher fines content than lower portions.

Inasmuch as setup phenomena are commonly seen in clayey soils, one can reasonably conclude that the increase in pile resistance can be partially attributed to the setup of this zone of the soil profile. The remainder of the resistance increase can be attributed to setup in the sand as discussed previously.

6.4.4 Comparison of measured response with predictive response

To better understand the load-transfer properties of the soil profile at the test site, comparisons were made between the measured response of the test pile with the response predicted by both the LCPC (Bustamante and Gianceselli, 1982; Tucker and Briaud, 1986) and Eslami and Fellenius (1997) methods.

Because the predictive methods produce estimates of ultimate load-bearing capacity, comparisons should be made using data recorded when the pile is loaded to the ultimate, or failure, load, as determined by the Davvison criteria. However, in this case, use of the Davisson failure loads is impractical. For the first static load test, the Davisson failure load was 650 kN, but the largest sustained load applied to the pile was 840 kN. During the second static load test, the maximum sustained load was 933 kN, less than the estimated Davisson failure load of 1030 kN. Thus, in the case of the first test, use of data recorded when the pile was loaded to 650 kN would not represent ultimate conditions. As for the second test, use of data corresponding to the failure load is impossible due to the fact that the pile was never loaded that high. Therefore, comparisons made with the predictive methods will be made at the largest sustained loads applied to the test pile.

6.4.4.1 Comparison of unit side resistance

Figures 6.24 and 6.25 display a graphical comparison between the predicted unit side resistance and the largest unit side resistance “measured” during the first and second load tests at Site 2, respectively. Of course the unit side resistance was not measured directly during the static load tests. Instead, it was calculated from the strain gauge data,

as discussed in the previous section. The predicted values shown in Figures 6.24 and 6.25 were presently previously in Table 5.5. The calculated values for the first test correspond to the peak sustained load of 840 kN and the values for the second load correspond to the peak sustained load of 933 kN; summaries of these values are contained in Tables A3 and A4, respectively.

A review of Figures 6.24 and 6.25 shows that the strata defined by changes in unit side resistance do not match with the soil layers defined in the generalized soil profile (Figure 3.7). This discrepancy is not unexpected—one would not necessarily expect that the soil profile interpreted from CPT data would forcibly correspond exactly with a profile defined by unit side resistance. Though the CPT approximates the behavior of a pile, there are two significant differences.

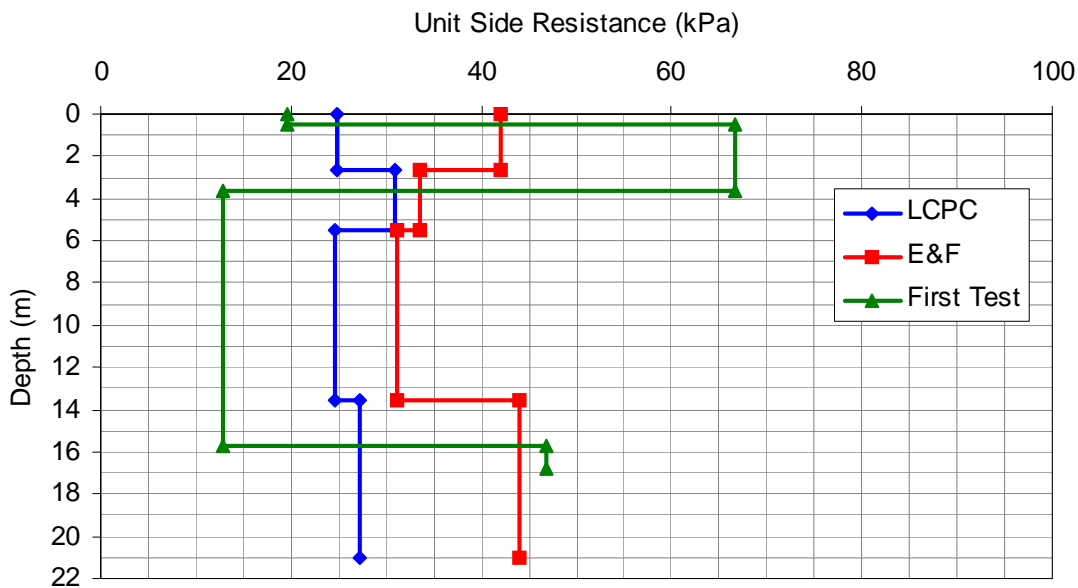


Figure 6.24 Comparison of measured values of unit side resistance for the first static load test with estimated values for Site 2.

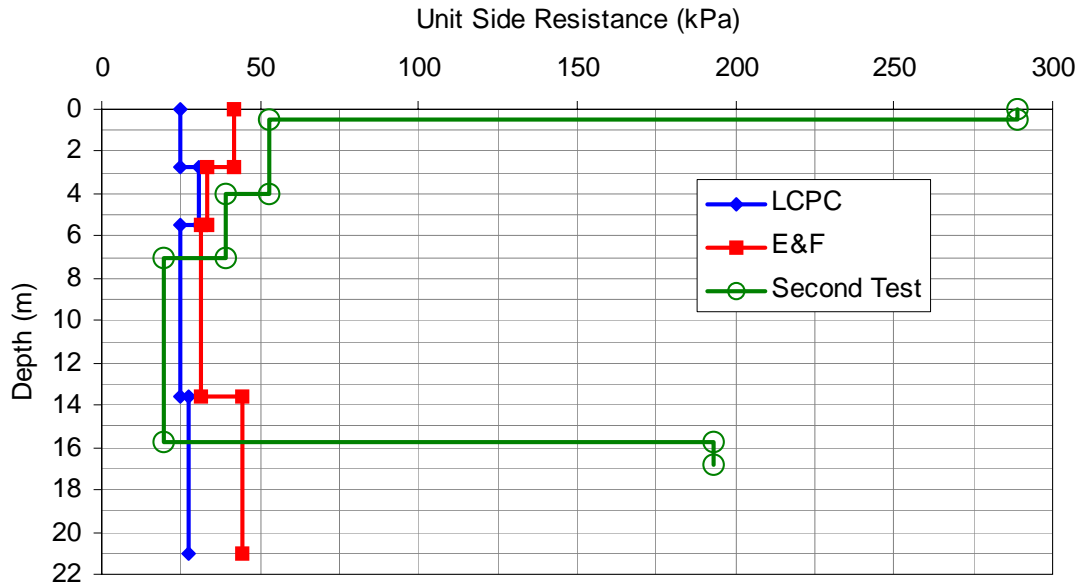


Figure 6.25 Comparison of measured values of unit side resistance for the second static load test with estimated values for Site 2.

First is the issue of scale—the test pile has a much larger diameter than the cone penetrometer. Smearing effects, where soil in the upper layers is forced into lower layers by the pile toe and subsequently smeared along the sides of the pile within the upper portions of the lower layer, become more pronounced for the test pile simply because more material from upper layers is smeared into lower layers by the pile than by the cone penetrometer. This is clearly evidenced by the fact that the major breaks in measured unit side resistance, shown in Figures 6.24 and 6.25, consistently occur approximately one meter below the layer boundaries shown in the generalized soil profile (Figure 3.7).

Second is data resolution. Data was recorded every 0.05 m throughout the entire depth of the cone penetrometer tests. On the test piles, the strain gauges were spaced approximately every 1.5 meters. Therefore the CPT has approximately 30 times the

vertical resolution as the test pile, allowing soil boundaries to be more accurately identified in the CPT data.

In order to overcome the limitations inherent in comparing stratified data with differing boundaries, the measured data was transformed so that all boundaries corresponded with those of the generalized soil profile. This transformation was accomplished by averaging the unit side resistance data for a given soil layer weighted by depth. Figures 6.26 and 6.27 show the transformed unit side resistance values corresponding to Figures 6.24 and 6.25, respectively.

For example, the extremely large unit side resistance calculated for the top layer (from 0 to 0.5 m depth) for the second static load test (shown in Figure 6.25), when combined with the lower unit side resistance calculated for the second layer (from 0.5 to 4 m depth), and transformed onto the generalized soil profile, results in a more reasonable value (see Figure 6.27). Table 6.6 tabulates the data contained in Figures 6.26 and 6.27.

Clearly, neither design method provided an accurate prediction of the unit side resistance through the entire profile. Nevertheless, the prediction is surprisingly good for certain intervals. The largest errors occur in the top-most and bottom-most layers. The error is greatest for the second test (Figure 6.27). This error is likely due to inaccuracies in the strain gauge data.

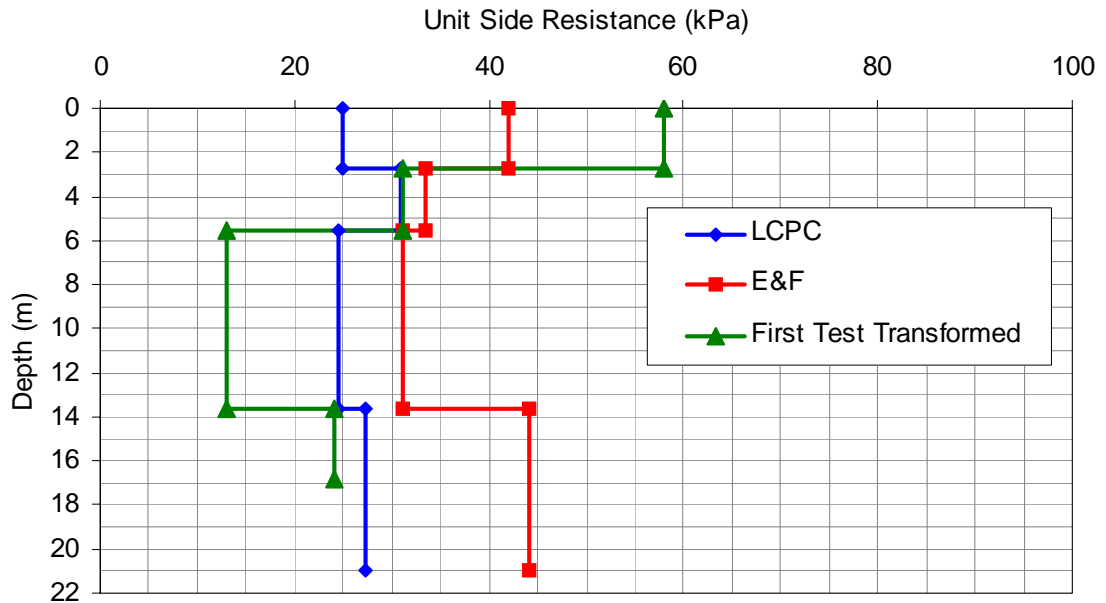


Figure 6.26 Comparison of measured and estimated values of unit side resistance values for the first static load test at Site 2. All values have been transformed such that layer boundaries correspond to the generalized soil profile.

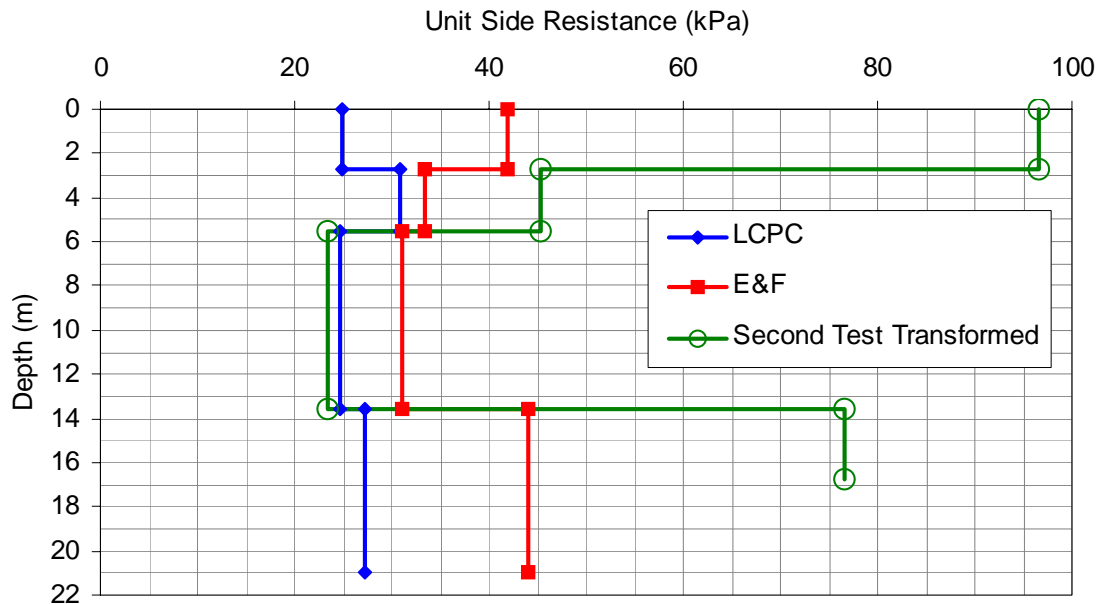


Figure 6.27 Comparison of measured values of unit side resistance for the second static load test with estimated values. All values have been transformed such that layer boundaries correspond to the generalized soil profile.

Table 6.6. Unit side resistance developed by the pile during static load testing at Site 2, transformed onto the generalized soil profile.

Depth (m)	Unit Side Resistance (kPa)			
	First Test	Second Test	LCPC	Eslami & Fellenius
0 - 2.7	58	96.5	24.9	42
2.7 - 5.5	31.2	45.4	30.9	33.5
5.5 - 13.6	12.9	23.3	24.6	31.1
13.6 - 16.8	24	76.5	27.2	44.1

For instance, the strain gauges in top-most layer experience the complex interaction between low confining pressures and high loads, possibly causing erroneous readings. In the bottom-most layer, only one strain gauge survived the rigors of pile driving, providing only a single data point for analysis.

In the second layer, the LCPC method matched almost exactly the unit side resistance measured during the first static test through it under-predicted the unit side resistance measured during the second static test by about 32 percent. The Eslami and Fellenius method also made a relatively good prediction for the second layer when compared with the first static load test though it under-predicted the second static test by about 26 percent. Both predictive methods over-predicted the unit side resistance in the third layer for the first load test. However, the LCPC method prediction was within 6% of the measured value for the second test.

One cause for these differences is the timing of the static load test relative to the time of pile driving. The first static load test was performed less than 24 hours after pile installation. The databases of load tests used to develop both the LCPC and Eslami and

Fellenius methods did not include tests performed so soon after pile installation. Thus, the comparison of unit side resistances made here is not strictly valid. Furthermore, as explained in Section 6.4.3, the occurrence of setup in the soil during the one-month period between load tests caused the pile to gain strength and the relationship between predicted and measured values of unit side resistance to change. For example, pile driving may have liquefied the sand layer between 6 and 14 m depth. As a result, the sand structure might have been severely weakened one day after pile driving, but could have re-established bonds over time.

While the LCPC method had greater success predicting magnitudes of side resistance, from a strictly conceptual point of view the Eslami and Fellenius method better matched the overall shape of the curves, and seems to provide a better match to the overall behavior of the soil-pile interface.

As mentioned in Section 5.1.1.3, strain gauges were not installed in the lower 3.7 m of the test pile, and the response of the bottom of the pile could not be measured. Therefore, before a quantitative comparison can be made with the predictive methods, the response of the test pile below a depth of 18.3 m must be determined.

Figure 6.28 shows the load-depth curves corresponding to the maximum sustained loads applied during the first and second static load tests at Site 2.

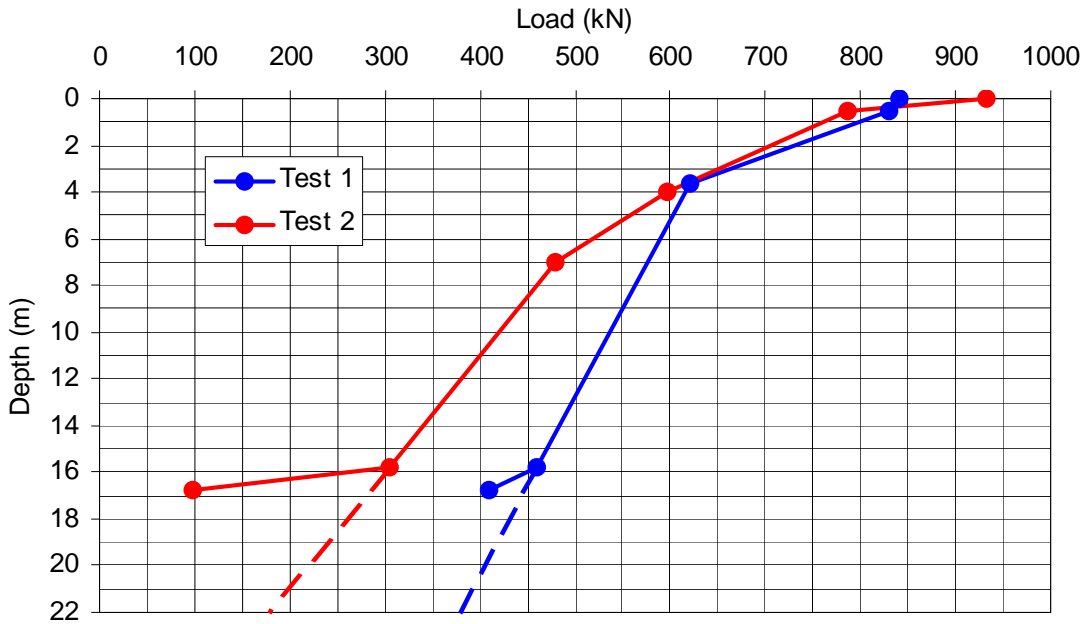


Figure 6.28 Load-depth curves corresponding to the largest sustained loads during each of the two static load tests performed at Site 2.

In order to estimate the response of the test pile below a depth of 18.3 m, the load-depth curve may be extrapolated downwards to the bottom of the test pile at a depth of 22 meters. It will be noticed that in Figures 6.28, the lowest segments of the load-depth curves exhibit fairly radical departures from the curve segment immediately above, indicating a marked increase in the unit side resistance of the soil-pile interface. If the load-depth curves are extended with the same slope as the lowest curve segments, the total side resistance of the pile will be greatly increased, causing an associated decrease in the end-bearing (discussed further below). The appropriateness of such a method is questionable considering the low level of confidence placed in the strain gauge data recorded at 18.3 m depth. In fact, extrapolation of the lowest curve segments from the second test would indicate that the entire applied load was resisted by skin friction in the

upper 18 m of the soil profile, with no side resistance or end-bearing being developed below that.

If, on the other hand, the response is determined by extending the load-depth curve using the curve segment immediately above the lowest segment, more realistic responses are produced. This has been done in Figure 6.28, as shown by the dashed lines. Table 6.7 summarizes the data shown in Figure 6.28.

Table 6.7. Total side resistance developed by the test pile during both static load tests at Site 2.

First Test		Second Test	
Depth (m)	Unit Side Resistance (kPa)	Depth (m)	Unit Side Resistance (kPa)
0 - 0.5	19.7	0 - 0.5	289
0.5 - 3.6	66.7	0.5 - 4.0	52.8
3.6 - 15.75	12.9	4.0 - 7.0	39.0
15.75 - 22	12.9	7.0 - 15.75	19.7
Total (kN)	462	15.75 - 22	19.7
		Total (kN)	754

Referring back to Table 5.5, it is remembered that the LCPC method predicted a total side resistance of 591 kN and the Eslami and Fellenius method predicted a total side resistance of 844 kN. Table 6.7 shows that the best match is between the second test and the Eslami and Fellenius method, with a difference of approximately 12 percent. The worst match was between the first test and the Eslami and Fellenius method with a

difference of over 82 percent. The difference between the LCPC method and the first and second tests was 28% and 22%, respectively.

6.4.4.2 Comparison of end-bearing

Because end-bearing was not measured directly, it must be calculated using the applied load and the load distribution in the pile as measured by the strain gauges. As mentioned in the previous section, because comparison at the Davisson failure load is impractical, comparisons will be made at the largest sustained applied load.

The end-bearing can be determined graphically by extending the load-depth curve to the depth of the bottom of the test pile (22 m), as was done in Figure 6.28. The load indicated by the curve at the bottom of the pile must then be equal to the amount of load resisted by end-bearing. This has been done as shown by the dashed line segments in Figure 6.28.

Figure 6.28 indicates that the end-bearing developed during the first and second test was 378 and 178 kN, respectively. Table 6.8 compares the two values of end-bearing calculated above with the values predicted by the LCPC and Eslami and Fellenius methods.

Table 6.8. Comparison of calculated and predicted values of end-bearing at Site 2.

	End-bearing (kN)	LCPC	Eslami and Fellenius
First Test	378	340	860
Second Test	178	340	860

When compared with the calculated values of end-bearing, there is good agreement between the end-bearing calculated for the first static test with the LCPC value, with a difference of 10 percent. The value from the second test did not compare favorably with the LCPC method, with the predicted value almost twice as large as the actual value. End-bearing from neither tests matched the value predicted by the Eslami and Fellenius method, which predicted an end-bearing over twice as large as was measured during the first test and almost five times larger than was measured during the second test.

The disparity between the measured end-bearing between the first and second test is possibly explained by the displacement of the test pile during the respective tests. In the first test, maximum pile head displacement reached approximately 67 millimeters. In the second test, pile head displacement was approximately 13 millimeters. The greater displacement in the first test caused greater end-bearing to develop where a lesser amount of end-bearing developed in the second test due to the lower displacement.

6.4.4.3 Comparisons with predictive methods summarized

While the unit side resistance values for the individual layers did not match well with the predicted values, the total side resistance measured during the second static load test matched remarkably well with the value predicted by the Eslami and Fellenius method, with a 12% difference. The relatively poor match obtained from the first static load test can be explained by the effects of “setup,” as discussed in Section 6.4.3.

The calculated end-bearing from the first static load test was in good agreement with the value predicted by the LCPC method, with a 10% difference. The relatively low

values of end-bearing calculated from the second static load test can be explained by the relatively small displacements encountered during the test. Higher displacements would likely have caused larger amounts of end-bearing to develop.

Overall, the Eslami and Fellenius method provided the best prediction of total side resistance and the LCPC method predicted the most accurate value of end-bearing.

6.5 Blast Test 1

The first blast test was performed 27 July 2005, using smaller charge weights (0.45 kg) than those used for the second blast (1.35 kg). Although the pilot liquefaction testing at Site 1 indicated that the larger charge weights would be necessary to produce liquefaction, these tests had been performed a month earlier when gaps had been observed between the blast hole casing and the surrounding ground. If, during the subsequent month, the ground had tightened in around the casing, then less energy would be required to produce liquefaction. Therefore, the first blast test was performed with lower charge weights to evaluate this possibility as it was desired to induce liquefaction in an incremental fashion more akin to the process observed during an earthquake.

For Blast Test 1, a total of 16, 0.45 kg (1 lb) explosive charges were detonated sequentially with a one-second delay between detonations. Charges were located at depths of 6.4 and 8.5 m below the ground surface in each of eight drill holes spaced evenly around a 10-m-dia. circle centered about the test pile. The eight explosive charges at 8.5 m were detonated first followed by the eight charges at 6.4 m.

6.5.1 Excess pore pressure generation and dissipation

Time histories of the first 30 seconds of the blast sequence showing the generation of excess pore pressure ratio for each of the five piezometers are presented in Figure 6.29. The pore pressure increased incrementally with each successive blast as expected and the behavior was relatively consistent at each depth. The piezometer records from depths of 6.7, 8.4, and 10.7 m exhibit an almost identical response pattern. While the excess pore pressure ratios routinely spiked well above 1.0, the residual excess pore pressure ratios reached a maximum of about 0.8 and 0.9. The piezometer located at 12.8 m depth recorded a response similar to that of the top three piezometers for the first three to four blasts. At that point the record diverged, reaching a maximum excess pore pressure ratio of approximately 0.6. The piezometer located at 16.8 m depth recorded a maximum excess pore pressure ratio of only 0.1, indicating that the soil at that depth never approached the liquefied state. These results confirmed that larger charge weights would be required to produce liquefaction within the target zone, despite potential decreases in the gap width around the blast hole casings.

Full time histories of the dissipation of excess pore pressure ratios for each of the five piezometers following blasting are presented in Figure 6.30. The pore pressures dissipated more quickly as the depth increased, indicating that the sand reconsolidated from the bottom to the top. Excess pore pressure dissipation was essentially complete after about 30 minutes.

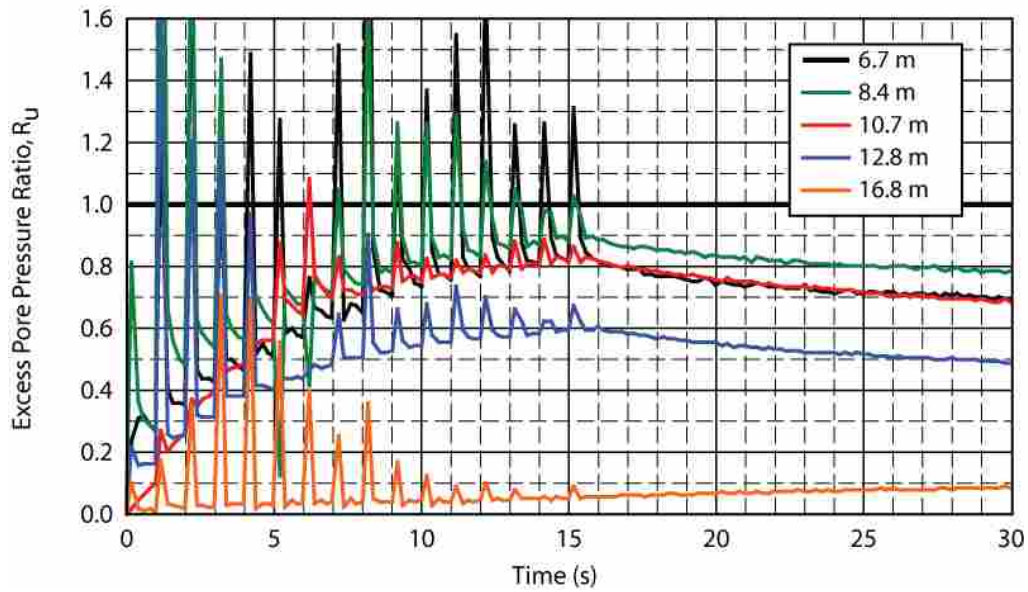


Figure 6.29 Plot of generation of pore pressure during the first blast test at Site 2.

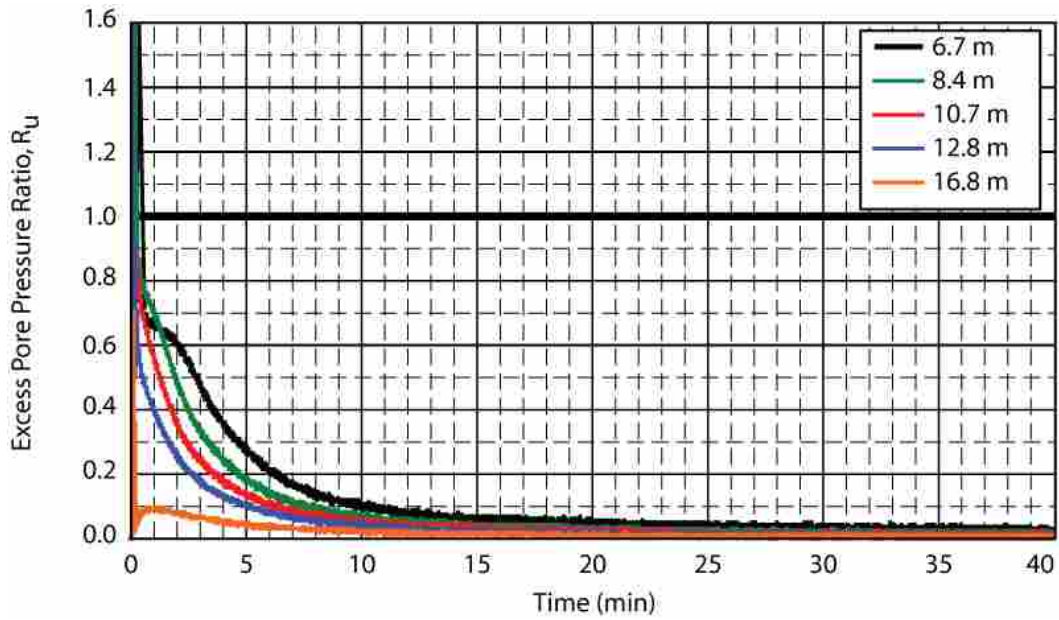


Figure 6.30 Dissipation of pore pressures during the first blast test at Site 2.

6.5.2 Blast induced settlement

A contour plot of the ground surface settlement following the first blast is provided in Figure 6.31. The maximum settlement was approximately 155 mm and this value occurred near the center of the test area. Contours of settlement are generally concentric about the center of the test area.

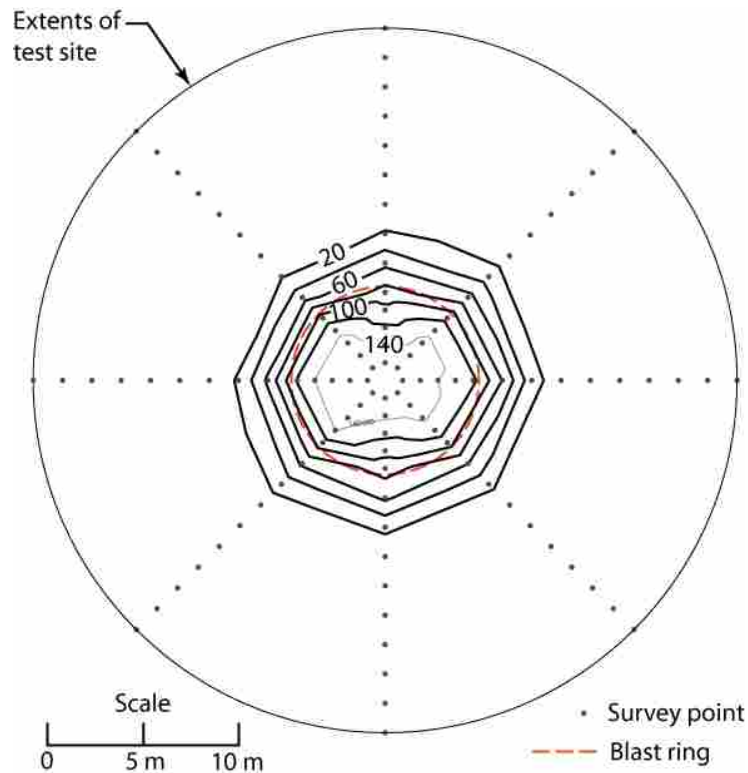


Figure 6.31 Contour plot of ground surface settlement caused by the first blast test at Site 2.

A plot of the average ground surface settlement with respect to distance from the center of the test area is provided in Figure 6.32. On average, settlement decreased to levels below the error of the survey (estimated at approximately ± 3 mm) at distances greater than about 11 m from the center of the test area.

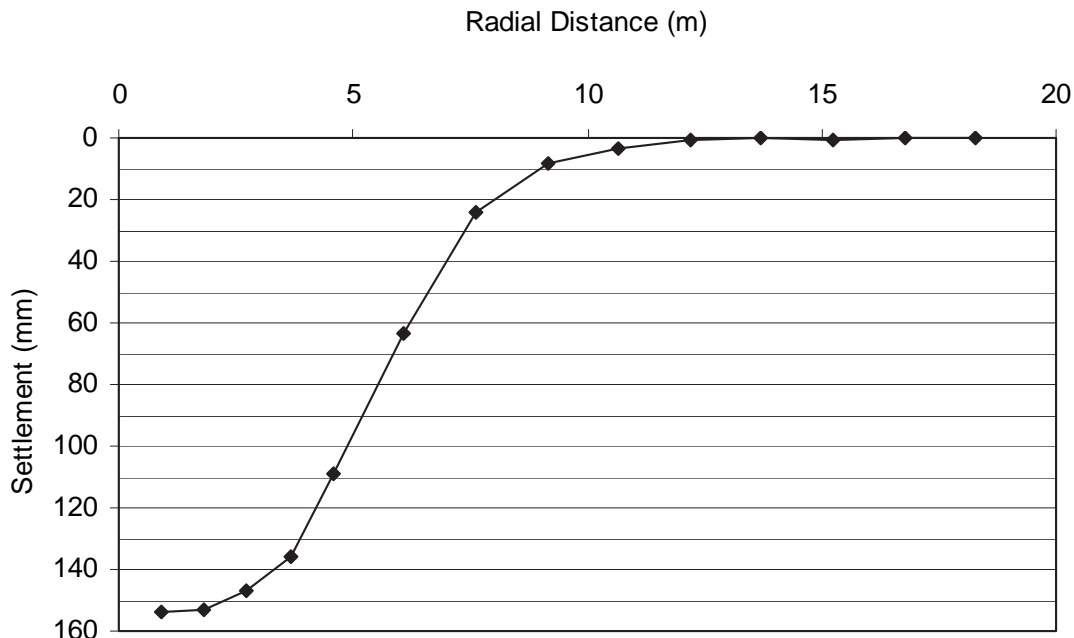


Figure 6.32 Variation of average settlement versus radial distance from the center of the test area caused by the first blast test at Site 2.

A plot of the settlement versus depth obtained from the Sondex tube is provided in Figure 6.33. Beyond a depth of 4 m, the settlement decreased in a fairly linear fashion with increasing depth until it reached zero settlement at 13.7 m depth. The fact that the settlement at the surface as measured by the Sondex tube is somewhat lower than the settlement measured by the level survey is easily explained. The soil near the surface was extremely dry and loose (see Section 3.5). Ideally, once the soil began to settle as a result of blasting, the plastic corrugated pipe would compress equally with the soil. However, with the soil in its loose, dry state at low confining pressure, the corrugated pipe was likely stiff enough to resist some of the compression induced in it as the soil around it settled. At greater depths the confining pressure would increase the soil strength relative to the corrugated pipe and lead to more consistent settlement between

the soil and the pipe. Based on the Sondex measurements, the average volumetric strain in the sand layer from 6 m to 13 m was approximately 1.3 percent.

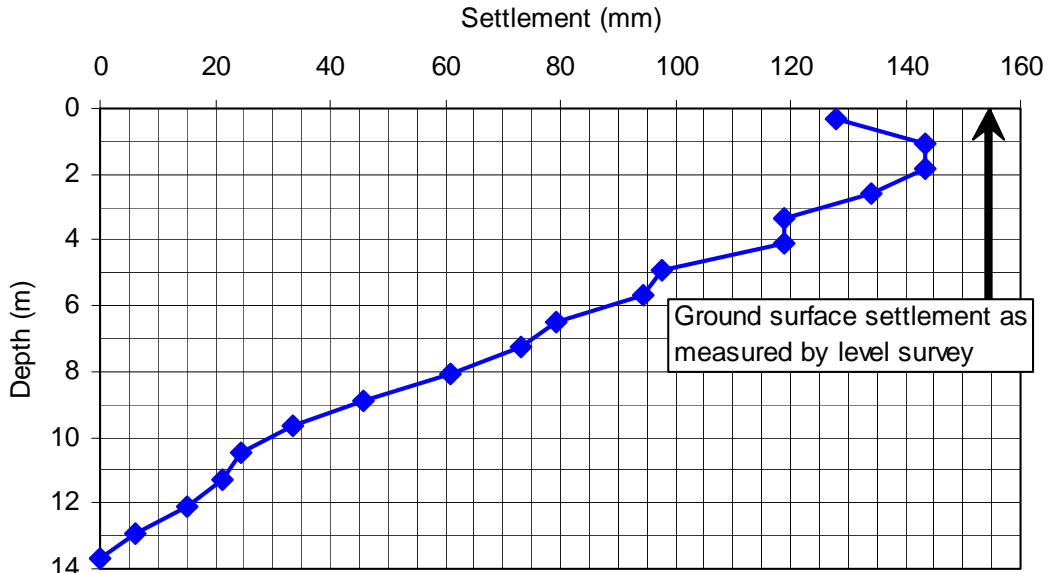


Figure 6.33 Settlement as a function of depth measured by the Sondex tube for the first test blast at Site 2.

6.5.3 Pile load transfer variations due to liquefaction

To analyze the load transfer properties of the soil-pile interface, a load was applied to the test pile before blasting and maintained during blasting until pore pressures had dissipated to near pre-blast levels. Figure 6.34 shows the load applied to the test pile as it varied with time throughout the test. The onset of blasting was set as time zero, therefore negative time values indicate the time before blasting.

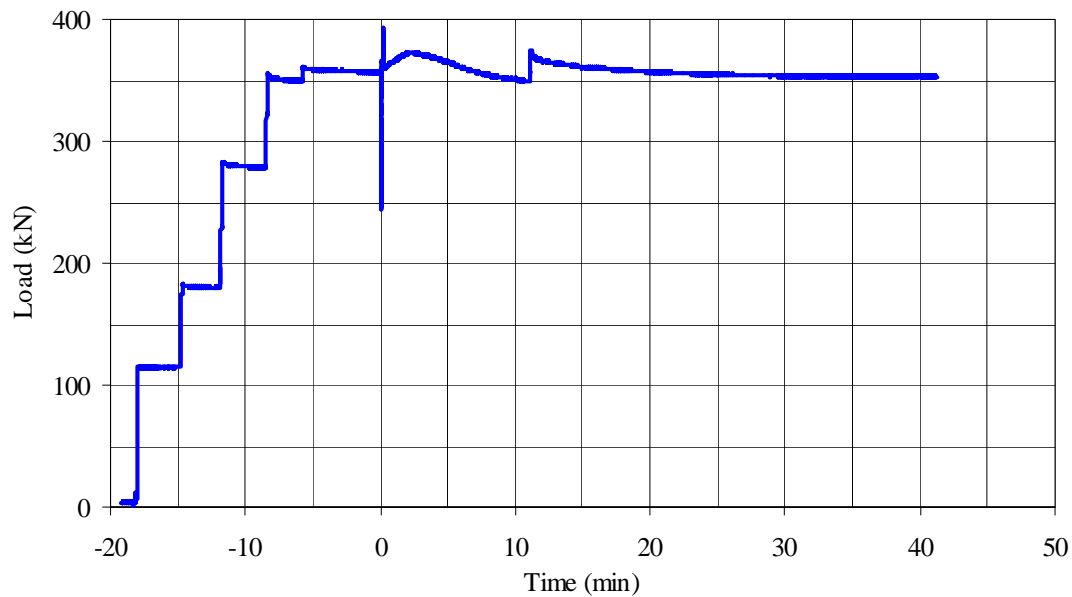


Figure 6.34 Load applied to test pile at Site 2 during the first blast test.

Measurements made with the strain gauges attached to the test pile were used to calculate the load carried by the pile as it varied with depth (see Section 6.4.3). Figure 6.35 shows the variation of load in the test pile with respect to depth at three distinct times: immediately before blasting, immediately after blasting, and at the point that surface settlement had ended. The strain gauges located at a depth of 16.8 m appear to have been damaged during blasting. As a result, data recorded at this depth will not be reported.

Immediately before blasting, a load of approximately 356 kN was applied to the test pile. A review of Figure 6.35 shows that the load transfer from the pile to the surrounding soil is greatest at the ground surface and decreases with depth. This indicates that the upper-most silty-sand layer provides the greatest transfer of load per unit of depth. The clayey silt layer provides a lesser amount of load transfer relative to

the soil layer above. At a depth of approximately 5 m, the load transfer curve becomes fairly linear, indicating that the load transfer is fairly constant in the underlying sands and silty sands.

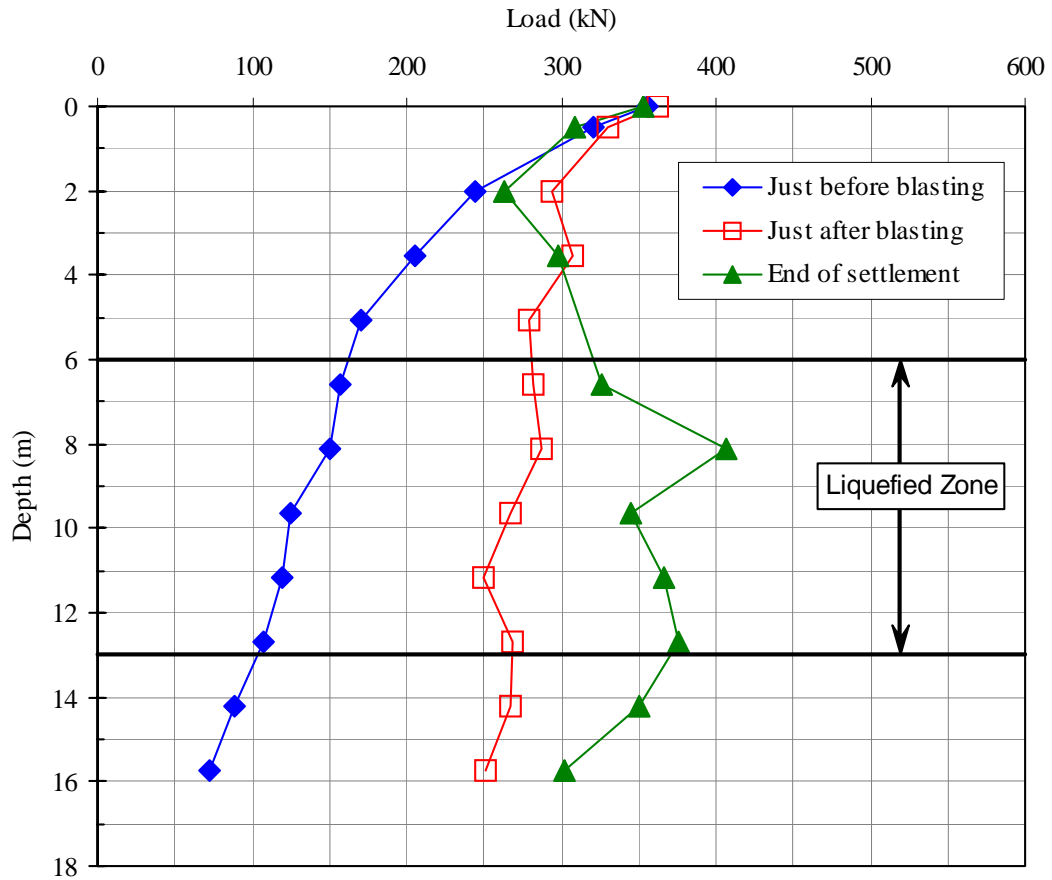


Figure 6.35 Variation of load transfer during the first blast test at Site 2.

At the onset of blasting, the test pile settled slightly so that the load applied by the hydraulic jacks dropped to a low of 243 kN, or about 68% of the applied load at the beginning of blasting. This load capacity was re-established by the end of the blasting by applying an additional 113 kN at the top of the pile. The load of 356 kN was maintained throughout the remainder of the test by adding hydraulic fluid to the jack as the pile

began to settle relieve the load. It appears that about 70 kN of the 113 kN reapplied to the pile was transferred by skin friction in the upper 2 m of the pile.

The load versus depth curve recorded immediately after blasting is fairly linear between a depth of 2 and 16 meters. It was assumed that liquefaction of the soil would cause the skin friction in the liquefied zone to decrease to essentially zero. That this did not occur may be explained by the fact that full liquefaction did not occur. A review of Figure 6.29 shows that the maximum sustained excess pore pressure ratio reached 0.9 at a depth of 6.7 m. At a depth of 12.8 m, the maximum sustained excess pore pressure ratio was only 0.6. Thus, while blasting caused the skin friction to decrease dramatically, there still remained a limited amount of positive skin friction. Indeed, the remaining skin friction appears to have been sufficient to transfer the remaining 43 kN between a depth of 2 and 16 meters.

Once excess pore pressure had dissipated and settlement stopped, the load versus depth curve in the partially liquefied zone developed a negative slope as shown in Figure 6.35. The negative slope indicates that negative skin friction had developed between depths of 2 and 13 m and was applying dragload on the pile.

Table 6.9 contains a summary of the skin friction produced within the target zone during the first blast test at Site 2. As can be seen, immediately before blasting began, the skin friction within the target zone was 7.97 kPa.. After the blast test, settlement of the soil relative to the pile caused negative skin friction to develop within the target zone, with an average value of -8.01 kPa. The similarity in magnitudes between the two values of skin friction indicates that the magnitude of negative skin friction produced as a

result of liquefaction is equal to the magnitude of positive skin friction existing before liquefaction.

Table 6.9 also contains a summary of values of unit side resistance within the target zone predicted by the LCPC and Eslami and Fellenius methods. The fact that the predicted values of skin friction are approximately four to five times larger than measured values may be partially explained by differences in the relative size of the load applied to the test pile compared to the load assumed in the predicted methods. The predictive methods produce maximum values of resistance and therefore assume a load approaching the failure load is applied to the pile. On the other hand, the test pile was loaded to 356 kN before blasting, only 35% of the Davisson failure load of 1030 kN. Therefore, in order to produce a valid comparison, the predicted values of unit side resistance should be compared to the measured values of unit side resistance when the pile is loaded at or near the failure load.

Table 6.9. Comparison of unit side resistance (skin friction) developed within the target zone immediately before blasting and at the end of settlement with predicted values of skin friction.

	Just before blasting	End of settlement	LCPC	Eslami and Fellenius
Skin Friction 6 - 13 m (kPa)	7.97	-8.01	24.6	31.1

6.6 Blast Test 2

The second blast test at Site 2 was performed approximately four hours after the first blast test at Site 2. A total of 16, 1.36 kg (3 lb) explosive charges (Pentex) were detonated sequentially with a one-second delay between detonations. Charges were

located at depths of 6.4 and 8.5 m below the ground surface in each of eight drill holes spaced evenly around a 10 m diameter circle centered about the test pile. The eight explosive charges at 8.5 m were detonated first followed by the eight charges at 6.4 m.

6.6.1 Pre-blast skin friction mobilization

Prior to blasting, the pile was loaded to approximately 536 kN using the quick maintained load procedure as discussed in Section 6.4.1. This load was chosen because it was estimated that at that load the skin friction would be completely mobilized from the ground surface through a depth of 15 meters. It was further estimated that the remaining non-mobilized skin friction below 15 m plus the toe bearing would be sufficient to support the pile against the negative skin friction that was expected to develop once blast testing commenced.

In order to calculate the degree to which the skin friction had been developed, it was necessary to first estimate the maximum possible skin friction that could be developed. Fortunately, these values are readily available from Figure 6.21 which depicts the T-Z curves developed from the second static load test performed at Site 2. The maximum values of skin friction are simply the largest values shown for each curve and may not represent the absolute maximum possible skin friction. However, inasmuch as the static load tests applied loads sufficient to cause the pile to plunge, the maximum values taken from the T-Z curves should be representative of the maximum skin friction values. Because these maximum values were determined from static load tests, they will be designated as $\tau_{\text{max-static}}$. These values correspond to the unit side resistance values taken from the right-most load-depth curve shown in Figure 6.19.

Figure 6.36 shows the load-depth curve for the pile immediately before blast testing. A simplified load-depth curve (shown as the dashed line) was developed in order to determine the unit side resistance acting on the pile immediately before blasting (see Section 6.4.3 for more information regarding the calculation of unit side resistance). Unfortunately, the strata delineated in Figure 6.36 do not correlate with the strata upon which the T-Z curves in Figure 6.19 are based, making comparisons difficult.

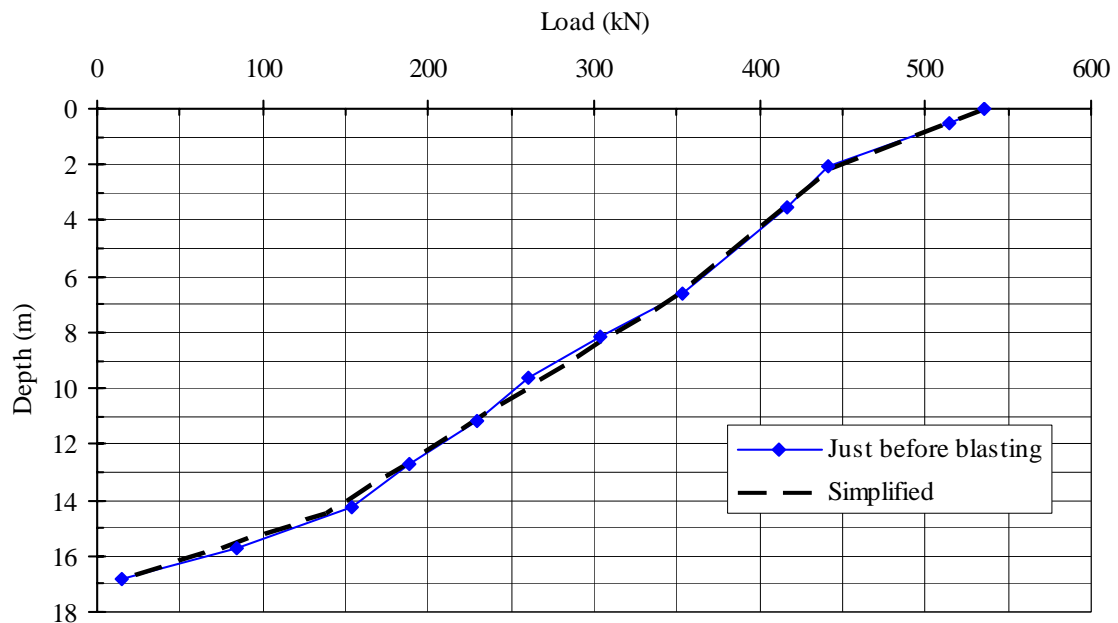


Figure 6.36 Measured and simplified load-depth curves for the test pile immediately before the second blast test at Site 2.

In order to facilitate comparison, the simplified load-depth curves from both Figures 6.19 and 6.36 were transformed onto the generalized soil profile as described in Section 6.4.4.1. The transformed values are depicted in Figure 6.37 and summarized in

Table 6.10. The unit side resistance values predicted by the Eslami and Fellenius and the LCPC methods are also included in Figure 6.37 for comparison purposes.

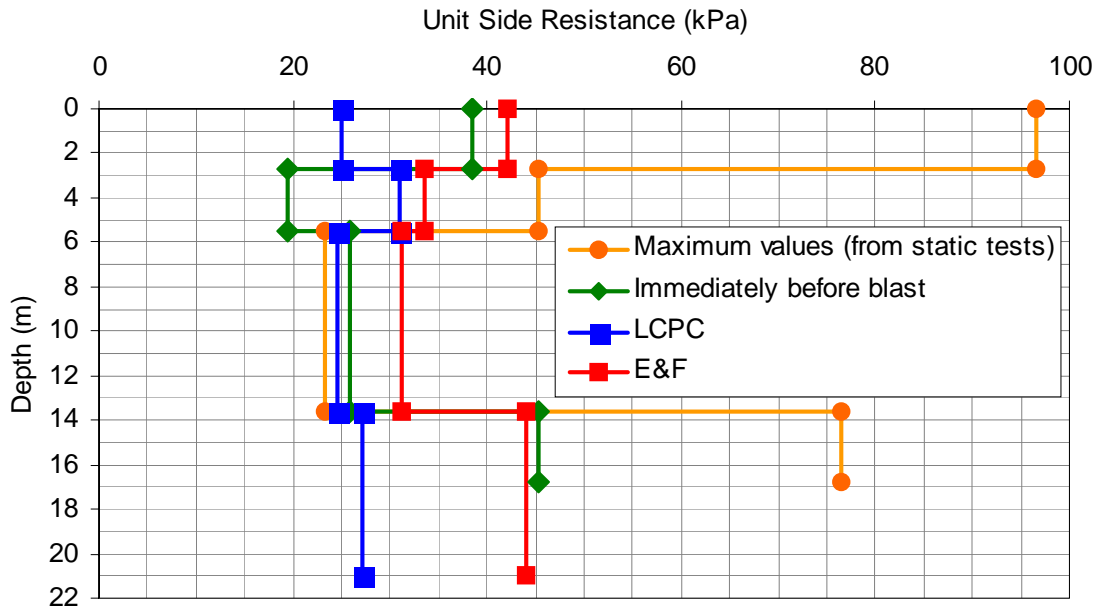


Figure 6.37 Comparison of unit side resistance values measured immediately before the second test blast and maximum measured values of unit side resistance at Site 2 with estimated unit side resistance values.

As can be seen from Figure 6.37, the skin friction was not completely mobilized throughout the depth of the soil profile. As indicated in Table 6.10, the average mobilized skin friction was 63% of the maximum static values obtained from the previous load tests. Also, between depths of 5.5 and 13.6 m, the unit side resistance from the static test and that measured immediately before blasting matched the value predicted by the Eslami and Fellenius method.

Table 6.10. Summary of unit side resistance, τ , as measured immediately before the second blast test at Site 2 compared with maximum unit side resistance values measured during the second static load test.

Depth Interval (m)	Unit Side Resistance, τ (kPa)	Maximum Unit Side Resistance, $\tau_{\text{max-static}}$ (kPa)	Percentage of $\tau_{\text{max-static}}$ (%)
0 - 2.7	38.5	96.5	40
2.7 - 5.5	19.4	45.4	43
5.5 - 13.6	25.8	23.3	111
13.6 - 16.8	45.3	76.5	59
Average:			63

6.6.2 Excess pore pressure generation and dissipation

Time histories showing the generation of excess pore pressure ratio for each of the five piezometers during the blast testing are plotted in Figure 6.38. The pattern of pore pressure generation was similar to that which occurred during the first blast test, i.e., a non-linear curve showing the greatest increases during the first several blasts and smaller increases in pressure with each subsequent blast. However, the rate of pressure generation is much higher for the second blast than for the first blast. For example, in the first blast, an R_u of 0.8 was obtained after nine to ten seconds whereas the same value was obtained in only about six seconds for the second blast. Such a response is consistent with the larger size of explosive charges used. The maximum excess pore pressure ratios were reached by the twelfth blast, with little to no increase with the last four blasts. This pattern was recorded by all piezometers, regardless of the depth.

As occurred during the first blast test, the top three piezometers (those at 6.7, 8.4, and 10.7 m) recorded similar responses. However, the piezometer at 12.8 m showed a somewhat slower rate of pore pressure generation relative to the top three piezometers.

After about 12 detonations, the residual excess pore pressure ratio for the piezometers at depths of 6.7, 8.4, 10.7, and 12.8 m was above 90 percent and there was little change in the ratio for the subsequent detonations. As in the first blast test, at a depth of 16.8 m, the excess pore pressure ratio remained quite low. In this case, it did not exceed 0.18. The reduced pore pressure ratio at a depth of 16.8 m is a result of two factors. First, the soil at this depth is further from the location of the blast charges and second, the sand at this depth has a higher relative density.

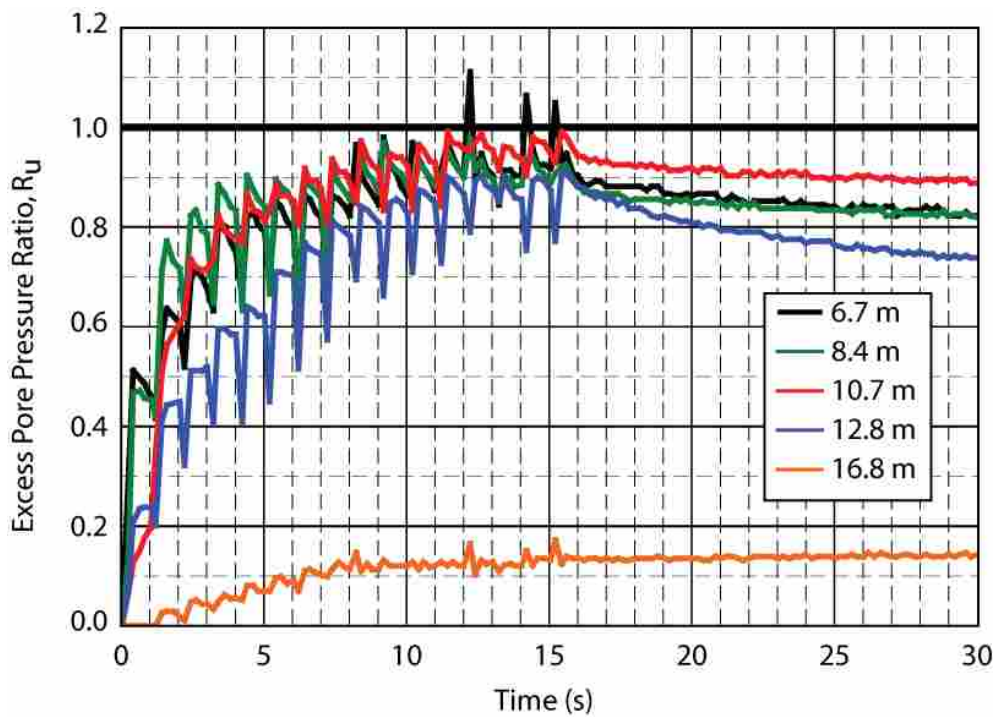


Figure 6.38 Generation of pore pressure during the second blast test at Site 2.

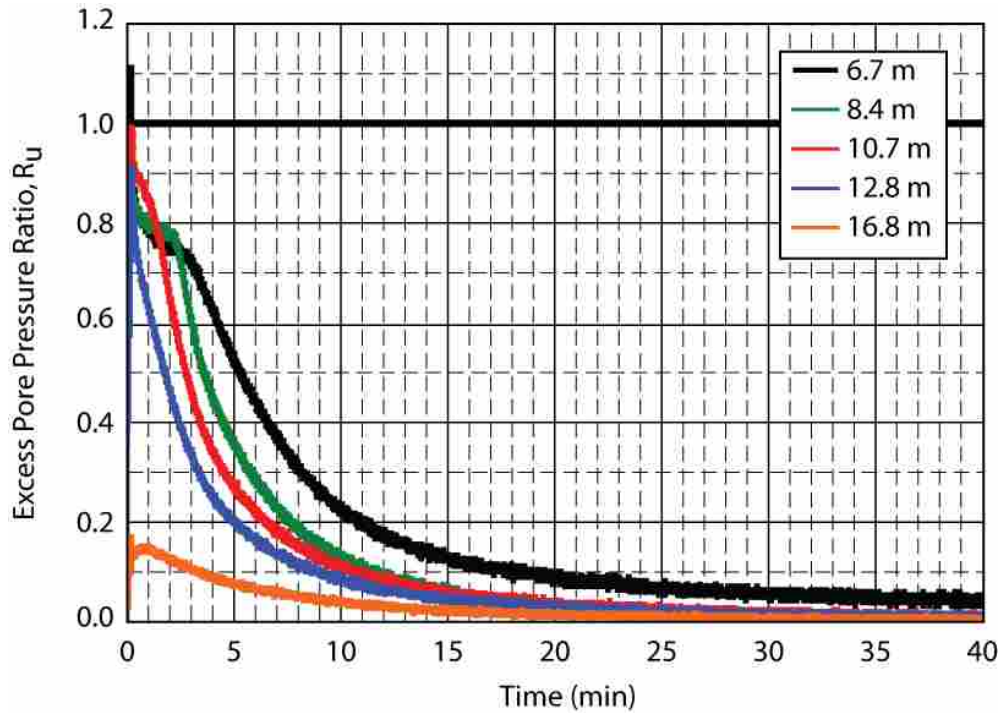


Figure 6.39 Dissipation of pore pressure after the second blast test at Site 2.

Time histories of the dissipation of excess pore pressure ratio for each of the five piezometers following blasting are presented in Figure 6.39. The pore pressures dissipated more quickly as the depth increased, indicating that the sand once again reconsolidated from the bottom to the top. Excess pore pressure ratios were less than 0.1 after about 25 minutes.

6.6.3 Blast-induced settlement

A contour plot of the ground surface settlement due to the second blast only is provided in Figure 6.40. The maximum settlement was approximately 270 mm and occurred near the center of the test area. Contours of settlement were generally concentric about the center of the test area.

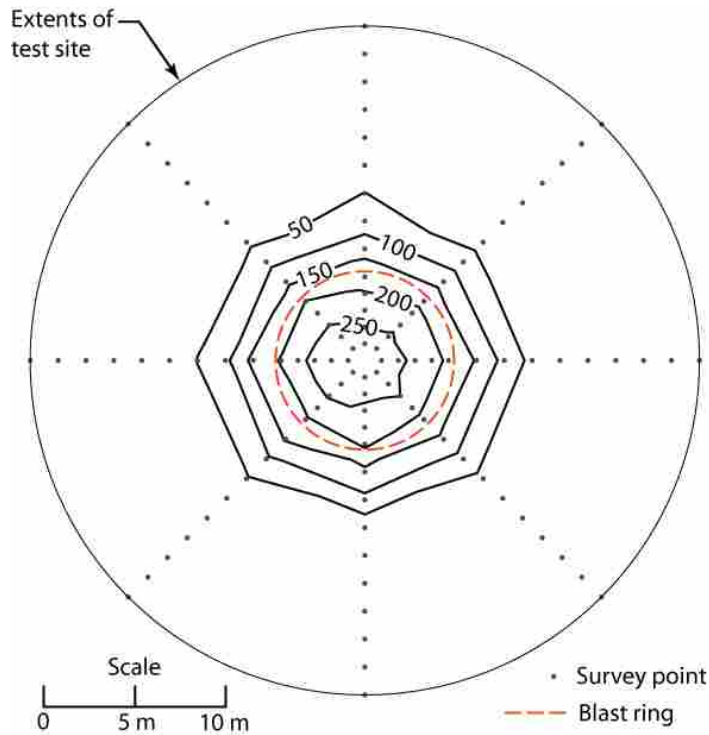


Figure 6.40 Contour plot of settlement caused by the second test blast at Site 2.

A plot of the average ground surface settlement with respect to distance from the center of the test area is provided in Figure 6.41 along with a similar plot from the first blast. Because the excess pore pressures induced in the second blast were much higher than for the first blast, the ground settlement within five meters of the center was typically about 1.7 times greater. On average, settlement was less than 3 mm at distances greater than about 12 m from the center of the test area.

A plot of the settlement versus depth obtained from the Sondex tube is provided in Figure 6.42. According to the level survey data, the ground surface settlement at the location of the Sondex tube was approximately 265 mm, which is similar to the average settlement recorded by the Sondex tube in the top 3.5 m.

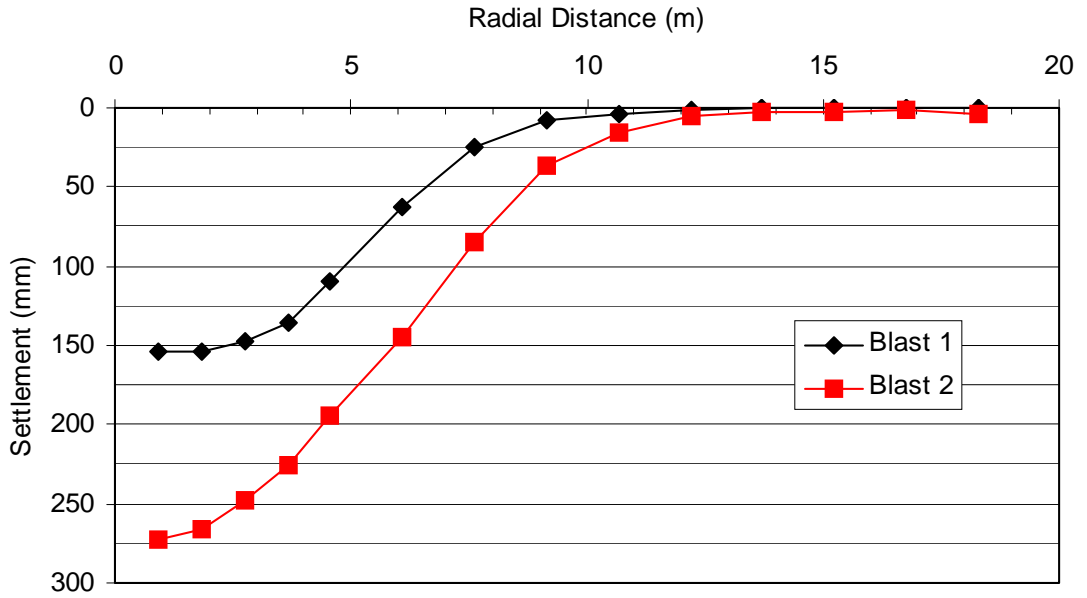


Figure 6.41 Comparison of average ground surface settlement caused by both blast tests at Site 2.

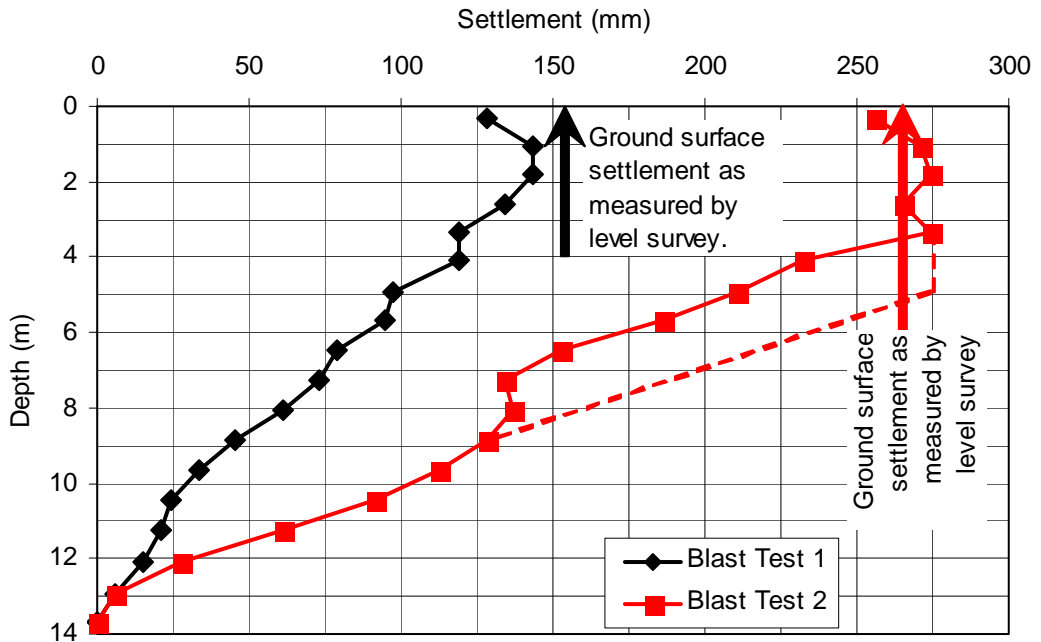


Figure 6.42 Comparison of settlement measured by the Sondex tube at Site 2 for both test blasts.

The settlement profile was nearly constant from the ground surface to a depth of about 3.5 m and then decreased essentially linearly until it reached zero at a depth of about 13.7 m. This settlement profile indicates that the upper 3.5 m settled as a block on top of an underlying liquefied layer extending from 3.5 m to about 13.6 m. However, the liquefiable sand layer begins at a depth of 5.5 meters. This discrepancy could be attributed to either slippage of the Sondex pipe within the clayey silt layer or settlement in the silt layer due to liquefaction.

The dashed line in Figure 6.42 represents the settlement versus depth profile assuming that slippage occurred between the Sondex tube and the clayey silt layer. This modified settlement profile indicates that the liquefied layer begins at a depth of about 5.0 meters. This is in reasonable agreement with the generalized soil profile.

The average volumetric strain of the target zone (6 to 13 m) is 2.3 percent. However, the possibility exists that the Sondex pipe could have slipped inside the sandy silt/clay zone from 3.5 to 5 m below the ground surface. For example, the settlement plot from the pilot liquefaction test (see Figure 4.19) did not show any appreciable settlement in this zone. If settlement is assumed to be negligible in this layer, then the average volumetric strain in the liquefied layer for test Site 2 would be 3.1 percent. Based on the Tokimatsu and Seed (1987) method, the expected liquefaction induced settlement in this zone would be approximately 3 percent.

Real-time settlement was measured using four string potentiometers and is shown in Figure 6.43. As can be seen, settlement occurs rapidly during and immediately following blasting. Approximately 80% of the settlement occurred within five minutes

after the onset of blasting. At five minutes after blasting, the excess pore pressure ratios in the target zone ranged from 0.2 at 12.8 m depth to 0.52 at 6.7 m depth, according to Figure 6.39

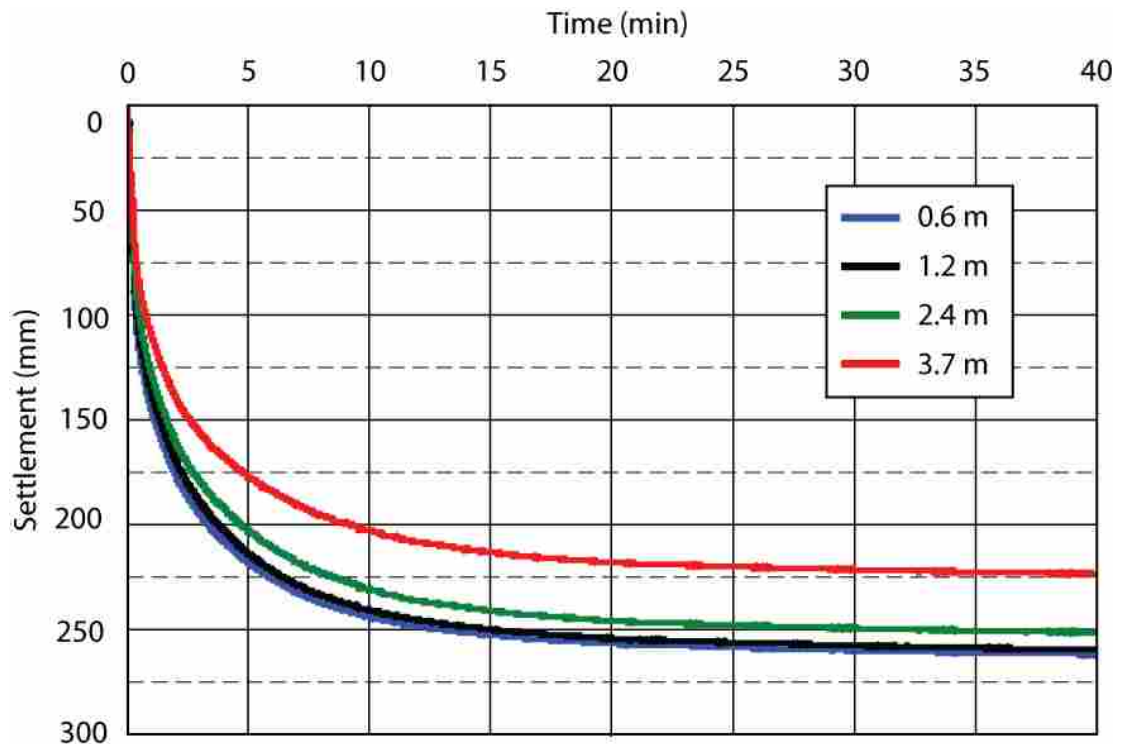


Figure 6.43 Real-time ground surface settlement measured by the string potentiometers during the second blast test at Site 2.

6.6.4 Pile load transfer variations due to liquefaction

To analyze the load transfer properties of the soil-pile interface, a load was applied to the test pile before blasting and maintained during blasting until pore pressures had dissipated to near pre-blast levels. Figure 6.44 shows the load applied to the test pile as it varied with time throughout the test. The onset of blasting was set as time zero, therefore negative time values indicate the time before blasting.

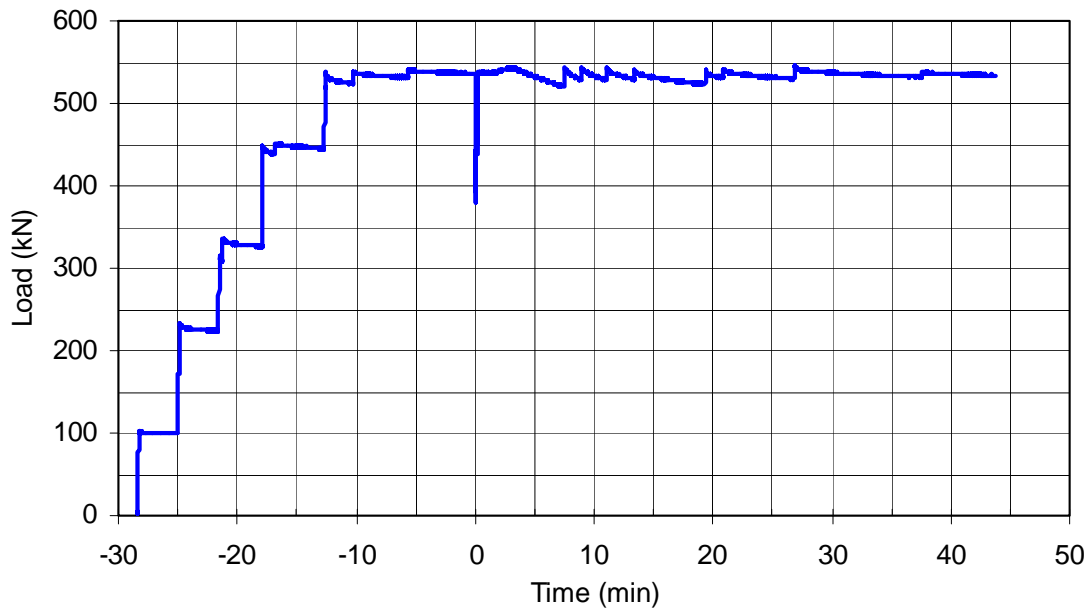


Figure 6.44 Load applied to test pile at Site 2 during the second blast test.

Measurements made with the strain gauges attached to the test pile were used to calculate the load carried by the pile as it varied with depth (see Section 6.4.3).

Figure 6.45 shows the variation of load in the test pile with respect to depth at three distinct times: immediately before blasting, immediately after blasting, and at the point that surface settlement had ended.

Immediately before blasting, a load of approximately 536 kN was applied to the test pile. The roughly linear decrease in pile load versus depth shown in Figure 6.45 indicates that the transfer of load out of the pile and into the soil through skin friction was fairly constant with depth.

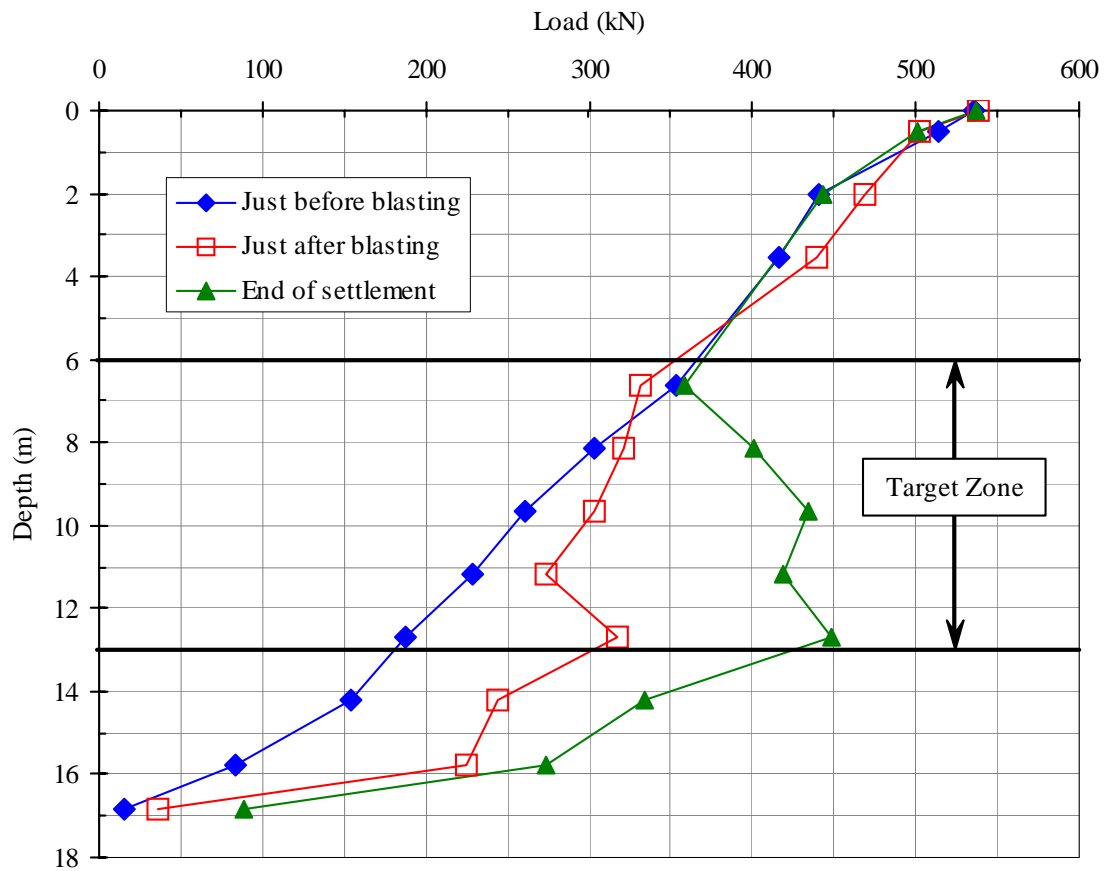


Figure 6.45 Variation of load transfer during the second blast test at Site 2.

At the onset of blasting, the test pile settled slightly so that the load applied by the hydraulic jacks dropped to a low of 380 kN, or about 71% of the applied load at the beginning of blasting. This load capacity was re-established by the end of the blasting by applying an additional 156 kN at the top of the pile. This load appears to have been transferred by skin friction to the upper section of the pile. As a result, the pile load versus depth curve in the upper 6 m of the profile is about the same as before the blast. It should be noted that the total measured skin friction from the ground surface to a depth of 6 m immediately prior to blasting was approximately 166 kN. Therefore, the

redevelopment of positive skin friction due to this applied load appears to be reasonable. The load of 536 kN was maintained throughout the remainder of the test by adding hydraulic fluid to the jack as the pile began to settle relieve the load.

Immediately following blasting, the load in the pile became much more constant with depth throughout the liquefied zone from a depth of about 6 to 13.5 m, thus indicating that skin friction in that zone had dropped to a relatively small value. The load originally carried by skin friction in the liquefied zone was then transferred to the lower end of the pile where liquefaction had not developed. This additional load was carried by skin friction which had yet to be fully mobilized in this somewhat denser sand. At this stage in the test, the ground around the pile had settled over 100 mm while the pile itself had settled 7 millimeters. The settlement of the pile developed due to the loss of skin friction on the pile in the liquefied zone and this movement mobilized the skin friction in the bottom segment of the pile and some additional end-bearing. For example, at the base of the liquefied zone the load in the pile became approximately 130 kN higher shortly after blasting.

Once excess pore pressure had dissipated and settlement stopped, the load versus depth curve in the previously liquefied zone developed a negative slope as shown in Figure 6.45. The negative slope indicates that negative skin friction had developed in this zone and was applying dragload on the pile.

The unit side resistance (skin friction) developed by the pile within the liquefied zone immediately before blasting is compared with the skin friction at the end of settlement in Table 6.11. The measured values of skin friction were calculated by

dividing the difference between the loads at 6.6 m and 12.7 m depth by the surface area of the pile between these two depths. Reviewing the values in Table 6.11, it can be seen that the negative skin friction at the end of settlement is equal to 53% of the positive skin friction developed just before blasting. This is a notable difference from the first blast test, where the negative skin friction developed after blasting was essentially equal to the positive skin friction before blasting. Possible explanations are discussed subsequently.

Values of skin friction within the liquefied zone predicted by the LCPC and Eslami and Fellenius methods are also included in Table 6.11 for comparison purposes. Here we see that the LCPC method produced a predicted value 7.5% lower than the skin friction measured just before blasting. Additionally, the Eslami and Fellenius method predicted a value that was almost 17% higher than the measured value.

Table 6.11. Comparison of unit side resistance values within the liquefied zone measured immediately before blasting and at the end of settlement with values predicted by the LCPC and Eslami and Fellenius methods.

	Just before blasting	End of settlement	LCPC	Eslami and Fellenius
Skin Friction 6 - 13 m depth (kPa)	26.6	-14.3	24.6	31.1

6.6.5 Absence of Downdrag in Upper “Crust”

Although the ground settled more than 270 mm by the end of settlement, the strain gauges do not indicate that any dragload developed in the soil above the liquefied zone. In fact, the load transfer curve at the end of ground settlement is almost identical to that immediately before blasting.

The lack of dragload in the upper 6 m of soil was an unexpected phenomenon. Instead, it was expected that dragload would develop, not only in the liquefied zone, but also in the upper non-liquefied crust. The causes behind this unexpected result are not readily apparent. However, some clues do exist.

A review of Figure 6.44 shows that the load applied to the pile by the hydraulic jacks did not remain constant. The test design called for the applied load to remain constant after all the explosive charges were detonated. However, the pressure in the hydraulic jacks would slowly bleed off, reducing the applied load as the pile settled. Therefore the hydraulic pump was turned on momentarily to restore the desired load applied to the test pile. This variation in applied load is exhibited by the “saw-tooth” patterns in Figure 8.45. It is possible that the settling ground surface caused downdrag forces on the upper 6 m of the test pile during the times of hydraulic pressure bleed-off. When the hydraulic pump was turned back on to restore pressure, the test pile would settle slightly relative to the soil, reversing the frictional forces on the pile.

Such a relative displacement, however, was not evident in the measured data. On the other hand, according to Bozozuk (1981), a relative settlement of only 5 mm is necessary to completely reverse any negative skin friction present. Though extra measures were taken to ensure accurate settlement measurements, such a small relative displacement would be difficult to detect given the difficulties encountered in measuring settlements as discussed in Section 4.4.1. Certainly, 5 mm of differential settlement is within the 5% error limit placed on the string potentiometers.

Further explanation for the absence of dragload may be found in the phenomenon described by Bozozuk (1981). As mentioned briefly in Section 2.2.1, Bozozuk observed that downdrag was absent in the upper layers of the soil profile of a pile pre-loaded by downdrag.

At the onset of blasting, the applied load dropped almost immediately from approximately 536 kN to approximately 380 kN, a reduction of 156 kN, or 29 percent. Though the hydraulic pump was turned on less than one second after the initiation of blasting, the required load could not be restored until 18 seconds after the start of blasting. Within this 18 second period, the pile settled approximately 7 mm while the ground surface near the pile settled more than 100 mm. This combination of large ground settlement relative to the pile and reduction in load produced conditions similar to those described by Bozozuk (1981). The large ground surface settlement relative to the pile imposed a drag load on the pile while the pile was in a partially unloaded state. Due to the rapidity of the ground settlement, this drag load would have developed in just a few seconds—instantaneously for all practical purposes. As the applied load was restored (relatively slowly compared to the time needed for downdrag to develop), some of the applied load would have been carried by the prestressed pile, allowing the soil around the pile to relax. Had the applied load remained constant throughout the test, the downdrag should have been clearly measured by the strain gauges, producing similarly shaped load distribution in the test pile as that labeled 10-yr. downdrag load shown in Figure 2.3.

Furthermore, it is possible that the variation of the applied load and the relatively frequent reversal of strains within the soil-pile interface disrupted the bonds forming between the soil and the pile. This could have led to decreased side resistance on the pile, causing the negative skin friction measured during the second test to be approximately half of the positive skin friction.

6.7 Post-Blast Site Characterization

To evaluate potential changes in the sand density due to the blast testing, an additional CPT sounding was performed shortly after the second blast test (July 28, 2006). This CPT sounding was performed within a meter of the CPT sounding performed before blast testing. Plots of the measured cone tip resistance, friction ratio, and pore pressure are provided in Figure 6.46 along with curves from the previous CPT soundings at the site and the interpreted soil profile. A plot of the relative density versus depth was also developed using Equation 2 and is compared with the plots from the previous sounding. Despite the fact that significant settlement (>500 mm) had occurred, there are only minor increases in the tip resistance and relative density. The lack of any increase in density may be attributed to damage to the soil structure due to blasting, which might not have been recovered at this point.

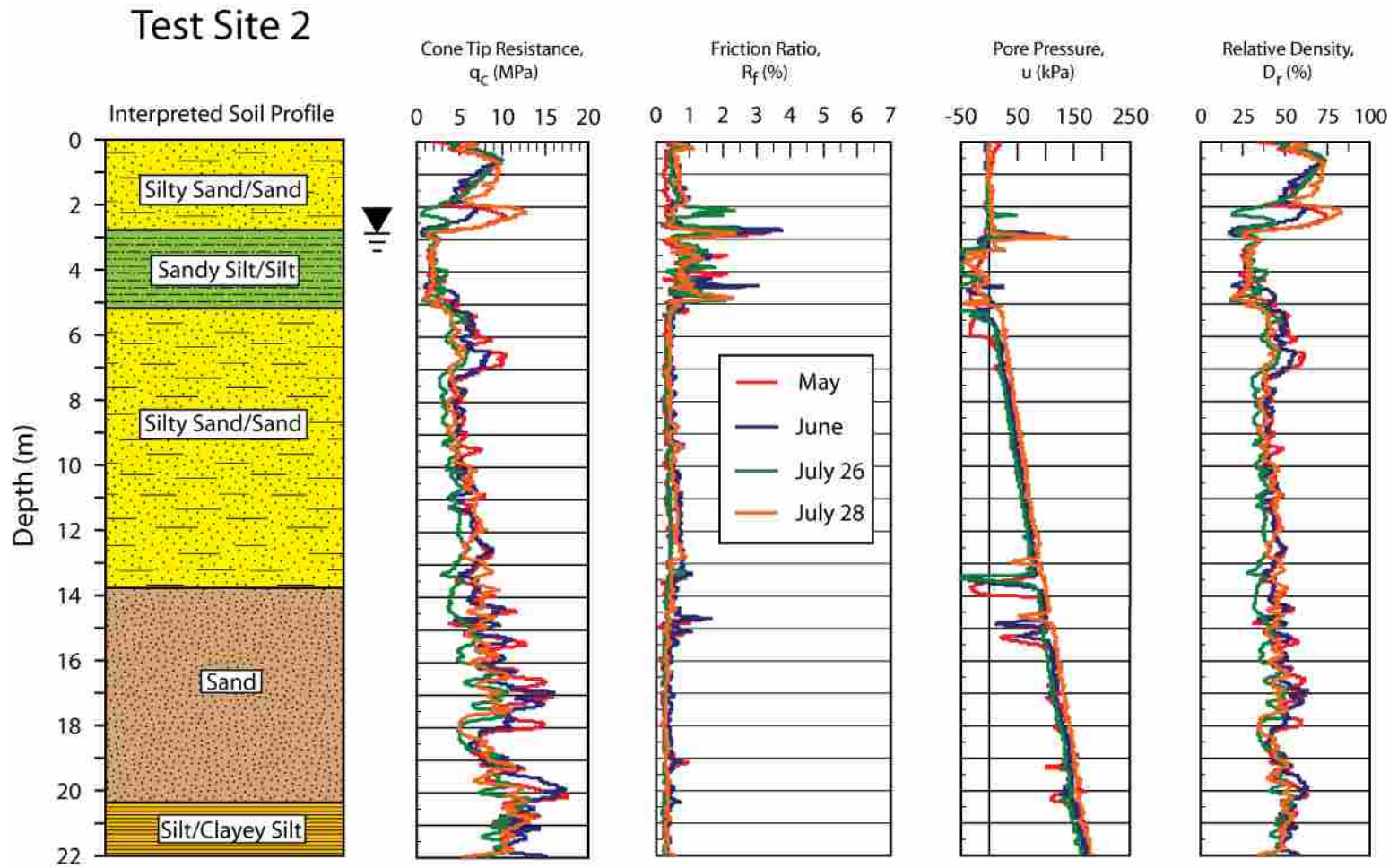


Figure 6.46 Comparison of CPT data for all soundings performed at Site 2.

7 Earthquake Drains

As mentioned in the introduction, one of the major objectives of this study was to evaluate the effectiveness of EQ drains in preventing liquefaction. Presumably the EQ drains would be able to dissipate the excess pore pressure quickly enough to prevent liquefaction. Drains were installed at Site 3 for full-scale blast testing and Site 2 remained untreated to act as the control. Liquefaction was induced at both sites using the same size and number of explosive charges. The time-rate of excess pore pressure dissipation at each site was then compared to determine the effectiveness of the EQ drains.

7.1 Drain Properties

The EQ drains used in this study consisted of corrugated, perforated drain pipe covered by a geosynthetic sleeve. The drain pipe used in the test had an inner diameter of 102 mm and an outer diameter of 121 mm, with corrugations 9.5 mm deep. The flow area was 81.7 cm². Three 25-mm-long slots were cut into each corrugation producing an orifice area of 40.2 cm²/m of length (see Figure 7.1). Each drain was cut to a length of 12.8 m before installation and a hemispherical cap was fitted to the bottom end of each drain to prevent sand from plugging the end of the drain.



Figure 7.1 Section of EQ Drain; light suspended on the inside illuminates the slots (after Rollins and Anderson, 2002).

Each length of drain pipe (with end cap) was slipped into a sleeve of geosynthetic fabric (model SB-252) manufactured by Synthetic Industries. The geosynthetic fabric was a polypropylene spunbond material with an apparent opening size of 50 microns. The grab tensile strength determined according to ASTM D-4632 was 178 N in the machine direction and 222 N in the cross machine direction.

7.2 Drain Installation

Between May 9 and 11, 2005, 35 earthquake drains were installed to a depth of 12.8 m using the same procedures as used to install the blast holes (see Section 4.2). Rather than the smooth mandrel, the finned mandrel (with 25-mm-thick walls) was used to install the drains (see Figure 4.3). The fins were designed to maximize energy transfer

into the soil, helping to consolidate the soil around the drain. The drains were installed in a triangular pattern at 1.22 m on center (see Figure 7.2).

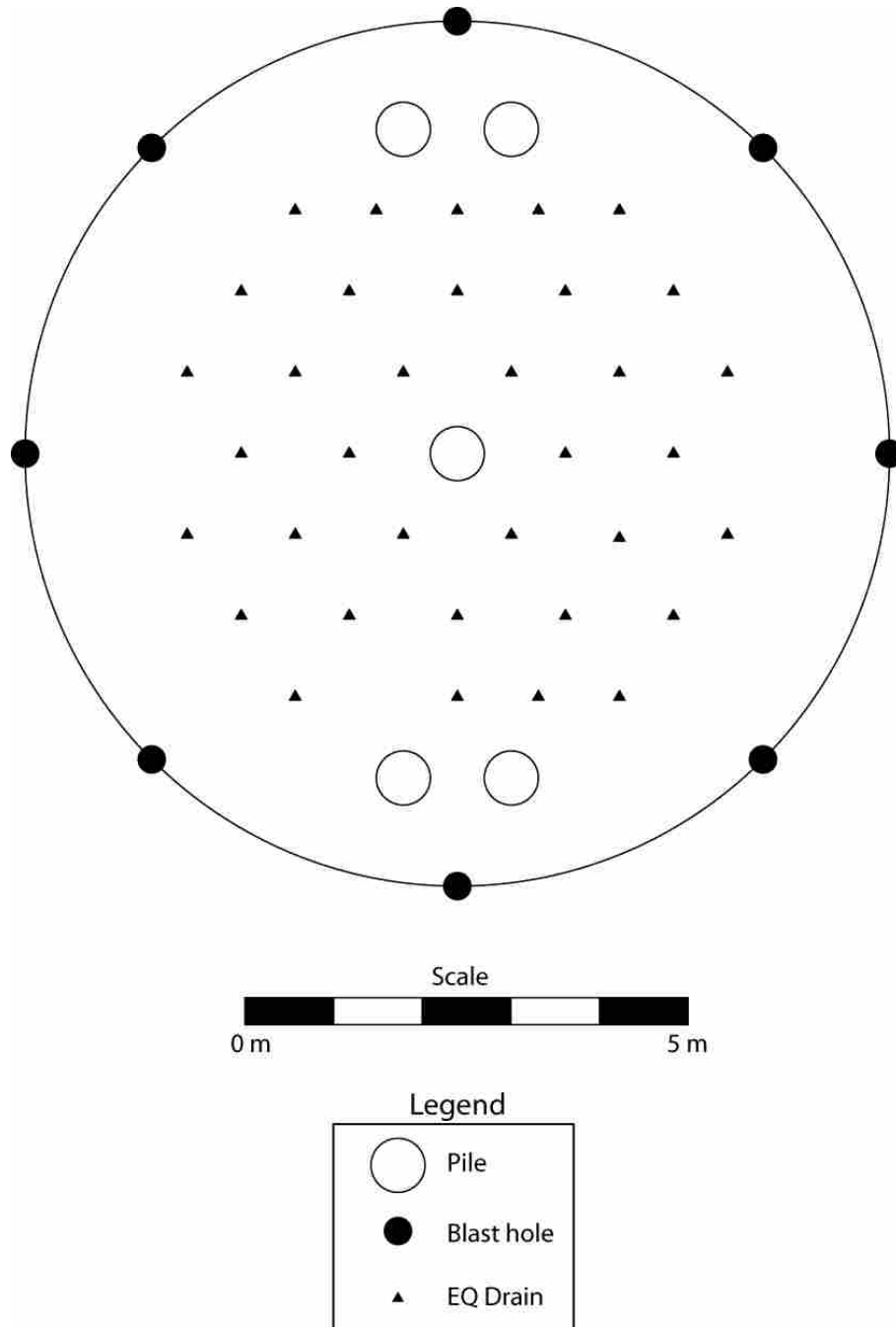


Figure 7.2 Layout of EQ drains at Site 3.

7.3 Drain Installation and Influence on Surrounding Soil

Inasmuch as the EQ drains are designed to mitigate against liquefaction in real-world use, it is probable that they would be used in conjunction with other anti-liquefaction measures. Accordingly, the drains were installed using a finned mandrel that caused soil densification during drain installation.

To evaluate changes in the sand density due to earthquake drain installation, ground settlement was measured approximately one month after installation (June 6, 2005) and an additional CPT sounding was performed at that same time.

A contour plot of the drain installation induced settlement is presented in Figure 7.3. The edge of the drain field was about 3 m from the center of the test area. At one location near the center of the test area, the settlement measured over 300 mm; however the average settlement within the treated area was approximately 200 millimeters. If it is assumed that this settlement was uniformly distributed along the length of the drain (13.7 m) then the average volumetric strain produced by installation would be approximately 1.5 percent. However, if the settlement is assumed to occur only within the liquefiable zone from 6 m to 13 m, then the average volumetric strain would be 2.9 percent.

A plot of the average settlement versus distance from the center of the test area is provided in Figure 7.4. The settlement within about 3 m of the center is relatively constant and would likely be representative of what would be expected after treatment of a large area with drains. Beyond 3 m, the settlement decreased significantly and was less than 3 mm beyond a distance of about 9 m from the center of the test.

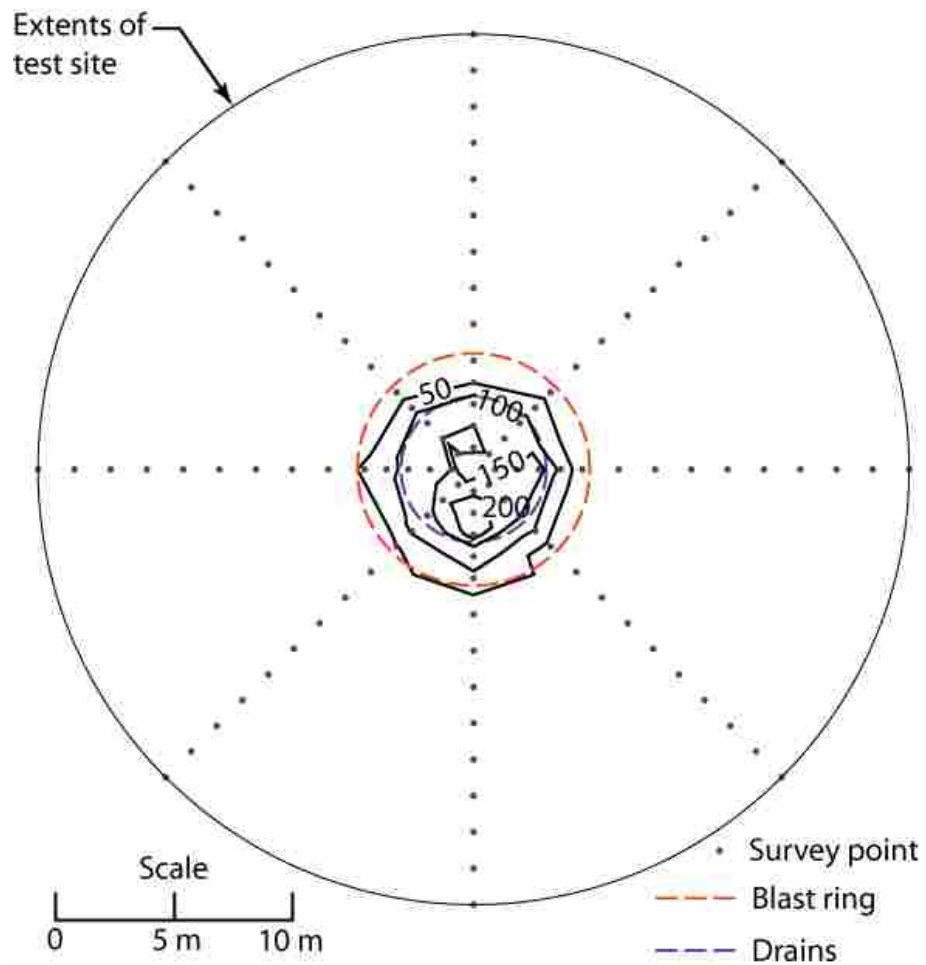


Figure 7.3 Contour plot of ground surface settlement caused by installation of earthquake drains at Site 3.

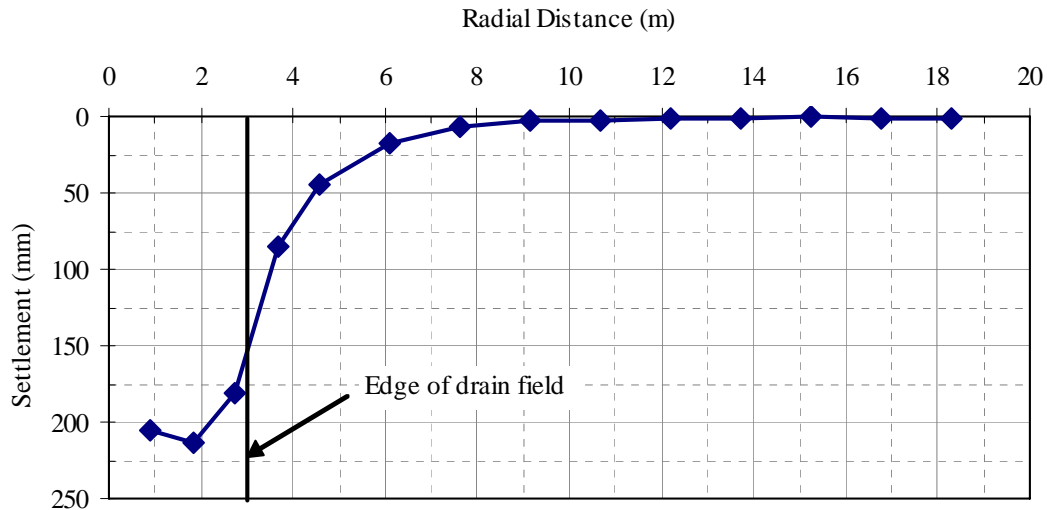


Figure 7.4 Average settlement versus distance curve caused by installation of EQ drains and blast holes at Site 3.

A CPT sounding after blast hole installation was performed within a meter of the original CPT sounding. Plots of the measured cone tip resistance, friction ratio, and pore pressure are provided in Figure 7.5 along with average curves from the previous CPT sounding at the site and the interpreted soil profile. A plot of the relative density versus depth was also developed using Equation 2 and is compared with the average plot from the previous sounding. Despite the fact that settlement occurred and clearly produced increased density in the liquefiable layer, there was no consistent increase in tip resistance, friction ratio or relative density. Apparently the disruption to the structure of the sand produced by the drain installation process decreased the penetration resistance more than the increased density increased the penetration resistance.

Test Site 3

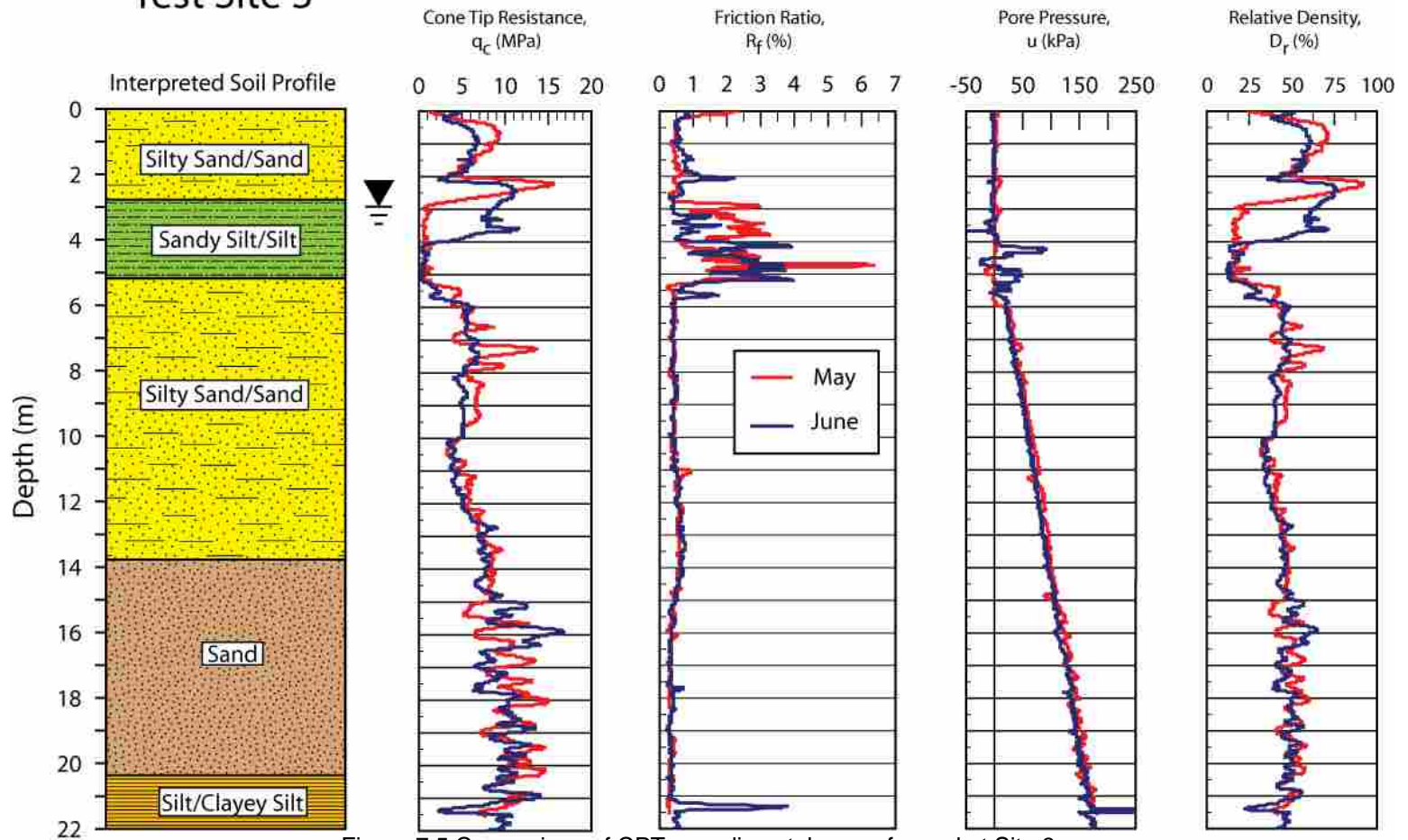


Figure 7.5 Comparison of CPT soundings taken performed at Site 3.

The finned mandrel caused localized settlement to occur within a circular area approximately 280 mm in diameter concentric about the center of each drain (see Figure 7.6). Settlement in this zone could approach 300 mm or more relative to the surrounding ground surface. It appears that the vibration of the mandrel as it was removed caused the surrounding soil to compact in a localized manner around the drains, producing this settlement.



Figure 7.6 View of localized settlement surrounding an EQ Drain. Localized settlement immediately surrounding the drains commonly exceeded 300 mm.

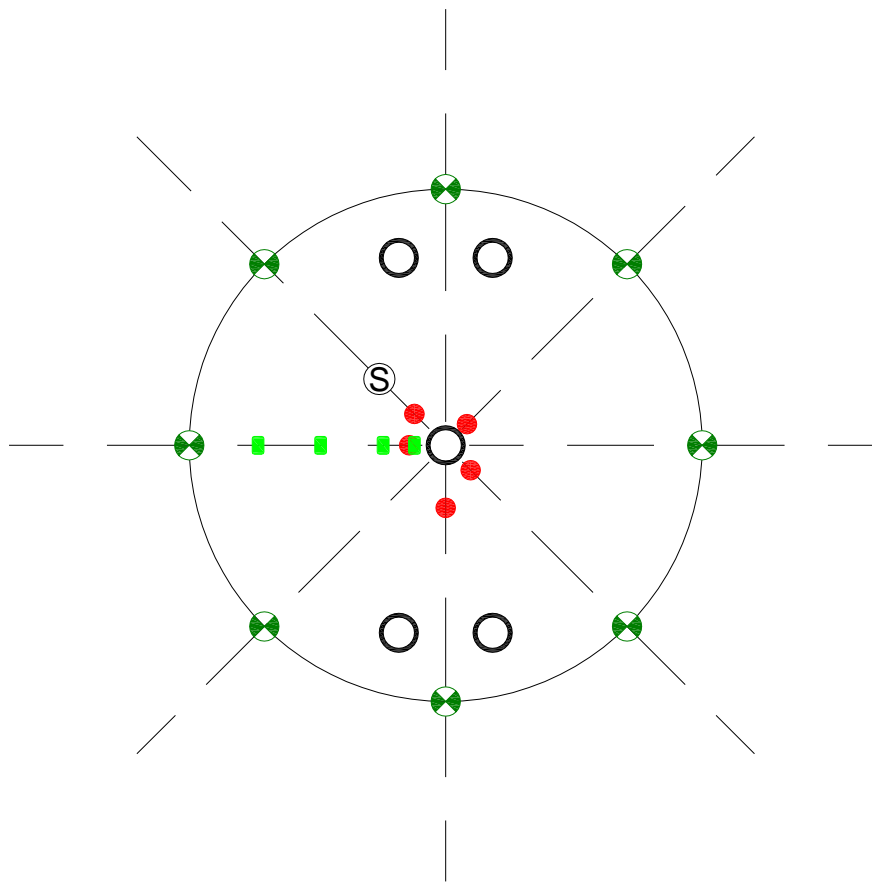
8 Site 3—Treated Area Pile Testing

8.1 Test Layout and Instrumentation

Plan and profile views of the layout of the test pile relative to the blast holes and instrumentation are shown in Figure 8.1 and Figure 8.2 respectively. Once again, the test pile was a 324-mm-dia. steel pipe pile with a 9.5 mm wall thickness and was driven closed-ended to a depth of 21.3 m (see Figure 8.2). The test pile was instrumented with strain gauges at 1.5 m intervals from the ground surface to a depth of 17.3 m (Figure 8.2).

The test pile was located at the center of the ring of blast holes having a radius of 4.9 m. One set of eight blast holes were distributed equally around the circumference of the ring. In each blast hole, blast charges weighting 1.35 kg each were located at depths of 6.4 m and 8.5 m below the ground surface as shown in Figure 8.2. This blasting pattern is identical to that for the second blast at Site 2.

Prior to driving the test pile, 34 earthquake drains were installed to a depth of about 12.8 m as shown in Figure 8.2. As described in Section 7.1 the drains had an outside diameter of 121 mm and were surrounded by a filter fabric sock to prevent infiltration of sand. The drains were installed in an equilateral triangle pattern with a spacing of 1.22 m center-to-center (see Figure 7.2).



- Piezometer
- ⊗ Blast hole
- Ⓢ Sondex tube
- String potentiometer
- Pile
- — Survey ray

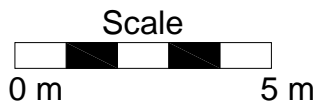


Figure 8.1 Plan view of pile foundation and instrumentation at at Site 3.

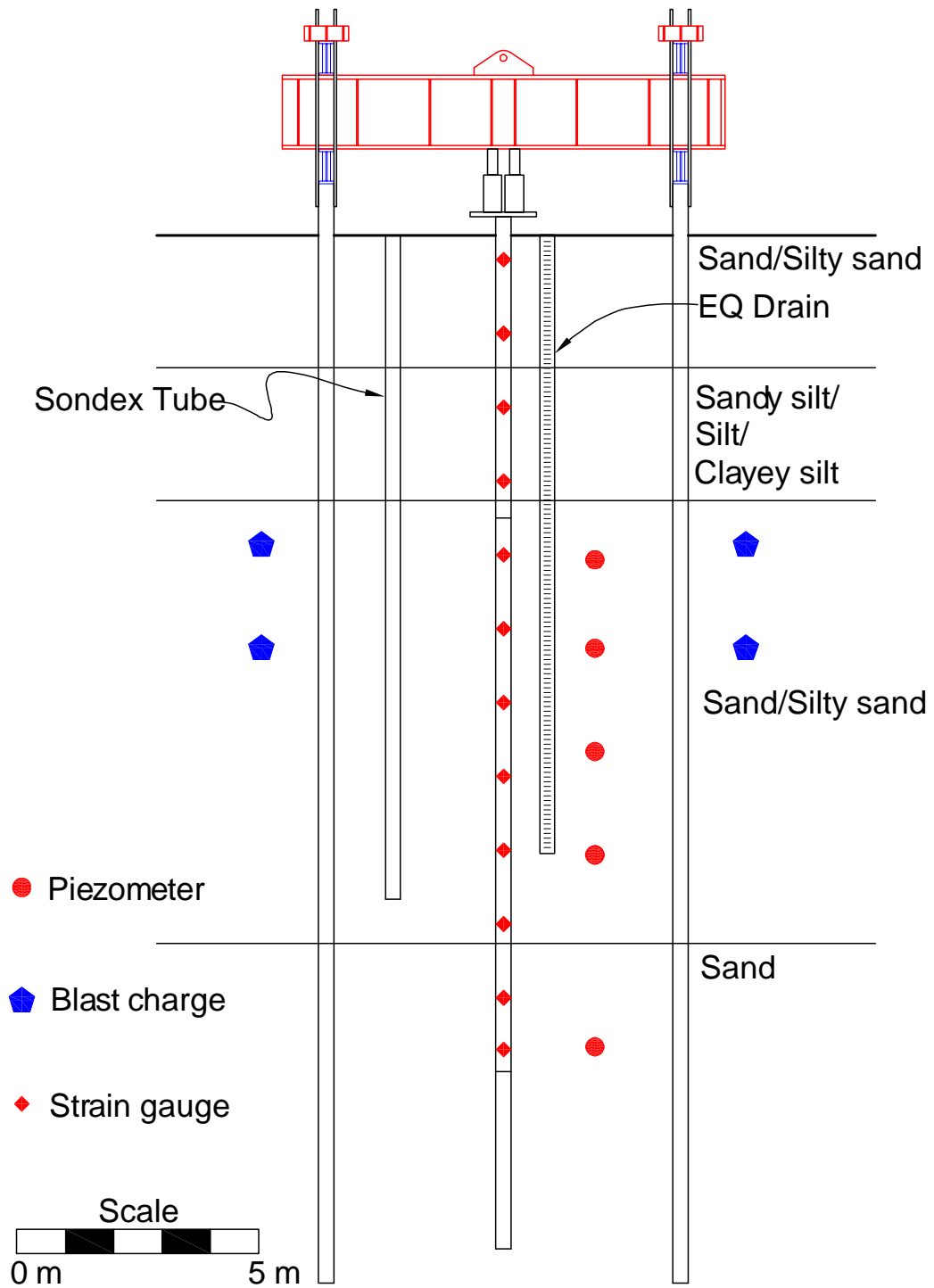


Figure 8.2 Profile view of pile foundation and instrumentation layout at Site 3.

Load was applied to a thick steel plate tack welded to the test pile using two 1,300 kN jacks which reacted against a deep steel beam (see Figure 5.10 and Figure 8.2). The arrangement of the reaction pile and load frame was identical to that described for the pile load test at Site 2. The load applied by each jack was measured by a load cell. The vertical displacement of the pile was measured using two string potentiometers attached to a tensioned cable which was positioned across the site. The cable was anchored at a distance of about 20 m from the center of test area so that it would not be affected by settlement produced by the blast liquefaction.

Settlement of the ground surface was monitored using a survey array as described in Section 4.4.1. The elevation of these survey markers was determined with a level survey prior to any construction at the site. Subsequent level surveys were used to evaluate settlement due to blast hole installation and pile installation, as well as blast testing. In addition to the conventional level surveys, surface settlement was also monitored as a function of time after blasting using an array of vertical string potentiometers attached to the tensioned cable running above the ground surface at the site. The string potentiometers were located at distances of 0.61, 1.22, 1.83 and 2.44 m from the center of the test area. Finally, the settlement as a function of depth was monitored using a Sondex settlement tube located at 1.83 m from the center of the test area as shown in Figure 8.1.

The generation and dissipation of excess pore pressure during the blasting process was monitored using five piezometers installed at depths of 6.7, 8.4, 10.7, 12.8 and

16.8 m below the ground surface as shown in Figure 8.2. The piezometers were typically located about 0.75 m from the center of the test pile.

8.2 Pile Installation and Influence on Surrounding Soil

The test pile and four reaction piles were driven at this test site between June 7 and 10, 2005. To evaluate potential changes in the sand density due to pile driving, the settlement was measured approximately one month after installation (July 25, 2005) and an additional CPT sounding was performed the next day (July 26, 2005). The maximum settlement was approximately 130 mm which occurred in between the two northern reaction piles (see Figure 8.1). In general settlement was less than 50 mm within a circular area 4 m in diameter centered about the test pile. Outside that area, settlement was less than 9 millimeters. These results suggest that relatively little change in sand density was produced by the installation of the piles.

The cone sounding after blast hole installation was performed within a meter of the original CPT sounding. Plots of the measured cone tip resistance, friction ratio, and pore pressure are provided in Figure 8.3 along with average curves from the previous two CPT soundings at the site and the interpreted soil profile. A plot of the relative density versus depth was also developed using Equation 2 and is compared with the average plot from the previous two soundings. Although there are some increases between 9 and 11 m depth, there is no indication that there was any significant overall increase or decrease in tip resistance, friction ratio, or relative density. The observed variations are likely due to natural variations in deposition and composition of the sand layers.

Test Site 3

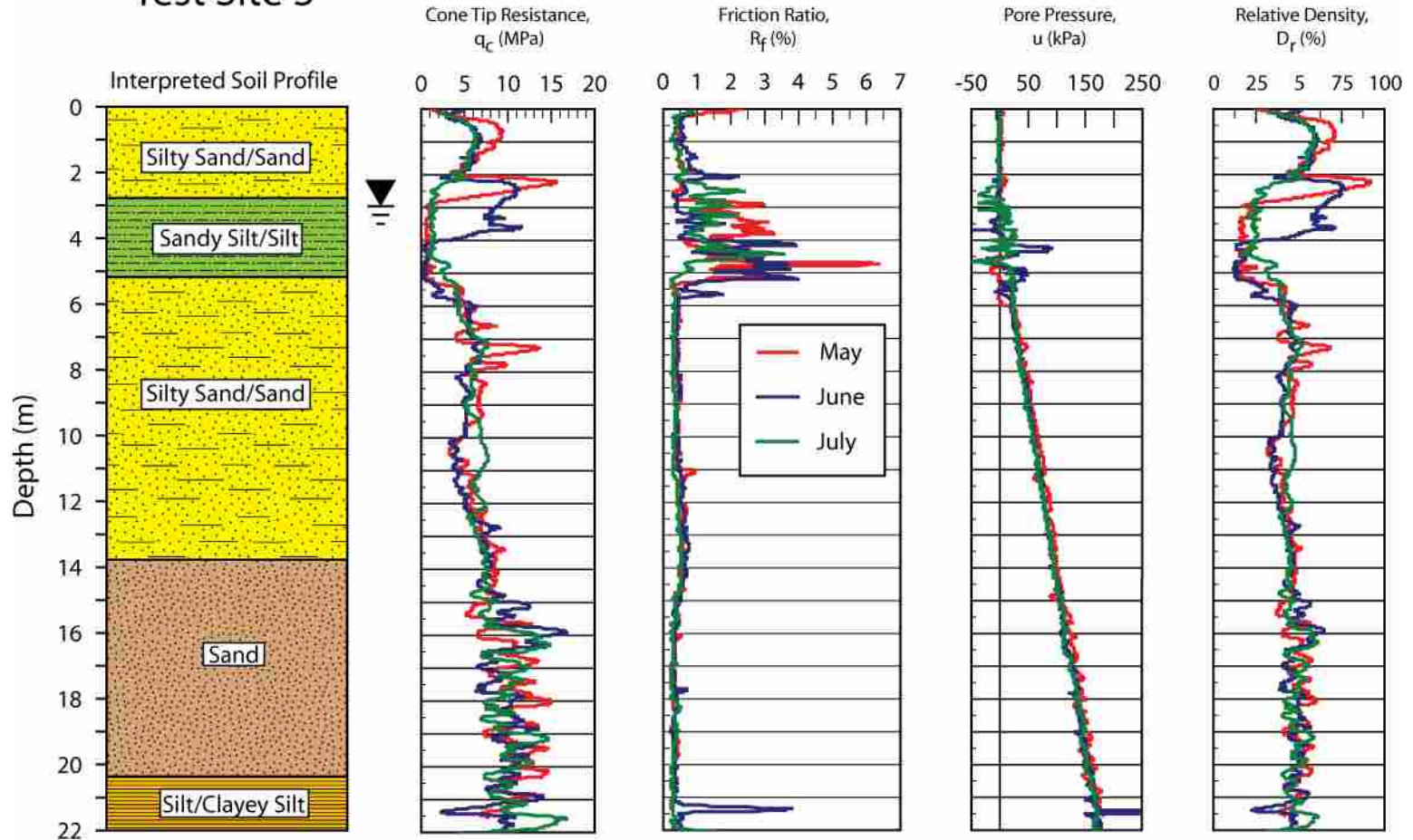


Figure 8.3 Comparison of CPT results from Site 3.

8.3 Pile Load Testing Prior to Blasting

Prior to blasting, two axial load tests were performed at Site 3 using the same procedure employed at Site 2 and described previously in Section 6.4. In contrast to the static load testing at Site 2, where the first test was performed less than one day after driving, the load testing at Site 3 was performed on July 28, 2005, approximately one and a half months after pile installation and two and a half months after drain installation. The second test was performed about one hour after the first test.

The first load test was continued until the pile began to plunge and the maximum settlement reached 69 mm, similar to the deflection reached during the first test at Site 2 (67 mm). The residual displacement at the end of this initial load test was 62 mm. The strain measurements at the end of the load test indicated that residual strain in the pile following the load test was very minor.

A plot of the applied pile head load versus pile head deflection for the two tests is provided in Figure 8.4. Based on the Davisson criteria, the failure load was 955 kN for the first test and 990 kN for the second test, a difference of only 3.5% (because the Davisson slope-offset line did not intersect the load-deflection curve from the second test, the failure load was approximated). This good agreement between the two test suggests that reloading had relatively little effect on the measured pile load capacity

By comparison, the failure load for the test pile at Site 2 was 650 kN for the first test (performed one day after pile driving) and 1030 kN for the second test (performed one and a half months after pile driving). The differences in failure load between the two sites is 32% for the first tests and only 4% for the second tests. The discrepancy in the

failure loads for the first two tests appears to be due to setup of the soil. The agreement for the second set of tests is very good and suggests that the two piles can be used for comparative studies.

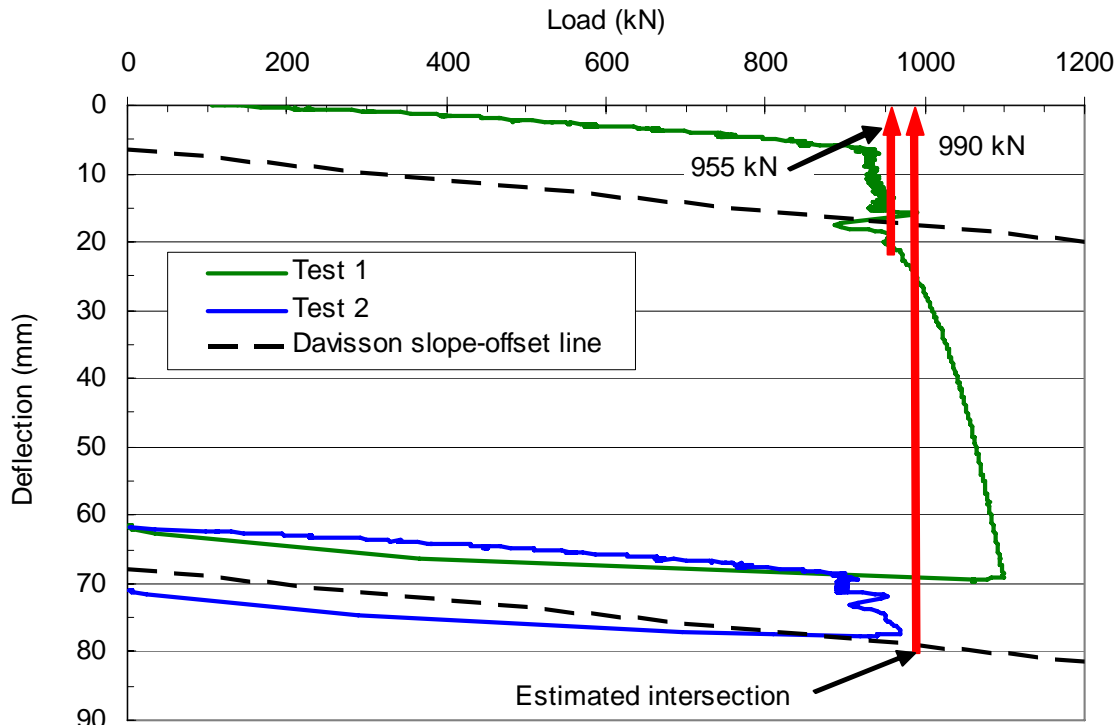


Figure 8.4 Pile-head-load versus pile-head-deflection curves from the two static axial load tests performed on the test pile at Site 3.

A comparison of the load versus deflection curves for two pile tests at Sites 2 and 3 is provided in Figure 8.5. The pile capacities for the first and second tests conducted Site 3 are generally quite consistent with each other and with the capacity for the second test at Site 2. These results suggest that the increased resistance after one month relative to one day after pile driving is a result of reconsolidation and redevelopment of the sand structure. This phenomenon is commonly referred to as setup.

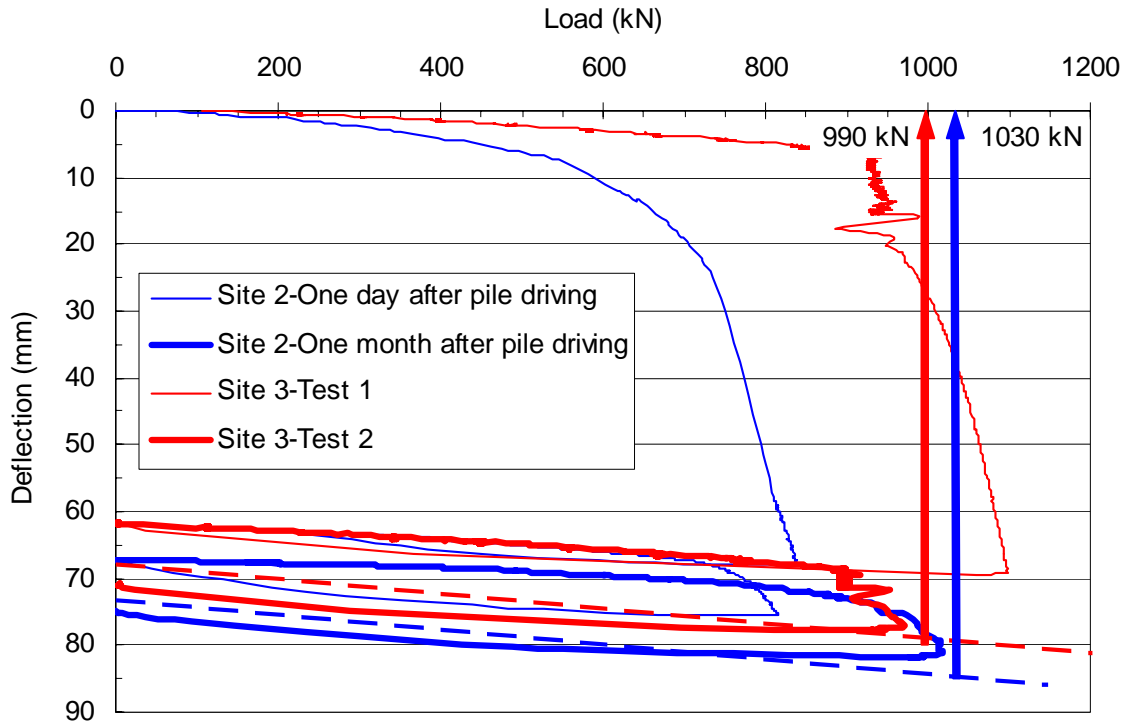


Figure 8.5 Comparison of pile-head-load versus pile-head-deflection curves for all static load tests performed at Sites 2 and 3.

8.3.1 Load transfer

Based on the strain gauge data, the load in the pile during the first static test was plotted as a function of depth for a number of load increments as shown in Figure 8.6. A similar plot was produced for the second static load test and is plotted in Figure 8.7.

As can be seen, the load-depth curves from both static load tests are quite similar, indicating that the load transfer was similar in both tests. T-Z curves were also developed for both static load tests as was done for the tests at Site 2 (refer to Sections 6.4.1 and 6.4.2).

Figures 8.8 and 8.9 show the simplified load-depth curves developed from the first and second static load tests performed at Site 3, respectively.

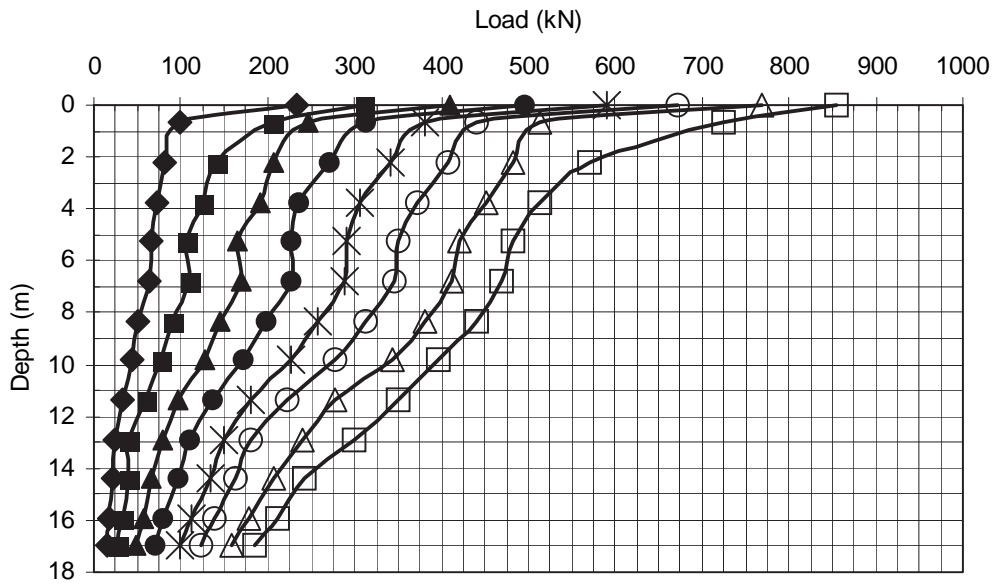


Figure 8.6 Load versus depth curves for the first static load test performed at Site 3.

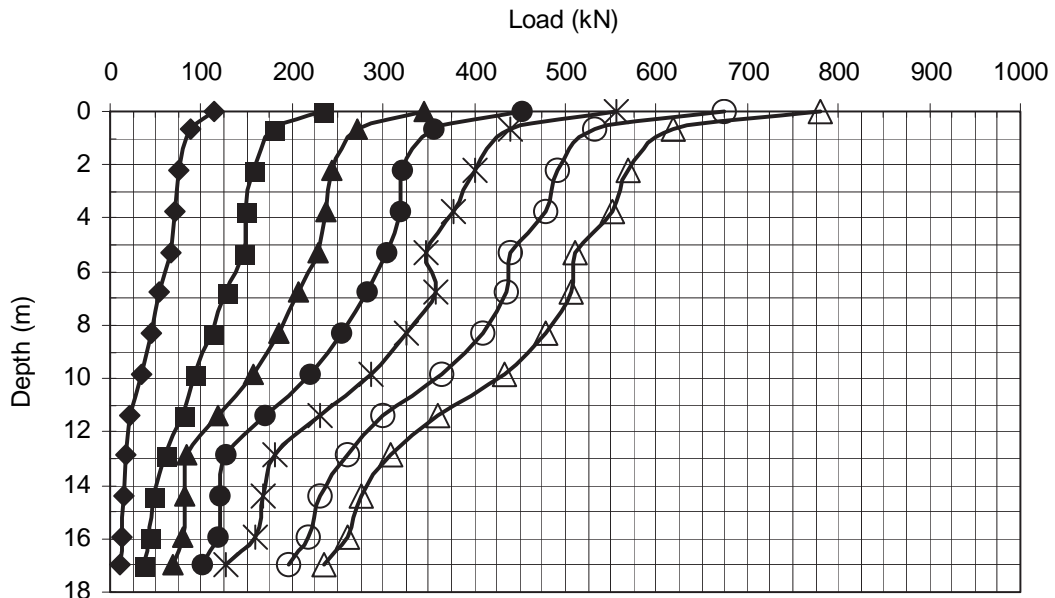


Figure 8.7 Load versus depth curves for the second static load test performed at Site 3.

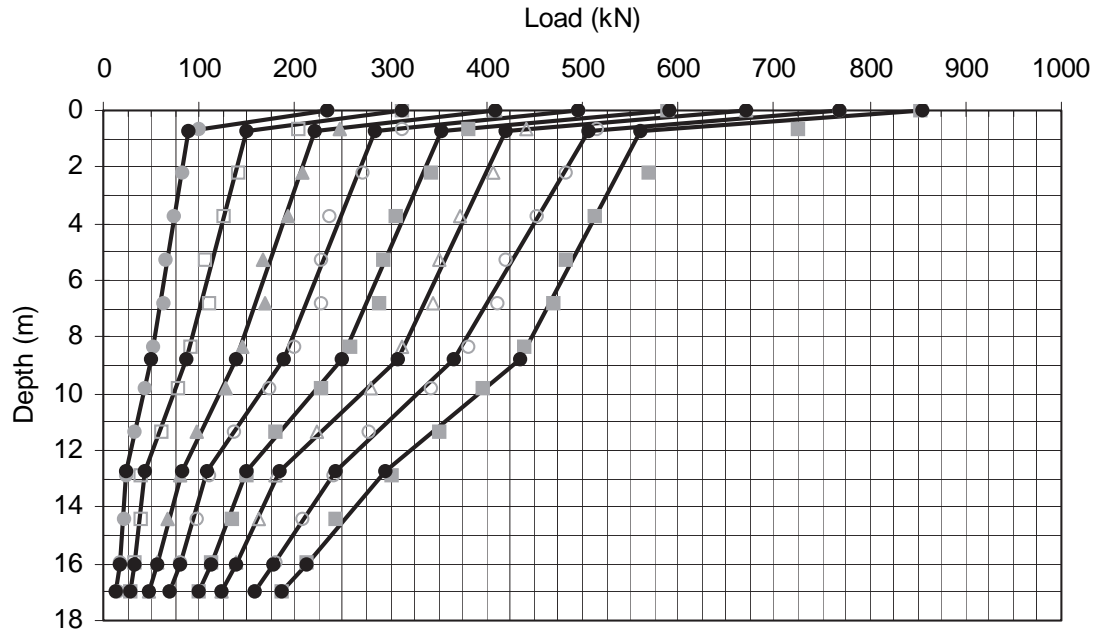


Figure 8.8 Simplified load-depth curves for the first static load test performed at Site 3.

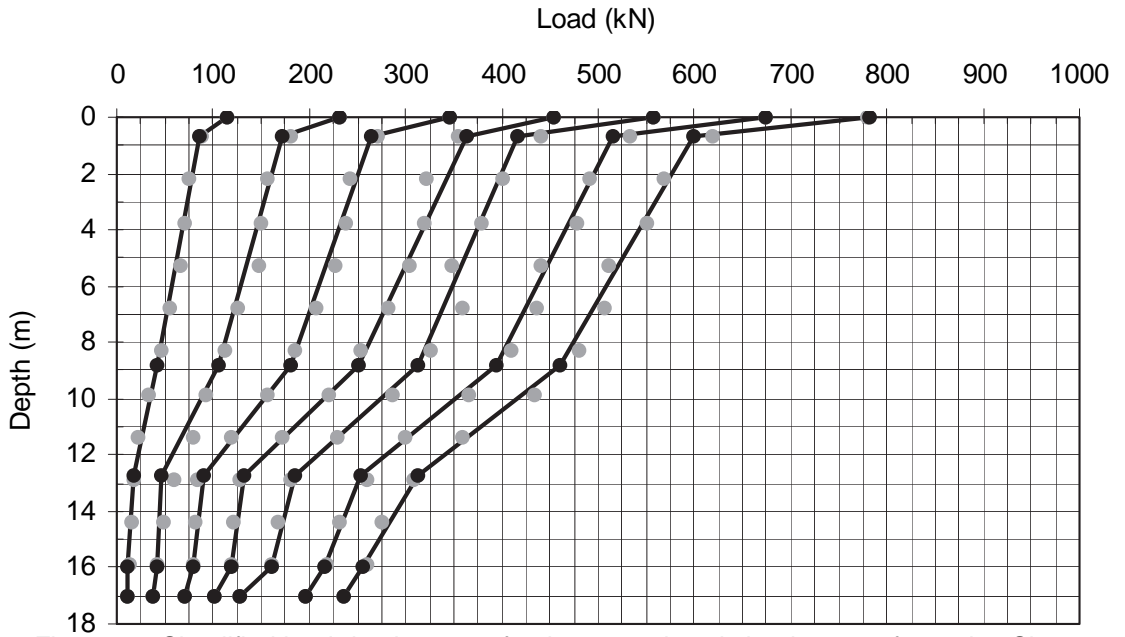


Figure 8.9 Simplified load-depth curves for the second static load test performed at Site 3.

The simplified curves were drawn more or less by eye, using piece-wise linear interpolation to attempt to capture the average trends in the recorded data. As the simplified curves were drawn, five distinct layers defined by the load transfer properties of the soil-pile interface became apparent. Summaries of unit side resistance and pile deflection values determined from the simplified load-depth curves from Site 3 are shown in Tables A7 through A10.

Using the data in Tables A7 through A10, T-Z curves for the first and second tests were drawn and are plotted in Figures 8.10 and 8.11, respectively. As can be seen in both figures, the curves for the interval from 0 to 0.7 m depth is much higher than the curves for the other depth intervals. This is likely due to errors in the data recorded by the strain gauges in the top-most tier.

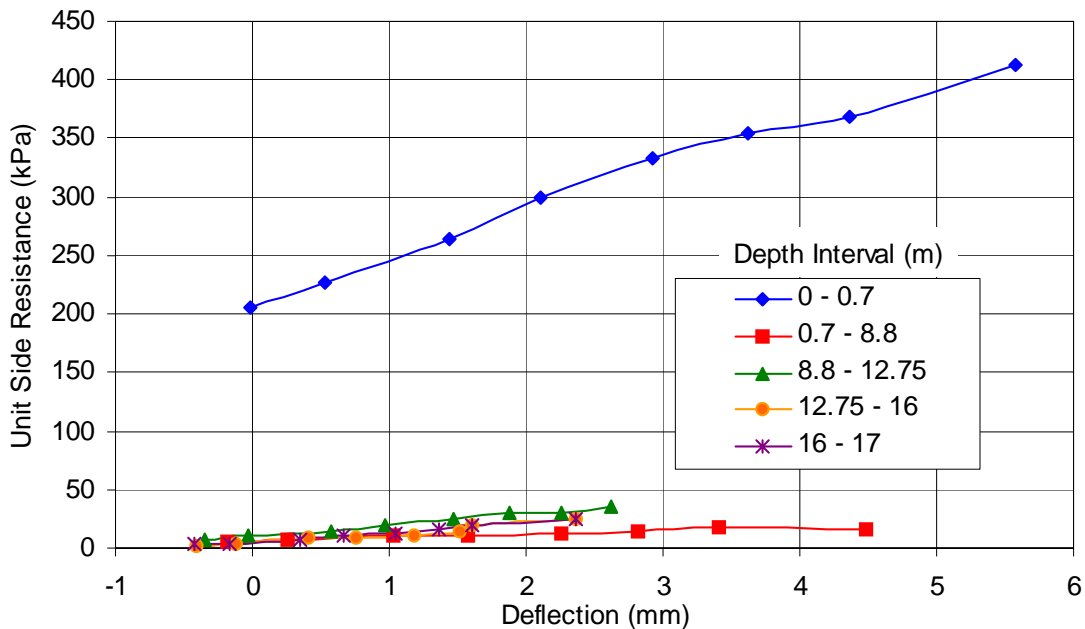


Figure 8.10 T-Z curves developed for the first static load test at Site 3.

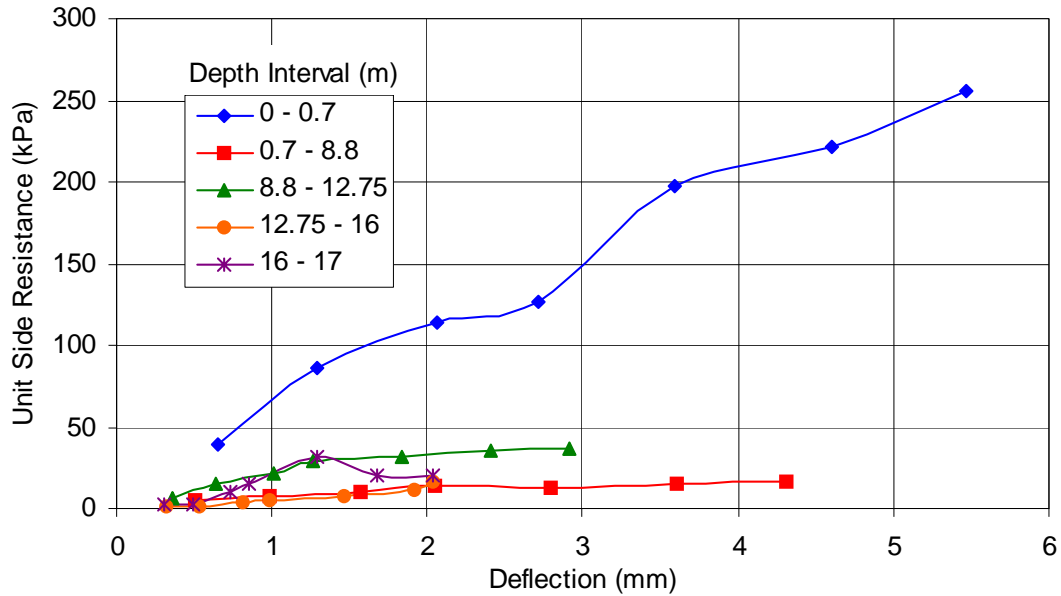


Figure 8.11 T-Z curves developed for the second static load test at Site 3.

The data in Figures 8.10 and 8.11 is re-plotted in Figures 8.12 and 8.13, this time without data from the top depth interval. A review of both figures shows similarities in the response of the pile during both load tests. For instance, the skin friction in each depth interval reaches a maximum at approximately the same deflection in both tests. Furthermore, the relative positions of the curves for each depth interval are similar. The most notable exception is the curve from 16 to 17 m depth, where strain gauge attrition was high, producing very little reliable data.

Comparisons between the T-Z curves developed for Site 3 and those from Site 2 are made difficult by the fact that the depth intervals differ between each site. However, certain similarities and differences are identifiable. For purposes of the present discussion, comparisons made between the two sites will reference Figures 6.23 and 8.13

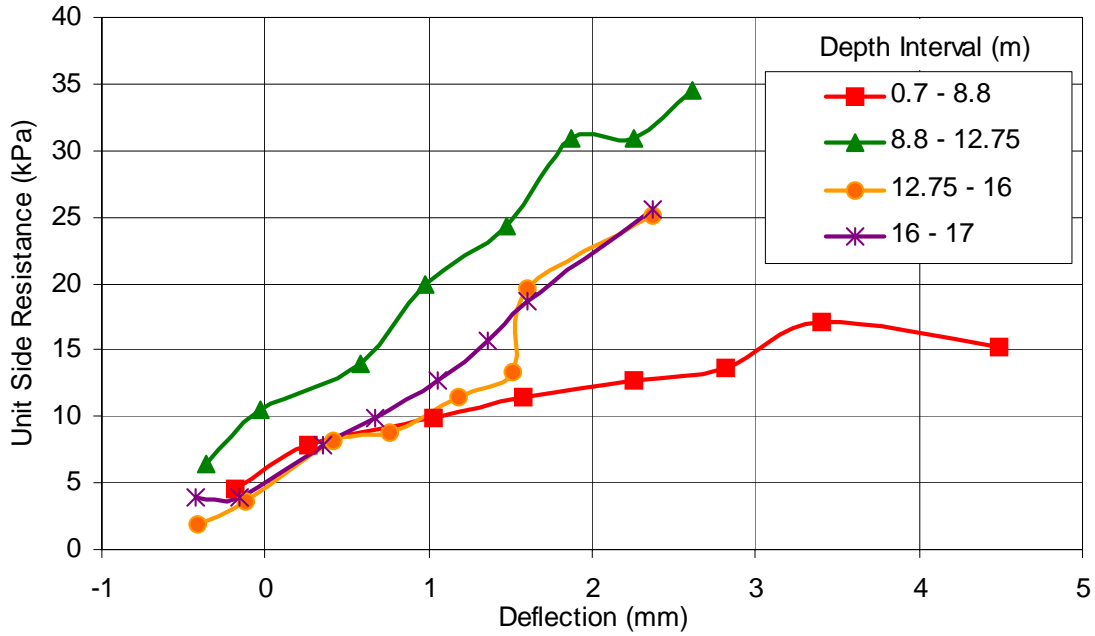


Figure 8.12 T-Z curves developed for the first static load test at Site 3 excluding data from the top depth interval.

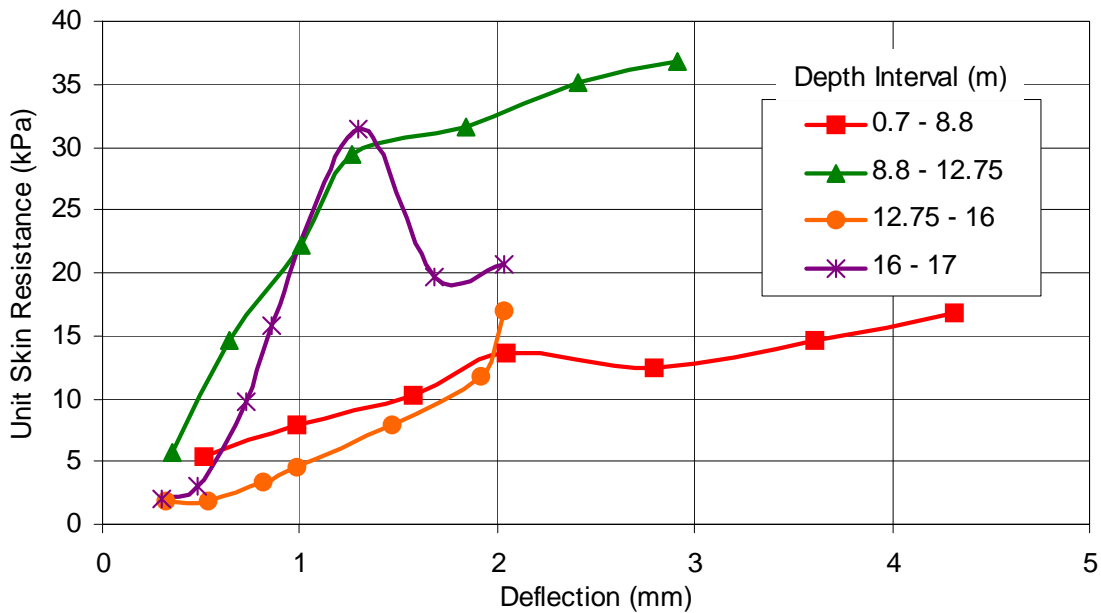


Figure 8.13 T-Z curves developed for the second static load test at Site 3 excluding data from the top depth interval.

The most obvious difference is seen in the top depth interval (from 0.5 to 4.0 m at Site 2 and 0.7 to 8.8 m at Site 3). Whereas at Site 2 the maximum side resistance was about 50 kPa, the maximum side resistance at Site 3 was approximately 17 kPa. The reason for the difference is not obvious, though it is likely attributable to the thickness of the depth intervals used in developing the T-Z curves at the different sites.

Generally, the measured unit side resistance values within the upper two meters were quite large. Deeper layers generally exhibited lower values of unit side resistances. At Site 2, the depth interval used to develop the top T-Z curve was 3.5 m thick, where the depth interval for the top curve at Site 3 was 8.1 m thick. Therefore, the curve from Site 3 would be expected to be lower than the comparable curve from Site 2 due to the lower unit side resistance values found in the deeper portions of the depth interval. However, while the maximum values are different, peak values occurred at approximately the same deflections (~6 mm at Site 2 and ~4.5 mm at Site 3).

Because the depths for the second depth interval at both sites are contained within the other intervals, comparisons will not be made for this interval.

The third depth interval (7.0 to 15.75 m at Site 2 and 12.75 to 16 m at Site 3) shows that similar maximum values occur at similar deflections. At Site 2, the maximum skin friction was approximately 22 kPa whereas the maximum skin friction at Site 3 was approximately 18 kPa. Both maximums occurred at a deflection of 2 millimeters.

8.3.2 Comparison of measured response with predicted response

As was done for the static load tests at Site 2, the pile response measured during static load testing at Site 3 is compared with the response predicted by the LCPC and the Eslami and Fellenius methods (see Section 6.4.4).

8.3.2.1 Comparison of unit side resistance

Comparisons between the predicted and measured unit shear resistance values were made for the two static load tests performed at Site 3, shown in Figure 8.14. The values shown in Figure 8.14 for the two predictive methods are summarized in Table 5.5. The values for the first and second load tests correspond to a peak sustained load of 854 kN and 781 kN, respectively, and are contained in Tables A7 and A8, respectively.

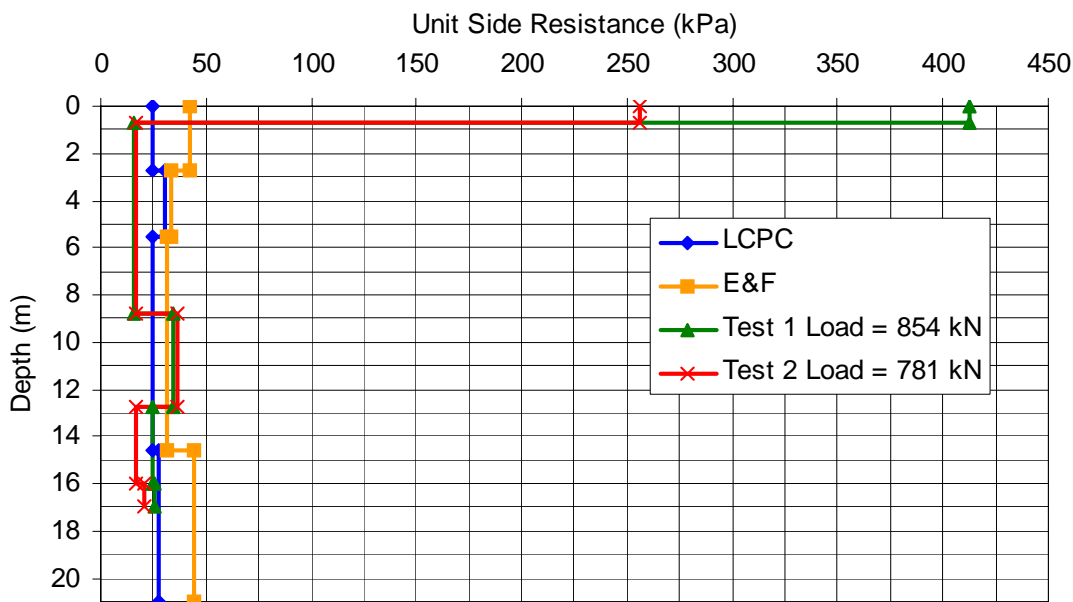


Figure 8.14 Comparison of measured unit side resistance values with those values predicted by the LCPC and Eslami and Fellenius methods.

In order to make comparisons more straight forward, the measured values of unit side resistance were transformed such that the boundaries between strata corresponded with the layer boundaries of the generalized soil profile. Figure 8.15 shows the transformed data in graphical format while Table 8.12 contains a numerical summary.

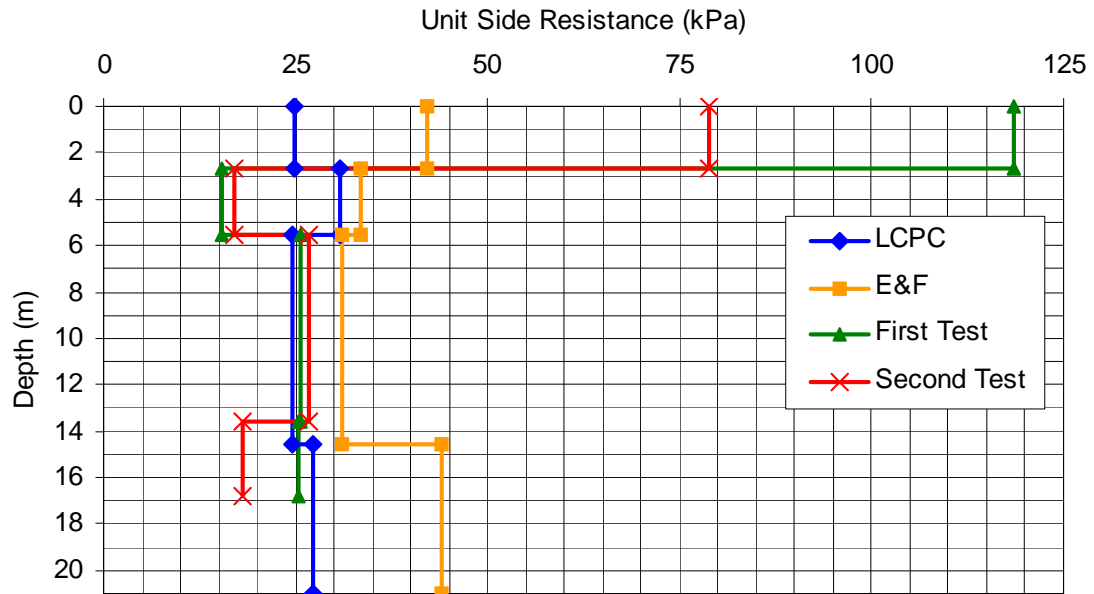


Figure 8.15 Comparison of transformed measured and predicted values of unit side resistance for Site 3.

Table 8.12. Comparison of transformed values of unit side resistance for Site 3.

Depth (m)	Unit Side Resistance (kPa)			
	First Test	Second Test	LCPC	Eslami & Fellenius
0 - 2.7	118.4	78.8	24.9	42.0
2.7 - 5.5	15.3	16.9	30.9	33.5
5.5 - 13.6	25.7	26.6	24.6	31.1
13.6 - 16.8	25.3	18	27.2	44.1

The first difference that will be noticed between the Figures 8.14 and 8.15 is the scale—the very large unit side resistance values in the upper 2.7 m of the soil profile have been dramatically reduced and a smaller scale can be used to show all of the data. Nevertheless, it seems unreasonable that the skin friction in this soil layer (from 0 to 2.7 m) would be so high. The large value is probably due to error in the strain gauge data. As mentioned previously, the reliability of the data from the top tier of strain gauges is suspect, at best.

However, skin friction values from the rest of the profile seem reasonable. Indeed, the measured skin friction within the third layer (from 5.5 to 13.7 m depth), which happens to contain the target zone (from 6 to 13 m depth), compare favorably with the predicted values. The measured skin friction from both test agrees relatively well with the predictive methods. In particular, comparison with the LCPC values (see Table 8.12) produced errors of only 4.5 and 8.1% for the first and second tests, respectively. This also agrees with the unit side resistance measurements made during the second static load test at Site 2 (see Section 6.4.4.1) where the difference between the measured value and that predicted by the LCPC method was less than six percent.

As was done for Site 2, the response of the bottom 3.7 m of the test pile had to be determined before numerical comparisons could be made between the measured response and the predicted response. Figure 8.16 shows the load-depth curves from the largest sustained loads applied during both static load tests performed at Site 3. Table 8.13 tabulates the data contained in Figure 8.16.

In contrast to Site 2, the bottom tier of strain gauges produced reliable data. Thus the response of the bottom of the pile could be determined by extrapolation of the bottom segment of the load-depth curves.

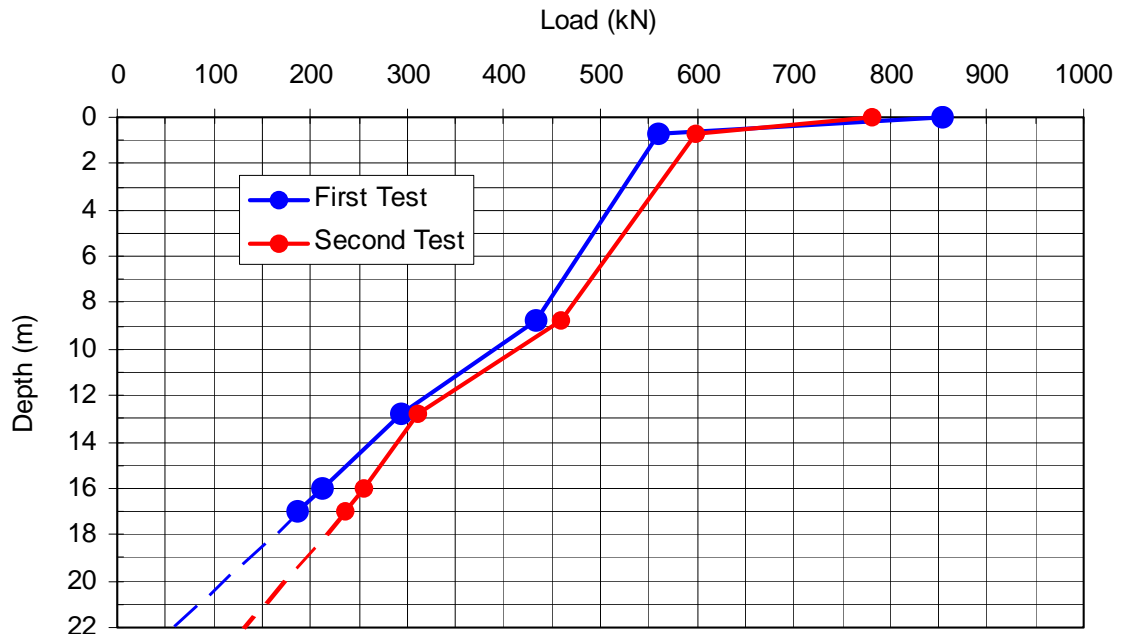


Figure 8.16 Load-depth curves corresponding to the largest sustained loads applied during each of the two static load tests at Site 3.

The difference between total side resistance values measured during the two tests may be related to the timing of the two tests. The first test was performed about one month after the pile was driven. Thus, the soil had a month in which to bond with the pile. On the other hand, the second load test was performed about one hour after the first test. Therefore, the soil had a relatively limited time in which any bonds disrupted during the first load test could reform. It is probable that few of the disrupted bonds could have reformed to their original strength in such a short time. Thus the total side resistance was lower for the second test than for the first.

Table 8.13. Side resistance developed during static load testing at Site 3.

Depth (m)	Unit Side Resistance (kPa)	
	First Test	Second Test
0 - 0.7	413	256
0.7 - 8.8	15.3	16.9
8.8 - 12.75	34.6	36.8
12.75 - 16	25.1	16.9
16 - 17	25.6	20.6
17 - 22	25.6	20.6
Total Side Resistance (kN)	798	651

Referring back to Table 5.5, it is remembered that the LCPC method predicted a total side resistance of 591 kN and the Eslami and Fellenius method predicted a total side resistance of 844 kN. Table 8.13 shows that the best match is between the first test and the Eslami and Fellenius method, with a difference of approximately 6 percent. However, the total side resistance measured during the second test was only 9% different from the value predicted by the LCPC method. The first test was 26% different from the LCPC value and the second test was 30% different from the Eslami and Fellenius value.

8.3.2.2 Comparison of end-bearing

Figure 8.16 indicates that the end-bearing developed during the first and second test was 56 and 179 kN, respectively. Table 8.14 compares the two values of end-bearing calculated above with the values predicted by the LCPC and Eslami and Fellenius methods.

Table 8.14. Comparison of calculated and predicted values of end-bearing.

	End-bearing (kN)	LCPC	Eslami and Fellenius
First Test	56	340	860

The difference between the end-bearing values measured at Site 3 is certainly related to the total side resistance developed during the load testing. For instance, because a relatively large amount of side resistance developed during the first load test, a lesser amount of end-bearing was needed to resist the total applied load. Conversely, a relatively small amount of side resistance developed during the second test, requiring a larger amount of end-bearing to resist the total applied load.

Table 8.14 shows that there was no good agreement between the measured and predicted values of end-bearing. However, the end-bearing measured during the second load test at Site 2 was 178 kN, only 1 kN (less than 1%) different from that measured at Site 3 during the second load test. This excellent agreement may suggest that the true end-bearing than can be reliably developed within this particular soil is approximately 180 kN. If so, both predictive methods produced wildly optimistic results. However, the LCPC method, with its smaller predicted value of end-bearing provides the better match.

8.3.2.3 Comparisons with predictive methods summarized

At both Sites 2 and 3, the Eslami and Fellenius method, with its larger predicted value of total side resisted, produced the best match with the total measured side resistance. In contrast, the LCPC method, with its lower predicted value of end-bearing provided the best match to the measured end-bearing at both sites.

8.4 Blast Test

The blast test at Site 3 was performed 28 July 2005, using a total of 16, 1.36 kg (3 lb) explosive charges, detonated sequentially with a one-second delay between detonations. Charges were located at depths of 6.4 and 8.5 m below the ground surface in each of eight drill holes spaced evenly around a 10-m-dia. circle centered about the test pile. The eight explosive charges at 8.5 m were detonated first followed by the eight charges at 6.4 m. This blasting pattern was identical to that used for the second blast test in the untreated test area at Site 2.

8.4.1 Pre-blast skin friction mobilization

Prior to blast testing, the test pile was loaded to approximately 500 kN using the quick maintained load procedure as discussed in Section 6.4.2. To determine the extent to which the skin friction had been mobilized, the same procedures described in Section 6.6.1 were followed here with a slight variation. At Site 3, both static load tests were performed less than 24 hours before blast testing and the results of both tests were similar. Hence, both static load tests represented the load-transfer properties of the soil-pile interface equally well. Therefore, the largest values of unit side resistance measured for each static load test were averaged together to produce a single set of largest unit side resistance values $\tau_{(\text{max-static})}$. This data set was then transformed onto the generalized soil profile. The simplified load-depth curve representing the conditions existing immediately before blast testing were also transformed onto the generalized soil profile and the results of both transformation were then compared. The results are shown graphically in Figure 8.17 and summarized in Table 8.15.

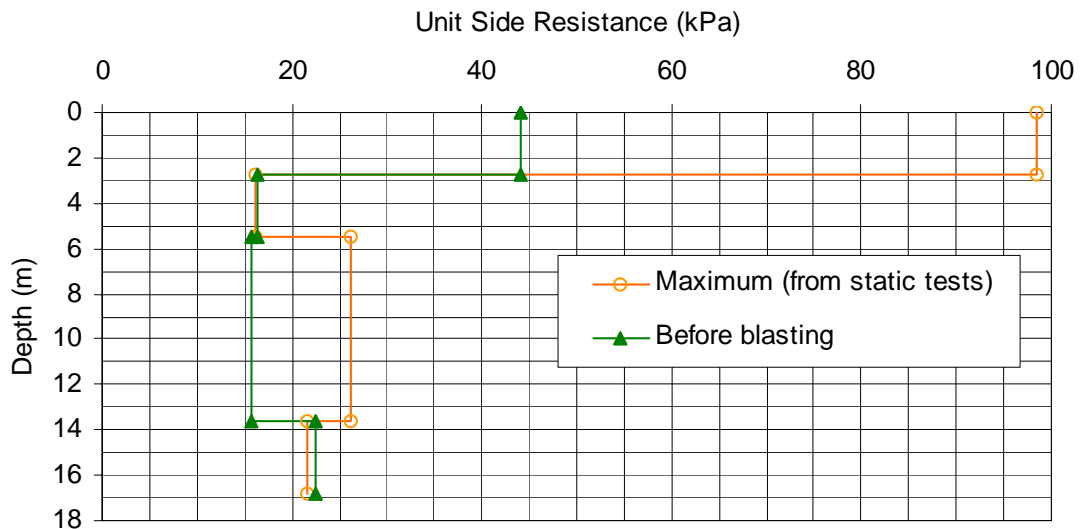


Figure 8.17 Comparison of unit side resistance mobilized immediately prior to blast testing with maximum values at Site 3.

Table 8.15. Summary of unit side resistance, τ , as measured immediately before the second blast test at Site 2 compared with maximum unit side resistance values measured during the second static load test.

Depth Interval (m)	Unit Side Resistance (just before blasting), τ (kPa)	Maximum Unit Side Resistance, $\tau_{(\text{max-static})}$ (kPa)	Percentage of $\tau_{(\text{max-static})}$ (%)
0 - 2.7	44.2	98.6	45
2.7 - 5.5	16.3	16.1	101
5.5 - 13.6	15.8	26.2	60
13.6 - 16.8	22.4	21.6	104
		Average	78

As can be seen in Figure 8.17, skin friction was fully mobilized in both the second and fourth layers in the generalized soil profile. In fact, the mobilized skin friction was slightly greater than the maximum values in both those layers. However, in the first and third layers, mobilized skin friction was only 45 and 60% of the maximum values,

respectively. Overall, 78% of the available skin friction was mobilized prior to blast testing.

8.4.2 Excess pore pressure generation and dissipation

Time histories showing the generation of excess pore pressure ratio for each of the five piezometers during the blast tests at Site 2 (untreated) and Site 3 (treated) are plotted in Figure 8.18 through Figure 8.22. For the piezometers at a depth of about 6.4 m (Figure 8.18), the drains initially reduced the rate of pore pressure generation by about half relative to the untreated site; however, after 16 detonations, the excess pore pressure ratio at Site 3 (the treated site) still reached 90 percent indicating that the soil was essentially liquefied.

A comparison of the piezometers located at 12.5 m depth (Figure 8.21) indicates that the drains were successful in limiting the excess pore pressure ratio to about 0.60 in contrast to the untreated site where liquefaction was produced. This is the location where the rate of pore pressure generation was somewhat smaller than that at the other depths as discussed in Section 6.6. This suggests that the drains can be successful if the load rate is not quite as severe as that produced with the larger charge weights. Furthermore, this indicates that drainage begins at the bottom of the liquefied zone, as shown by Brennan and Madabhushi (2002).

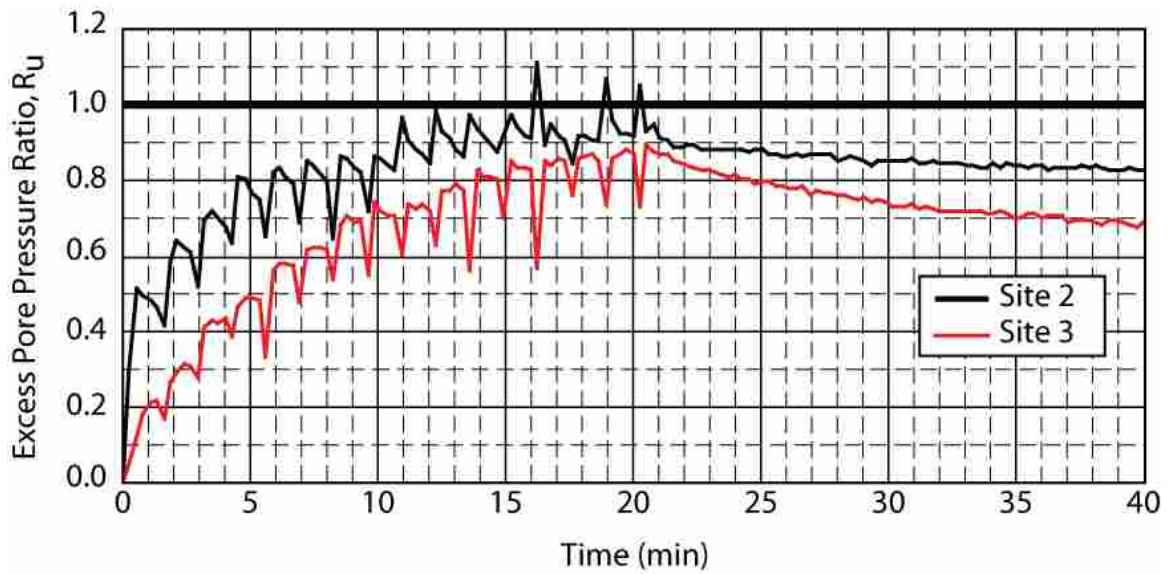


Figure 8.18 Comparison of pore pressure generation at Sites 2 and 3 recorded at 6.7 m and 6.4 m depth. The piezometer at Site 2 was located at 6.6 m and the piezometer at Site 3 was located at 6.4 m depth.

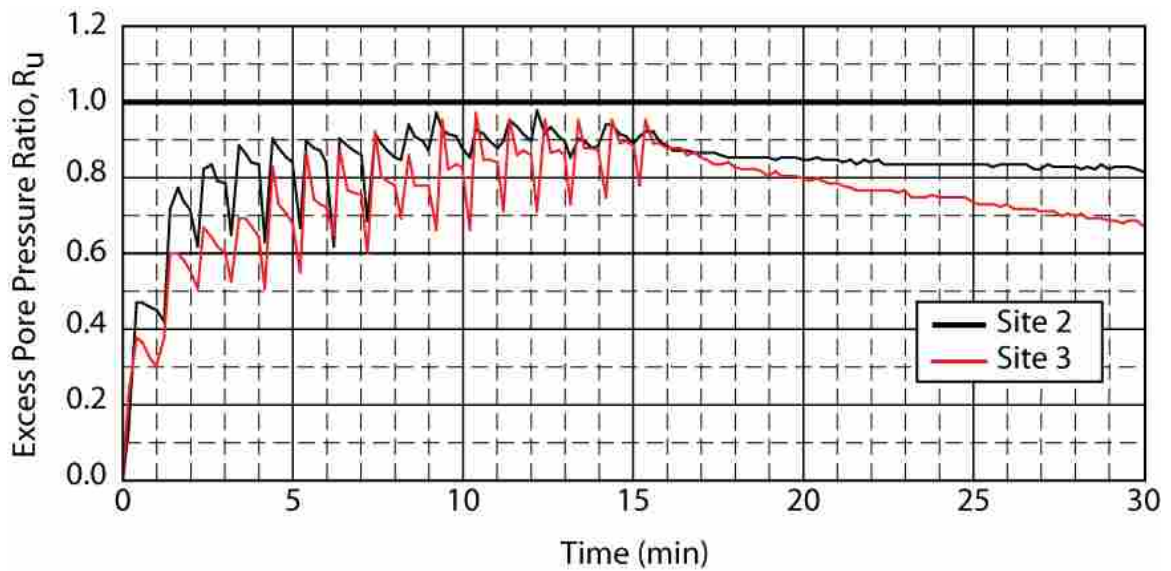


Figure 8.19 Comparison of pore pressure generation at Sites 2 and 3 recorded at 8.5 m depth.

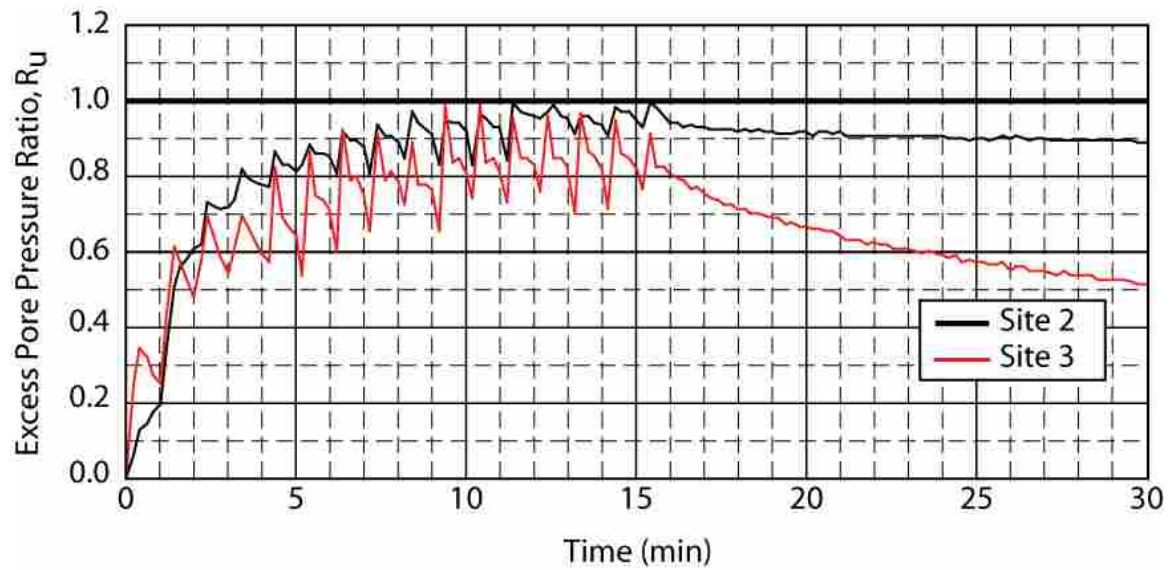


Figure 8.20 Comparison of pore pressure generation at Sites 2 and 3 recorded at 10.7 m depth.

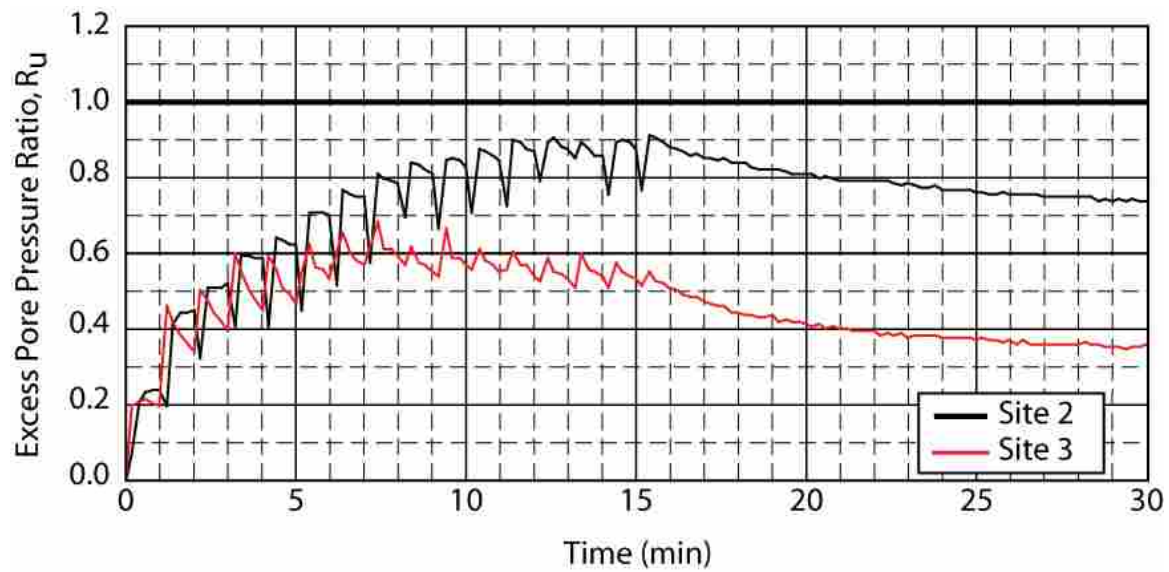


Figure 8.21 Comparison of pore pressure generation at Sites 2 and 3 recorded at 12.8 m and 12.5 m depth. The piezometer at Site 2 was located at 12.8 m depth and the piezometer at Site 3 was located at 12.5 m depth.

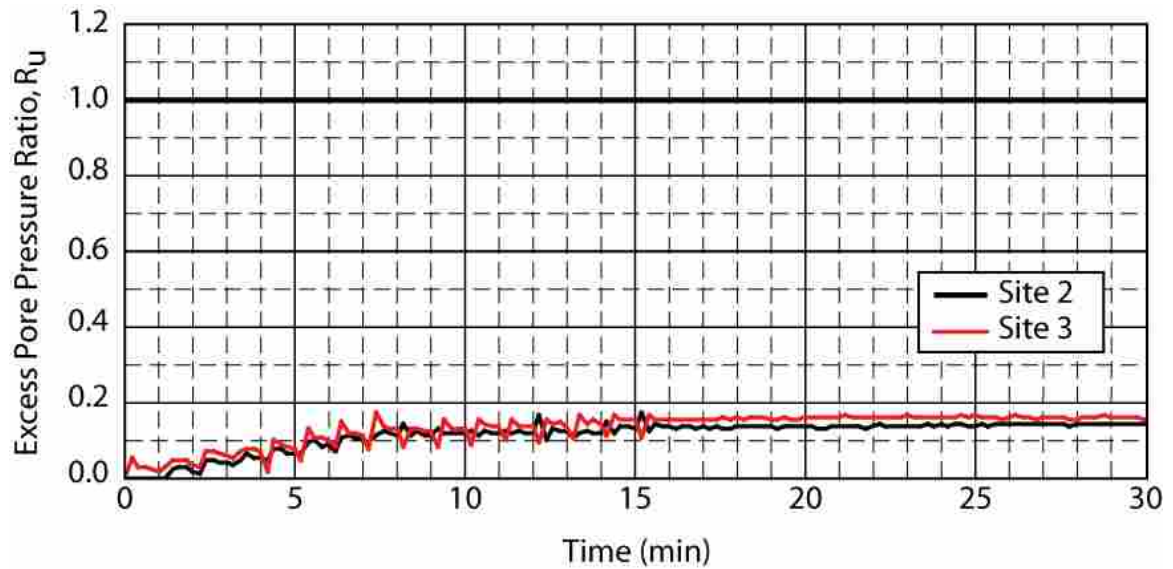


Figure 8.22 Comparison of pore pressure generation at Sites 2 and 3 recorded at 16.8 m depth.

At the other piezometer depths, evidence of increased pore pressure dissipation was apparent during the one-second interval between detonations; however, the difference in excess pore pressure ratio between the treated and untreated sites was typically less than 0.20 and liquefaction was still produced by the sequence of blast detonations. Of course, the piezometers at a depth of 16.8 were located below the zone treated with drains and the pore pressure response is almost identical at both sites.

Time histories of the dissipation of excess pore pressure ratio for each of the five piezometers following blasting are presented in Figure 8.23 through Figure 8.27. Each of the piezometers at Site 3 clearly demonstrate that the drains produced substantial increases in the rate of pore pressure dissipation relative to Site 2 where drains were not used. In contrast, the rate of dissipation was almost identical for the piezometers below the depth treated with drains. The difference in dissipation rate is particularly pronounced for the top three piezometer locations. In this region, upward water flow and

the restriction of drainage provided by the upper silty clay layer resulted in a significant lag in pore pressure dissipation for the untreated site. In contrast, all the piezometers in the area treated with drains show rapid decreases in pore pressure at the end of blasting.

The results of this test clearly indicate that the drains are increasing the rate of dissipation at the treated site. However, the increased drainage is apparently insufficient to prevent liquefaction at all but the 12.5 m depth. This situation could potentially be remedied by using larger drains or placing the drains at closer spacings. Evaluation of these possibilities will be examined in subsequent sections of this report.

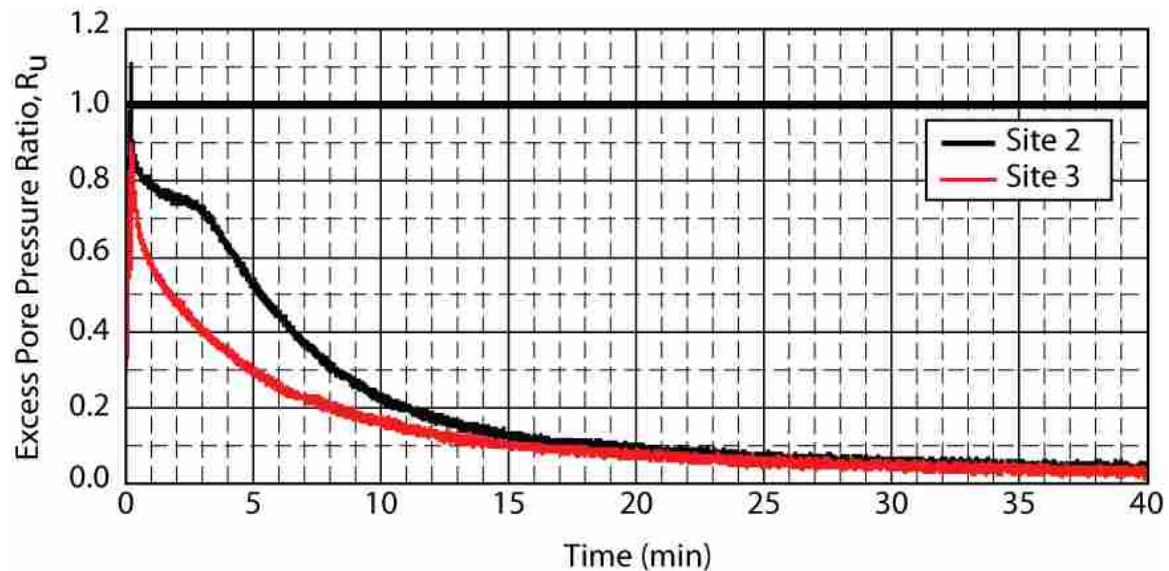


Figure 8.23 Comparison of pore pressure dissipation at Sites 2 and 3 recorded at 6.7 m and 6.4 m depth. The piezometer at Site 2 was located at 6.7 m and the piezometer at Site 3 was located at 6.4 m depth.

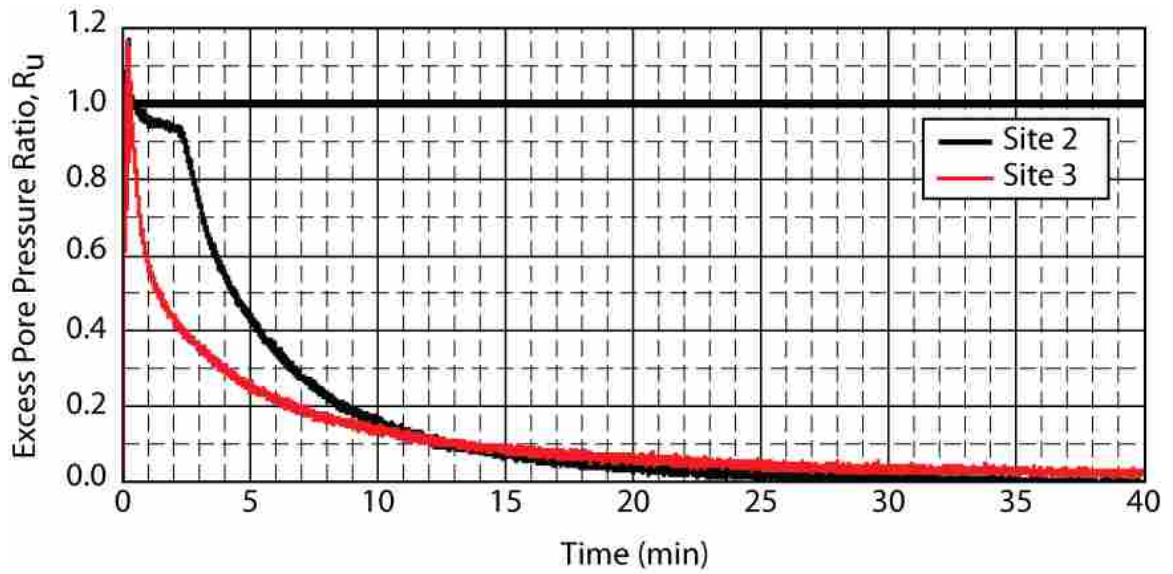


Figure 8.24 Comparison of pore pressure dissipation at Sites 2 and 3 recorded at 8.5 m depth. Piezometers at both sites were located at 8.5 m depth.

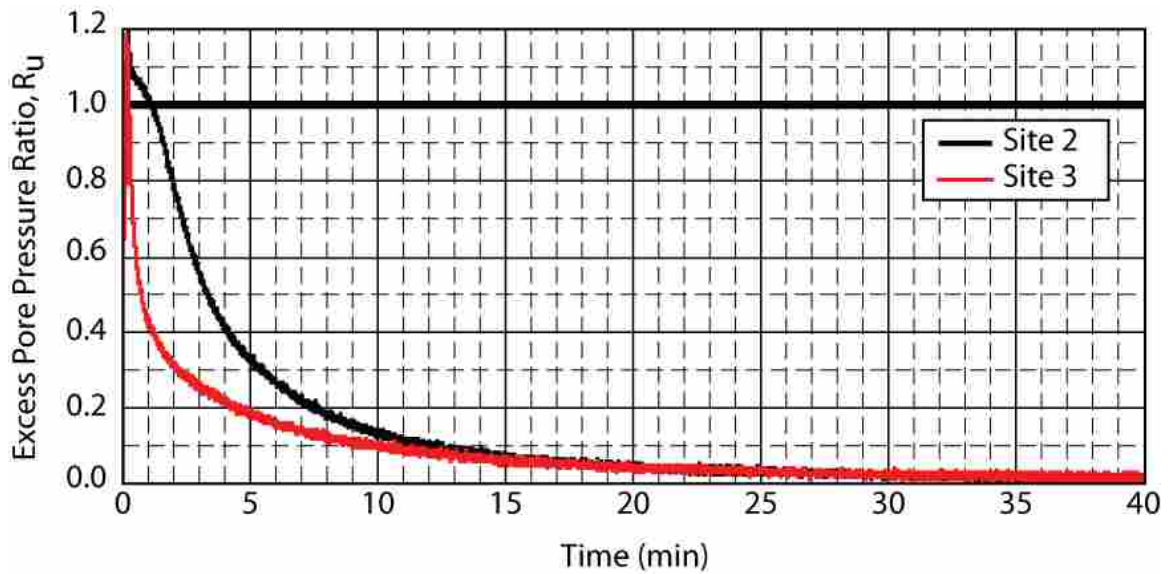


Figure 8.25 Comparison of pore pressure dissipation at Sites 2 and 3 at 10.7 m depth. Piezometers at both sites were located at 10.7 m depth.

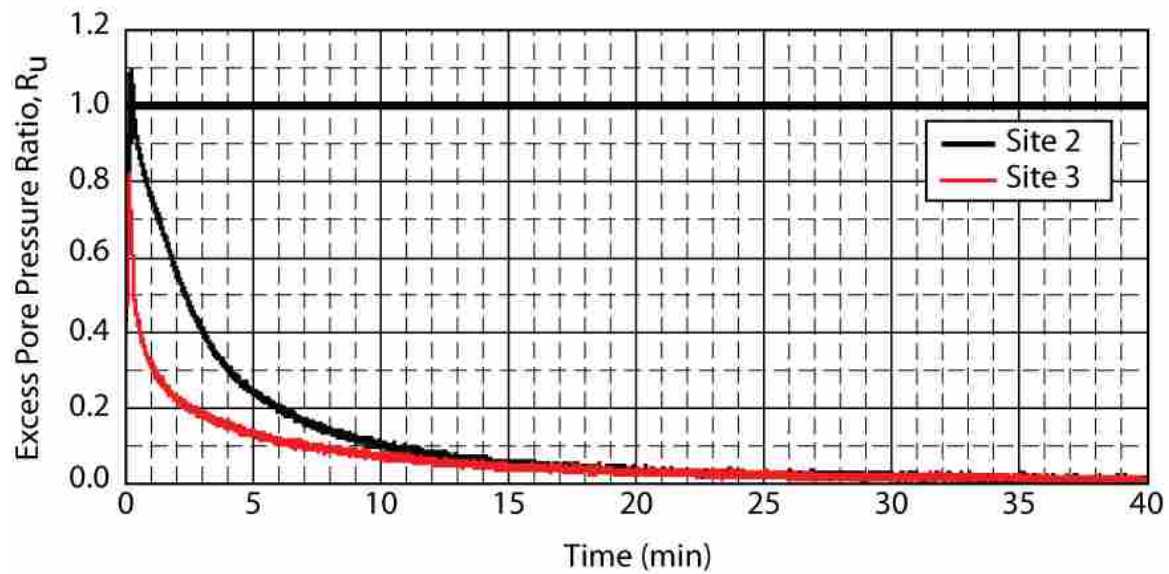


Figure 8.26 Comparison of pore pressure dissipation at Sites 2 and 3. The piezometer at Site 2 was located at 12.8 m depth and the piezometer at Site 3 was located at 12.5 m depth.

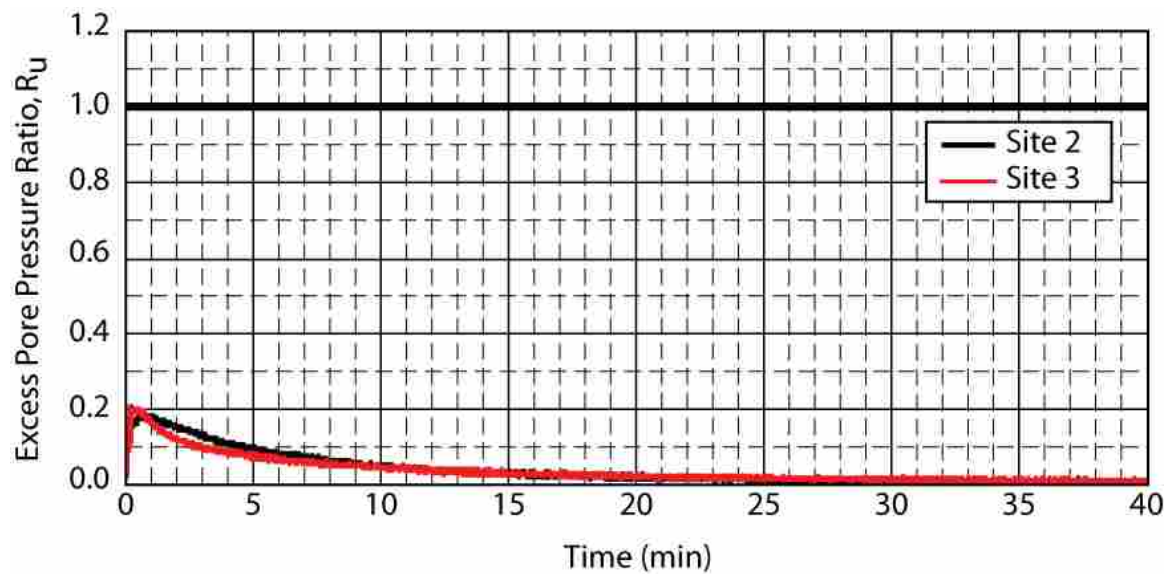


Figure 8.27 Comparison of pore pressure dissipation at Sites 2 and 3 measured by piezometers located at 16.8 m depth.

8.4.3 Blast-induced settlement

A contour plot of the ground surface settlement following the test blast is provided in Figure 8.28. The maximum settlement was approximately 270 mm which occurred to the right of center, as the site is shown in Figure 8.28. Within the blast ring, the settlement varied by about 100 mm between individual settlement measurement points. However, outside the blast ring, settlement was relatively uniform. Contours of settlement were generally concentric about the center of the test area.

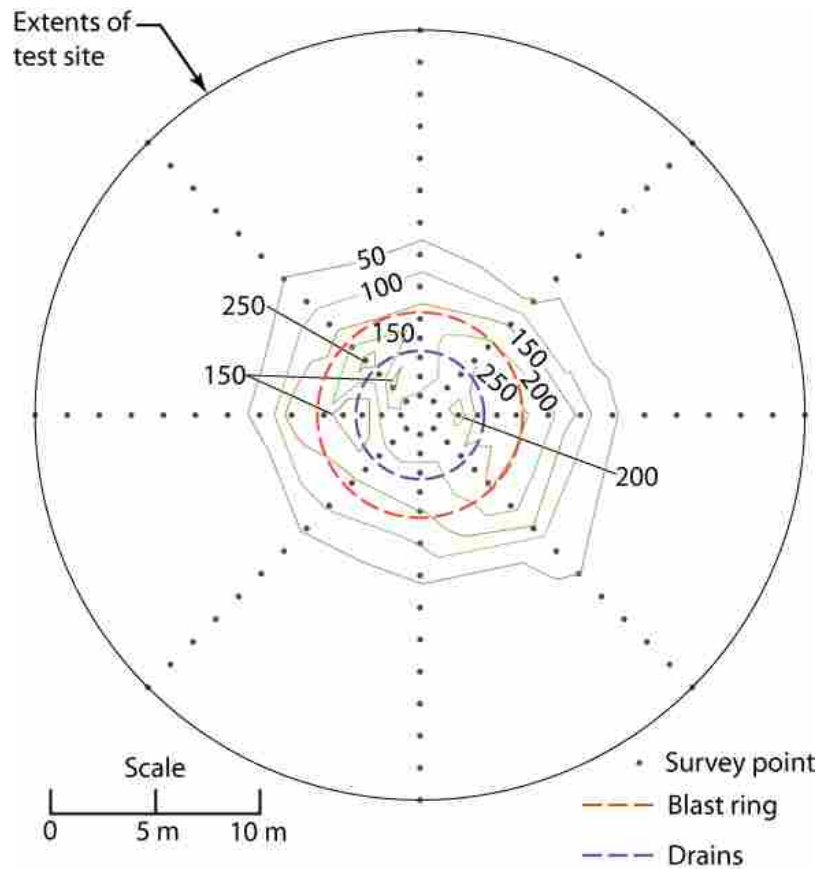


Figure 8.28 Contours of ground surface settlement caused by blasting at Site 3.

A plot of the average ground surface settlement with respect to distance from the center of the test area is provided in Figure 8.29 along with a similar curve of settlement

for the second blast test at the untreated area. In general, ground surface settlement was almost identical outside the area treated with drains. The major differences occurred within a circular area within four meters of the center of the test site which corresponds with the treated area. On average, the settlement in the treated area was 17% lower than settlement in the untreated area. In addition, the settlement in the drained area is more uniform than that in the untreated area, which would be beneficial in minimizing differential settlements to structures over these treated areas.

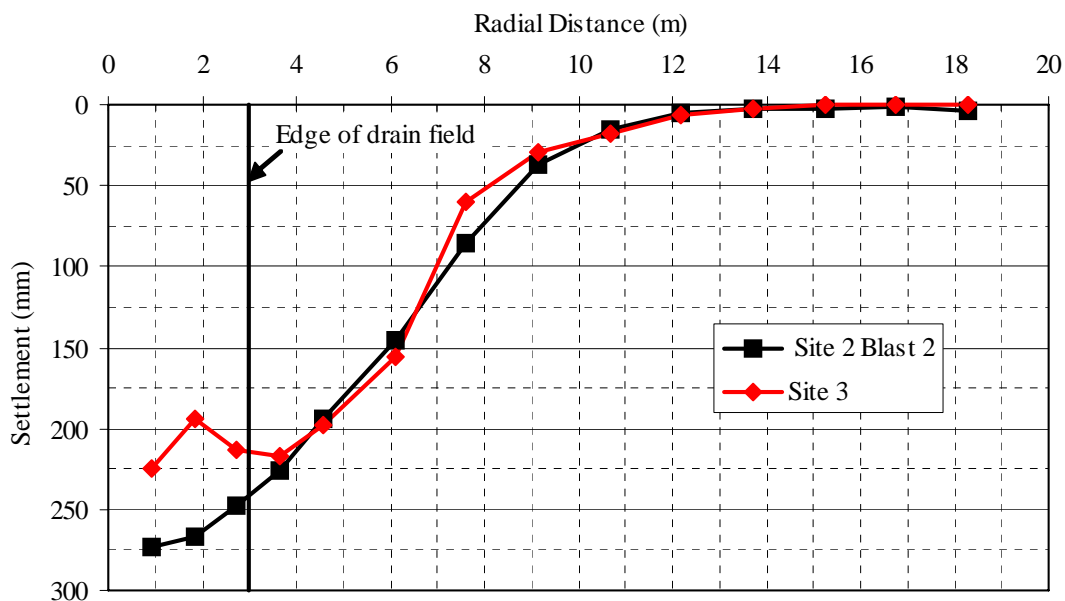


Figure 8.29 Comparison of average ground surface settlement caused by blast testing at Sites 2 and 3.

A plot of the settlement versus depth obtained from the Sondex tube is provided in Figure 8.30. Once again the top layer appears to settle as a block over the liquefied sand, although the effect was less pronounced than that at Site 1 or Site 2. Settlement in the liquefied zone is relatively linear and decreases to essentially zero at a depth of about

14 m. Based on the measurements the average volumetric strain in the sand layer from 6 to 13 m was 1.6 percent. This volumetric strain is 50% less than the 2.4 percent volumetric strain measured for the second test blast in the untreated liquefied sand at Site 2.

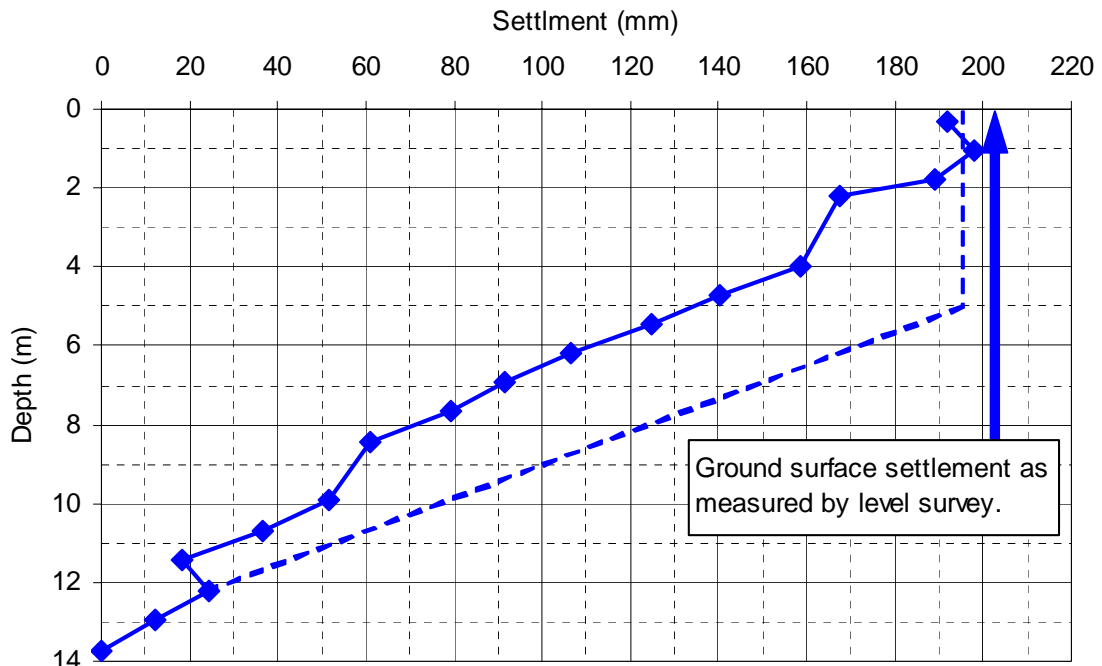


Figure 8.30 Settlement profile measured with the Sondex tube at Site 3.

It should be noted that settlement profile recorded by the Sondex tube may deviate somewhat from the actual settlement profile due to poor compaction of soil around the Sondex tube. As noted in Section 4.4.3, the Sondex tubes used at Sites 2 and 3 were installed with a rotary drill (the Sondex tubes installed with the vibrating mandrel had collapsed). After installation of the Sondex tube in the bore hole, the annulus was filled with pea gravel.

At Site 2, the pea gravel packing was compacted tightly against the Sondex tube. However, at Site 3, irregularities in the annulus prevented good compaction of the pea gravel packing, which seems to have allowed the Sondex tube to slip in the upper few meters of the soil profile. The settlement profile that would result if settlement is assumed to be uniform to a depth of 6 m (as was assumed at Site 2), is shown in Figure 8.30 as the dashed blue line. In this case, the volumetric strain from 6 m to 13 m depth would be 2.2%, which matches quite well with the 2.4% volumetric strain at Site 2.

Plots of settlement versus time are shown in Figure 8.31 for the string potentiometers installed on the ground surface located 1.2, 2.4, and 3.7 m from the center of the test site. The settlement measured by the string potentiometers was as expected. Maximum settlement occurred near the center and decreased with increasing distance from the center of the test area. The settlement occurs very rapidly during and after blasting. About 60% of the settlement occurred within 23 seconds of the onset of blasting, corresponding to an average R_u of 85% in the liquefied zone. About 90% of the settlement was complete within four minutes after blasting corresponding to an average excess pore pressure ratio of 40% in the target zone (6 to 13 m). The remaining 10% of the settlement took approximately 55 minutes to develop.

A plot of the normalized settlement versus time curves for string potentiometers located 1.2 m from the center of the test areas at Sites 2 and 3 is provided in Figure 8.32. These curves clearly show that settlement occurs much more rapidly at Site 3, likely due to the increased rate of dissipation provided by the drains relative to the untreated site.

This plot provides additional evidence of the efficacy of the drains in increasing the pore pressure dissipation rate.

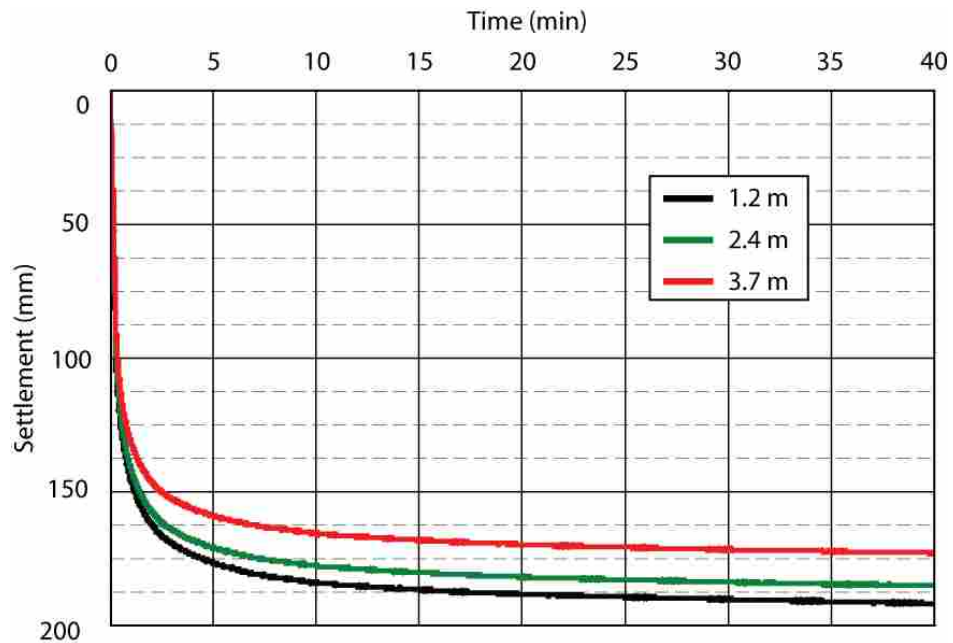


Figure 8.31 Real-time settlement measured during blast testing at Site 3.

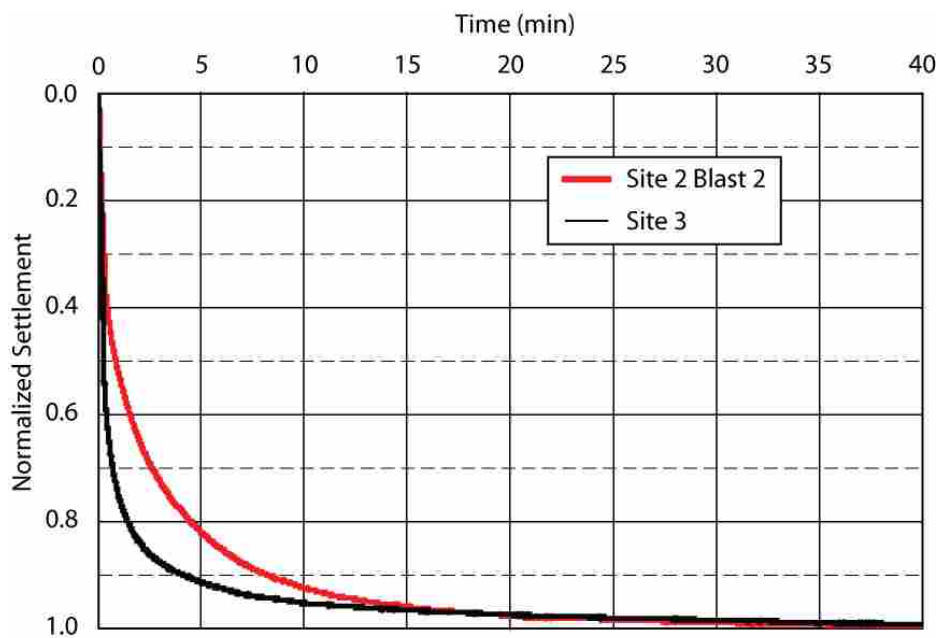


Figure 8.32 Comparison of normalized settlement at Sites 2 and 3.

8.4.4 Pile load transfer variations due to liquefaction

To analyze the load transfer properties of the soil-pile interface, a load was applied to the test pile before blasting and maintained during blasting until pore pressures had dissipated to near pre-blast levels. Figure 8.33 shows the load applied to the test pile as it varied with time throughout the test. The onset of blasting was set as time zero, therefore negative time values indicate the time before blasting.

Figure 8.34 is a plot showing the load in the test pile versus depth for the blast test at Site 3 based on strain gauge measurements. As was done for Site 2, load versus depth curves are provided for the case immediately prior to blasting, immediately after blasting, and at the end of settlement.

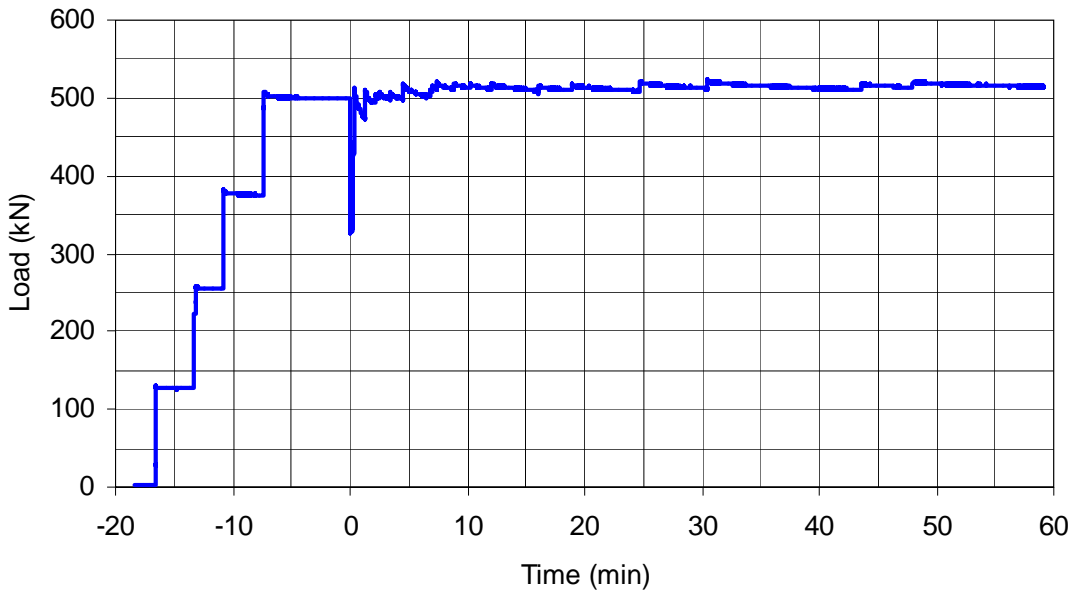


Figure 8.33 Load applied to the test pile during blast testing at Site 3.

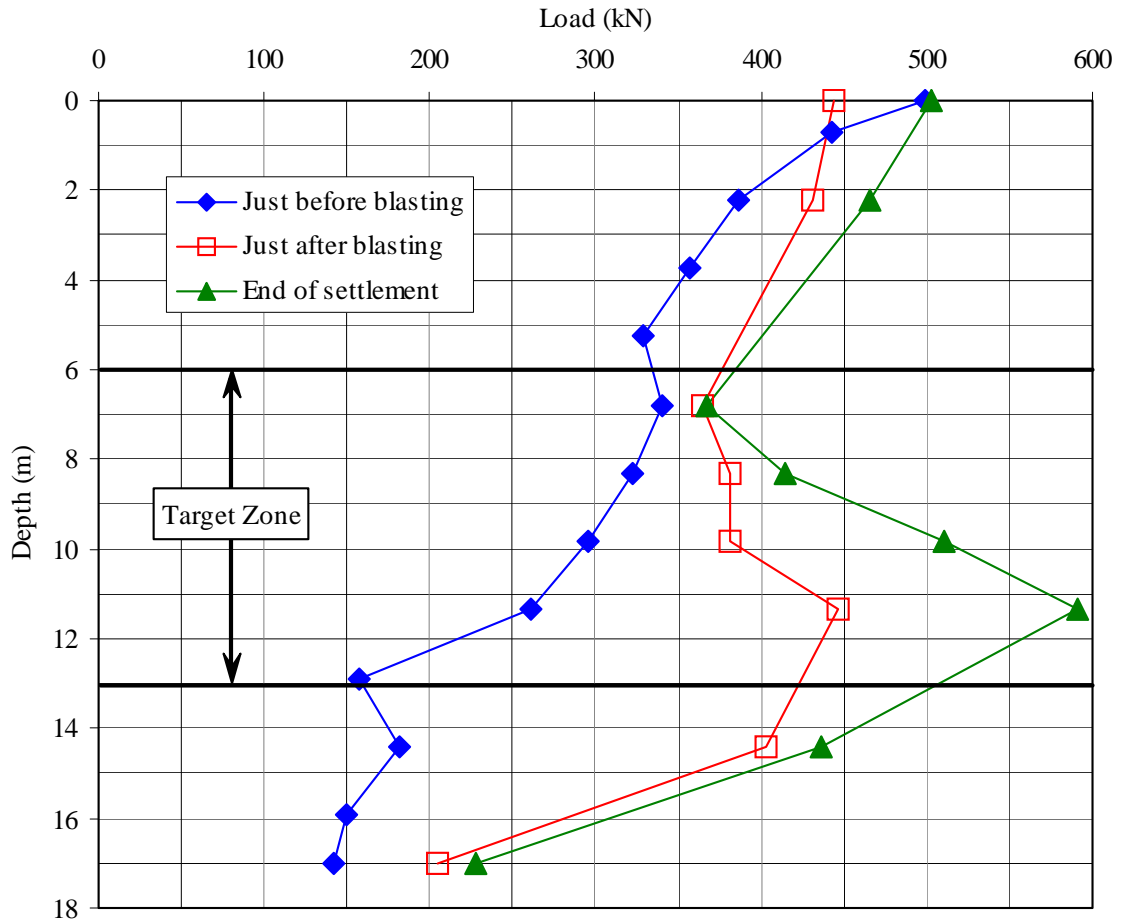


Figure 8.34 Plot of load in test pile at Site 3 immediately before the blast, immediately after the blast, and the end of settlement.

Table 8.16. Comparison of unit side resistance values within the liquefied zone measured immediately before blasting and at the end of settlement with values predicted by the LCPC and Eslami and Fellenius methods.

	Just before blasting	End of settlement	LCPC	Eslami and Fellenius
Skin Friction 6 - 13 m depth (kPa)	17.2	-48.0	24.6	31.1

The values of skin friction measured within the target zone immediately before blasting and at the end of settlement are summarized in Table 8.16. This table also

contains the values of skin friction predicted to develop within the target zone by both the LCPC and Eslami and Fellenius methods.

Immediately prior to blasting, a load of approximately 500 kN was applied to the test pile and this load was resisted primarily by positive skin friction with a minor contribution from end-bearing. Just after the blast, the load at the pile head dropped to about 325 kN (see Figure 8.33) because of settlement of the pile relative to the reaction frame and the hydraulic pump was activated to bring the load back up to the original value. At this stage, the load versus depth curve still indicates positive skin friction down to the top of the liquefied zone, but with a relatively small amount of negative skin friction within the liquefied zone. The absence of downdrag within the upper non-liquefied crust may be a result of the variation in applied load due to blasting, as discussed in Section 6.6.5.

The rapid development of negative skin friction at Site 3 relative to that observed at Site 2 is likely due to the drainage provided by the drains which accelerated the settlement process. At the end of settlement, skin friction still appears to be positive in the soil above the liquefied zone, although attrition of the strain gauges makes a detailed assessment difficult. The negative skin friction in the zone that liquefied has become greater and was equal to or somewhat higher than the positive skin friction in this zone prior to blasting. The increase in negative skin friction appears to have been resisted by a combination of increased skin friction as well as some increase in the end-bearing resistance relative to the conditions before blasting.

Figure 8.35 is a plot comparing the load versus depth curves for the test piles for the second blast at Site 2 and the test blast at Site 3 at two different times—just before blasting and at the end of settlement. The load versus depth curves before blasting appear to be reasonably comparable, although the curves from Site 3 indicates greater end-bearing resistance. At the end of settlement, the curves are again comparable in shape, though the negative skin friction in the liquefied zone is higher for Site 3 than for Site 2. Table 8.17 contains a summary of the skin friction developed within the target zone during blast testing at both Sites 2 and 3.

Table 8.17. Comparison of unit side resistance (skin friction) values developed within the target zone immediately before blasting and at the end of settlement measured during the blast tests at Sites 2 and 3 with values predicted by the LCPC and Eslami and Fellenius methods.

	Skin Friction, 6 - 13 m (kPa)			
	Just before blasting	End of settlement	LCPC	Eslami and Fellenius
Site 2, Blast 1	7.97	-8.01	24.6	31.1
Site 2, Blast 2	26.6	-14.3	24.6	31.1
Site 3	17.2	-48.0	24.6	31.1

The higher negative skin friction could result from the increased rate of pore pressure dissipation which would allow the liquefied sand to return to a solid state more rapidly. The difference in negative skin friction values measured at Sites 2 and 3 may also be a result of the movement of ground water due to blast testing. The soil-pile interface likely acts as a preferential pathway for ground water seepage. At Site 3, where the EQ drains provided low resistance pathways for pore pressure dissipation, the

movement of water along the soil-pile interface was probably relatively minor in comparison to that which took place in the drains.

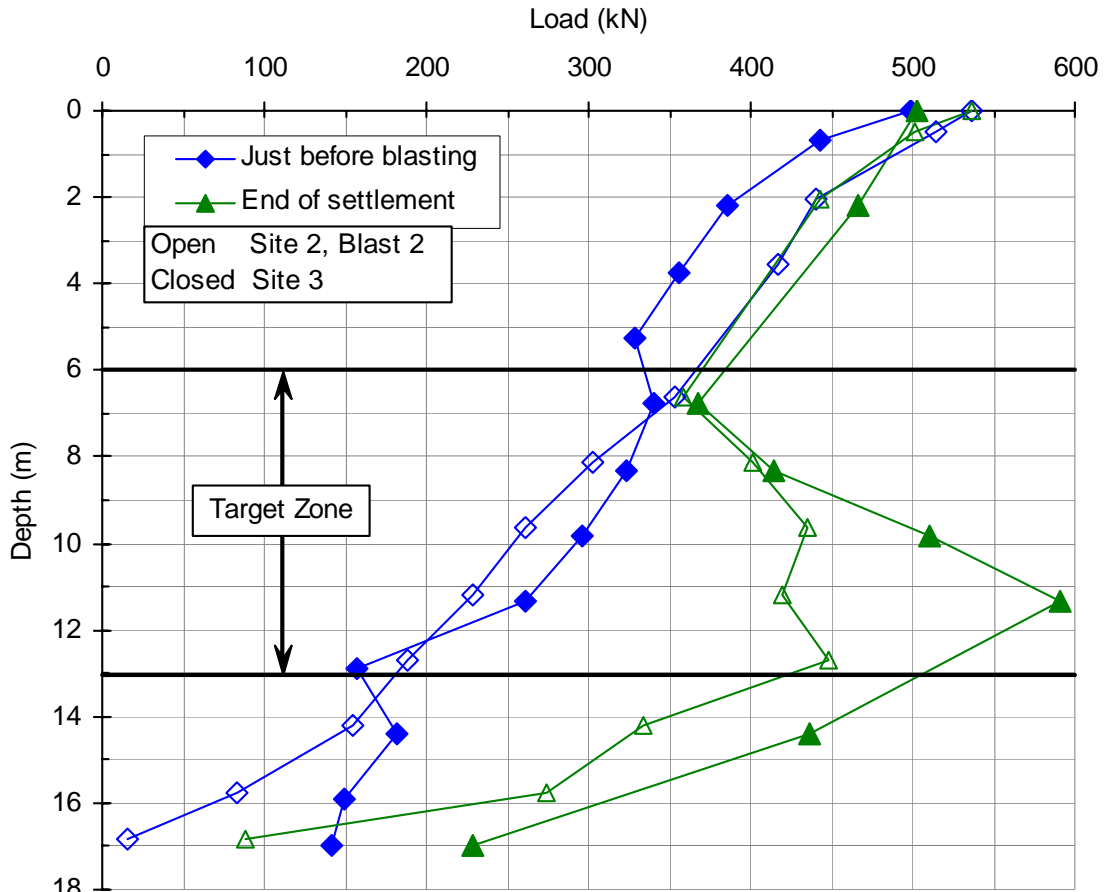


Figure 8.35 Comparison of load versus depth curves for the test piles at Sites 2 and 3.

However, at Site 2, where no EQ drains were installed, the soil-pile interface would have provided a pathway whereby pore pressures could more easily dissipate compared to the surrounding soil. The presence of flowing groundwater at relatively high pressures along the surface of the pile could have decreased the amount of skin friction that developed along the pile, as seen in Figure 8.35.

9 Computer Analysis of Blast Liquefaction Tests

While the blast liquefaction tests clearly indicated that pore pressure dissipation rates were significantly increased with the use of EQ drains, the drains in their present configuration were insufficient to prevent liquefaction during blasting. To provide increased understanding of the behavior of the drains for different drain configurations, i.e., different center-to-center spacings and drain diameters, along with less demanding earthquake events (different amplitude of shaking and number of cycles), analyses were performed using the computer program FEQDrain (Pestana *et al.*, 1997). During this study, the soil properties in the computer model were first calibrated using the measured settlement and pore pressure response from the blast test at Site 3. Then, the calibrated soil properties were held constant while the drain configuration or “earthquake event” was varied.

FEQDrain uses an axi-symmetric finite element model of the soil profile and composite drain system. The program models an individual drain within a grid of drains using a “radius of influence” concept based on the drain spacing. The computer program calculates the excess pore pressure ratio in each soil layer within the radius of influence. This is done by accounting for the generation of pore pressure produced by the earthquake and the dissipation of pore pressure provided by flow to the drains.

The program is capable of accounting for head loss in the drain and storage in the drain as water levels change during pore pressure build-up. FEQDrain can also account for non-linear increases in the modulus of compressibility of the soil as the excess pore pressure ratio increases. In addition to computing pore pressure response, the program can compute the settlement accompanying drainage and dissipation of excess pore pressures.

9.1 Mathematical Formulation

The response of the soil under the influence of seismic shaking as modeled by FEQDrain is controlled by the solution to the following equation

$$\left(\nabla k \frac{\nabla \gamma}{\gamma_w} \right) = m_v \left(\frac{\partial u}{\partial t} - \frac{\partial u_g}{\partial t} \right) \quad (10)$$

where: k = hydraulic conductivity

u = pore pressure

∇ = space gradient operator

γ_w = unit weight of water

m_v = coefficient of volumetric compressibility

u_g = excess pore pressure generated by cyclic loading

t = time

The development of Equation 10 is fully described in Pestana *et al.* (1997) and will not be discussed in full here. However, it should be mentioned that several underlying assumptions must be satisfied in order for Equation 10 to be valid. These assumptions include: (1) continuity of flow and that flow is governed by Darcy's law; (2)

the soil is completely saturated; and (3) the change in porosity due to seismically induced compression is equivalent to the change in volumetric strain.

Naturally emplaced deposits of soil commonly contain thin layers of finer-grained material interspersed with coarser-grained material, causing the soil to exhibit anisotropic flow properties. The flow through such soils can therefore be described by the use of horizontal and vertical hydraulic conductivities, k_h and k_v . Under conditions of axial symmetry, Equation 10 becomes

$$\frac{\partial}{\partial r} \left(\frac{k_h}{y_w} \cdot \frac{1}{r} \frac{\partial u}{\partial x} \right) + \frac{\partial}{\partial z} \left(\frac{k_v}{y_w} \cdot \frac{\partial u}{\partial z} \right) = m_v \left(\frac{\partial u}{\partial t} - \frac{\partial u_g}{\partial t} \right) \quad (11)$$

To solve Equation 11, values for m_v and u_g must be calculated for each time step of the simulation.

9.1.1 Soil compressibility

FEQDrain calculates the change in volumetric compressibility, m_v , due to increases in R_u , using the equation developed by Seed *et al.* (1975a)

$$\frac{m_v}{m_{v0}} = \frac{\exp(y)}{1 + y + y^2 / 2} \geq 1 \quad (12)$$

where: $y = a \cdot R_u^b$

$a = r(1.5 - D_r)$

$b = 3(4)^{-D_r}$

D_r = initial relative density

m_{v0} = initial value of volumetric compressibility

The relationship defined by Equation 12 is plotted in Figure 9.3b for various values of relative density. During post earthquake analysis, the value of m_v does not decrease from the highest value obtained with Equation 12, as suggested by Seed *et al.* (1975a).

9.1.2 Pore pressure generation

The generation of pore pressure is modeled in FEQDrain by first transforming the irregular seismic loading into an equivalent number of uniform cycles occurring during a specified period of time, as described by Seed *et al.* (1975a)

$$\frac{\partial u_g}{\partial t} = \frac{\partial u_g}{\partial N} \cdot \frac{\partial N}{\partial t} \quad (13)$$

$$\frac{\partial N}{\partial t} = \begin{cases} N_{eq} / t_d & (0 < t \leq t_d) \\ 0 & (t > t_d) \end{cases} \quad (14)$$

where: N = the accumulated number of cycles at time t

N_{eq} = equivalent number of uniform cycles

t_d = time period of shaking (typically equivalent to time of strong motion)

Based on extensive laboratory experiments using cyclic triaxial and simple shear tests, the relationship between u_g and N can be described by

$$R_u = \frac{u_g}{\sigma'_0} = \frac{2}{\pi} \arcsin \left(\frac{N}{N_l} \right)^{\frac{1}{2\theta}} \quad (15)$$

where: R_u = excess pore pressure ratio

σ'_0 = initial mean effective stress under triaxial conditions or the initial vertical stress for simple shear conditions

N_l = number of uniform stress cycles causing liquefaction in a cyclic undrained test

θ = an empirical constant, typically equal to 0.7

Taking the derivative of Equation 15 we obtain

$$\frac{\partial u_g}{\partial N} = \frac{\sigma'_0}{\theta \cdot \pi \cdot N_l} \cdot \frac{\tan(\pi \cdot R_u / 2)}{\sin^{2\theta}(\pi \cdot R_u / 2)} \quad (16)$$

Substituting Equation 13 and Equation 16 back into Equation 13, the rate of pore pressure generation becomes

$$\frac{\partial u_g}{\partial t} = \frac{\sigma'_0}{\theta \cdot \pi} \cdot \left(\frac{N_{eq}}{N_l \cdot t_d} \right) \cdot \frac{\tan(\pi \cdot R_u / 2)}{\sin^{2\theta}(\pi \cdot R_u / 2)} \quad (17)$$

The rate of pore pressure generation, $\partial u_g / \partial t$, is dependent upon the previous cyclic loading history represented by the current value of pore pressure ratio, R_u .

9.1.3 Boundary conditions

Figure 9.1 depicts the configuration of a typical vertical drain installed in a potentially liquefiable soil profile. The soil profile contains n different soil layers, each with individual properties, to depth H . A single vertical drain penetrates the full depth of the soil layer. Because FEQDrain can not model partially penetrating drains, the soil profile modeled by FEQDrain must terminate at the bottom of the drain. It is assumed that the soil layers below the bottom of the drain make no contribution to the drain so FEQDrain models the bottom of the soil profile as a no-flow boundary.

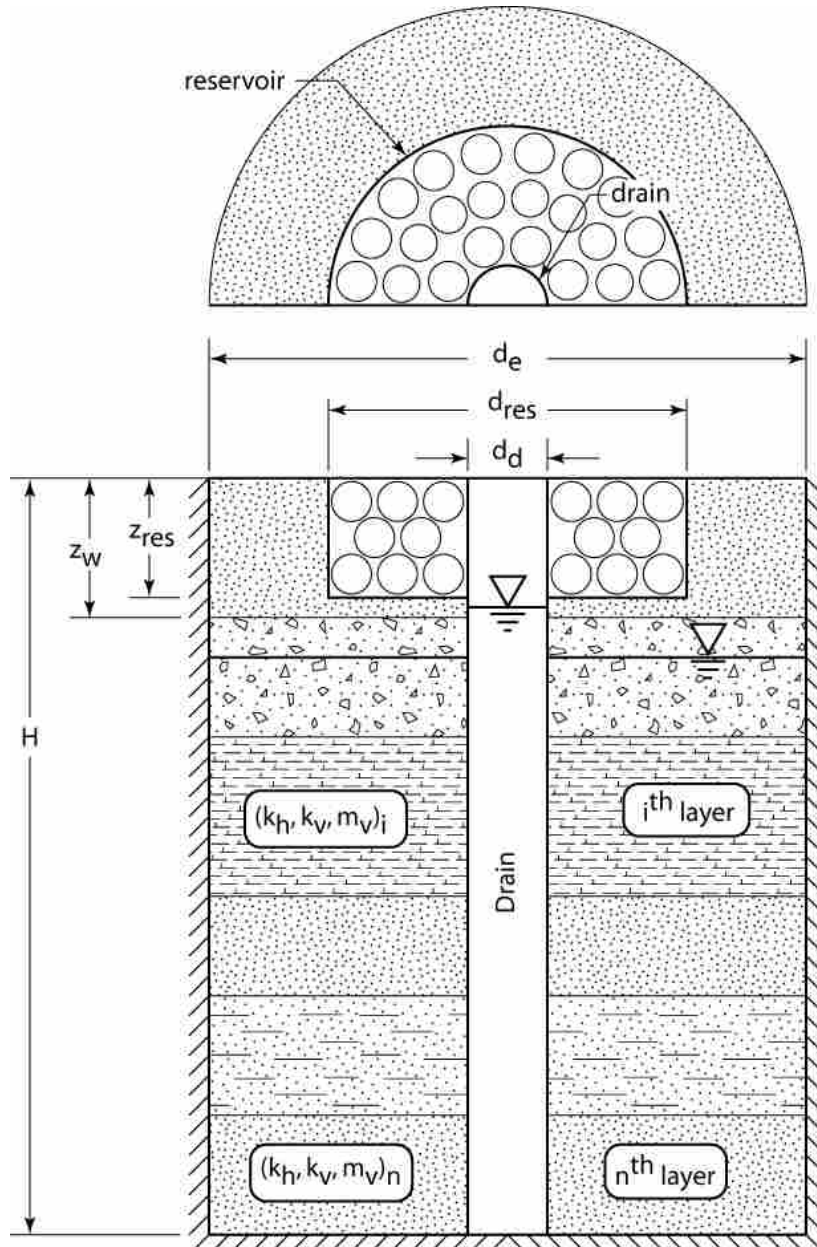


Figure 9.1 Boundary conditions for analysis of EQ drains (after Pestana *et al.*, 1997).

As discussed in Section 2.1.1.1, earthquake shaking induces horizontal hydraulic gradients to develop around vertical drains, beginning at the drain and progressing radially outwards. These horizontal gradients cause pore water to flow towards the vertical drain, dissipating the pore pressure rise caused by the earthquake. The spatial extent to which the horizontal gradients develop is called the zone or diameter of influence, d_e (shown in Figure 9.1). For a single drain, d_e is limited only by the hydraulic conductivity of the soil and the duration and strength of earthquake shaking. For a cluster of drains, d_e is limited by the center-to-center spacing of the drains. As the horizontal hydraulic gradients extend outwards from the drains due to earthquake shaking, at some point the respective zones of influence from each drain will intersect. The intersection of the zones of influence constitutes a no-flow boundary between drains and is modeled as such in FEQDrain.

In many soil profiles, the water table exists at some distance below the ground surface with the soil above the water table in an unsaturated condition. As the water level rises in the drain due to earthquake shaking, a part of the water in the drain can flow out of the drain into the unsaturated soil. This retards the rate at which the water level rises in the drain which also slows the rate at which static water pressure rises in the drain. This phenomenon is modeled in FEQDrain through the use of a reservoir as shown in Figure 9.1. The water level in the drain is calculated by FEQDrain based on the volume of water expelled from the soil profile compared with the volume of the drain. Once the water level in the drain rises to the bottom of the reservoir, the water level rise is then calculated based on the volume of the drain.

9.2 Calibration of Computer Model

The soil parameters used in the computer model had to be calibrated before the model could be used to evaluate the drains installed at Site 3.

9.2.1 Selection of soil input parameters

The basic soil profile and layer thickness values used in the analysis of each EQ drain test area are based on the CPT profiles previously shown in Figure 8.3. The soil profile was divided into 6 separate layers. The top two layers represent the silty sand layer and the clayey silt layers respectively (see Figure 3.7). The boundaries of the bottom four layers were located such that the piezometers were located at the center of each layer. This arrangement allowed the soil properties to varied individually for each piezometer to assist in the calibration of the FEQ drain model.

The five most important soil properties in matching the pore pressure history and settlement are: horizontal hydraulic conductivity (k_h), vertical hydraulic conductivity (k_v), modulus of compressibility (m_v), relative density (D_r), and the number of cycles required to cause liquefaction (N_L). The determination of each of these properties is discussed in the following sections.

9.2.1.1 Hydraulic conductivity

Horizontal hydraulic conductivity is perhaps the most important factor governing the rate of dissipation. As k_h increases, the rate of dissipation increases. In general, the vertical hydraulic conductivity does not greatly influence the response because most of the drainage is radial or horizontal, except for very shallow depths. Reflective of this,

Seed and Booker (1977) used $k_v = 0$ in original computations for their design charts. In relatively uniform sands, k_v has little effect as shown by Pestana *et al.* (1997); however, in layered soil strata, k_v can sometimes be important. Typical ranges of k_h as a function of soil type are provided by Pestana *et al.* (1997) based on recommendations from Terzaghi and Peck (1948) as shown in Table 9.1. A review of the data in Table 9.1 indicates that significant variation can occur within a given soil type due to minor variations in fines content and density. Other investigators have indicated that the variation in k_h within a given soil type could be as much as two orders of magnitude (Freeze and Cherry, 1979).

Table 9.1. Typical values for horizontal hydraulic conductivity (k_h) from Pestana *et al.*, 1997 (after Terzaghi and Peck, 1948).

Soil Type	Particle Size (mm)	Coefficient of hydraulic conductivity (cm/s)
Very fine sand	0.05-0.10	0.001-0.005
Fine sand	0.10-0.25	0.005-0.01
Medium sand	0.25-0.50	0.01-0.1
Coarse sand	0.50-1.00	0.1-1.0
Small pebbles	1.00-5.00	1.0-5.0

Due to layering effects and soil structure orientation under stress, the horizontal hydraulic conductivity is typically higher than the vertical hydraulic conductivity. Typical ratios of horizontal to vertical hydraulic conductivity for various soil conditions are given in Table 9.2.

The horizontal hydraulic conductivity used in this study was initially selected based on the value measured *in situ* by the packer tests as shown previously in Figure 3.10. The ratio of k_h/k_v was generally assumed to be 10. In an iterative process, adjustments were made to the k_h values used in FEQ drain to improve the agreement between the computed and measured pore pressure response in the various soil layers. The final profiles of k_h versus depth for Site 3, the EQ drain Test Area is shown in Figure 9.2. The range of measured/expected values of k_h , as measured by Rollins and Anderson (2002) at a site approximately 30 m south of the current test location is also shown in Figure 2.2. Although the k_h values for the two lowest layers remained within the expected range, the values of k_h in the two upper liquefiable layers fell somewhat above the measured range. Nevertheless, the values are still reasonable for the soil types involved.

Table 9.2. Relationship between k_h and k_v from Pestana *et al.* (1997).

Description	k_h/k_v
Uniform (clean sands)	1.5-2.0
Moderately anisotropic (silt seams)	4.0-5.0

9.2.1.2 Modulus of compressibility

The modulus of compressibility (m_v) is a measure of the vertical strain produced in a soil by a change in vertical stress. This parameter is roughly equivalent to the inverse of the elastic modulus or Young's modulus. Although m_v is often measured for clays while pore pressures dissipate, very few studies have made measurements of m_v for

sands during pore pressure dissipation. Lee and Albaisa (1974), reported that m_v for sand ranged from 2×10^{-5} (dense soil) to 4×10^{-5} (loose soil) m^2/kN and was significantly affected by relative density. A summary of values of m_v found in the literature (Pestana *et al.*, 1997) indicates that m_v can range from 2×10^{-5} to 1×10^{-4} m^2/kN .

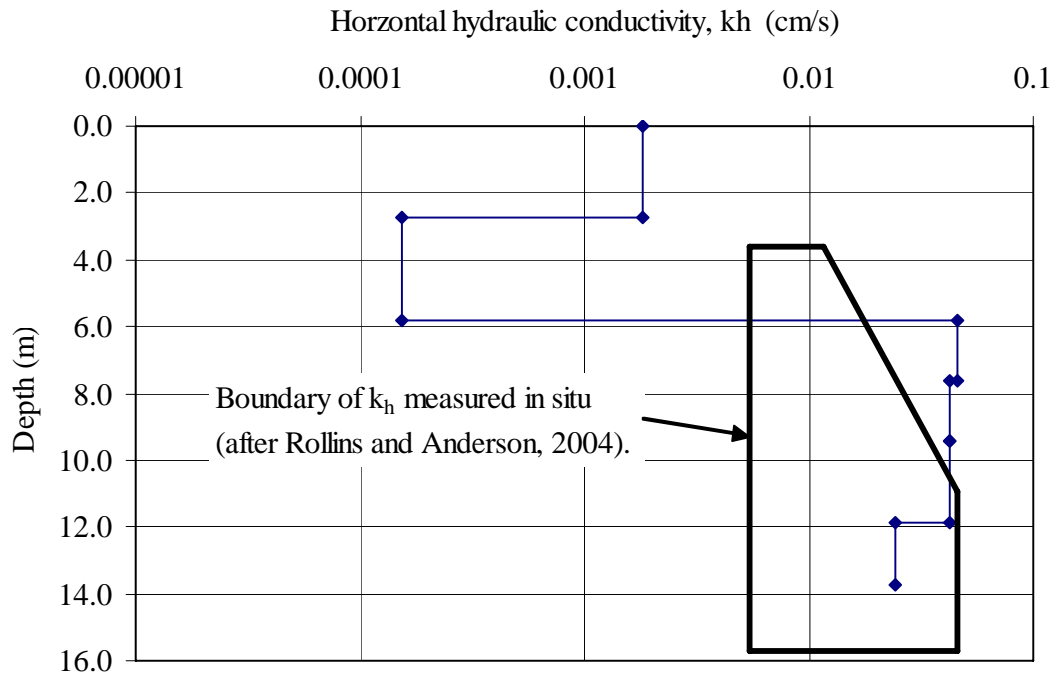


Figure 9.2 Comparison of calibrated values of horizontal hydraulic conductivity (k_h) versus depth with values measured in situ by Rollins and Anderson (2004).

However, as the excess pore pressure ratio (R_u) increases beyond about 0.60, the m_v can increase significantly as shown in Figure 9.3a. In these cases, the increase in m_v is dependent on both the relative density and the excess pore pressure ratio. Seed *et al.* (1975a) developed a relationship to account for the variation in m_v with D_r and R_u as shown in Figure 9.3b. This relationship is used in the computer model FEQDrain.

It was impossible to calibrate the FEQDrain model such that both the measured and calculated values of R_u and settlement matched at the same time. Because the settlement calculations used in FEQDrain are based on the poorly understood and difficult to measure m_v parameter, it was decided to calibrate the FEQ drain model based primarily on excess pore pressure ratios.

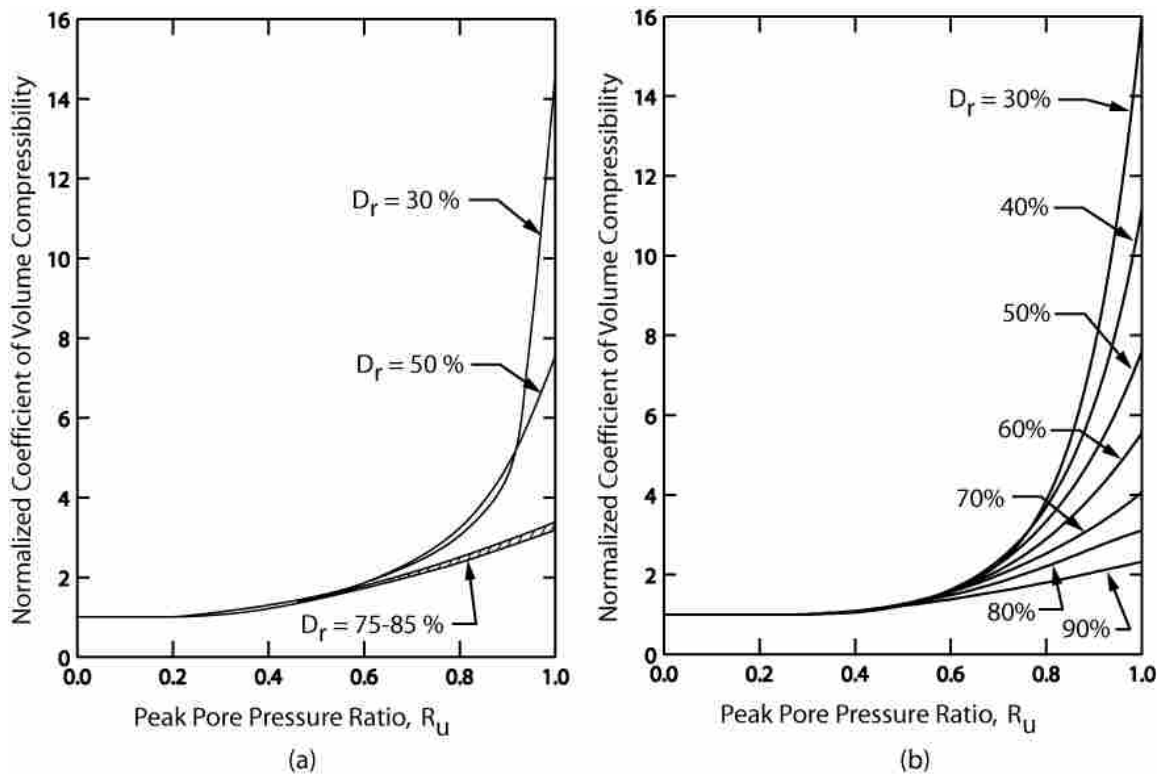


Figure 9.3 Variation in normalized coefficient of compressibility (M_v/M_{v_i}) versus peak pore pressure ratio (R_u) for sands of various relative densities (D_r) from (a) laboratory tests (after Lee and Albaisa, 1974), and (b) as modeled in FEQDrain (after Seed *et al.*, 1975a).

9.2.1.3 Relative density

The estimates of relative density were made based on the initial values provided by the CPT soundings. This parameter was not modified greatly during the calibration.

9.2.1.4 Number of cycles to cause liquefaction

Another important characteristic of the soil is the number of cycles required to cause liquefaction (N_L). The N_L for the blast simulation was obtained by determining the time at which liquefaction occurred using the pore pressure ratio versus time plot measured at Site 2 as shown in Figure 6.38. As can be seen, the upper three liquefiable layers liquefied after 10 to 14 blasts while the bottom layer never fully liquefied. For the analyses conducted in this study, the best agreement with the measured response was obtained when N_L was assumed to be 11 cycles for the upper three liquefiable layers and 16 cycle for the bottom liquefiable layer.

9.2.1.5 Summary of calibrated values

The final, calibrated soil properties for Site 3 obtained by trial and error with FEQDrain are shown in Table 9.3.

9.2.1.6 Drain input properties

The outside radius of the drain was 121 mm which corresponds to a drain area of 115.0 square centimeters. The radius of the area of influence was 0.64 m which represents a drain spacing of 1.22 m in a triangular grid. The area of openings per unit length in the perforated pipe was 0.004 m²/m of length and the constant associated with head loss through the perforations was taken as 1.0.

The head loss due to vertical resistance in the drain (H_{drain}) was given by

$$H_{drain} = 0.5(Q * z)^2 \quad (18)$$

where Q is flow rate and z is depth.

Table 9.3. Summary of input properties for FEQDrain analyses.

	Layer Thickness	Depth to sublayer (m)	Calibrated soil properties
Layer 1	2.744 m 9 sublayers	0.3049	Sand/Silty sand $K_h = 1.83 \times 10^{-4}$ cm/s $K_v = 1.83 \times 10^{-3}$ cm/s $M_v = 2.099 \times 10^{-5}$ m ² /kN $D_r = 0.6$
		0.6098	
		0.9146	
		1.2195	
		1.5244	
		1.8293	
		2.1341	
		2.4390	
		2.7439	
Layer 2	3.049 m 10 sublayers	3.0488	Sandy silts/Silts/Clayey silts $K_h = 1.524 \times 10^{-5}$ cm/s $K_v = 1.524 \times 10^{-6}$ cm/s $M_v = 8.359 \times 10^{-5}$ m ² /kN $D_r = 0.7$
		3.5370	
		3.6585	
		3.9634	
		4.2683	
		4.5732	
		4.8780	
		5.1829	
		5.4878	
5.792			
Layer 3	1.829 m 6 sublayers	6.0976	Sand/Silty sand $K_h = 4.572 \times 10^{-3}$ cm/s $K_v = 4.572 \times 10^{-4}$ cm/s $M_v = 1.045 \times 10^{-4}$ m ² /kN $D_r = 0.3$
		6.4024	
		6.7073	
		7.0122	
		7.3171	
Layer 4	11.829 m 6 sublayers	7.6220	Sand/Silty sand $K_h = 4.267 \times 10^{-3}$ cm/s $K_v = 4.267 \times 10^{-4}$ cm/s $M_v = 1.045 \times 10^{-4}$ m ² /kN $D_r = 0.3$
		7.9268	
		8.2317	
		8.5366	
		8.8415	
Layer 5	2.439 m 8 sublayers	9.1463	Sand/Silty sand $K_h = 4.267 \times 10^{-3}$ cm/s $K_v = 4.267 \times 10^{-4}$ cm/s $M_v = 1.045 \times 10^{-4}$ m ² /kN $D_r = 0.3$
		9.4512	
		9.7561	
		10.061	
		10.366	
		10.671	
		10.976	
11.208			
Layer 6	1.83 m 6 sublayers	11.585	Sand/Silty sand $K_h = 2.408 \times 10^{-3}$ cm/s $K_v = 2.408 \times 10^{-4}$ cm/s $M_v = 1.045 \times 10^{-4}$ m ² /kN $D_r = 0.3$
		11.890	
		12.195	
		12.50	
		12.805	
		13.110	
		13.415	
		13.720	

9.2.2 Other required input parameters

To simulate the blast detonation series as an earthquake event in FEQDrain, the equivalent number of cycles (N_q) due to the “earthquake” loading that occurred as a result of the detonations and the duration of the “earthquake” event needed to be determined. This was accomplished by counting pulse peaks recorded by the piezometers. Sixteen detonations with a delay of 1.0 second between each detonation produced sixteen relatively distinct peaks. These detonations were taken to be the cycles for the blast simulation in FEQDrain. The duration (t_d) of the explosions was taken from the same plot of pore pressure generation. The event lasted approximately 15.5 seconds so 16 seconds was used for t_d .

The hydraulic head boundary at the top of the drain is set equal to the ground elevation because water could flow away from the drain above this level. The volume of water necessary to raise the water level above the ground water surface was specified as a “reservoir”. The reservoir volume was set equal to the inside area of the drain multiplied by the depth to the static water table.

9.2.3 Measured and computed pore pressure and settlement

A comparison of the measured and computed excess pore pressure ratios for 300-second time histories at depths of 6.7, 8.5, 10.8 and 12.8 m at Site 3 are presented in Figures 9.4 through 9.7, respectively. The computed response does not account for the peaks and troughs in the time history produced by each blast detonation, but the average or residual pore pressure is reasonably well captured. The agreement between measured and computed pore pressure response is also reasonable.

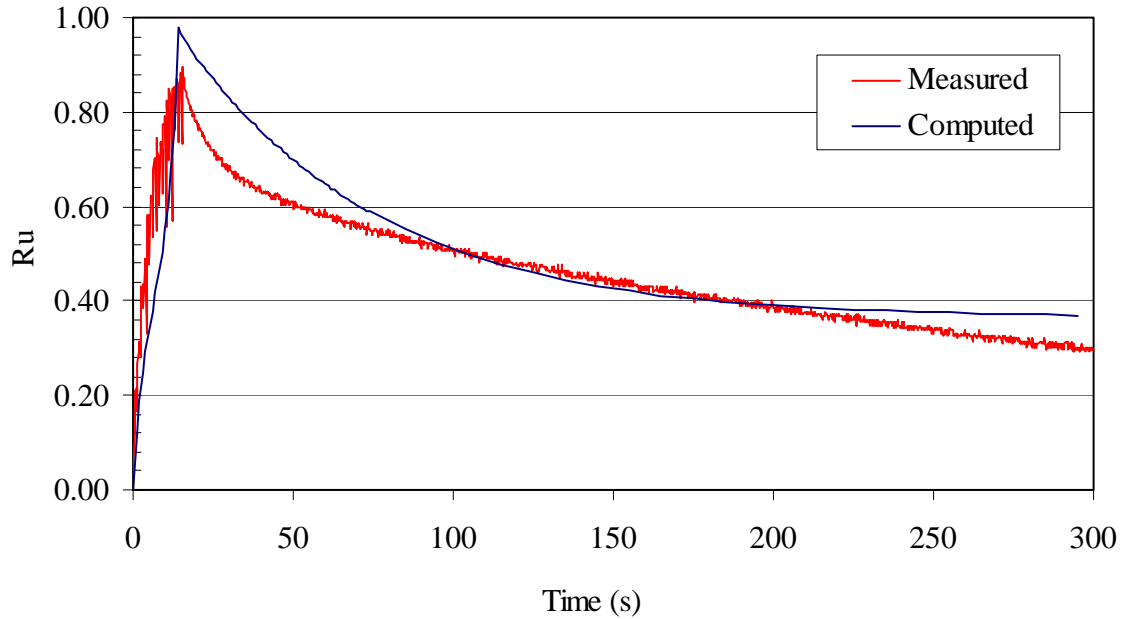


Figure 9.4 Comparison of measured and computed excess pore pressure ratios for the blast test at Site 3 at a depth of 6.7 m.

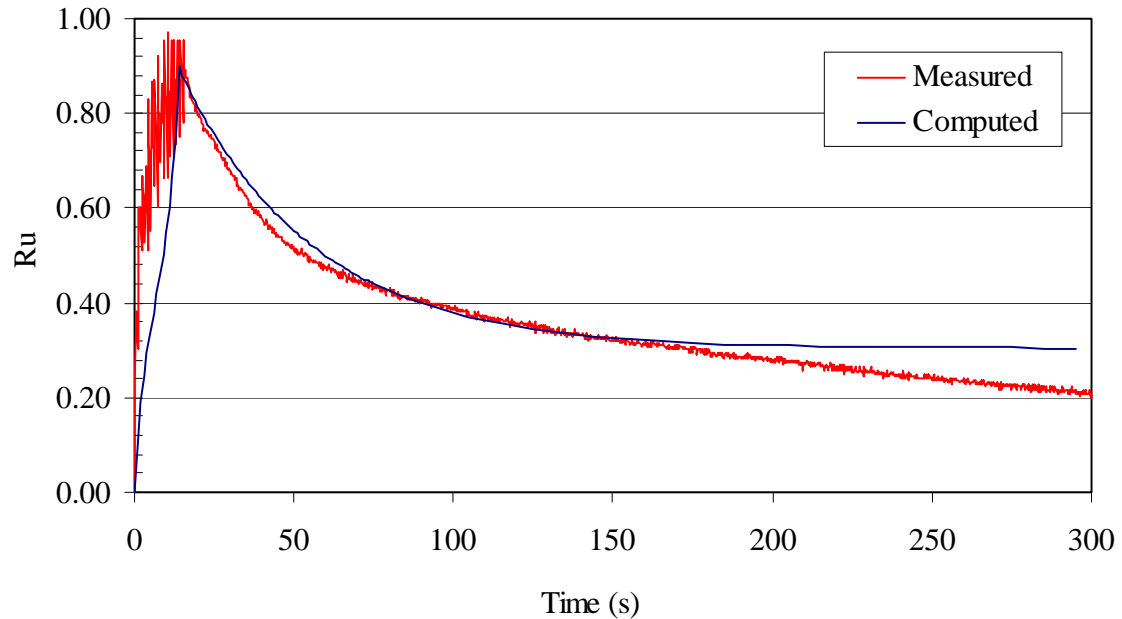


Figure 9.5 Comparison of measured and calculated excess pore pressure ratios for the blast test at Site 3 at a depth of 8.5 m.

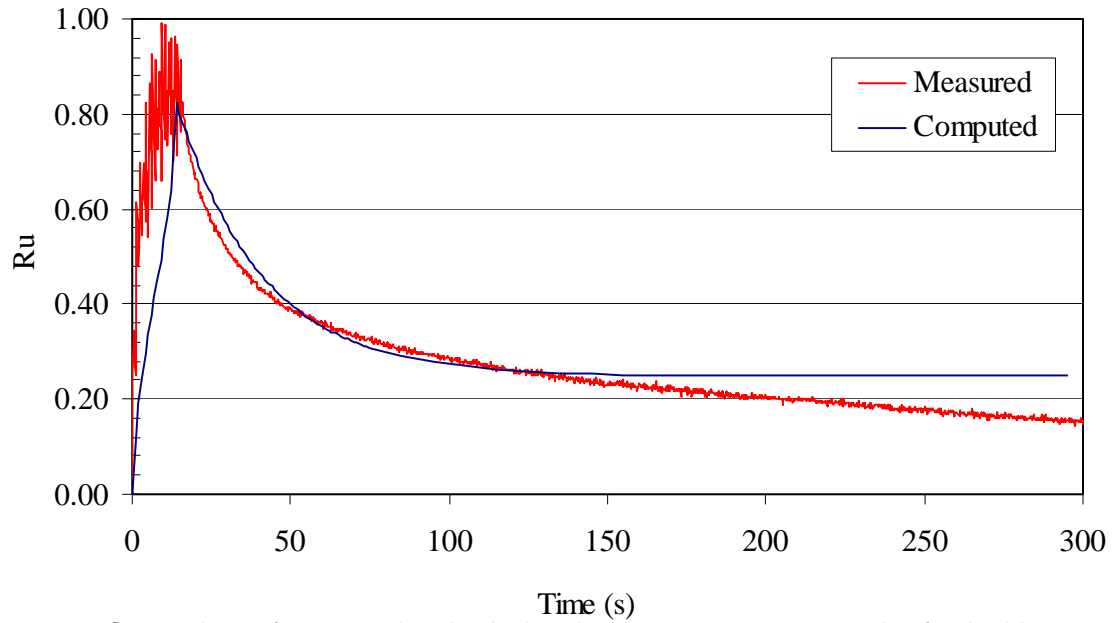


Figure 9.6 Comparison of measured and calculated excess pore pressure ratios for the blast test at Site 3 at a depth of 10.8 m.

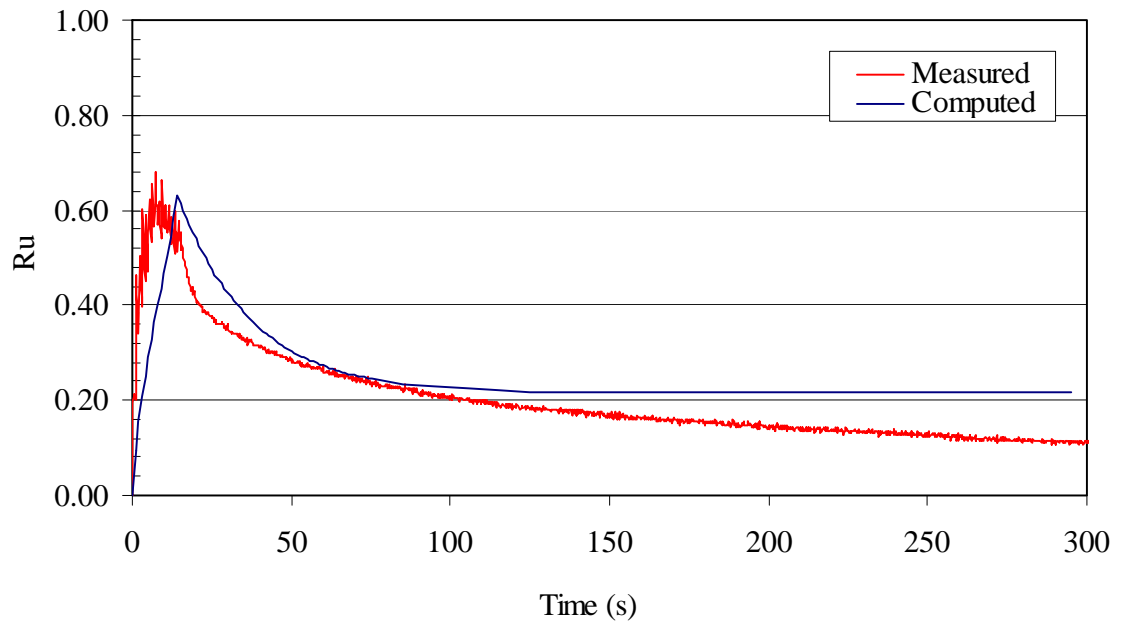


Figure 9.7 Comparison of measured and calculated excess pore pressure ratios for the blast test at Site 3 at a depth of 12.8 m.

While the portion of the calculated curves representing the generation of pore pressures do not match precisely the measured curves, in general the peak excess pore pressure ratios were successfully matched. Additionally, reasonable matches were found for the dissipation of pore pressures out to times between 150 and 200 seconds.

9.3 EQ Drain Performance with Different Drain Arrangements

Once a reasonable match was obtained with the pore pressure response for the blast events using FEQDrain, various drain size and spacing configurations were simulated to measure the efficacy of the EQ drains in preventing liquefaction. Table 9.4 provides a summary of the simulations performed. In all, three configurations were simulated: Simulation 1 used a smaller drain spacing; Simulation 2 used a larger drain diameter; and Simulation 3 used both a smaller drain spacing and larger drain diameter. Maximum values of measured R_u and maximum calculated values of R_u and settlement are also included in Table 9.4. The drain configuration used in the blast testing is also included for comparison.

Table 9.4. Summary of results for various drain size and spacing configuration simulations with FEQDrain.

Simulation/Test	Nominal drain diameter (cm)	Triangular drain spacing (m)	Maximum R_u	Maximum settlement (mm)
Blast test	10	1.22	0.98	156
Simulation 1	10	0.91	0.56	58
Simulation 2	15.25	1.22	0.63	66
Simulation 3	15.25	0.91	0.39	38

Calculated R_u time histories of the three simulations are compared with measured R_u time histories from the blast testing at Site 3 for depths of 6.7, 8.5, 10.8, and 12.8 m depth in Figures 9.8 through 9.11, respectively.

As can be seen in the table and figures representing the three trial simulations, all three configurations of drain size and spacings were successful in limiting the generation of pore pressures sufficiently to prevent liquefaction. As expected, Simulation 3 was the most successful inasmuch as it used a combination of smaller drain-to-drain spacings and a larger diameter drain.. Simulation 2, using just a smaller drain-to-drain spacing was the next most successful in limiting pore pressure generation. The least effective simulation was Simulation 2, which used just a larger drain diameter.

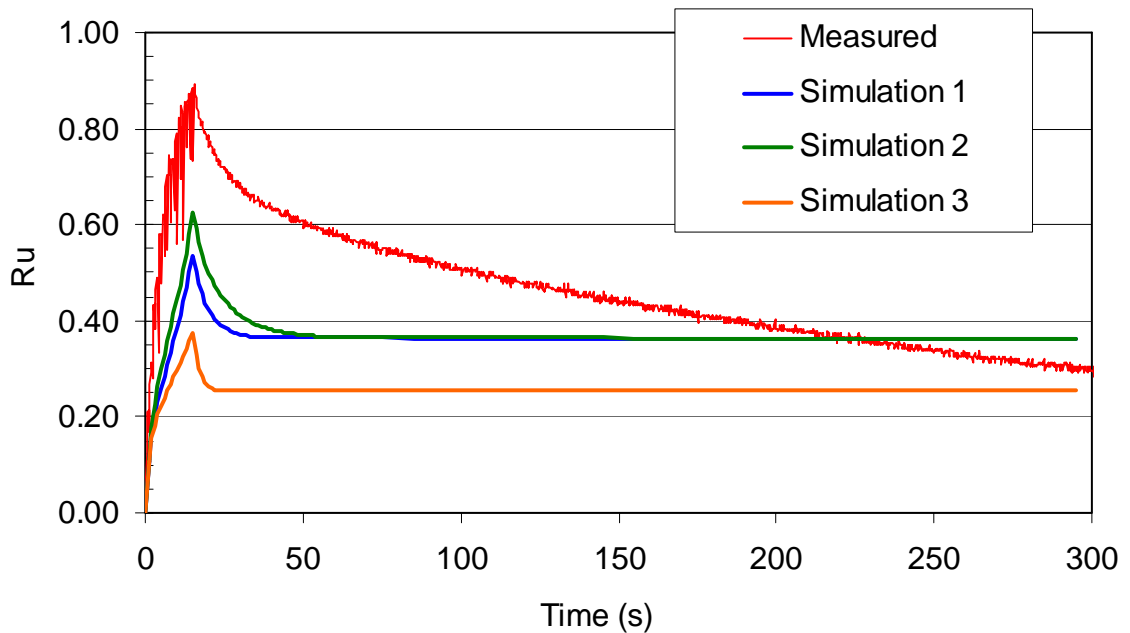


Figure 9.8 Comparison of R_u values measured during blast testing and calculated values for Simulations 1 through 3 at 6.7 m depth.

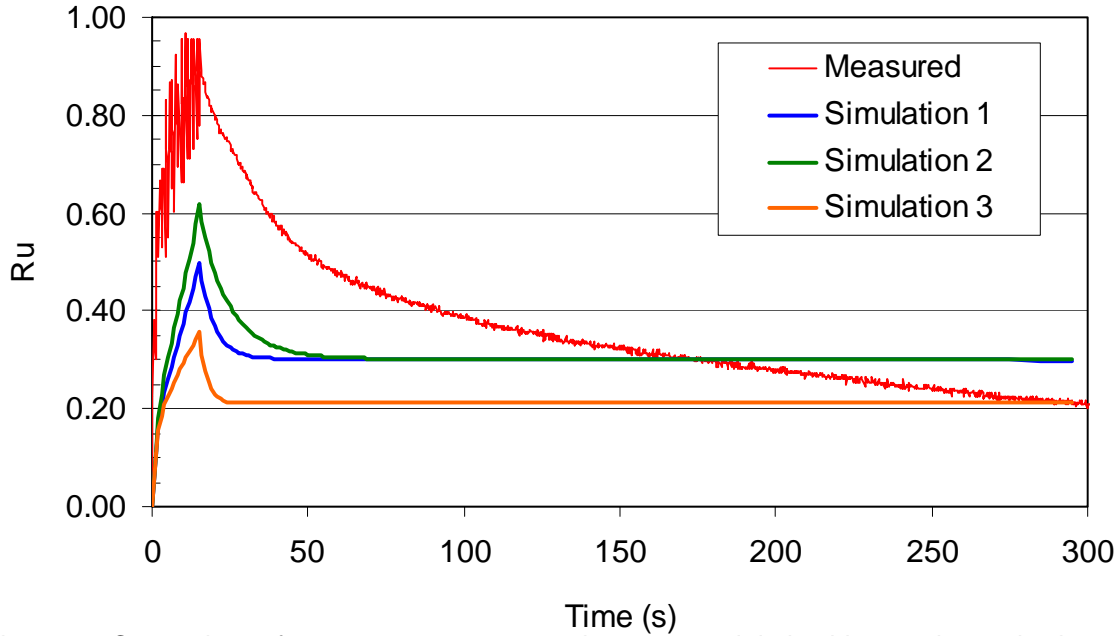


Figure 9.9 Comparison of excess pore pressure ratios measured during blast testing and values calculated by FEQDrain for Simulations 1 through 3 for a depth of 8.5 m.

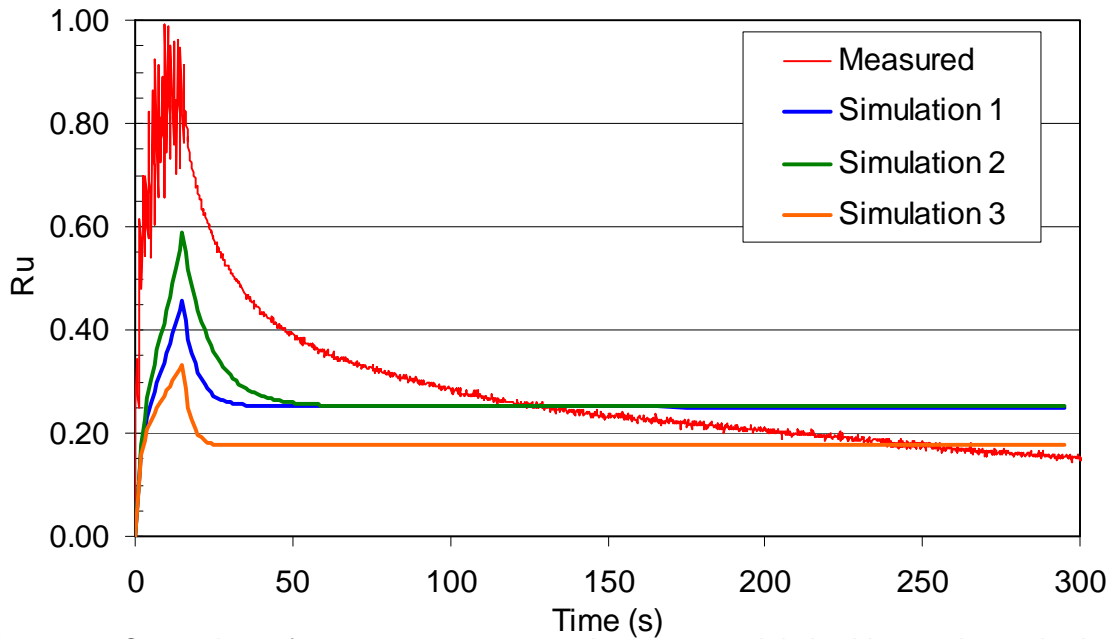


Figure 9.10 Comparison of excess pore pressure values measured during blast testing and values calculated by FEQDrain for Simulations 1 through 3 at a depth of 10.8 m.

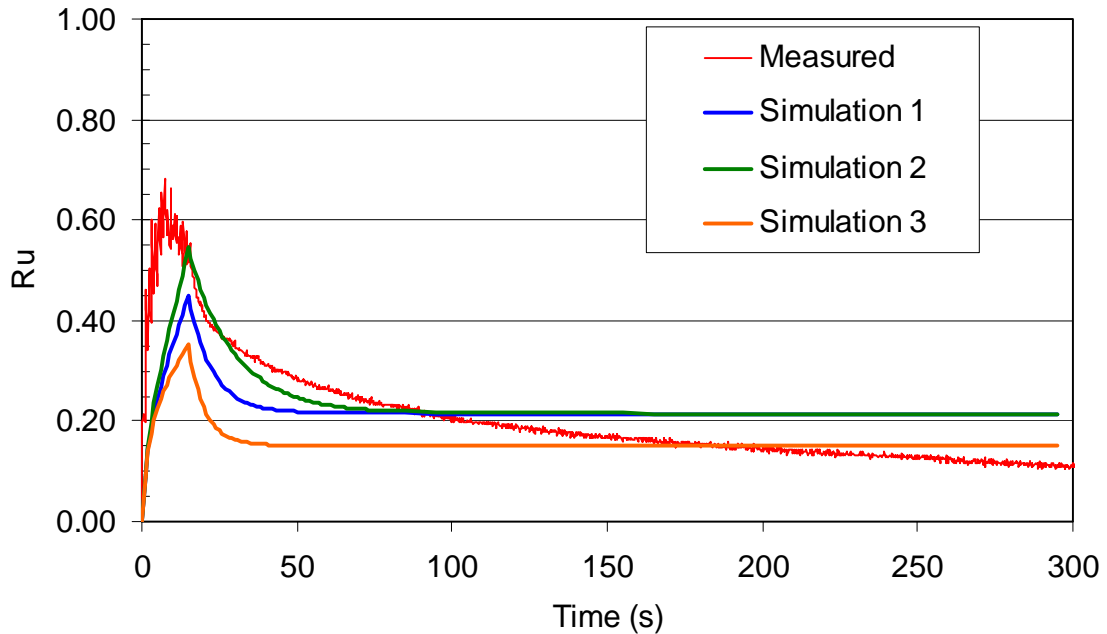


Figure 9.11 Comparison of excess pore pressure values measured during blast testing and values calculated by FEQDrain for Simulations 1 through 3 at a depth of 12.8 m.

9.4 EQ Drain Performance Under Different Earthquake Loadings

Inasmuch as the test blast loading does not directly correspond to any type of earthquake loading, it is instructive to estimate the maximum magnitude of earthquake for which the EQ drain configuration installed at Site 3 would have prevented liquefaction, herein termed the “maximum design earthquake.” FEQDrain was used to determine this magnitude.

FEQDrain utilizes two parameters to characterize the earthquake loading conditions—the equivalent number of cycles due to earthquake loading, N_{eq} , and the equivalent time of earthquake shaking, t_d , which is also called the duration of strong motion (Pestana *et al.*, 1997). These two parameters are often correlated with earthquake magnitude. Seed and Idriss (1982) developed the relationship between the equivalent

number of cycles due to earthquake loading and earthquake magnitude shown in Table 9.5. Seed *et al.* (1975) related the duration of strong motion to earthquake magnitude as shown in Table 9.6.

Table 9.5. Equivalent number of cycles due to earthquake load, N_{eq} (from Seed and Idriss, 1982).

Magnitude	N_{eq}
5.25	2-3
6	5-6
6.75	10
7.5	15
8.5	26

Table 9.6. Duration of earthquake strong motion (from Seed *et al.*, 1975).

Magnitude	Duration (s)
5.5-6	8
6.5	14
7	20
7.5	40
8	60

To change the magnitude of earthquake simulated by FEQDrain, only the parameters N_{eq} and t_d need be changed. In order to estimate the maximum design earthquake, a test magnitude was chosen with appropriate values of N_{eq} and t_d taken from Tables 9.5 and 9.6. For instance, a magnitude 7 event corresponds to $N_{eq} \approx 13$ and $t_d \approx 20$. After performing the analysis with FEQDrain, the calculated pore pressures were then compared against the limiting value. As discussed in Section 1.1.1, it appears that

excessive soil settlement can be adequately prevented if the maximum pore pressure ratio is limited to 0.4 (see Figure 1.6). Accordingly, FEQDrain analyses were performed using various values of N_{eq} and t_d until the maximum pore pressure ratio was less than or equal to 0.4. All other input parameters were maintained equal to the values used in the calibrated model.

Throughout blast testing and computer analysis, it was observed that at any given time, excess pore pressure ratios were greatest near the surface and decreased with increasing depth. This is most likely due to the upward flow of pore water caused by the blast or earthquake loading. This phenomenon is inter-related with the phenomenon described by Brennan and Madabhushi (2002) where the lowest layers of liquefied soil drain first, followed by the upper layers.

Several FEQDrain analyses were performed, changing the values of N_{eq} and t_d until the maximum excess pore pressure ratio within the liquefied zone reached 0.4. Table 9.7 contains a summary of the earthquake loading parameters and the results of the FEQDrain analysis that were produced at this level of shaking.

As might be expected, the limiting excess pore pressure ratio could not be obtained exactly, rather it was bracketed. The size of earthquake that produced the calculated excess pore pressure ratios in Table 9.7 is equivalent to approximately M6.5. Estimated settlement was limited to 23 mm, which is acceptable for almost all applications.

Table 9.7. Summary of input parameters and analysis results for the maximum design earthquake with limiting excess pore pressure ratio located at 5.5 m depth.

N_{eq}	t_d	Magnitud e	R_{u-max}	Settlement (mm)
9	15	6.5	0.38	23
9	14	6.5	0.41	23

9.5 Considerations in Design of Drain Spacing

The results of the testing and analysis clearly indicate the need for an accurate assessment of the horizontal permeability (hydraulic conductivity) of the soil in the profile when determining the required drain spacing. Perhaps the simplest and most reliable means of obtaining this information is to conduct borehole permeability tests at the site using a double packer approach as outlined in Designation E-18 in the Earth Manual published by the US Bureau of Reclamation (1974). This procedure makes it possible to evaluate the permeability in 1.5 to 3 m intervals along the length of the borehole. Alternatively, these permeability tests can also be performed inside one of the drains during installation to verify design assumptions. Although correlations can be used to estimate permeability coefficients, they must be chosen conservatively in order to ensure that overly optimistic values are not used. Use of conservative permeability values can easily lead to a design with an increased cost that greatly exceeds the cost of several simple *in situ* permeability tests.

The analysis also indicates the importance of evaluating the drain performance for a range of soil conditions rather than just a mean value to assure that performance will be satisfactory. Improved drain performance can be achieved by decreasing the drain spacing or increasing the drain diameter; however, these options have cost consequences.

For example, decreasing the drain spacing from 1.22 m spacing to 0.91 m spacing will increase the number of required drains by a factor of about 75% which will significantly increase the cost of the treatment.

Finally, the computer analysis highlights the importance of having a flexible numerical model which can easily incorporate variations in soil layer, soil properties and drain properties. Although simplified charts for selecting drain diameter and spacing have been developed by Seed and Booker (1977) and Onoue (1988), they generally do not allow an engineer to account for layered soil profiles and more complex boundaries which are often encountered in real-life applications.

10 Site 4—Statnamic Testing

Statnamic testing was undertaken in conjunction with Dr. Patricia Gallagher of Drexel University, who was investigating the liquefaction mitigation properties of colloidal silica grout (Gallagher *et al.*, 2007). Only the test results directly applicable to the development of downdrag will be presented here.

10.1 *Site Description*

The statnamic test site (Site 4) was located approximately 20 m northwest of Site 3 (see Figure 3.3). Due to the extensive subsurface characterization that had taken place previous to testing, it was assumed that the soil properties of the statnamic test site would be very similar to those of surrounding test sites. Nevertheless, a CPT sounding was performed prior to testing to provide site specific data. The CPT results for Site 4 are shown in Figure 10.1 together with the interpreted soil profile.

Figure 10.2 shows a comparison of cone tip resistance, Q_c , and relative density, D_r , measured by the first CPT performed at each of the four test sites. The CPT data from Sites 1 through 3 are grayed out slightly in order to show more clearly the results from the statnamic site. Figure 10.2 shows that the soil properties of the statnamic test site are generally similar to those of the other test sites. Notwithstanding, two relatively

large discrepancies are apparent, both occurring within the top 5.5 m of the soil profile. Between ground surface and 2 m depth, there is a large shift of both Q_c and D_r to the right, indicating that the soil within this interval is stronger and denser than that at the other sites. The second discrepancy occurs between 2.5 and 5 m depth. While the magnitude of the deflection of Q_c and D_r within this interval is equal to or less than that which occurred at the other test sites, the values do not decrease as rapidly with depth as occurred at the other sites. This indicates that the thin sand layer present at the other sites is much thicker at the statnamic site. This minor variation in soil profile is probably represents the remnants of a small stream channel that developed as the delta that makes up the test site evolved. Since the two deviations in soil profile occurred above the target zone of liquefaction, they should not have a negative impact on the liquefaction potential of the site.

10.2 Test Description

The statnamic test utilizes relatively slow-burning fuel pellets to accelerate a large mass vertically away from the top of a given test pile, exerting an axial force on the test pile. Depending upon the amount of fuel and size of reaction mass used, applied loads on the order of several meganewtons may be applied to the test pile without the need for the large and expensive load frames required for static tests of comparable load size. The relatively long burn time of the explosive charge allows the generated load to be applied for a relatively long time—long enough that the stress wave extends the full length of the pile before the load begin to dissipates. In this manner, a static load may be applied to a pile using dynamic loading techniques. thus giving rise to the term “statnamic.”

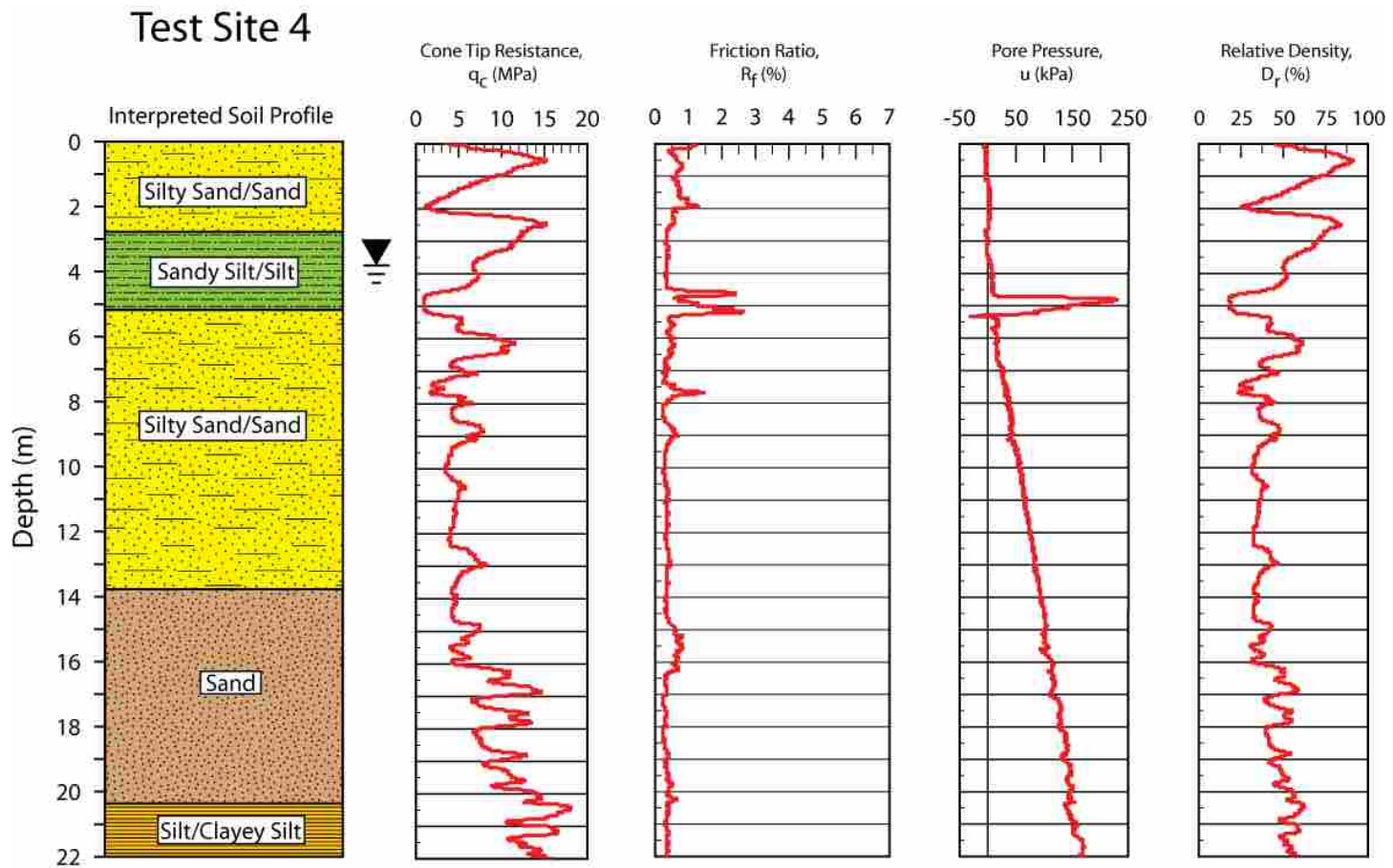


Figure 10.1 Results of the CPT sounding performed at Site 4.

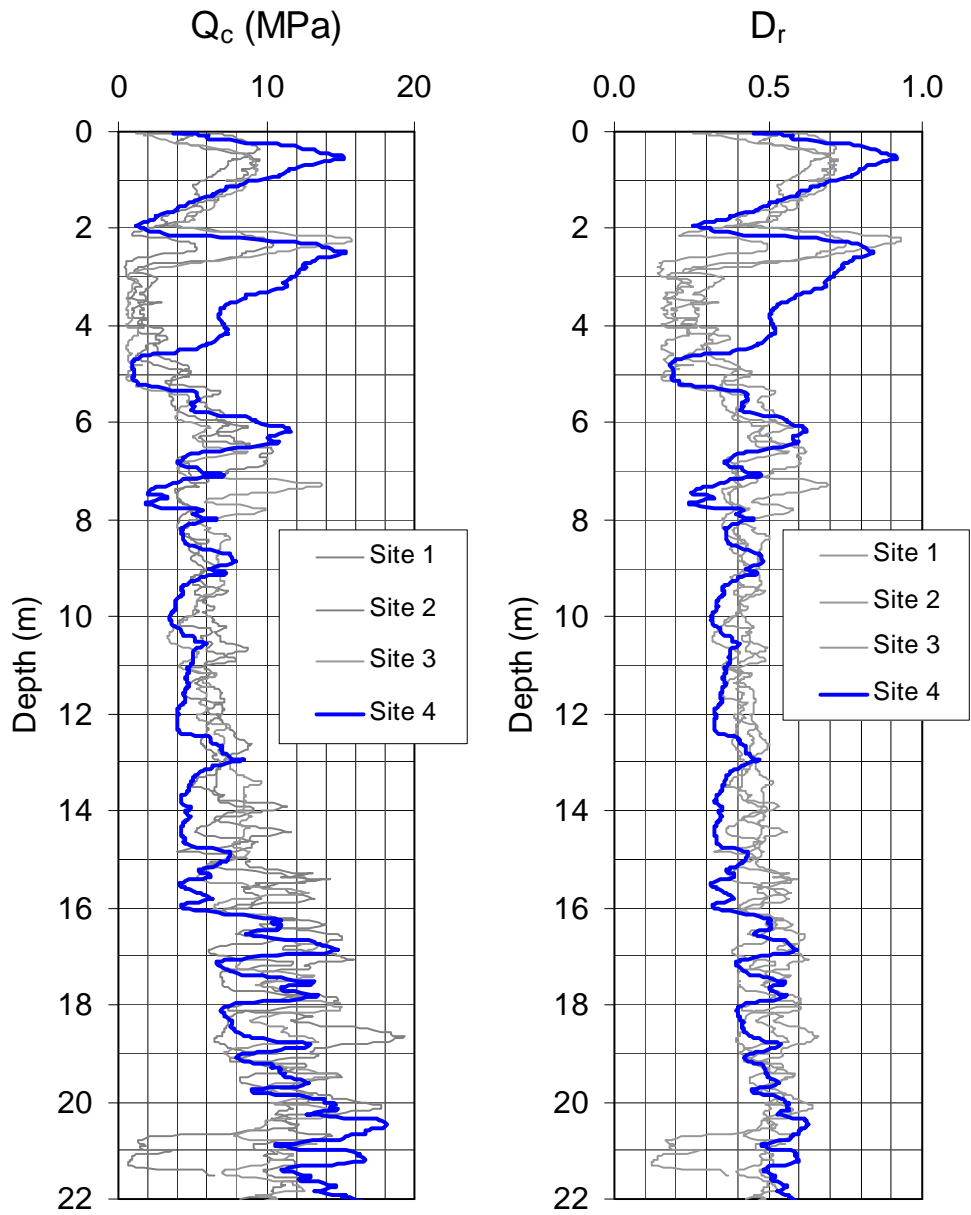


Figure 10.2 Comparison of cone tip resistance, Q_c , and relative density, D_r , for all four test sites from the first CPT soundings performed at each test site.

10.2.1 Test apparatus description

The statnamic testing apparatus as installed at the test site consisted of a central piston and silencer, several reaction masses, and a catch mechanism (see Figures 10.3 and 10.4). The piston, which holds the explosive charge, was secured to the top of the test pile. A combination pile cap/load cell placed between the pile and piston measured the load applied to the pile. The silencer rests on top of the piston and transfers the load from the explosive charge to the reaction masses. The reaction masses consisted of water-filled steel containers with circular openings at the center. These openings allowed the reaction masses to be lowered down over the silencer. The bottom-most mass rested on a large shoulder at the bottom of the silencer; each reaction mass was also securely attached to the silencer to ensure that the reaction mass-silencer assembly functioned as a single unit. The catch mechanism surrounded the entire assembly and served as a guide for the reaction mass-silencer assembly during testing. The catch mechanism also caught the mass-silencer assembly after the explosive charge had been detonated, preventing the assembly from impacting the piston. Further information regarding statnamic testing apparatus and its application can be found at <http://www.statnamic.com>.

10.3 Test Instrumentation and Monitoring

10.3.1 Test pile

A single test pile was driven at the center of the test site. The pile was identical to the test piles installed at both Sites 2 and 3—324 mm in diameter, 22 m in length, instrumented with 48 strain gauges (refer to Sections 5.1.1 and 5.1.2 for further information regarding the design and construction of the test piles). This test pile was

driven at the same time as the other piles, using the same procedures (see Section 5.1.3 for a complete description of the pile driving procedures).



Figure 10.3 Photograph of the static testing apparatus installed at Site 4.

10.3.2 Blast hole layout

Eight blast holes were located on the perimeter of a circle 10 m in diameter, centered about the test pile. A total of 16, 1.36 kg explosive charges (Pentex) were placed in the blast holes, creating two decks. The lower deck was placed at a depth of 8.5 m and the upper deck was placed at a depth of 6.4 m.

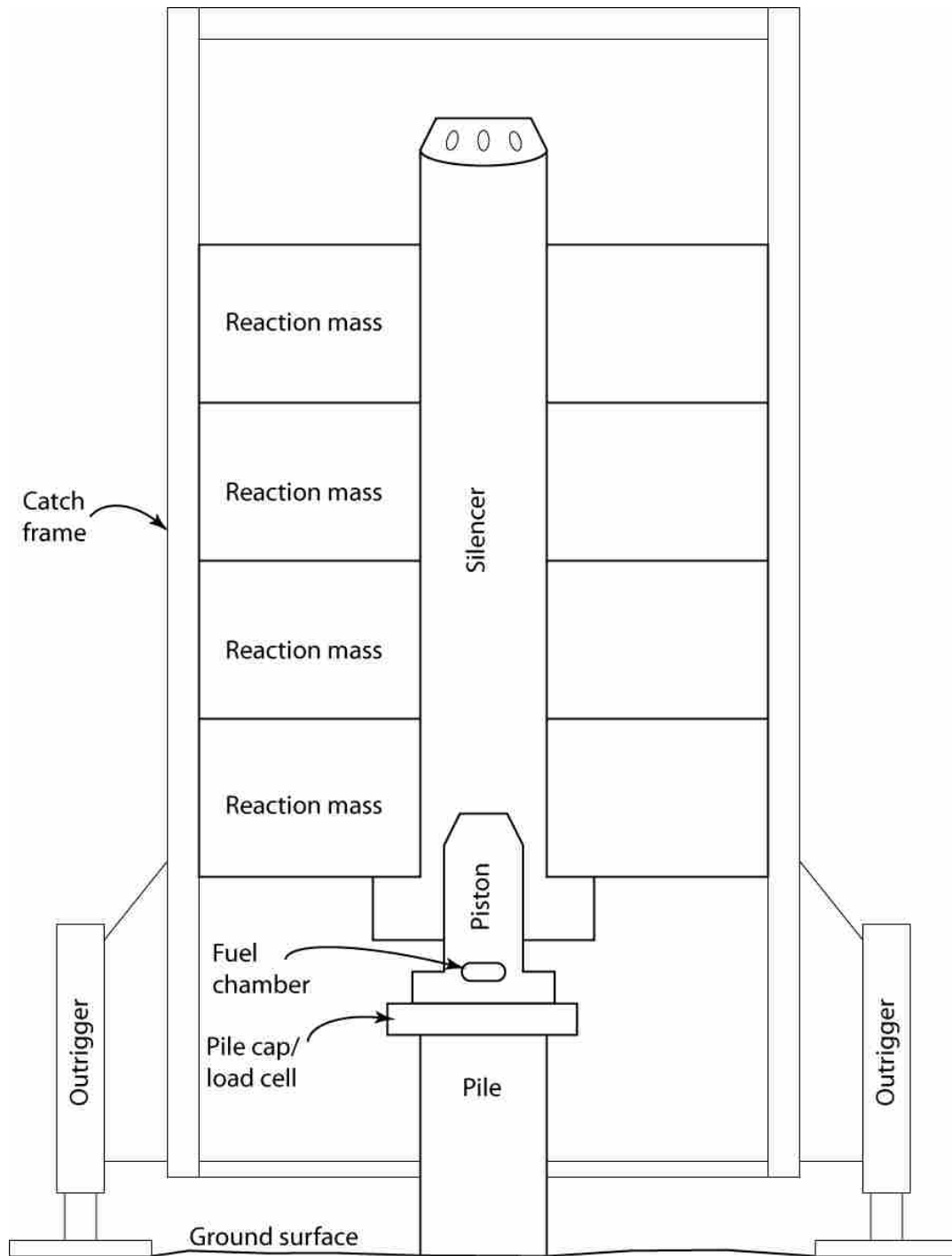


Figure 10.4 Schematic diagram of the static testing apparatus. Drawing not to scale.

10.3.3 Pore pressure monitoring

A single piezometer was installed to monitor pore pressures. This piezometer was installed to a depth of 6.7 m and was located approximately 2.75 m from the center of the test site. Installation of the piezometer followed the same procedures outlined in Section 4.3.

10.3.4 Settlement monitoring

Total ground surface settlement was measured using a level survey grid similar in design to those used at the other three test sites (see Section 4.4.1). In this case, however, only six rays were used instead of eight. Measurement points were located along each ray using the same spacings as used at the other test sites.

10.4 *Statnamic Load Testing*

In order to compare the ultimate strength of the test pile at Site 4, two statnamic tests were performed before blast testing. The corresponding load-deflection curves for the two tests are shown in Figure 10.5.

When both curves are considered together, the load-deflection curve is approximately linear up to a load of approximately 1250 kN. At this point, the curve begins to bend downwards, indicating the rate of strength development for a given amount of displacement begins to decrease. The applied load reached a maximum of approximately 1480 kN at a maximum deflection of 9.5 millimeters.

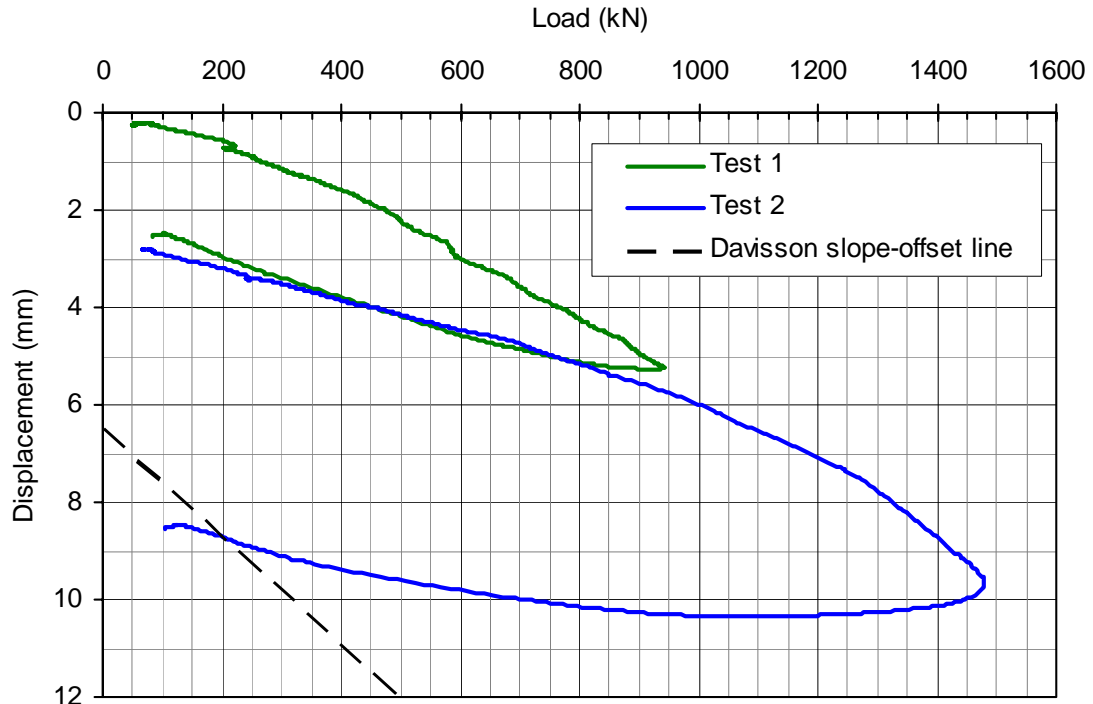


Figure 10.5 Pile-head-load versus pile-head-deflection curves from the two static load tests performed at Site 4.

While the maximum load applied during the second test exceeded the maximum sustained load during any of the static load tests performed at any other test site, the measured load-deflection curve did not intersect the Davisson slope-offset line. Thus, Davisson failure load is indeterminate. Furthermore, at the maximum load, the slope of the load depth curve is either parallel to or divergent from the slope of the Davisson line. Therefore, no estimate of the Davisson failure load is possible.

Nevertheless, comparisons made with the static load tests performed at Sites 2 and 3 may provide some insight into the bearing capacity of the static test pile. Figure 10.6 shows the load-deflection curves from the first load tests performed at Sites 2 and 3 and both load tests performed at Site 4.

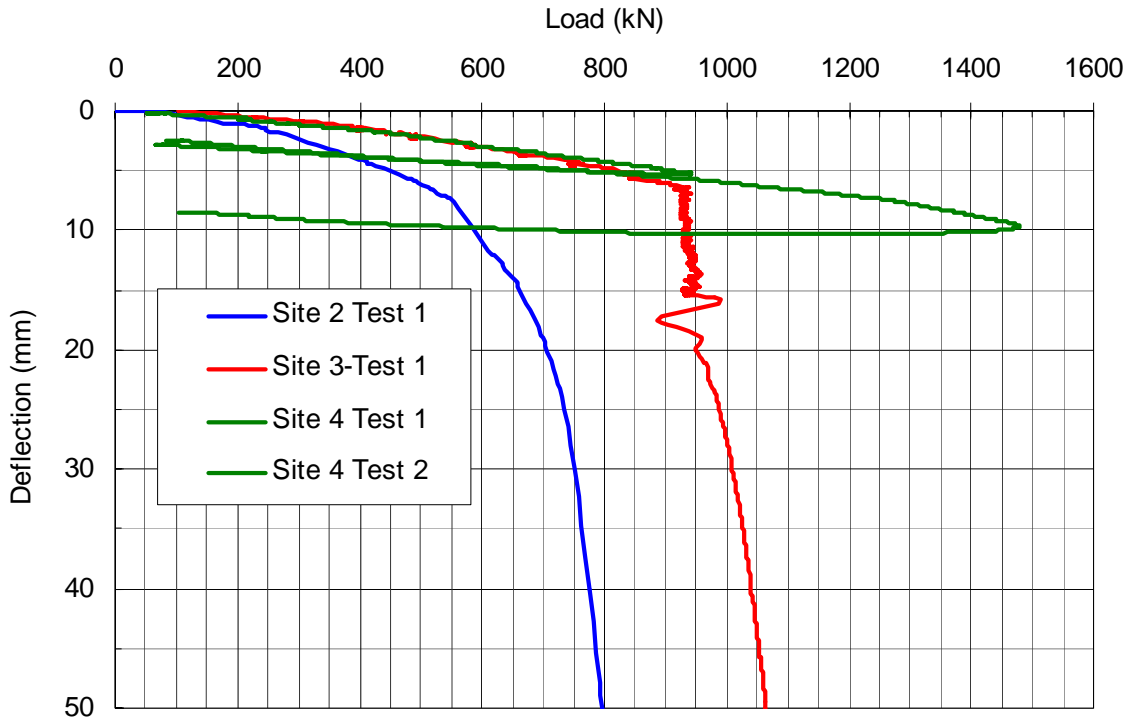


Figure 10.6 Comparison of pile-head-load versus pile-head-deflection curves for Sites 2, 3, and 4.

As can be seen in Figure 10.6, there is good agreement between the load-deflection curves from the first tests performed at Sites 3 and 4. Indeed, there is essentially no difference between the two curves up to a load of 650 kN, where they begin to diverge slightly. Then, at a load of about 925 kN, the load-deflection curve from Site 3 breaks rapidly away from that of Site 4.

Of course, the greatest difference is seen between the loads at which plunging of the pile began. At Site 2, the test pile began to settle quite rapidly at a load of 600 kN. At Site 3, the test pile began to plunge at 925 kN. On the other hand, the load-deflection curves from Site 4 do not indicate that the pile began to plunge. Indeed, the shape of the curve suggests that load in excess of 2000 kN could have been easily supported.

The increase in capacity may be attributed to strength gain with time and/or higher density within the upper layers of the soil profile. Load test results from Sites 2 and 3 suggest that the soil gains strength with increased time after pile driving. Whereas the static load tests were performed over three months after driving, it is reasonable to expect greater capacity. It is not clear, however, at what point the strength gain with time reaches a maximum.

Referring to Figure 10.2, it is seen that Site 4 exhibited slightly higher cone tip resistance within the upper 5 m of the soil profile, as compared to the other sites. The relative density was, thus, correspondingly higher. The greater relative density of the soil would result in higher side resistance of the pile, increasing the overall capacity.

10.5 Blast Testing

Blast testing was carried out using the same blasting sequence used at the other three test sites (see Section 4.1). Unfortunately, several wires connecting the explosive charges to the control unit were cut during blasting, leaving four live charges in the ground. Due to the premature termination of blasting, the static test was not initiated. Later, the four live charges were successfully detonated by the licensed blaster.

10.5.1 Ground surface settlement

Figure 10.7 shows the average settlement due to blast testing as measured by the level survey. As can be seen, the settlement curve has a similar shape to those produced at the other test sites, with the greatest amounts of settlement occurring near the center. Beyond 15 m from the center of site, essentially no settlement took place.

The greater amount of settlement at Site 4 is likely due to the fact that two distinct blast series took place. As mentioned previously, two explosive charges remained undetonated during blast testing; the two remaining charges were later detonated. However, due to safety concerns, no one was allowed to enter the test site until those two charges were detonated. This prevented measurement of the settlement caused by just the first blast. Thus, the settlement shown in Figure 10.7 is a result to two blast sequences.

When compared to other sites, the settlement at Site 4 is not unexpected. For instance, the total maximum settlement caused by the three blast sequences at Site 1 was approximately 570 mm while the total maximum settlement caused by the two blasts at Site 2 was approximately 440 mm, bracketing the maximum value at Site 4.

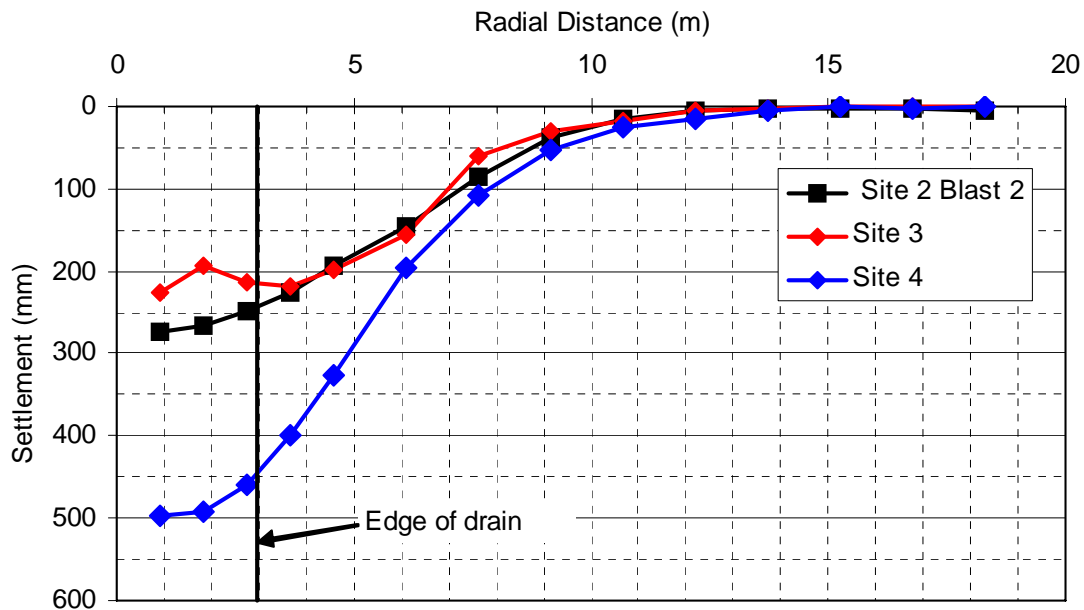


Figure 10.7 Average ground surface settlement versus distance caused by blasting at Site 4.

10.5.2 Pore pressure generation

Figure 10.8 shows the excess pore pressure ratio calculated from pore pressure data recorded at 6.7 m depth during the first 30 seconds of the blast test at Site 4. The detonations of the twelve charges are clearly shown by the spikes in R_u . Disregarding the peaks in pore pressure, the general response shows that the soil did indeed liquefy due to blasting. Figure 10.8 indicates that Site 4 produced a pore pressure response similar to those observed at both Sites 2 and 3, where liquefaction was reached after the detonation of 11 or 12 charges.

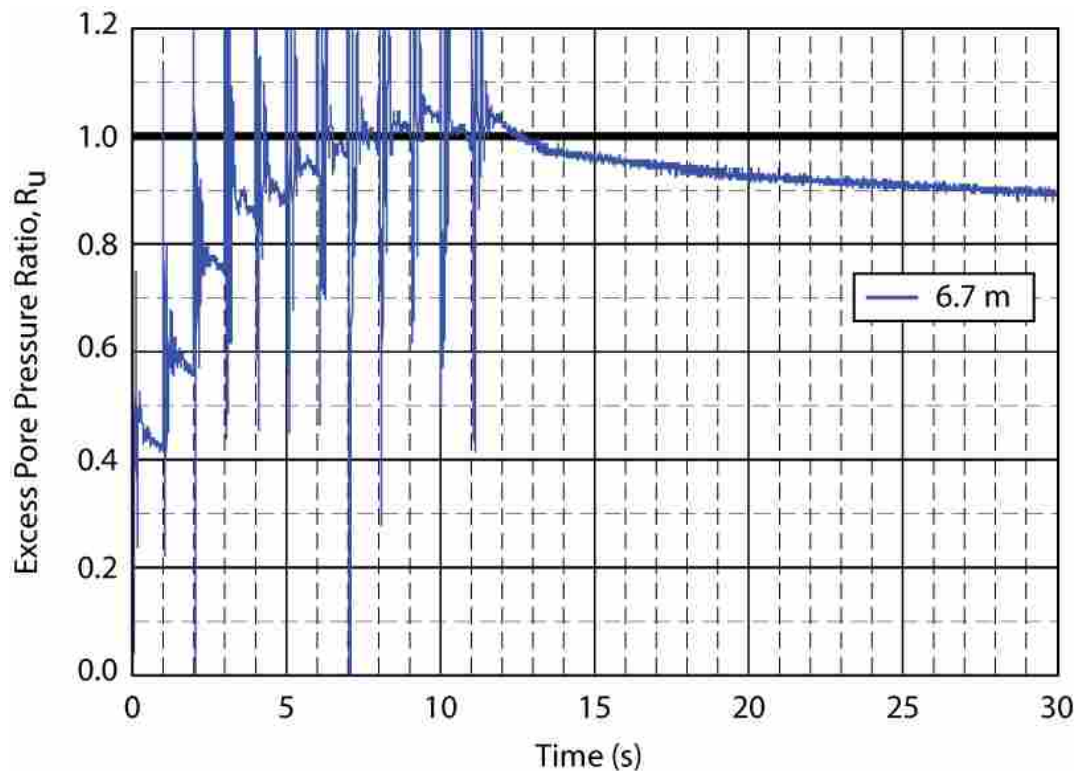


Figure 10.8 Generation of pore pressure during the blast test at Site 4.

10.5.3 Load transfer

Though the statnamic test was aborted, data recording continued uninterrupted, allowing the analysis of a the variation of load transfer in the test pile. In this case, the test pile experienced a static load, equal to the weight of the statnamic apparatus. Because the applied load remained constant, analysis of the load transfer data was not complicated by a fluctuating applied load as occurred at both Sites 2 and 3. Without the complications of a fluctuating load, any downdrag that develops should be much easier to see, with downdrag developing from the ground surface and continuing to the neutral plane. Such a curve is shown in Figure 2.2 and described by Bozozuk (1981).

Because the statnamic test pile had been installed for almost four months before testing occurred, strain gauge attrition was of concern. Gauge tests before blasting indicated that actual attrition rates were low. However, blasting caused the failure of a great number of gauges, causing data interpretation to be difficult.

Figure 10.9 compares the load-depth curve measured for the statnamic pile shortly after blasting with those of the other two test piles (Sites 2 and 3) as measured at the end of settlement. At the time represented by the load-depth curve from Site 4, the excess pore pressure ratio at 6.7 m depth was 0.99, indicating that the soil had become fully liquefied.

Though the load-depth curve recorded for the statnamic pile, as shown in Figure 10.9, is not as well-defined as those of the other two test piles, it is obvious that downdrag did indeed develop. Furthermore, downdrag began at the ground surface, just as expected. The fact that the “crust” produced downdrag at the statnamic site, when the

applied load remained constant throughout the test provides extra support to the theory that the fluctuating loads at Sites 2 and 3 produced positive skin friction in the crust.

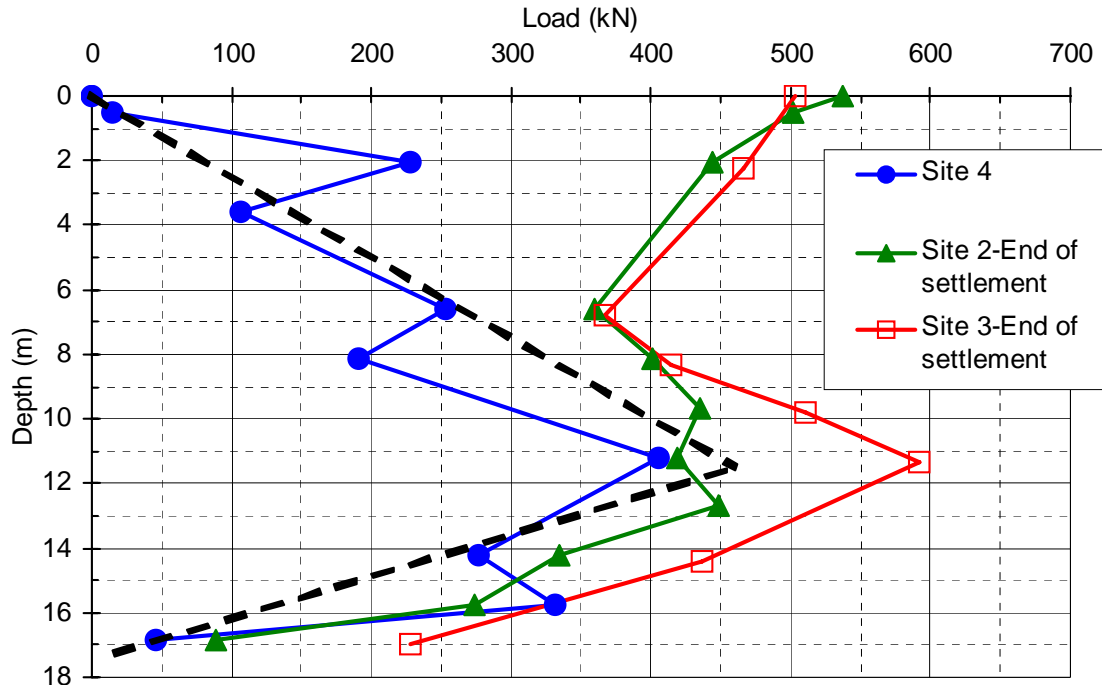


Figure 10.9 Comparison of load-depth curves from Sites 2, 3, and 4.

What is not obvious is the location of the neutral plane, the depth where the load-depth curve reverses slope. Under the loading conditions existing during the static blast test, one would expect that the neutral plane would occur somewhere near the bottom of the liquefied zone.

Theoretically, once liquefaction has occurred, the soil above the liquefied zone, the “crust,” will settle as a single unit, causing downdrag to develop beginning at ground surface. In addition, it is possible that downdrag will also develop within the liquefied zone itself as the liquefied soil settles and reconsolidates. If the sum of the applied load

and drag load is greater than the resistive forces acting on the pile below the zone of liquefaction, the pile will settle until force equilibrium is achieved. If pile settlement is sufficient, perhaps as little as 5 mm, the negative skin friction produced at the very bottom of the liquefied zone will reverse, generating positive skin friction, causing the neutral plane to adjust upwards into the liquefied zone. Whereas the static test pile extended approximately 8.5 m below the liquefied zone and the applied load was relatively small, it would not be expected that the test pile would need settle much to restore force equilibrium after the onset of liquefaction.

Visual analysis of the load-depth curves recorded at Sites 2 and 3 indicates that the neutral plane occurs at approximately 11.5 m depth, approximately one meter above the bottom of the liquefied zone. Thus far, the theory set out above seems to hold. With the relatively large loads applied to the test piles at Sites 2 and 3, one might expect that the pile settlement would have caused the neutral plane to adjust farther up into the liquefied zone. However, at Sites 2 and 3, downdrag developed only within the liquefied zone, reducing the load that may have otherwise occurred, necessitating less pile settlement to restore force equilibrium.

The dashed lines in Figure 10.9 represent the likely load versus depth profile at the site at the end of settlement. The upper line segment was based on the strain measurements at 0, 0.5, 3.8, and 6.6 m below the ground surface. The force introduced in the pile from the negative skin friction from the ground surface to 6 m depth (~250 kN) is approximately equal to the load transferred to the soil by positive skin friction at Sites 2

and 3. This agreement suggests that the dashed pile load versus depth curve is reasonable.

The lower dashed line segment is based on the strain measurements at depths of 14.2 and 16.8 m. The slope of this curve is also in reasonably good agreement with the slope of the curve in this depth range measured at Sites 2 and 3.

The slope of the dashed load versus depth segment in the liquefied soil zone from 6 m to 12 m is based primarily on the results from the tests at Site 2. Unfortunately, nearly all the strain gauges within this zone were apparently damaged by the blasting and the results from the remaining gauges are questionable. The dashed line segment splits the difference between the measured load at depths of 8 and 11.25 m.

Table 10.1 contains a summary of the skin friction values measured within the target zone during blast testing compared with values predicted by LCPC and the Eslami and Fellenius methods. The value from Site 4 was actually measured very shortly after the end of blasting, even though it is listed in the “End of settlement” column. Its placement is appropriate because the “End of settlement” column contains the values of skin friction developed due to liquefaction and subsequent settlement.

As can be seen, the negative skin friction developed at Site 4 compares reasonable well with that at Site 3. This agreement is probably due to effects from the grouting that had been performed at Site 4. As mentioned in Section 10, part of the testing performed at Site 4 involved the use of a colloidal silica grout to prevent liquefaction. A full description of the grouting procedures and results is beyond the scope of this dissertation

and will not be included here. Nevertheless, a short discussion is made here of the possible effects of the grouting on the reaction of the test pile.

Table 10.1. Comparison of unit side resistance (skin friction) values developed within the target zone immediately before blasting and at the end of settlement measured during the blast test at Sites 2, 3, and 4 with values predicted by the LCPC and Eslami and Fellenius methods.

	Skin Friction, 6 - 13 m (kPa)			
	Just before blasting	End of settlement	LCPC	Eslami and Fellenius
Site 2, Blast 1	7.97	-8.01	24.6	31.1
Site 2, Blast 2	26.6	-14.3	24.6	31.1
Site 3	17.2	-48.0	24.6	31.1
Site 4	N/A	-40.2	24.6	31.1

The blast test at Site 4 was performed after grouting with the colloidal silica had taken place. In short, the colloidal silica grout behaves as a gel, acting as an elastic binder between and around the particles of soil. It is conceivable that the grout prevented large scale deformations within the soil structure, allowing the bonds between the grouted soil and the test pile to remain essentially intact, thus allowing relatively large amounts of negative skin friction to develop. In addition, the absence of a fluctuating applied load did not continually disrupt the bonds between the test pile and soil, allowing even more negative skin friction to develop.

10.6 *Implications for Design of Deep Foundations*

A major objective of this study was to quantify the amount of downdrag that could be expected to develop on a pile foundation during liquefaction. As explained previously, downdrag may develop in two distinct parts of the soil profile—the upper, non-liquefied “crust,” and the lower, liquefied zone. The total amount of downdrag that develops on a pile is the sum of the two parts.

In the modified neutral plan solution developed by Boulanger and Brandenberg (2004), it was assumed that the amount of downdrag in the liquefied zone is negligible. Testing undertaken for this dissertation clearly shows this assumption is not necessarily correct. While pore pressures remain high within the liquefied zone, i.e., $R_u \approx 1.0$, the skin friction drops to essentially zero, causing no downdrag (see Figures 6.45 and 8.34). However, as pore pressures dissipate, skin friction returns, allowing downdrag to develop within the liquefied zone.

For the first blast test at Site 2, where no EQ drains were installed, negative skin friction after within the liquefied zone after blasting was essentially equal to the positive skin friction before blasting. During the second test at Site 2, negative skin friction in the liquefied zone was approximately one-half the value of the positive skin friction. At Site 3, where EQ drains were installed, negative skin friction within the liquefied zone was approximately equal to the positive skin friction. At Site 4, the negative skin friction was almost double that of the positive skin friction. With negative skin friction of comparable, or even greater magnitude as positive skin friction, it seems unwise to neglect the contribution to downdrag from within the liquefied zone.

The test results from the static test site clearly show that negative skin friction can develop in the non-liquefied soil above the liquefied layer in cases where the applied load remains constant. Therefore, in no instance should the dragload from the non-liquefied crust be ignored. In many cases, the greatest contribution to dragload could be produced by the non-liquefied crust.

The degree to which the downdrag within the liquefied zone affects the design of pile foundations depends upon the thickness of the liquefied layer. The thicker the layer, the greater the dragload that may develop. Therefore, downdrag within the liquefied layer may be safely ignored only when the liquefied zone is quite thin. On the other hand, when a thick liquefied zone exists near the surface, the non-liquefied crust may actually be quite thin relative to the liquefied zone. Under these conditions, the total dragload will arise almost entirely from the downdrag within the liquefied layer, the neglect of which would introduce very serious errors into the design.

Furthermore, while the magnitude of negative skin friction values measured in this study could provide easy rules of thumb for design, these values should only be used for design purposes with considerable judgement. The values of downdrag provided here constitute only the beginnings of a database of liquefaction-induced downdrag. Expansion of this database should be pursued before relationships regarding the development of appropriate negative skin friction are developed.

It is conceivable that many factors may influence the magnitude of negative skin friction that may develop on a pile due to liquefaction. For instance, as relative density increases, the negative skin friction after liquefaction is likely to increase. Other possible

influencing factors include pile material (steel vs. concrete), effective load, friction angle, and earth pressure coefficient, among others.

Negative skin friction would be expected to be higher for concrete piles than steel piles. In addition, negative skin friction might be expected to increase with increases in the vertical effective stress (or depth), friction angle, and earth pressure coefficient. To evaluate these hypotheses, additional field testing would be highly desirable.

11 Conclusions

From the foregoing data and subsequent analyses and interpretations, multiple conclusions can be drawn:

1. Besides providing drainage, EQ drains provide a side benefit of inducing significant settlement during installation. This leads to increased density and a lower compressibility which both reduce the amount of settlement and increase the rate of pore pressure dissipation relative to untreated sites. In this study, drain installation using vibration produced volumetric strain of about 2.9%.

2. The presence of earthquake drains (1.22 m drain spacing and 100 mm drain diameter), significantly increased the rate of excess pore water pressure dissipation relative to an untreated area, but did not prevent liquefaction for the blast sequence. Nevertheless, liquefaction induced settlement was reduced from about 270 mm at the untreated site to 220 mm at the site with drains, a reduction of 17%.

3. Computer analyses using FEQDrain, back-calculated from the measured response, indicate that the vertical drains could successfully limit pore pressure buildup and settlement for the same blast sequence with somewhat smaller drain spacing (0.9 m) or larger drain diameter (150 mm). Additional analyses indicate that the drain could prevent liquefaction and resulting settlement for less demanding earthquake events.

Lower-bound permeability values were necessary to calibrate the numerical model to the measured response. These results highlight the need to avoid overly optimistic permeability values in drain design.

4. Liquefaction at the site without drains (Site 2) initially reduced the side friction in the liquefied zone to approximately zero. As pore pressures dissipated and the sand settled, negative skin friction developed with a maximum values ranging from about one-half to one times the initial positive skin friction.

5. At the site treated with EQ drains (Site 3), negative skin friction developed in the liquefied zone almost immediately after the blasting ended. The negative skin friction had a magnitude almost three times larger than the positive skin friction prior to the blasting. The higher negative skin friction values at the site with drains relative to the untreated site is likely a result of the more rapid drainage which led to greater effective stress and hence greater skin friction during settlement.

6. Negative skin friction was not observed for the non-liquefied soil, or “crust,” above the liquefied zone at either Site 2 or Site 3, despite the fact that ground settlement exceeded 220 millimeters. This likely resulted from downward movement of the pile relative to the soil at the surface caused by the fluctuation in applied load during testing.

7. Negative skin friction was observed in the non-liquefied crust at Site 4, where the applied load on the pile remained constant.

8. The magnitude of negative skin friction values measured during testing are valid only for the specific conditions under which the test were performed. For instance, soils with different relative densities and at different depths will most likely cause

different amounts of downdrag from those measured in this study. Usage of the values of downdrag reported in this study for design purposes is not encouraged. Values reported here constitute only the beginnings of a database of measured values of downdrag induced by liquefaction.

9. The increased downdrag load produced by negative skin friction at all three test sites was resisted by increased friction and end-bearing resistance in the denser sand below the liquefied zone. Settlement of the test piles at Sites 2 and 3 was limited to less than 7 to 10 millimeters. Settlement of the static test pile was approximately 20 millimeters. The greater amount of settlement can be attributed to the greater amount of surface settlement at the static test site.

10. Although EQ drains have the potential to mitigate liquefaction hazard, the use of drains around piles to prevent negative skin friction does not generally appear to be a viable option. Analyses suggest that it will be very difficult to reduce settlement sufficiently to prevent negative friction. If negative friction does develop, test results suggest the magnitude will actually be greater if drains are used. This fact should not be overlooked if piled foundations are to be used in conjunction with EQ drains. Depending upon the thickness of the potentially liquefiable zone, the drag force produced by liquefaction could become quite great, causing excessive settlement to occur.

11. Computer analyses indicate that EQ drains have the potential to reduce settlement and pore pressures sufficiently to prevent damage to shallow foundations, slopes, embankments, retaining structures and other systems for many earthquake events.

12. Selection of an appropriate drain spacing should be accomplished using a numerical model such as FEQDrain which can account for variations in soil properties and drain properties. Horizontal permeability, which is critical to such analyses, should be measured in-situ to provide reliable designs and avoid unnecessary costs.

References

- Andrus, R.D. and Stokoe, K.H., II (2000). "Liquefaction resistance of soils from shear-wave velocity." *Journal of Geotechnical and Geoenvironmental Engineering*, 126(11), 1015-1025.
- Bozozuk, M. (1981). "Bearing capacity of pile preloaded by downdrag." *Proceedings, 10th International Conference on Soil Mechanics and Foundation Engineering, Vol. 2*, Stockholm, Sweden, 631-636.
- Boulanger, R.W and Brandenberg, S.J. (2004) "Neutral plane solution for liquefaction-induced downdrag on vertical piles." *Proceedings, ASCE Geo-Trans conference*, ASCE, Los Angeles, CA, 470-479.
- Brennan, A.J. and Madabhushi, S.P.G. (2002). "Effectiveness of vertical drains in mitigation of liquefaction." *Soil Dynamics and Earthquake Engineering*, 22(9), 1059-1065.
- Brennan, A.J. and Madabhushi, S.P.G. (2006). "Liquefaction remediation by vertical drains with varying penetration depths." *Soil Dynamics and Earthquake Engineering*, 26(5), 469-475.
- Bustamante, M., and Gianselli, L. (1982). "Pile bearing capacity predictions by means of static penetrometer CPT." *Proceedings, 2nd European symposium on penetration testing*, Amsterdam, Netherlands, 493-500.
- Eslami, A., and Fellenius, B.H. (1997). "Pile capacity by direct CPT and CPTu methods applied to 102 case histories." *Canadian Geotechnical Journal*, 34(6), 886-904.
- EQE (1995). "The January 17, 1995 Kobe Earthquake, Summary Report," <http://www.absconsulting.com/resources/Catastrophe_Reports/Kobe,%20Japan%20EQ%201995.pdf> (March 12, 2008).
- Fellenius, B.H., (1972). "Down-drag on piles in clay due to negative skin friction." *Canadian Geotechnical Journal*, 9(4), 323-337.

- Gallagher, P.M., Conlee, C.T., and Rollins, K.M., (2007). "Full-scale testing of colloidal silica grouting for mitigation of liquefaction risk." *Journal of Geotechnical and Geoenvironmental Engineering*, 133 (2), 186-196.
- Gohl, B. (2002). "Report on gravel drain testing at south end of George Massey Tunnel." *Prepared for Buckland & Taylor, Ltd. and British Columbia Ministry of Transportation, Pacific Geodynamics, Inc., Vancouver, BC, Canada.*
- Harada, N., Towhata, I., Takatsu, T., Tsunoda, and S., Sesoy, V. (2006). "Development of new drain method for protection of existing pile foundations from liquefaction effects." *Soil Dynamics and Engineering*, 26(2-4), 297-312.
- Holzer, T.L. (1998). "Introduction" The Loma Prieta, California, earthquake of October 17, 1989-Liquefaction, U.S. Geological Survey Professional Paper 1551-B, U.S. Government Printing Office, B1-B8.
- Johannessen, I.J. and Djerrum, L. (1965). "Measurement of the compression of a steel pile to rock due to settlement of the surrounding clay." *Proceedings, 6th International Conference on Soil Mechanics and Foundation Engineering, Vol. 2*, International Society for Soil Mechanics and Geotechnical Engineering, Montreal, Canada, 261-264.
- Kulhawy, F.H. and Mayne, P.W. (1990). Manual on estimating soil properties for foundation design, Electric Power Research Institute, Palo Alto, California, Research Report EERI EL-6800.
- Lee, K.L. and Albaisa, A. (1974) "Earthquake induced settlements in saturated sands." *Journal of Geotechnical Engineering Division, ASCE*, 100(GT4), 387-406.
- Lee, W. (2006). "Numerical modeling of blast-induced liquefaction." Doctoral dissertation, Brigham Young University, Provo, Utah.
- Lew, M. and Hudson, M. B., (2004). "Liquefaction basics." *Structure magazine*, June, 2004.
- Monahan, P.A., Luternauer, L., and Barrie, J.V., (1995). "The geology of the CANLEX phase II sites in Delta and Richmond British Columbia." *In Proceedings of the 48th Canadian Geotechnical Conference, Vancouver, B.C., pp. 59-68.*
- National Research Council (1985). "Liquefaction of soils during earthquakes." National Academy Press, 240 p.

- Onoue, A. (1988). "Diagrams considering well resistance for designing spacing ratio of gravel drains." *Soils and Foundations*, Japanese Soc. of Soil Mechanics and Foundation Engineering, 28(3), 160-168.
- Pestana, J.M., Hunt, C.E. and Goughnour, R.R. (1997). "FEQDrain: A finite element computer program for the analysis of the earthquake generation and dissipation of pore water pressure in layered sand deposits with vertical drains," Earthquake Engineering Research Center, Report No. UCB/EERC 97-17
- Rathje, E.M., Chang, W.-J, Cox, B.R., and Stoke, K.H.II (2004). "Effect of prefabricated vertical drains on pore pressure generation in liquefiable sand." *Proceedings, 11th International conference on soil dynamics and earthquake engineering*, Stallion Press, Vol. 2, 529-536.
- Robertson, P.K., Campanella, R.G., Gillespie, D., and Grieg, J. (1986). "Use of piezometer cone data". *Proceedings, Use of in-situ tests in geotechnical engineering*, ASCE, Blacksburg, VA, 1263-80.
- Robertson, P.K., Wride, C.E., List, B.R., Atukorala, U., Biggar, K.W., Byrne, P.M., Campanella, R.G., Cathro, D.C., Chan, D.H., Czajewski, K., Finn, W.D.L., Gu, W.H., Hammamji, Y., Hofmann, B.A., Howi, J.A., Hughes, J. Imrie, A.S., Kinrad, J.M., Küpper, A., Law, T., Lord, E.R.F., Monahan, P.A., Morgenstern, N.R., Phillips, R., Piché, R., Plewes, H.D., Scott, D., Segó, D.C., Sobkowicz, J., Stewart, R.A., Watts, B.D., Woeller, D.J., Youd, T.L., and Zavodni, Z., (2000). "The Canadian Liquefaction Experiment: an overview." *Canadian Geotechnical Journal*, 37(3), 499-504.
- Rollins, K. M. and Anderson, J.K.S., 2004. "Performance of vertical geocomposite drains based on full-scale testing at Massey Tunnel, Vancouver, B.C.", Final Report, NCHRP-IDEA Project 94, Transportation Research Board, Washington, D.C., 107 p
- Rollins, K.M., Goughnour, R.R., Anderson J.K.S. and McCain, A. (2004). "Liquefaction hazard mitigation using vertical composite drains." *Procs. 13th World Conf. on earthquake Engineering*, Earthquake Engineering Research Institute, Vancouver, B.C., 210-220.
- Rollins, K.M., Lane, J.D., Dibb, E., Ashford, S.A., and Mullins, A.G. (2005). "Pore pressure measurement in blast-induced liquefaction experiments." *Transportation Research Record 1936, "Soil Mechanics 2005"*, Transportation Research Board, Washington DC, p. 210-220.

- Seed, H.B., Martin, P.P., and Lysmer, J. (1975a). "The generation and dissipation of pore water pressures during soil liquefaction." Earthquake Engineering Research Center, Report No. UCB/EERC 75-26.
- Seed, H.B., Idriss, I.M., Makdisi, F., and Mannerjee, N. (1975b). "Representation of irregular stress time histories by equivalent uniform stress series in liquefaction analyses." Earthquake Engineering Research Center, Report No. UCB/EERC 75-29.
- Seed, H.B., and Booker, J.R. (1977). "Stabilization of potentially liquefiable sand deposits using gravel drains," *Journal of Geotechnical Engineering Division*, ASCE, 103(GT7), 757-768.
- Seed, H.B., and Idriss, I.M. (1982). "Ground motions and soil liquefaction during earthquakes." Earthquake Engineering Research Institute, 83 pages.
- Tokimatsu, K., and Seed, H.B. (1987). "Evaluation of settlements in sands due to earthquake shaking," *Journal of Geotechnical and Environmental Engineering*, 103(8), 861-878.
- Tucker, L. M., and Briaud, J. L. (1986). "User's Manual for PILECPT." Texas A&M University, Civil Engineering Department, 25 pages.
- U.S. Bureau of Reclamation (1974). "Earth Manual, 2nd Edition." U.S. Department of the Interior, U.S. Government Printing Office, Washington, D.C., 573-593.
- Wride, C.E (Fear), Robertson, P.K., Biggar, K.W., Campanella, R.G., Hofman, B.A., Hughes, J.M.O., Küpper, A., and Woeller, D.J. (2000). "Interpretation of in situ test results from the CANLEX sites," *Canadian Geotechnical Journal*, 37(3), 505-529.
- Youd, T.L., Idriss, I.M., Andrus, R.D., Arango, I., Castro, G., Christian, J.T., Dobry, R., Finn, W.D.L., Harder, L.F., Hynes, M.E., Ishihara, K., Koester, J.P., Liao, S.S.C., Marcuson, W.F., Martin, G.R., Mitchell, J.K., Moriwaki, Y., Power, M.S., Robertson, P.K., Seed, R.B., and Stokoe, K.H. (2001). "Liquefaction resistance of soils: Summary report from the 1996 NCEER and 1998 NCEER/NSF workshops on evaluation of liquefaction resistance of soils." *Journal of Geotechnical and Geoenvironmental Engineering*, 127(10), 817-833.

Appendix A

Table A1. Summary of pile driving data for the pile foundation installed at Site 2.

Pile:	Test Pile		NE		NE		SE		SW	
Depth (m)	Drop Height (m)	Blows	Drop Height (m)	Blows	Drop Height (m)	Blows	Drop Height (m)	Blows	Drop Height (m)	Blows
0.3	0.6	9					0.6	6		
0.6	0.6	8	0.6	10			0.6	5		
0.9	0.9	8	1.2	4	1.2		0.9	4	0.9	12
1.2	0.9	7	1.2	3	1.2		0.9	5	0.9	4
1.5	0.9	8	1.2	3	1.2	10	1.2	4	1.2	5
1.8	0.9	8	1.2	0	1.2	2	1.2	4	1.2	3
2.1	0.9	6	1.2	4	1.2	2	1.2	4	1.5	4
2.4	1.2	5	1.5	2	1.2	1	1.2	5	1.5	4
2.7	1.2	4	1.5	1	1.2	2	1.2	4	1.2	4
3.0	0.9	7	1.5	2	1.2	2	1.5	3	1.2	3
3.4	0.9		1.5	3	1.2	3	1.5	3	1.5	3
3.7	0.9	8	1.5	2	1.2	2	1.5	3	1.5	3
4.0	0.9	3	1.5	3	1.2	2	1.5	3	1.5	2
4.3	0.9	3	1.5	3	1.5	3	1.5	2	1.5	3
4.6	1.2	4	1.5	4	1.5	3	1.5	3	1.5	4
4.9	1.2	4	1.5	3	1.5	2	1.5	4	1.5	3
5.2	1.2	6	1.5	3	1.5	2	1.5	4	1.5	4
5.5	1.2	8	1.5	3	1.5	3	1.5	6	1.5	5
5.8	1.2	6	1.5	4	1.5	4	1.5	6	1.5	5
6.1	1.8	7	1.5	6	1.5	5	1.5	6	1.5	6
6.4	1.8	6	1.5	6	1.5	5	1.5	7	1.5	8
6.7	1.8	6	1.5	7	1.5	6	1.5	6	1.5	6
7.0	1.8	5	1.5	6	1.5	6	1.5	6	1.5	6
7.3	1.8	4	1.5	6	1.5	7	1.5	6	1.5	5
7.6	2.1	4	1.5	6	1.5	6	1.5	6	1.5	6
7.9	2.1	4	1.5	8	1.5	6	1.5	6	1.5	6

Table A1. Continued

Pile:	Test Pile		NE		NE		SE		SW	
	Drop Height (m)	Blows	Drop Height (m)	Blows	Drop Height (m)	Blows	Drop Height (m)	Blows	Drop Height (m)	Blows
8.2	2.1	5	1.5	8	1.5	7	1.5	6	1.5	7
8.5	2.1	5	1.5	8	1.5	7	1.5	6	1.5	7
8.8	2.1	5	1.5	6	0.6	10	1.5	9	1.5	7
9.1	2.1	5	1.5	6	1.5	7	1.5	9	1.5	8
9.4	2.1	5	1.5	6	1.5	7	1.5	9	1.5	9
9.8	2.1	6	1.5	9	1.5	7	1.5	8	1.5	10
10.1	2.1	6	1.5	10	1.5	5	1.5	9	1.5	10
10.4	2.1	8	1.5	9	1.5	6	1.5	10	1.5	9
10.7	2.1	9	1.5	8	1.8	6	1.5	10	1.5	11
11.0	2.1	7	1.5	10	2.1	6	1.5	12	1.5	13
11.3	2.1	9	1.5	10	2.1	7	1.5	11	1.5	15
11.6	2.1	10	1.5	11	2.1	7	1.5	10	1.5	15
11.9	2.1	9	1.5	0	2.1	7	0.6	10	1.8	0
12.2	2.1	10	2.1	8	2.1	9	1.2	0	1.8	11
12.5	2.1	12	2.1	7	2.1	9	2.4	7	2.1	8
12.8	2.1	10	2.4	10	2.1	9	2.4	6	2.1	9
13.1	2.1	11	2.4	4	2.1	10	2.4	7	2.1	5
13.4	2.1	11	2.4	5	2.1	11	3.0	6	2.1	9
13.7	2.1	11	2.4	6	2.1	11	3.0	5	2.1	8
14.0	2.1	13	2.4	6	2.1	13	3.0	6	2.1	8
14.3	2.1	13	2.4	7	2.1	12	3.0	0	2.1	9
14.6	2.1	12	2.4	7	2.4	13	3.0	6	2.1	8
14.9	2.1	14	2.4	7	2.4	13	3.0	0	2.1	9
15.2	2.1	12	2.7	7	2.4	12	3.0	6	2.1	10
15.5	2.1	12	2.7	7	2.4	13	3.0	7	2.1	10
15.8	2.1	11	2.7	7	1.8	15	3.0	6	2.1	9
16.2	2.1	13	2.7	9	1.8	13	3.0	0	2.1	10
16.5	2.1	13	2.7	10	1.8	0	3.0	7	2.1	11
16.8	2.1	14	2.7	8	1.8	0	3.0	6	2.1	11
17.1	2.1	14	2.7	9	1.8	14	3.0	7	2.1	9
17.4	2.1	11	2.7	9	2.4	12	3.0	7	2.1	10
17.7	2.1	12	2.7	9	2.4	13	3.0	8	2.1	10
18.0	2.1	14	2.7	9	2.4	15	3.0	8	2.1	11
18.3	2.1	13	2.7	8	2.4	13	3.0	8	2.1	9
18.6	2.1	12	2.7	9	2.4	15	3.0	9	2.1	9
18.9	2.1	14	2.7	10	2.4	17	3.0	8	2.1	10
19.2	2.1	14	2.7	11	2.7	13	3.0	10	2.1	11

Table A1. Continued

Pile:	Test Pile		NE		NE		SE		SW	
	Drop Height (m)	Blows	Drop Height (m)	Blows	Drop Height (m)	Blows	Drop Height (m)	Blows	Drop Height (m)	Blows
19.5	2.1	15	2.7	11	2.7	14	3.0	12	2.1	12
19.8	2.1	16	2.7	11	2.7	0	3.0	11	2.1	12
20.1	2.1	17	2.7	11	2.7	14	3.0	11	2.1	13
20.4	2.1	15	2.7	12	2.7	16	3.0	9	2.1	11
20.7	2.1	14	2.7	12	2.7	13	3.0	0	2.1	11
21.0	2.1	8	2.7	12	2.7	13	3.0	10	2.1	12
21.3			2.7	15	2.7	12	3.0	11	2.1	11
21.6			2.7	14	2.7	12	3.0	12	2.1	13

Table A2. Summary of pile driving data for the pile foundation installed at Site 3.

Pile:	Test Pile		NE		NE		SE		SW	
	Drop Height (m)	Blows	Drop Height (m)	Blows	Drop Height (m)	Blows	Drop Height (m)	Blows	Drop Height (m)	Blows
0.3	0.6	6	1.5	1			0.6	1	1.2	
0.6	0.6	8	1.5	1	1.2		0.6	1	1.2	1
0.9	0.6	10	1.5	3	1.2	8	0.6	1	1.2	1
1.2	0.6	8	1.5	1	1.2	3	0.6	2	1.2	1
1.5	0.9	8	1.5	6	1.2	4	0.6	2	1.2	1
1.8	0.9	9	1.5	2	1.2	4	0.9	2	1.2	2
2.1	0.9	8	1.5	2	1.2	3	0.9	1	1.2	2
2.4	0.9	6	1.5	2	1.2	3	0.9	4	1.2	3
2.7	0.9	4	1.5	3	1.2	3	0.9	3	1.2	3
3.0	0.9	6	1.5	2	1.2	3	0.9	7	1.2	5
3.4	0.9	4	1.5	3	1.2	2	0.9	5	1.2	5
3.7	0.9	4	1.5	2	1.5	3	1.2	4	1.2	4
4.0	0.9	4	1.5	3	1.5	3	1.2	4	1.2	3
4.3	0.9	4	1.5	2	1.5	2	1.2	3	1.2	2
4.6	0.9	3	1.5	3	1.5	3	1.2	3	1.2	3
4.9	0.9	4	1.5	3	1.5	3	1.2	2	1.2	3
5.2	0.9	2	1.5	3	1.5	4	1.2	3	1.2	4
5.5	1.8	8	1.5	4	1.5	4	1.2	4	1.5	5
5.8	1.8	8	1.5	3	1.5	4	1.2	6	1.5	5

Table A2. Continued

Pile:	Test Pile		NE		NE		SE		SW	
	Drop Height (m)	Blows	Drop Height (m)	Blows	Drop Height (m)	Blows	Drop Height (m)	Blows	Drop Height (m)	Blows
6.1	1.8	7	1.5	3	1.5	4	1.2	6	1.5	5
6.4	2.4	6	1.5	4	1.5	4	1.2	5	1.5	6
6.7	2.4	7	1.5	5	1.5	5	1.2	6	1.5	7
7.0	2.4	6	1.5	5	1.5	4	1.2	7	1.5	7
7.3	2.4	6	1.5	4	1.5	5	1.2	7	1.5	9
7.6	2.4	5	1.5	5	1.5	5	1.2	9	1.8	9
7.9	2.4	5	1.5	6	1.5	5	1.2	8	1.5	8
8.2	2.4	6	1.5	6	1.5	5	1.2	7	1.5	8
8.5	2.4	5	1.5	6	1.5	5	1.2	8	1.5	8
8.8	2.4	5	1.5	6	1.5	5	1.2	8	1.5	9
9.1	2.4	4	1.8	6	1.5	6	1.2	10	1.5	10
9.5	2.4	4	1.8	8	1.5	8	1.2	11	1.5	10
9.8	2.4	5	1.5	8	1.5	7	1.2	11	1.5	10
10.1	2.4	6	1.5	7	1.5	7	1.2	11	1.5	9
10.4	2.4	5	1.5	8	1.5	8	1.2	12	1.5	10
10.7	2.4	5	1.5	7	1.5	8	1.2	13	1.5	10
11.0	2.4	6	1.5	9	1.5	8	1.2	11	1.5	12
11.3	2.4	6	1.5	9	1.5	9	1.2	11	1.5	15
11.6	2.4	6	1.5	11	1.5	12	1.2	14	1.5	14
11.9	2.4	7	1.5	9	2.1	9	No data collected			
12.2	2.4	8	2.4	8	2.1	7				
12.5	2.4	8	2.4	9	2.1	8				
12.8	2.4	10	2.4	9	2.1	8				
13.1	2.4	11	2.4	6	2.1	6				
13.4	2.4	11	2.4	9	2.4	9				
13.7	2.4	11	2.4	9	2.4	9				
14.0	2.4	10	2.4	10	2.4	10				
14.3	2.4	11	2.4	9	2.7	9				
14.6	2.4	11	2.4	9	2.7	11				
14.9	2.4	12	2.4	9	2.7	11				
15.2	2.4	13	2.4	9	2.7	12				
15.5	2.4	13	2.4	13	2.7	12				
15.9	2.4	12	2.4	11	2.7	14				
16.2	2.4	13	2.4	12	2.7	14				
16.5	2.4	12	2.4	11	2.7	14				
16.8	2.4	12	2.4	11	2.7	13				
17.1	2.4	12	2.4	11	2.7	12				

Table A2. Continued

Pile:	Test Pile		NE		NE		SE		SW		
	Depth (m)	Drop Height (m)	Blows	Drop Height (m)	Blows	Drop Height (m)	Blows	Drop Height (m)	Blows	Drop Height (m)	Blows
	17.4	2.4	13	2.4	10	2.7	13	No data collected			
	17.7	2.4	12	2.4	10	2.4	14				
	18.0	2.4	12	2.4	11	2.4	11				
	18.3	2.4	13	2.4	10	2.4	12				
	18.6	2.4	12	2.4	11	2.4	12				
	18.9	2.4	12	2.4	11	2.4	12				
	19.2	2.4	14	2.4	12	2.4	13				
	19.5	2.4	14	2.4	14	2.4	12				
	19.8	2.4	13	2.4	13	2.4	13				
	20.1	2.4	14	2.4	14	2.4	12				
	20.4	2.4	16	2.4	14	2.4	12				
	20.7	2.4	16	2.4	15	2.4	13				
	21.0	2.4	17	2.4	15	2.4	12				
	21.3			2.4	15	2.4	14				

Table A3. Summary of unit side resistance, T (kN/m²), for the six simplified load-depth curves for the first static load test at Site 2.

Depth Interval (m)	Applied load (kN)					
	60	95	185	385	730	840
0 - 0.5	9.8	19.7	-9.8	-9.8	-2.0	19.7
0.5 - 3.6	4.8	9.5	22.2	34.9	58.7	66.7
3.6 - 15.75	2.4	3.0	6.9	10.0	12.8	12.9
15.75 - 16.8	9.4	-0.9	14.0	25.3	37.4	46.8

Table A4. Summary of unit side resistance, T (kN/m²), for the nine simplified load-depth curves for the second static load test at Site 2.

Depth Interval (m)	Applied load (kN)								
	116	221	321	423	539	621	726	822	933
0 - 0.5	17.7	60.9	80.6	123.8	165.1	190.7	228.0	259.5	289.0
0.5 - 4.0	13.2	19.1	27.0	28.4	35.1	38.5	41.0	46.6	52.8
4.0 - 7.0	5.9	11.8	16.4	22.6	23.3	26.2	33.1	34.1	39.0
7.0 - 15.75	3.7	7.3	11.0	14.6	19.8	21.8	22.0	23.1	19.7
15.75 - 16.8	3.7	9.4	19.7	32.8	44.9	63.7	101.1	128.2	192.8

Table A5. Summary of calculated deflections, Z (mm), for the six simplified load-depth curves for first static load test at Site 2.

Depth Interval (m)	Applied Load (mm)					
	60	95	185	385	730	840
0 - 0.5	0.12	0.14	0.90	3.82	23.8	67.8
0.5 - 3.6	0.08	0.07	0.76	3.52	23.2	67.1
3.6 - 15.75	-0.03	-0.09	0.42	2.63	21.4	65.0
15.75 - 16.8	-0.10	-0.20	0.18	1.95	19.9	63.3

Table A6. Summary of calculated pile deflection, Z (mm), for the nine simplified load-depth curves for the second static load test at Site 2.

Depth Interval (m)	Applied load (kN)								
	116	221	321	423	539	621	726	822	933
0 - 0.5	0.34	0.56	0.85	1.27	1.96	2.46	3.29	4.38	6.64
0.5 - 4.0	0.25	0.41	0.61	0.96	1.57	2.01	2.76	3.78	5.95
4.0 - 7.0	0.14	0.20	0.30	0.53	1.02	1.37	2.00	2.92	4.98
7.0 - 15.75	0.05	0.01	0.01	0.10	0.45	0.68	1.14	1.91	3.76
15.75 - 16.8	0.00	-0.11	-0.18	-0.17	0.07	0.21	0.55	1.20	2.88

Table A7. Summary of unit side resistance, T (kN/m²), for the simplified load-depth curves for the first static load test at Site 3.

Depth Interval (m)	Applied load (kN)							
	234	311	409	496	590	671	769	854
0 - 0.7	205	226.1	264	299.1	332.8	353.8	367.9	412.8
0.7 - 8.8	4.6	78	10	11.4	12.7	13.6	17.1	15.3
8.8 - 12.75	6.5	10.5	13.9	19.9	24.4	30.9	30.9	34.6
12.75 - 16	1.8	3.6	8.2	8.8	11.5	13.3	19.7	25.1
16 - 17	3.9	3.9	7.9	9.8	12.8	15.7	19.7	25.6

Table A8. Summary of unit side resistance, T (kN/m²), for the simplified load-depth curves for the second static load test at Site 3.

Depth Interval (m)	Applied load (kN)						
	114	232	346	453	557	674	781
0 - 0.7	39.3	85.7	113.7	126.4	198.0	221.9	255.6
0.7 - 8.8	5.5	7.9	10.3	13.6	12.5	14.7	16.9
8.8 - 12.75	5.7	14.7	22.1	29.4	31.6	35.1	36.8
12.75 - 16	1.8	1.8	3.3	4.5	7.9	11.8	16.9
16 - 17	2.0	2.9	9.8	15.7	31.5	19.7	20.6

Table A9. Summary of calculated pile deflection, Z (mm), for the simplified load-depth curves for the first static load test at Site 3.

Depth Interval (m)	Applied load (kN)							
	234	311	409	496	590	671	769	854
0 - 0.7	-0.02	0.53	1.44	2.11	2.92	3.63	4.37	5.59
0.7 - 8.8	-0.18	0.26	1.04	1.58	2.25	2.82	3.41	4.49
8.8 - 12.75	-0.36	-0.03	0.58	0.98	1.47	1.88	2.26	3.16
12.75 - 16	-0.41	-0.12	0.42	0.76	1.18	1.52	1.81	2.62
16 - 17	-0.43	-0.16	0.35	0.67	1.05	1.36	1.60	2.37

Table A10. Summary of calculated pile deflection, Z (mm), for the simplified load-depth curves for the second static load test at Site 3.

Depth Interval (m)	Applied load (kN)						
	114	232	346	453	557	674	781
0 - 0.7	0.65	1.29	2.06	2.72	3.59	4.6	5.47
0.7 - 8.8	0.51	0.98	1.57	2.05	2.79	3.61	4.32
8.8 - 12.75	0.36	0.64	1.01	1.26	1.84	2.41	2.91
12.75 - 16	0.32	0.53	0.81	0.98	1.46	1.91	2.32
16 - 17	0.30	0.49	0.73	0.86	1.29	1.68	2.03